**Doctoral Thesis**

# Modeling of Gravitational Wave signals emitted from binary systems containing accretion disk

---


By

**Sangita Chatterjee**

Index No.: 193/16/Phys./25

Registration No.: SOPHY1119316

**Supervisors: Dr. Soumen Mondal & Dr. Prasad Basu**



*A thesis submitted in fulfilment of the requirements for the degree of Doctor of Philosophy in the Relativity & Cosmology Research Center, Department of Physics at the Jadavpur University, Kolkata 700032*

**December, 2023**

# Declaration by the student

I, **Sangita Chatterjee** Index No. **193/16/Phys/25**, Registration No. **SOPHY1119316** dated 15/11/2016, a student of Relativity & Cosmology Research Center, Department of Physics of the PhD Programme of the Jadavpur University, Kolkata 700032 , hereby declare that this thesis is my own work and, to the best of my knowledge, it neither contains materials previously published or written by any other person, nor it has been submitted for any degree/diploma or any other academic award anywhere before.


**Sangita Chatterjee**
Relativity & Cosmology Research Center, Department of Physics
Jadavpur University, Kolkata 700032

JADAVPUR UNIVERSITY
KOLKATA-700032, INDIA

## CERTIFICATE FROM THE SUPERVISORS

This is to certify that the thesis entitled "**Modeling of Gravitational Wave signals emitted from binary systems containing accretion disk**" submitted by Smt **Sangita Chatterjee**( Index No. **193/16/Phys./25**,Registration No.:SOPHY1119316) who got her name registered on **15th November 2016** for the award of Ph. D. (Science) Degree of Jadavpur University, is absolutely based upon her own work under the supervision of **Dr. Soumen Mondal, Associate Professor, Department of Physics, Jadavpur University and Dr. Prasad Basu, Assistant Professor, Department of Physics, Cotton University** and that neither this thesis nor any part of it has been submitted for either any degree / diploma or any other academic award anywhere before.

Soumen Mondal 06/12/2023

**Dr. Soumen Mondal**
**Associate Professor**
**Department of Physics**
**Jadavpur University**
**Kolkata- 700032**

Dr. Soumen Mondal
Associate Professor
Department of Physics
Jadavpur University
Kolkata - 700032

Prasad Basu 06/12/23

**Dr. Prasad Basu**
**Assistant Professor**
**Department of Physics**
**Cotton University**
**Assam 781001**

Dr. Prasad Basu
Assistant Professor
Department of Physics
Cotton University, Guwahati-781001

# Acknowledgements

Obtaining a Ph.D. is a long and difficult process that requires constant self-motivation. I am grateful to several individuals for their invaluable assistance and encouragement during this journey.

I'd want to express my gratitude to my supervisors, Dr. Soumen Mondal and Dr. Prasad Basu. I am grateful to them for selecting me as their graduate student. I'd want to thank them for all of their talks, expertise, and real criticism on my work over the years. Even with their hectic schedules, they always made time for discussion. Their optimistic demeanor and enthusiasm inspired me to broaden my views and seek out interesting problems. I would also like to thank the Department of Physics at Jadavpur University for giving me this opportunity to do my research work. I express my gratitude to all the academic and non-academic staff of Jadavpur University. I thank all the professors who taught me during my PhD coursework. My sincere thanks also goes to my early life teachers, they had greatly shaped my academic inclinations.

I would like to convey my heartfelt thanks to the State Government Fellowship Scheme of Jadavpur University and the DST Women Scientist Scheme-A (WOS-A), Government of India, for financial assistance during the research process. Their financial assistance has really aided me in completing my work effectively.

I would also like to thank all the labmates at the Relativity & Cosmology Research Center, particularly Soumen Bera and Tapan Sasmal, for their help. I'd also like to mention my friends from Jadavpur University, Chetana Ghosal and Bidisha Mondal. These folks are really motivating and lovely company. Regardless of the terrible circumstances, they continued to motivate me over the years.

Next, I am eternally grateful to my wonderful parents, Samir Chatterjee and Krishna Chatterjee, who believed in me even when I was dubious and constantly reminded me to "don't lose faith." Everything I am today and everything I may become tomorrow is a result of their sacrifices. There aren't enough words to express my gratitude to them. They constantly urge me to follow my heart and offer me their complete support, no matter what decision I make. Their unfailing devotion has given me the confidence to confront any problems in my life with optimism. Their unconditional love and trust in me greatly aided me in moving forward. I would like to thank my uncle Sisir Chatterjee for his unconditional support and blessing. I would like to mention my sister, Paramita Chatterjee, with whom I had an extravagant childhood and who I still like spending time with. I would like to mention the name of the sweetest kid, Putu (Preosi). Nothing quite compares to your love; your life was a blessing, but unfortunately, we lost you. We missed you beyond measure.

Among my friends, I like to thank Ripon, Yeasin, Sweet, Fitu, Nishar, Manzar, Sananda, Argha, Soumyadeep, Sraboni, Sampa, Laltu, and Gublu for their well wishes and for making my life more enjoyable. Life here would not have been the same without them.

Finally, a special thanks to the very special person who has accompanied me totally during this whole journey and promised to accompany me for the rest of my life. Thank you, Ripon, for the time spent together and, hopefully, for many more yet to come.

Lastly, I would like to thank everyone that I was unable to include here. It had been a journey that was prolonged and unforgettable!

*To **Preosi(Putu)** you have gone far too soon dear..*

# List of Publications

**Publications in Journals:**

1. **Sangita Chatterjee**, S. Mondal and P. Basu, "Vertical Equilibrium Model for Accretion flow: An exact General Relativistic self consistent analysis" The Astrophysical Journal (ApJ-5.521), 941, 2, 131. doi 10.3847/1538-4357/ac9f15 (Dec 2022).

2. **Sangita Chatterjee**, S. Mondal and P. Basu, "Detectability of gas-riched E/IMRI's in LISA band: Observable signature of transonic accretion flow." .Monthly Notices of the Royal Astronomical Society (MNRAS-5.235), 526, 5612–5627. doi 10.1093/mnras/stad3132 (Oct 2023).

3. P. Basu, **Sangita Chatterjee**, and S. Mondal "Optimal orbital parameters in detecting the gas-riched E/IMRIs in LISA." -under review in MNRAS.

4. **Sangita Chatterjee**, S. Mondal and P. Basu, "Constraining the parameters of an EMRI embedded in accretion disk from the detected GW strain" –Ready for submission.

**Publications in proceedings:**

1. **Sangita Chatterjee**, S. Mondal and P. Basu,"An improved approach to find the height of the accretion disk" Journal of Physics: Conference Series, Volume 1579 article id. 012008 (July,2020)

2. **Sangita Chatterjee**, S. Mondal and P. Basu "Impact of accretion disk on the gravitational wave profile emitted from binary merger" Journal of Physics: Conference Series, Volume 2349 article id 012005 (Oct, 2022)

# Abstract

**Modeling of Gravitational Wave signals emitted from binary systems containing accretion disk**

**Sangita Chatterjee**

**Index No : 193/16/Phys/25 dated 15/11/2016**

The binary systems of compact objects (neutron star, black hole, white dwarf) are one of the most important class of sources of gravitational wave (GW). By analyzing the GW waveform emitted from them one could check various predictions of general relativity both in the weak and strong field limit (Amaro-Seoane et al. and references therein). With the proposed launch of the space based GW detector LISA extreme and intermediate mass ratio inspirals (EMRI/IMRI), in which a stellar mass compact object ($10-10^3 M_\odot$) orbits a central super-massive black hole ($10^5-10^8 M_\odot$), have drawn the special attention of scientific community because of their detectability by LISA. Extreme or Intermediate mass ratio binary systems (E/IMRI) are believed to be present at the centre of the galaxies. For such systems, since the central black hole is extremely massive than its orbiting companion, the companion essentially behaves as a test particle following geodesic of the space-time given solely by the central black hole. Thus, observing the emitted GW from such systems one would be able to trace the trajectory of the orbiting object, from which a map of the space time can be obtained and therefore, test of general theory of relativity(GTR) can be done even in the very strong field regime. Detecting GW signals coming from distant sources is a formidable task as they have very small signal to noise ratio. Matched filtering technique, which basically cross correlates the incoming gravitational-wave signal with a bank of theoretically produced templates representing the expected signal as a function of the parameters of the source, is used for this purpose. It is therefore, extremely important to generate the theoretical wave form accurately, which in turn requires an exact modeling of the dynamics of the companion. Real E/IMRI systems are most likely to have massive accretion disks that may be as massive as the primary supermassive black hole. Therefore, in contrast to its ideal model, the accretion disk is a third crucial part of the actual E/IMRI system. This disk can exert non negligible hydrodynamic drag on the compact objects rotating around the central black hole. Hence, the gravitational wave (GW) signal emitted from an E/IMRI may be modified due to the modified motion of orbiting companion by the influence of hydrodynamic drag of the disk. The purpose of this dissertation is to predict the characteristic signature provided by the accretion disks encircling the center supermassive black hole of an E/IMRI on the emitted gravitational wave signal. As low-frequency (milli-hertz) GW astronomy develops, we expect to soon detect signals from merging SMBH systems. Understanding how an accretion disk affects an inspiralling SMBH binary is the main goal of this research, with the underlying aim of applying this information to interpret and support future GW detections. We study the influence of these disks on the emitted GW profile using a semi-relativistic formalism in the Kerr background. There are several potential accretion disk model and transonic solutions is one of them. We consider the transonic flow to describe the accretion flows around the active galactic nuclei(AGN). The influence of the disks could be identified through the difference in the infall time or from the acquired phase shift due to an extra disk-torque on the companion. Without incorporating such effects leads to error in parameter

estimations such as masses of the companions, chirp mass, and more importantly the emitted GW strains amplitude. We compute the signal-to-noise ratio (SNR) of the detectability of these modifications and found that these changes are detectable through the last few years of observation by LISA (in some cases as small as six months) for EMRIs residing within redshift $z = 1$ from the detector and for the accretion rate of the primary black hole of the order of $\dot{M} = 0.01\dot{M}_E - 1\dot{M}_E$. The emitted GW varies depending on the initial systems orbital parameters and the accretion flow variables. We conduct an accurate investigation, by fixing the disk attributes and by altering the orbital parameters, mass ratio of the EMRI and spin of SMB to obtain the best-fitted optimal orbital parameters to enhance the detection ability of the accretion disk effect from the observed gravitational wave(GW) signal. We also check for the sensitivity of the detection of emitted GW to the chosen hydrodynamic model by varying the disk parameters, accretion rate and duration of observation of E/IMRIs, and find that in comparison with other disk models, transonic solution offers relatively better observable signatures in detecting the gas-riched E/IMRI's within the LISA band. Such observations of GW will help one to probe the nature of the accretion flow and verify various paradigms of accretion physics.

# CONTENTS

# LIST OF FIGURES

# LIST OF TABLES

# Chapter 1

# Introduction

## 1.1 Motivation

One of the major goals of the GW-Astrophysics community is to use the GW observational data to infer the knowledge of extreme space time conditions in the presence of compact objects and to gain information about the unseen BH parameters such as mass, spin, etc., to conclude their astrophysical origins. Gravitational wave astronomy started with the detection of the ripples in space time emitted from a source of a binary merger of two black holes situated almost over a billion light years away using an earth-based detector: Advanced Laser Interferometer Gravitational-wave Observatory (LIGO)(Abbott & et. al., 2016). Ground-based GW detectors made several detections in the high-frequency range from the sources of stellar mass compact objects. To probe the milliHertz frequencies from SMBH, which believed to be present at the center of galaxies, a space-based GW detector e.g. Laser Interferometer Space Antenna (LISA), is in the framing phase. The primary motivation of this dissertation is to achieve an accurate GW waveform for EMRI, including environmental effects, using a general relativistic framework for observation by LISA for the purpose of precise data analysis.

Now this accurate assessment based on the considerations of all the factors introducing errors in gravitational wave (GW) signals is crucial for their full utilization. One can classify these error-producing factors among three types: Theoretical, Astrophysical, and instrumental. The Theoretical challenges appear due to incomplete modeling of gravitational wave templates. Since Einstein's equations of General Relativity (GR) are solved for the source using approximation approaches either analytical or numerical, the templates used for data analysis are not the exact solutions and can induce errors in parameter estimation (Cutler & Vallisneri, 2007). The astrophysical-induced corrections to waveforms arise because one typically assumes the binary is isolated from ambient electromagnetic (EM) or matter fields and external perturbers when modeling GWs from black hole (BH) or neutron star (NS) binary coalescences. In reality, the supermassive black hole (SMBH) in the galactic center is expected to have an obstreperous environment and the possible modifications to the emitted gravitational wave (GW) may arise due to (a) the presence of an accretion disk in a binary system, (b) influence of other gravitating objects (c) tidal disruption if the companion is a star (d) dark matter halos (e) cosmological evolution, etc (Barack & Cutler, 2004a) (see figure 1.1). The Instrumental errors (Carré & Porter, 2010) are related to possible detector-related problems, characterizing detectors' noise strain, lowering the detectable signal-to-noise ratio, distance of the source up to which the detector sensitivity ranges, favorable orientation concerning the desired source, etc. In this work, we consider the most important Astrophysical effects that a thin accretion disk with transonic accretion flow might have

on the emitted gravitational wave from an EMRI that is embedded in it. The accretion scenario is the most interesting one as it provides some of the brightest emissions in the Universe (Lynden-Bell, 1978). Understanding the significance of the disk on the binary BH system and its effects on the GW helps us to probe several astrophysical phenomena. If a coalescing compact BH binary system, encounters a sufficient amount of gas while moving through an accretion disk, it will experience a gravitational force, that can act to either accelerate or decelerate the inspiral. The presence of the disk also indicates that companion BH might get a chance to accrete, which, in turn will change its mass, spin, and momentum. Thus, proper modeling of the source is important as it drifted from the vacuum predictions of GR treatment in the presence of a disk. The detection of GW depends on the matched filtering technique with the theoretically produced waveform templates. If the presence of environmental noises are not included in the templates, it will spoil the precision of GW astronomy.

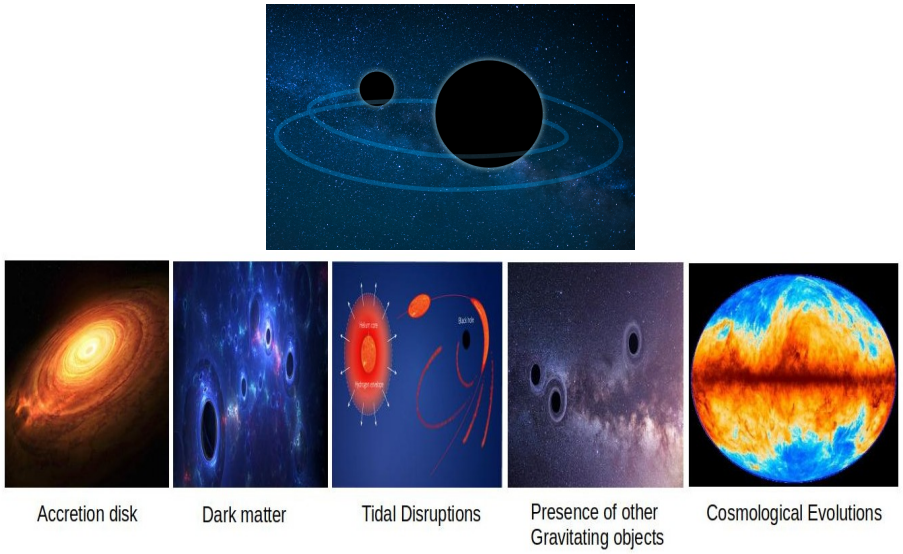


**Figure 1.1:** There are divergent pictures of several perturber i.e. real EMRIs posses impact from the surrounding environment (bottom) instead of suffering only couple interactions(top).

Accretion disks are discussed in length in Chapter 2, we have included a few lines here to explain why we chose accretion disks among other astrophysical challenges.

1. An active galactic nuclei (AGN) in a gas-rich environment will naturally accrete matter in the form of an accretion disk (Figure 2.4). These disks may be as large as the central massive black hole (BH)(Mayer, 2013).

2. Among the aforesaid perturbers, the rest-mass density of the accretion disk surpasses the others.

3. Numerous celestial objects, such as planets, stars, and black holes, are formed and evolve as a result of accretion disks. But, our understanding of these disks is restricted since they can only be investigated through electromagnetic observations. Probing the accretion disk with GW results in vice versa impact for both the accretion theory and for GW field.

Accretion disk: a rapidly circulating fluid governed by central compact objects that gingerly float towards it, is itself a very interesting astrophysical phenomenon and its presence around the

SMBH is inevitable (Mayer, 2013). The hydrodynamical equations that describe an accretion flow are the conservation of mass and energy, equation of state, transport equation, etc. So far several accretion flow models have been developed starting from Bondi spherical flow to the TCAF model. The theory of accretion disks in Astrophysics is still an ongoing area of research. A detailed study of accretion models shows that there is presently no relativistically precise accretion rate in curved space time available. Thus, as our primary investigation advances, we additionally compute a precise relativistic formalism to derive the vertical height of the accretion disk in terms of the spin parameter. This additional motivation of this dissertation aims to present a new relativistic approach to obtain the formula for mass flux in the background of curved space-time and establish a complete general relativistic relation between the vertical height and the accretion rate. Consideration of this mathematically rigorous and correct formulation provides more accurate modeling of transonic accretion flow surrounding the central SMBH and parameter estimation from the emitted GW would provide precise information regarding the existing environments of the binary system.

## 1.2 Compact Objects

In the course of evolution, a normal star maintains its stellar structure by balancing the gravitational attraction inside with the thermal pressure caused by the thermonuclear reactions. A star whose thermal pressure would fail to balance the gravitational attraction started to contract. Depending on the mass of the normal star, the stars end up among the possibility of a white dwarf, neutron star, or black hole. When the mean mass of the main sequence stars is $M \leq 4M_{\odot}$, the white dwarfs(WD) are formed. White dwarf's inward gravitational pull is balanced by the electron degeneracy pressure. There is an upper limit for white dwarf's masses, which is given by the Chandrasekhar limit, $M_{wd} \leq 1.44M_{\odot}$. Compact stars of masses larger than the Chandrasekhar limit are unable to stop the collapse by the electron degeneracy pressure. The star started contracting until the neutron gas in the star became degenerate and provided a balance by neutron degeneracy pressure to the gravitational attraction and formed another compact object named Neutron star (NS). The mass range of an NS lies between $1.4M_{\odot} - 3M_{\odot}$. For a sufficiently high-mass compact object, even the neutron degeneracy pressure is unable to stop its collapse. They have to go on contracting until the gravitational attraction is so strong that even light cannot escape. This configuration of compact objects is known as a black hole (BH)-the strangest thing in existence which is always cherished by curiosity and contradiction. One can classify the black holes based on their masses, in 4 different types: primordial, stellar mass, intermediate mass (IMBH), and supermassive (SMBH). The formation of primordial BHs is described by the perturbation in homogeneous density field. Its masses range from the cloud droplet mass to the mass of the earth. The next one i.e. the stellar mass BH of masses $\geq 4M_{\odot}$ is the product of the supernova explosion of a massive star. IMBHs are assumed to be formed by accretion and their mass is $\geq 10^3 M_{\odot}$. SMBH are known to be present at the center of galaxies. The supermassive star that has evolved to the critical density for collapse is believed to be the progenitor of this type of black hole(mass $\geq 10^6 M_{\odot}$). Its duly presence in the galactic center was initially proposed by the discovery of a quasar (Schmidt, 1963). Lynden-Bell & Rees (1971) also suggests the presence of a massive black hole even in the center of our galaxy Milky Way. In 2020, Andrea M. Ghez and Reinhard Genzel

won the Nobel Prize in physics for the discovery of a massive black hole in our galaxy which they shared with Roger Penrose. Ghez and Genzel observe independently the orbital dynamics of stars near the central parsec of the nucleus and provide the expected mass of the nucleus as four-million solar masses (Ghez & et. al., 2008; Genzel et al., 2010). Very recently, Event Horizon Telescope (EHT) observations and Very Long Baseline Interferometry (VLBI) provided the first image of Sagittarius A* (Sgr A*), the SMBH in the Center of the Milky Way was published (Akiyama & et. al., 2022) along with the 2019 EHT observation of the first image of a massive black hole from our neighborhood galaxy M87 (Event Horizon Telescope Collaboration & Akiyama et. al., 2019). All these events have proved many predictions and enriched Astronomy and Astrophysics. However, in one sentence we can say that black holes are the ultimate fate of every luminous object. This strange object, among all the other astrophysical things, could be mathematically described using only three parameters: mass, momentum, and charge. The exact solution of the Einstein field equation yields four types of black holes based on these three parameters. The simplest one is the Schwarzchild solution which depends only on black hole mass and was calculated considering the gravitational field outside a spherically symmetric system in vacuum. The metric for the same is given by,

$$ds^2 = (1 - \frac{2M}{r})dt^2 - \frac{1}{(1 - \frac{2M}{r})}dr^2 - r^2 d\theta^2 - r^2 \sin^2\theta d\phi^2 \tag{1.1}$$

Next a BH system with mass and momentum is considered and the solution for the same was first calculated by Kerr(1963). In Boyer and Lindquist's reference frame the solution is given in Chapter 3 equation (3.10). For Kerr parameter $a = 0$, this reduce to Schwarzchild case.

Another solution for BH representing it by mass and charge is given by the Reissner-Nordström metric as

$$ds^2 = (1 - \frac{2M}{r} + \frac{Q^2}{r^2})dt^2 - \frac{dr^2}{(1 - \frac{2M}{r} + \frac{Q^2}{r^2})} - r^2 d\theta^2 - r^2 \sin^2\theta d\phi^2 \tag{1.2}$$

For $Q = 0$, this solution turns into Schwarzchild case. The complete solution including mass momentum and charge is provided by the Kerr-Newman metric in Boyer-Lindquist coordinate as,

$$ds^2 = (1 - \frac{2Mr - Q^2}{\Sigma})dt^2 + \frac{(2Mr - Q^2)2a\sin^2\theta}{\Sigma}dtd\phi - \frac{\Sigma}{\Delta}dr^2 - \Sigma d\theta^2 - \frac{A\sin^2\theta}{\Sigma}d\phi^2 \tag{1.3}$$

where $\Delta = r^2 - 2Mr + a^2 + Q^2$, $\Sigma = r^2 + a^2\cos^2\theta$, $(r^2 + a^2)^2 - \Delta a^2 \sin^2\theta$.

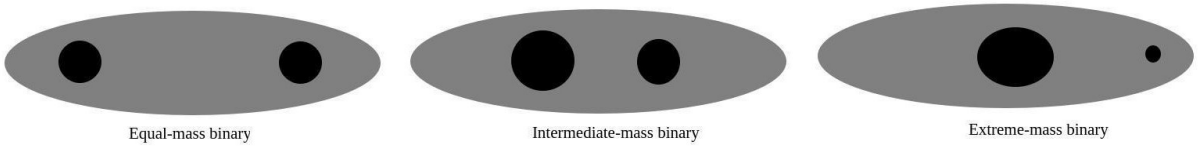


**Figure 1.2:** Binary Black hole

It is well known that almost 85% stars are bound to a binary system, so it is quite obvious that binary compact objects will be the majority compared to a single compact object. For a stellar mass compact object dynamic processes and mutual capture also result in a binary system. The detection of the first GW by LIGO already confirms the existence of such an astrophysical system and by now, several binary systems have been detected. The SMBH binary system is assumed the result of a galaxy merger. Based on the ratio of the masses of the two companions of a binary

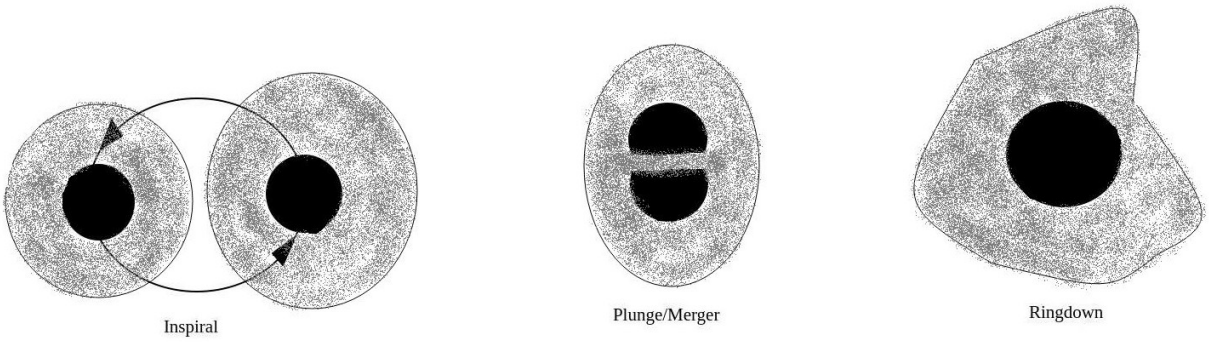


**Figure 1.3:** Life cycle of binary black hole

system, they are classified among equal-mass-ratio binary, intermediate-mass-ratio binary, and extreme-mass-ratio binary systems (see figure 1.2). The orbital dynamics of the binary of compact object is divided into three parts depending on the orbital separation relative to each other : (a) Inspiral stage when the two companions are at a relatively long distance apart and the orbital shrink rate is much smaller than the orbital frequency. This stage is longer compared to others and the GW emitted in this stage is very weak; (b) Plunge and Merger stage when two objects reach the innermost stable circular orbit (ISCO), in this stage, maximum GW emission takes place with maximum amplitude ; (c) Ringdown stage, when the two BH approach the photon sphere of each other and eventually create a single black hole and emit GW with decreasing amplitude from the merger stage (see figure 1.3).

## 1.3 Gravitational wave (GW)

In the 20th century, Einstein formulated the general theory of relativity which describes the gravitational interaction as the outcome of the geometry of space time (Einstein, 1915a,b). Unlike Newtonian gravity theory, in Einstein's GR, both space and time are subject to deformation, and that depends on the mass/energy content of the particular environment. Ever since this theory was formulated, it has undergone a series of tests and passed with dignity. Recently, the scope for experimental/observational study of gravity in the relativistic regime by detecting the emitted gravitational wave (GW) seems possible through the massive achievement of human ingenuity and patience especially thanks to the effort of the decades-long collaboration involving thousands of scientists around the globe working on the gravity wave observatories. The reasons behind the efforts to observe GW are verification of the predictions of GR and to obtain accurate information from distant sources which is impossible through EM waves. The GW emitted and reached the detector almost without scattering by any matter present in its way. So GW even can bring information from the strongest gravity places which EM could not. Because of these aspects, the detection and analysis of the GW remains primary interest to the physicists, they started theoretically computing the GW waveform generated by possible astrophysical systems and devising new detectors to detect such waveform. It becomes like a competition to compute the exact waveform for different types of astrophysical and cosmological sources through analytical calculation and numerical simulation. In GR, Einstein's field equation relates the space-time curvature to the mass-energy density, and in the weak field limit, the wave-like solution of this equation gives

us the GW. Physically, GW is the strain in space time generated due to the fluctuations in the curvature of space time. The properties of this wave are similar to electromagnetic(EM) wave, which is, emitted due to the time variation of dipole moment of charge distribution. In the case of GW, the moment corresponds to the mass distribution and since the dipole moment does not change in this case due to conservation laws of momentum, one has to consider the time variation of the quadrupole moment. In the coming section, we will discuss the mathematical theory for GW, possible sources of GW, and different detectors.

### 1.3.1 Theory of GW

To discuss the basics of gravitational wave theory, we have to derive the wave solution of the Einstein equation. The direct approach is "Linearized theory" applied across a flat space-time, and using an appropriate gauge helps to obtain a simple form of solution in a space devoid of matter. This solution is discussed in many literature, and we follow mainly Misner et al. (1973); Rezzolla (2003); Maggiore (2007).

#### 1.3.1.1 Linearized Einstein Equations

We consider geometrized units in which gravitational constant and speed of light are chosen to be unity i.e. $G = c = 1$. Einstein's field equation that relates an equivalence between matter-energy and curvature is,

$$G_{\mu\nu} = R_{\mu\nu} - \frac{1}{2} g_{\mu\nu} R = 8\pi T_{\mu\nu} \tag{1.4}$$

In this 10 linearly independent equations, $g_{\mu\nu}$ and $G_{\mu\nu}$ are metric and Einstein tensors respectively, $R_{\mu\nu}$ and $R = g^{\mu\nu} R_{\mu\nu}$ are the Ricci tensor and Ricci scalar respectively, and $T_{\mu\nu}$ is the stress-energy tensor of the matter in the space-time under consideration.
Einstein equation (1.4) gives the solution as a gravitational wave under some idealized assumptions. A linearized approach or 'Weak field approximation' to the general theory of relativity is one of them. For the wave-like solution of the equation, a space-time is considered with very slight curvature with a metric which is of flat space-time but for tiny deviation on non-zero curvature, i.e.

$$g_{\mu\nu} = \eta_{\mu\nu} + h_{\mu\nu} + \mathcal{O}([h_{\mu\nu}]^2) \tag{1.5}$$

Where

$$\eta_{\mu\nu} = diag(-1, 1, 1, 1) \tag{1.6}$$

and to stick to the linearized approach it was assumed that

$$|h_{\mu\nu}| \ll 1 \tag{1.7}$$

For this $g_{\mu\nu}$, the linearized Christoffel symbols need to be derived. The expression for Christoffel symbol is,

$$\Gamma^{\mu}_{\alpha\beta} = \frac{1}{2} g^{\mu\nu} (g_{\nu\alpha,\beta} + g_{\beta\nu,\alpha} - g_{\alpha\beta,\nu}) \tag{1.8}$$

Using (1.5) , $\Gamma^{\mu}_{\alpha\beta}$ takes the form,

$$\begin{aligned}\Gamma^{\mu}_{\alpha\beta} &= \frac{1}{2}\eta^{\mu\nu}(h_{\nu\alpha,\beta} + h_{\beta\nu,\alpha} - h_{\alpha\beta,\nu}) \\ &= \frac{1}{2}(h_{\alpha}{}^{\mu}{}_{,\beta} + h_{\beta}{}^{\mu}{}_{,\alpha} - h_{\alpha\beta}{}^{,\mu})\end{aligned} \tag{1.9}$$

Now for the linearized Christoffel symbols the Ricci tensor takes the form,

$$\begin{aligned}R_{\mu\nu} &= \Gamma^{\alpha}_{\mu\nu,\alpha} - \Gamma^{\alpha}_{\mu\alpha,\nu} \\ &= \frac{1}{2}(h_{\mu}{}^{\alpha}{}_{,\nu\alpha} + h_{\nu}{}^{\alpha}{}_{,\mu\alpha} - h_{\mu\nu,\alpha}{}^{\alpha} - h_{\alpha}{}^{\alpha}{}_{,\mu\nu}) \\ &= \frac{1}{2}(h_{\mu}{}^{\alpha}{}_{,\nu\alpha} + h_{\nu}{}^{\alpha}{}_{,\mu\alpha} - h_{\mu\nu,\alpha}{}^{\alpha} - h_{,\mu\nu})\end{aligned} \tag{1.10}$$

where $h = h^{\alpha}_{\alpha} = \eta^{\mu\alpha}h_{\mu\alpha}$ is the trace of the perturbation applied to the flat metric. The Ricci scalar can be obtained by,

$$R \equiv g^{\mu\nu}R_{\mu\nu} \equiv \eta^{\mu\nu}R_{\mu\nu} \tag{1.11}$$

Using all these values in the Einstein equation (1.4) provide us,

$$h_{\mu\alpha,\nu}{}^{\alpha} + h_{\nu\alpha,\mu}{}^{\alpha} - h_{\mu\nu,\alpha}{}^{\alpha} - h_{,\mu\nu} - \eta_{\mu\nu}(h_{\mu\alpha,}{}^{\alpha\beta} - h_{,\alpha}{}^{\alpha}) = 16\pi T_{\mu\nu} \tag{1.12}$$

Here a notation is introduced,

$$\bar{h}_{\mu\nu} = h_{\mu\nu} - \frac{1}{2}\eta_{\mu\nu}h \tag{1.13}$$

and the equation (1.12) takes the form,

$$-\bar{h}_{\mu\nu,\alpha}{}^{\alpha} - \eta_{\mu\nu}\bar{h}_{\alpha\beta,}{}^{\alpha\beta} + \bar{h}_{\nu\alpha,}{}^{\alpha}{}_{\mu} = 16\pi T_{\mu\nu} \tag{1.14}$$

The first term in equation (1.14) is nothing but the d$'$Alembertian operator,

$$\bar{h}_{\mu\nu,\alpha}{}^{\alpha} = \Box\bar{h}_{\mu\nu} \tag{1.15}$$

The eqn.(1.14) is form invariant under a coordinate perturbation $x^{\mu} = x^{\mu} + \xi^{\mu}(x)$, where $\xi^{\mu}$s are of the same order as $h_{\mu\nu}$. Using this coordinate freedom one can choose a coordinate condition (gauge condition) such as eqn.(1.16).

$$\bar{h}^{\mu\alpha}{}_{,\alpha} = 0 \tag{1.16}$$

This is equivalent to the Lorentz gauge condition in electromagnetism and is the weak field version of the harmonic gauge condition $g_{\mu\nu}\Gamma^{\lambda}_{\mu\nu} = 0$. Eqn.(1.16) gives us,

$$\Box\bar{h}_{\mu\nu} = -16\pi T_{\mu\nu} \tag{1.17}$$

The next step towards deriving a wave equation is to consider a vacuum space-time so that $T_{\mu\nu}$ becomes zero. Finally, the Einstein equation takes the form,

$$\Box\bar{h}_{\mu\nu} = 0 \tag{1.18}$$

Thus, in the Lorentz gauge, the propagation of gravitational wave takes place as a perturbation to the flat space-time.

The condition stated by eq (1.16) does not fully fix the coordinates of linearized theory. There is still uncertainty in further "gauge changes" (infinitesimal coordinate transformations), $\xi_\mu$, that meet a limiting criterion in order to preserve eq (1.16),

$$\xi^{\alpha}_{\mu,\alpha} = 0. \tag{1.19}$$

Therefore, then the coordinate transformation is given by,

$$x^{\mu}_{New} = x^{\mu}_{OLD} + \xi_\mu \tag{1.20}$$

and the gauge transformation is,

$$\bar{h}_{\mu\nu New} = \bar{h}_{\mu\nu OLD} - \xi_{\mu,\nu} - \xi_{\nu,\mu} + \eta_{\mu\nu}\xi^{\alpha}_{,\alpha} \tag{1.21}$$

#### 1.3.1.2 Plane wave solution in vacuum

The solution to (1.18) is a plane wave type,

$$\bar{h}_{\mu\nu} = \mathcal{R}[A_{\mu\nu}e^{(ik_\alpha x^\alpha)}] \tag{1.22}$$

$\mathcal{R}$ is there to consider the real part of the solution only. $A$ and $k$ are the amplitude tensor and a null four vector satisfying

$$k_\alpha k^\alpha = 0 \tag{1.23}$$

and

$$A_{\mu\alpha}k^\alpha = 0 \tag{1.24}$$

The plane wave (1.22) travels in the direction $\vec{k} = (k_x, k_y, k_z)/k^0$ with the frequency $\omega \equiv k^0 = (k^j k_j)^{1/2}$. The amplitude tensor $A_{\mu\nu}$ of (1.22) has 10 independent components. But the orthogonality of $A_{\mu\nu}$ and $k_\mu$ ($A_{\mu\alpha}k^\alpha = 0$)remove four of the ten components and the chosen global Lorentz gauge removes 4 more degrees of freedom which allows two degrees of freedom for GW.

From the above condition thus we get,

$$\xi^\mu \equiv -iC^\mu e^{(ik_\beta x^\beta)}. \tag{1.25}$$

#### 1.3.1.3 Transverse and Traceless (TT) gauge

Equ (1.17) provides the basics regarding the GW generation. However, we are more interested in the propagation of GW and its interaction with other bodies, and therefore Equ (1.18) (where $T_{\mu\nu} = 0$ ) is of prime interest.

The d'Alembertian operator $\Box = \eta_{\mu\nu}\partial^\mu\partial^\nu = -\partial_0^2 + \nabla^2$ of equation (1.18) implies that the GW travels with speed of light. We could see from equations (1.16)-(1.21), that the metric's form can be substantially simplified outside of the source however, eq. (1.16) does not entirely fix the gauge; in particular under the transformation eq (1.20), $\partial^\alpha\bar{h}_{\mu\alpha}$ transform as,

$$\partial^\alpha \bar{h}_{\mu\alpha} = \partial^\alpha \bar{h}_{\mu\alpha} - \Box\xi_\mu \tag{1.26}$$

with $\Box\xi_\mu = 0$. This also imply $\Box\zeta_{\mu\nu} = \partial_\mu\xi_\nu + \partial_\nu\xi_\mu - \eta_{\mu\nu}\partial_\rho\xi^\rho = 0$ since $\Box$ commutes with $\partial_\mu$.

Therefore equation (1.21) shows that, from the 6 independent components of $\bar{h}_{\mu\nu}$ which satisfy $\Box\bar{h}_{\mu\nu} = 0$ we can subtract $\zeta_{\mu\nu}$ that satisfy $\Box\zeta_{\mu\nu} = 0$ with 4 arbitrary function $\xi_\mu$. This means we are able to choose the functions to apply four constraints on $h_{\mu\nu}$. More specifically we can choose $\xi^0$ in a way so that we $\bar{h} = 0$ i.e $\bar{h}_{\mu\nu} = h_{\mu\nu}$ and the three function $\xi^i(x)$ so that $h^{0i}(x) = 0$. With this set up, and considering $\mu = 0$, using the Lorentz condition (eq (1.16)) provides,

$$\partial^0 h_{00} + \partial^i h_{0i} = 0 \quad \text{this imply} \quad \partial^0 h_{00} = 0 \tag{1.27}$$

A time independent $h_{00}$ refers to the static part of GW interaction. The GW itself is the time dependent part. For the GW $\partial^0 h_{00} = 0$ implies $h_{00} = 0$ and we also consider the other four components $h_{0\mu} = 0$. Therefore the spatial components $h_{ij}$ are left which under Lorentz gauge gives,

$$\partial^j h_{ij} = 0 \tag{1.28}$$

The condition of vanishing trace is $h^i_i = 0$.

In conclusion, we get,

- **(a) Orthogonality Condition :** If $A$ and $k$ are selected to be orthogonal,

$$A_{\mu\nu}k^\nu = 0 \tag{1.29}$$

four components of the amplitude tensor can be provided.

This condition imply $h_{ij,j} = 0$ i.e. spatial components of $h_{\mu\nu}$ are divergence free.

- **(b) Global Lorentz frame :** A global Lorentz frame relative to an observer with four-velocity $u^\nu$ may be specified, similar to that in Special Relativity. Three components of the amplitude tensor are specified using the orthogonality of the four velocity with the amplitude tensor

$$A_{\mu\nu}u^\nu = 0 \tag{1.30}$$

To obtain one more component of amplitude tensor, further constraint needs to satisfy

$$k^\mu A_{\mu\nu}u^\nu = 0 \tag{1.31}$$

This condition gives $h_{\mu 0} = 0$ i.e. only the spatial components of $h_{\mu\nu}$ are non zero.

- **(c) Infinitesimal gauge transformation :** One final independent component in amplitude tensor obtained by considering an infinitesimal displacement vector $\xi^\mu = iC^\mu e^{ik_\alpha x^\alpha}$ so that,

$$A^\mu_\mu = 0 \tag{1.32}$$

which implies $h = h^j_j = 0$. This implies the spatial components of $h_{\mu\nu}$ are trace free and $\bar{h}_{\mu\nu} = h_{\mu\nu}$.

The conditions mentioned above in (a), (b) and (c) are known as Transverse and Traceless (TT) gauge. By imposing the Lorentz gauge we deduct 4 degrees of freedom from a total 10 and the residual gauge that satisfy $\Box\xi_\mu = 0$ further reduced 4 more degrees of freedom and the GW left with 2 degrees of freedom. The TT gauge can not be applied inside the source as there $\Box\bar{h}_{\mu\nu} \neq 0$.

In this TT gauge, the non zero components of Riemannian Tensor are

$$R_{j0k0} = R_{0j0k} = -R_{j00k} = -R_{0jk0} \tag{1.33}$$

Where we can write

$$R_{j0k0} = -\frac{1}{2}h^{TT}_{jk,00} \tag{1.34}$$

Under TT gauge, $h^{TT}_{jk} \propto e^{i\omega t}$. Therefore $h^{TT}_{jk,00} \sim -\omega^2 e^{i\omega t} \sim R_{j0k0}$. Thus $R_{j0k0} = \frac{1}{2}\omega^2 h^{TT}_{jk}$.

#### 1.3.1.4 Effect of incident gravitational wave on the separation of two particles

To know the effects of incident gravitational wave, we consider the separation between two particles A and B, and also consider a coordinate system $x^{\hat{\alpha}}$ in the position of particle A. The metric along the world line of A can be written as,

$$ds^2 = -d\tau^2 + \delta_{ij}dx^i dx^j + \mathcal{O}(|x^{\hat{j}}|^2)dx^{\hat{\alpha}}dx^{\hat{\beta}} \tag{1.35}$$

Upon incident GW, the geodesic deviation equation can be written as,

$$u^\gamma u^\beta V^\alpha_{;\beta\gamma} = -R^\alpha_{\beta\gamma\delta}u^\beta V^\gamma u^\delta \tag{1.36}$$

or,

$$u^\gamma u^\beta \left(\frac{D^2V^\alpha}{D\tau^2}\right) \equiv u^\gamma u^\beta \left(\frac{d^2V^\alpha}{d\tau^2} + \Gamma^\alpha_{\beta\gamma}\frac{dV^\alpha}{d\tau}\frac{dV^{beta}}{d\tau}\right) = -R^\alpha_{\beta\gamma\delta}u^\beta V^\gamma u^\delta \tag{1.37}$$

Now defining $n^{\hat{j}}_B = x^{\hat{j}}_B - x^{\hat{j}}_A = x^{\hat{j}}_B$, the equation (1.37) take the form,

$$\frac{D^2x^{\hat{j}}_B}{D\tau^2} = -R^{\hat{j}}_{0\hat{k}0}x^{\hat{k}}_B \tag{1.38}$$

Around the particle $A$, the affine connections vanish (i.e. $\Gamma^{\hat{j}}_{\hat{\alpha}\hat{\beta}} = 0$) and the covariant derivative (1.38) can be written as an ordinary differential equation. Again, the coordinate system $x^{\hat{\alpha}}$ moves with the particle $A$, thus the proper time and the coordinate time coincide at first-order metric perturbation. Thus (1.38) take the form,

$$\frac{d^2x^{\hat{j}}_B}{dt^2} = \frac{1}{2}\left(\frac{\partial^2 h^{TT}_{\hat{j}\hat{k}}}{\partial t^2}\right)x^{\hat{k}}_B \tag{1.39}$$

whose solution has the form,

$$x^{\hat{j}}_B(t) = x^{\hat{k}}_B(0)\left[\delta_{\hat{j}\hat{k}} + \frac{1}{2}h^{TT}_{\hat{j}\hat{k}}(t)\right] \tag{1.40}$$

The solution (1.40) indicates in the reference frame co-moving with $A$, the particle $B$ is seen oscillating with an amplitude proportional to $h^{TT}_{\hat{j}\hat{k}}$. Now these waves are transverse and will produce deformation in a plane orthogonal to their direction of propagation. Thus if the two particles lie along the path of propagation, $A$ will record no oscillation.

#### 1.3.1.5 Polarisation of plane waves

If we consider a planar GW propagating along $z$ direction, then,

$$h^{TT}_{xx} = -h^{TT}_{yy} = \mathcal{R}\{A_+ \exp[-i\omega(t-z)]\} \tag{1.41}$$

$$h^{TT}_{xy} = h^{TT}_{yx} = \mathcal{R}\{A_\times \exp[-i\omega(t-z)]\} \tag{1.42}$$

where $A_+$ and $A_\times$ are two modes of polarisation.

The gravitational waves can be decomposed into two linearly or circularly polarised waves. The polarisation tensor for linearly polarised waves is defined by

$$\boldsymbol{e}_+ \equiv \vec{e_x} \bigotimes \vec{e_x} - \vec{e_y} \bigotimes \vec{e_y} \tag{1.43}$$

$$\boldsymbol{e}_\times \equiv \vec{e_x} \bigotimes \vec{e_x} + \vec{e_y} \bigotimes \vec{e_y} \tag{1.44}$$

The polarisation tensor for circularly polarised waves are denoted by $\boldsymbol{e_R}$ (clockwise) and $\boldsymbol{e_L}$ (counter clockwise) and given by,

$$\boldsymbol{e_R} \equiv \frac{e_+ + ie_\times}{\sqrt{2}} \tag{1.45}$$

$$\boldsymbol{e_L} \equiv \frac{e_+ - ie_\times}{\sqrt{2}} \tag{1.46}$$

The $h^{TT}_{ij}$ for linearly polarised case can be written in a matrix form as,

$$h^{TT}_{ij} = \begin{bmatrix} e_+ & e_\times & 0 \\ e_\times & -e_+ & 0 \\ 0 & 0 & 0 \end{bmatrix} cos(\omega t - z) = \Lambda_{ij,kl} h_{kl} \tag{1.47}$$

Where, $\Lambda_{ij,kl} = P_{ik}P_{jl} - \frac{1}{2}P_{ij}P_{kl}$. The projection operator $P_{ij}$ is given by,

$$P_{ij} = \delta_{ij} - n_i n_j \tag{1.48}$$

$\boldsymbol{n}$ is the unit vector along the direction of propagation)

The two polarisation states defined by the matrix above are the basis of GW. Any real combination of these two produced a linearly polarized GW and a complex combination produced an elliptically polarised plane GW. The effects of these two polarisation states on a circular ring are shown in figure 1.4.

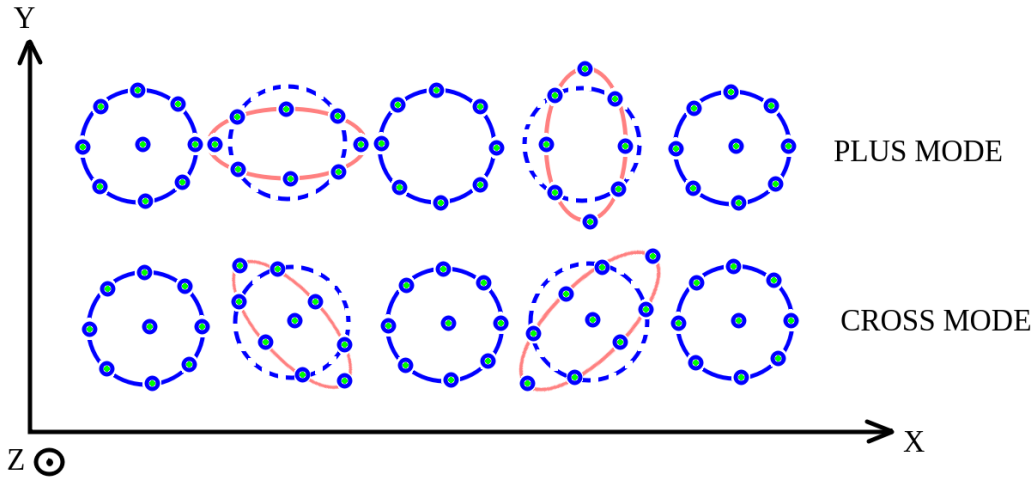


**Figure 1.4:** GW-Polarisation

#### 1.3.1.6 Momentum loss by GW emission

Let us again consider the metric,

$$g_{\mu\nu} = \eta_{\mu\nu} + h_{\mu\nu} \tag{1.49}$$

The Ricci tensor for this can be written as,

$$R_{\mu\nu} = R^{(0)}_{\mu\nu} + R^{(1)}_{\mu\nu} + \mathcal{O}(h^2) \tag{1.50}$$

where $R^{(0)}_{\mu\nu} = 0$. $R^{(1)}_{\mu\nu}$ depict the changes in volume for the $h_{\mu\nu}$ and is given by,

$$R^{(1)}_{\mu\nu} = \frac{1}{2}[\partial^\lambda \partial_\lambda h_{\mu\nu} - \partial_\lambda \partial_\mu h^\lambda_\nu - \partial_\lambda \partial_\nu h^\lambda_\mu + \partial_\mu \partial_\nu h^\lambda_\lambda] \tag{1.51}$$

Now from the Einstein equation we get,

$$R^{(1)}_{\mu\nu} - \frac{1}{2}\eta_{\mu\nu} R^{(1)\lambda}_{\lambda} = -8\pi[T_{\mu\nu} + t_{\mu\nu}] = -8\pi\tau_{\mu\nu} \tag{1.52}$$

Here $\tau_{\mu\nu}$ is the source term and $t_{\mu\nu}$ represented the higher order terms of $G_{\mu\nu}$ given by,

$$t_{\mu\nu} = \frac{1}{8\pi}[G_{\mu\nu} - G^{(1)}_{\mu\nu}] \tag{1.53}$$

where $G^{(1)}_{\mu\nu}$ is the first order terms of Einstein tensor given by,

$$G^{(1)}_{\mu\nu} = R^{(1)}_{\mu\nu} - \frac{1}{2}\eta_{\mu\nu} R^{(1)\lambda}_{\lambda} \tag{1.54}$$

Equation (1.53) is the field equation for $h_{\mu\nu}$ with the source term,

$$\tau_{\mu\nu} = T_{\mu\nu} + t_{\mu\nu} \tag{1.55}$$

Now $G^{(1)}_{\mu\nu}$ satisfy the Linearized Bianchi identity so that we can write,

$$\partial_\mu G^{(1)}_{\mu\nu} = 0 \tag{1.56}$$

The source term mentioned earlier, satisfies the continuity equation and hence

$$\frac{\partial}{\partial x^\mu}\tau^{\mu\nu} = 0 \tag{1.57}$$

Therefore the four vector $P^\mu$ can be defined as,

$$P^\mu = \int \tau^{0\mu} d^3x \tag{1.58}$$

and

$$\frac{dP^\mu}{dt} = -\int \tau^{i\mu} n_i ds \tag{1.59}$$

Here $n_i$ is the unit vector normal to the surface. Now if $\tau_{\mu\nu}$ represents the stress-energy tensor of a gravitational field then $P^\mu$ is the energy-momentum four-vector and $\tau^{i\mu}$ is the flux of the gravitational field.

#### 1.3.1.7 Quadrupole nature of Gravitational Wave

Let us first estimate the amount of energy radiated by an oscillating electric dipole d per unit time in electrodynamics,

$$L_{\text{electric dipole}} = \frac{Energy}{Time} = \frac{2}{3}(\ddot{d}^2) \tag{1.60}$$

where $d = qx$ and $\ddot{d} = q\ddot{x}$, $q$ is the charge and $x$ distance of separation. The dot represent the derivative w.r.t time. A similar analogy for gravitational wave, for a system of N point like particle of mass $m_A(A = 0, 1, ..., N)$ yield,

$$d = \sum_{A=1}^{N} m_A x_A \tag{1.61}$$

Therefore

$$\dot{d} = \sum_{A=1}^{N} m_A \dot{x}_A = p = \text{linear momentum} \tag{1.62}$$

Now conservation of linear momentum gives, $\ddot{d} = \dot{p} = 0$. Therefore

$$L_{\text{mass dipole}} = 0 \tag{1.63}$$

There is no mass dipole radiation in general theory of relativity analogous to no monopole radiation in electrodynamics. Therefore we have to consider higher order moment.

The energy loss by an oscillating electric quadrupole is

$$L_{\text{electric quadrupole}} = \frac{1}{20}(\dddot{Q}_{jk}\dddot{Q}_{jk})^2 \tag{1.64}$$

where

$$\dddot{Q}_{jk} = \sum_{A=1}^{N} q_A \left[ (x_A)_j (x_A)_k - \frac{1}{3} \partial_{jk} (x_A)_i (x_A)^i \right] \tag{1.65}$$

Analogous to this electric quadrupole case, the energy emitted by a mass quadrupole can be found as,

$$L_{\text{mass quadrupole}} = \frac{1}{5} \frac{G}{c^5} \left\langle \dddot{M}_{jk} \dddot{M}_{jk} \right\rangle^2 \tag{1.66}$$

Here $M_{jk}$ is the mass quadrupole given by,

$$M_{jk} = \sum_{A=1}^{N} m_A \left[ (x_A)_j (x_A)_k - \frac{1}{3} \partial_{jk} (x_A)_i (x_A)^i \right] \tag{1.67}$$

By calculating the time derivative of $M_{jk}$ one can calculate the $L_{\text{mass quadrupole}}$ which dimensionally looks like,

$$L_{\text{mass quadrupole}} = \frac{G}{c^5} \frac{(\text{mass of the system}) \times (\text{size of the system})^2}{(\text{time})^3} \sim \frac{GMv^2}{c^5 T} \tag{1.68}$$

This quadrupole moment radiate gravitational wave. This also clearly indicates the mass quadrupole become considerable only for large masses moving with relativistic velocity and this condition only fulfilled by astrophysical sources.

#### 1.3.1.8 The quadrupole formula

Analogous to electrodynamics, to formulate the equations for GW radiation, the assumptions are that the typical velocity of the source is small compared to light speed and has a negligible self-gravity. We consider that the dimension of the source is $d$ and the velocity is $v$. The typical frequency $\omega_{gw} \sim \frac{v}{d} (\therefore \lambda_{gw} \sim \frac{1}{\omega_{gw}})$ . Therefore smaller $v$ implies $\lambda_{gw} \gg d$.

In the Lorentz gauge (Harmonic coordinate condition) the solution for $h_{\mu\nu}$ is given by,

$$\bar{h}_{\mu\nu} = \int e_{\mu\nu}(\vec{x}, \omega) e^{(\vec{k}.\vec{x} - \omega t)} d\omega \tag{1.69}$$

where $\vec{k} = \omega \hat{x}$ and $e_{\mu\nu}(x, \omega) = \frac{4}{x} \tilde{T}_{\mu\nu}(\vec{k}, \omega)$.

where $\tilde{T}_{\mu\nu}(\vec{k}, \omega)$ is the Fourier transform of $T_{\mu\nu}(\vec{k}, \omega)$ given by,

$$\tilde{T}_{\mu\nu}(\vec{k}, \omega) = \int T_{ij}(\vec{x}, \omega) d^3x \tag{1.70}$$

The transverse traceless gauge provide,

$$h_{ij}^{TT} = \Lambda_{ij,lm} \bar{h}_{lm} \tag{1.71}$$

Now for source for which $h_{\mu\nu}$ is small (weak self-gravity), $\tau_{\mu\nu} = T_{\mu\nu}$, therefore from equation (1.55) we get,

$$\frac{\partial^2}{\partial x^i \partial x^j} T^{ij}(\vec{x},\omega) = -\omega^2 T^{00}(\vec{x},\omega) \tag{1.72}$$

Using the above equation, we get,

$$[h_{ij}^{TT}(t,\vec{x})]_{quad} = \frac{1}{r}\frac{2G}{c^4}\Lambda_{ij,kl}(\hat{n})\ddot{M}^{kl}(t-x) \tag{1.73}$$

where,

$$M^{kl} = \left(M^{kl} - \frac{1}{3}\delta^{kl}M_{ii}\right) + \frac{1}{3}\delta^{kl}M_{ii} \tag{1.74}$$

where $M_{ii}$ is the trace of $M_{ij}$. Here we also can define mass quadrupole moment $Q_{ij}$ as

$$Q^{ij} \equiv M^{ij} - \frac{1}{3}\delta^{ij}M_{kk} = \int d^3x\rho(t,x)(x^i x^j - \frac{1}{3}r^2\delta^{ij}) \tag{1.75}$$

Therefore equation (1.73) becomes,

$$[h_{ij}^{TT}(t,\vec{x})]_{quad} = \frac{1}{r}\frac{2G}{c^4}\ddot{Q}_{ij}^{TT}(t-x) \tag{1.76}$$

From here, we can obtain the two polarisation amplitudes for a GW propagating along $z$ direction as,

$$\begin{aligned} h_+ &= \frac{1}{r}\frac{2G}{c^4}(\ddot{M}_{11} - \ddot{M}_{22}) \\ h_\times &= \frac{2}{r}\frac{G}{c^4}\ddot{M}_{12} \end{aligned} \tag{1.77}$$

Using the quadrupole formula loss rates of energy and angular momentum are calculated as,

$$\frac{dE}{dt} = \frac{1}{5}\left\langle \frac{d^3Q_{ij}}{dt^3}\frac{d^3Q_{ij}}{dt^3} \right\rangle \tag{1.78}$$

and

$$\frac{dL}{dt} = \frac{2}{5}\epsilon_{ijk}\left\langle \frac{d^2Q_{jl}}{dt^2}\frac{d^3Q_{lk}}{dt^3} \right\rangle \tag{1.79}$$

The total radiated power in the quadrupole approximation is given by,

$$P_{quad} = \frac{G}{5c^5}\left\langle \dddot{Q}_{ij}\dddot{Q}_{ij} \right\rangle = \frac{G}{5c^5}\left\langle \dddot{M}_{ij}\dddot{M}_{ij} - \frac{1}{3}(\dddot{M}_{kk})^2 \right\rangle \tag{1.80}$$

We calculate these loss rates for an extreme mass ratio inspiral and discussed these in detail in chapter 3.

### 1.3.2 Sources of GW

Systems with perfect spherical symmetry or perfect axisymmetry could not produce GW. Only sources that suffer an acceleration and cause a time variation in quadrupole moment emit GW.

In this section, we provide a short overview on possible sources of GW (for details check Moore et al. (2015); Sathyaprakash & Schutz (2009); Cutler & Thorne (2002); Schutz (1989)).

#### 1.3.2.1 Human made sources

Technically, any mass can produce GW but among all the fundamental interactions, gravitational is the weakest one. As a result, the generated waves within the Earth's environment would be far too weak to detect with present-day detection capacity. Therefore, sources that produce strain within detectable range must be massive ones that are moving at very high speed. Hence sources with astrophysical/cosmological origin are the most eligible system for detection. We categorize these sources as follows.

#### 1.3.2.2 Gravitational collapse of massive stars

Supermassive stars, at the end of their life cycle start to collapse to form neutron stars or BH. The asymmetry associated with the collapse triggers GW radiation, whose amplitude depends on the amount of asymmetry during the star collapse. One of the interesting cases of star collapse results in type II supernova explosions. When the core of a spinning star starts collapsing, the rotation causes nonspherical collapse, and the resultant type II supernova explosion emits GW. When the GW radiation emits, it will take some energy and angular momentum with it, and its amount depends on the geometry of the collapse. The rate of this core collapse supernova in our galaxy Milky way is estimated to be one per few ten years. The amplitude of GW emitted from such systems, is expected to be detected through the ground-based GW detectors.

#### 1.3.2.3 Spinning and Accreting neutron stars

Pulsars that are the spinning neutron stars emit periodic GW if they are not symmetric concerning the spinning axis. The frequency of the emitted signal depends on the frequency of rotation of the neutron star. Often, the neutron stars power up by accretion. Accretion leads to a change in the energy and angular momentum of the system, and a state of configuration reached when the momentum gained by the infalling material leads to a non-axisymmetric rotational instability. Further accretion implied the emission of GW, which carried away the additional angular momentum from the system. These types of sources then become continuous sources for GW.

#### 1.3.2.4 Quasi-normal modes of black hole

When a black hole is perturbed, it vibrates in quasi-normal mode (QNM) and emits GW. The characteristic of the emitted gravitational radiation i.e. its amplitude, frequency, etc depends on the mass and angular momentum of the BH.

#### 1.3.2.5 Stochastic background

GW emitted from different discrete sources (astrophysical, cosmological) even from the processes like Big Bang, superpose and create a random gravitational wave field, which creates a stochastic background of GW signals. Successful observation ability of these signals reveals useful information regarding the early universe, galaxy formation, particle physics, etc.

#### 1.3.2.6 Binary systems

So far, the sources of gravitational waves, that have been directly detected are the compact objects binary system. Until now, almost 22 sources have been detected and among them, 18 are binary BH, 2 are binary NS, and 2 are binary BH-NS systems. From the data, it is confirmed that the most promising sources of GW are the binaries of compact objects. Such systems consist of three parts as discussed in §1.2 and thereby the amplitude and frequency of the emitted GW changes accordingly see figure 1.5. At the initial stage, the binary system emits low frequency GW which lies in the frequency band of LISA. As the binary system moves closer to each other for coalescence, the amplitude and frequency of emitted GW increases. The detectability of ground-based detectors lies in this frequency band. A brief detail on several GW detectors is discussed in the coming section.

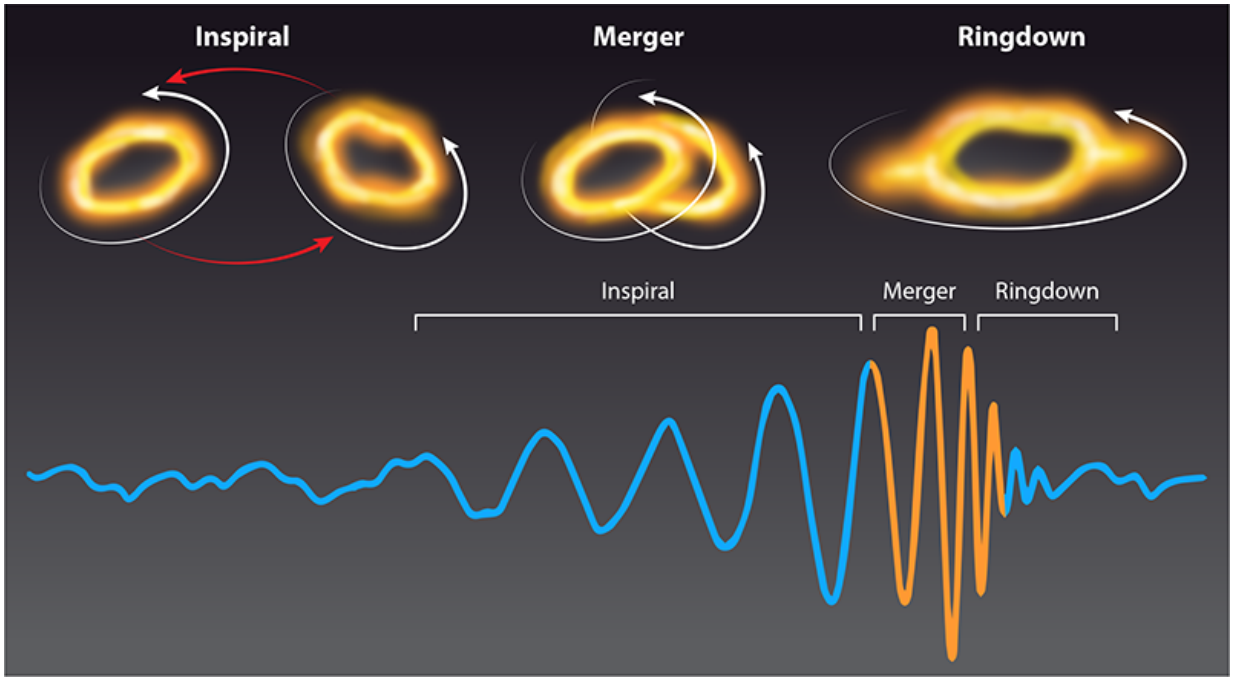


**Figure 1.5:** This depicts a standard gravitational-wave signal from two black holes merging. Post-Newtonian series expansion can explain the inspiral phase, whereas linear perturbation theory (blue parts of the signal) can explain the late portion of the ringdown phase. Nonlinear space time dynamics, however, are evident in the merger and early ringdown (orange part of the signal). Image Credit : (Top) Kip Thorne; (Bottom) Abbott & et. al. (2016); adapted by APS/Carin Cain

### 1.3.3 Detection Of GW

In 1974, Hulse and Taylor (Hulse & Taylor, 1974) provide the first evidence of GW existence by observing the binary pulsar PSR 1913+16, where they explain the shrinking orbiting radius of the system through the emission of GW. This indirect evidence increases the interest of physicists and astrophysicists in the direct observation of GW. However, the main challenge in the way of detection was the very small effect of the GW. The GW is a spherical wave, and its amplitude decreases with the distance from its source. Several detection procedures and hence several detectors, therefore made to detect such a small amplitude wave to predict the dynamics of distant massive objects. Almost 50 years later of indirect evidence of GW provided by Hulse and Taylor,

direct detection and information extraction from the detected waves become possible. According to its characteristic frequencies (see figure 1.6), GWs can be classified following Thorne (1995) as

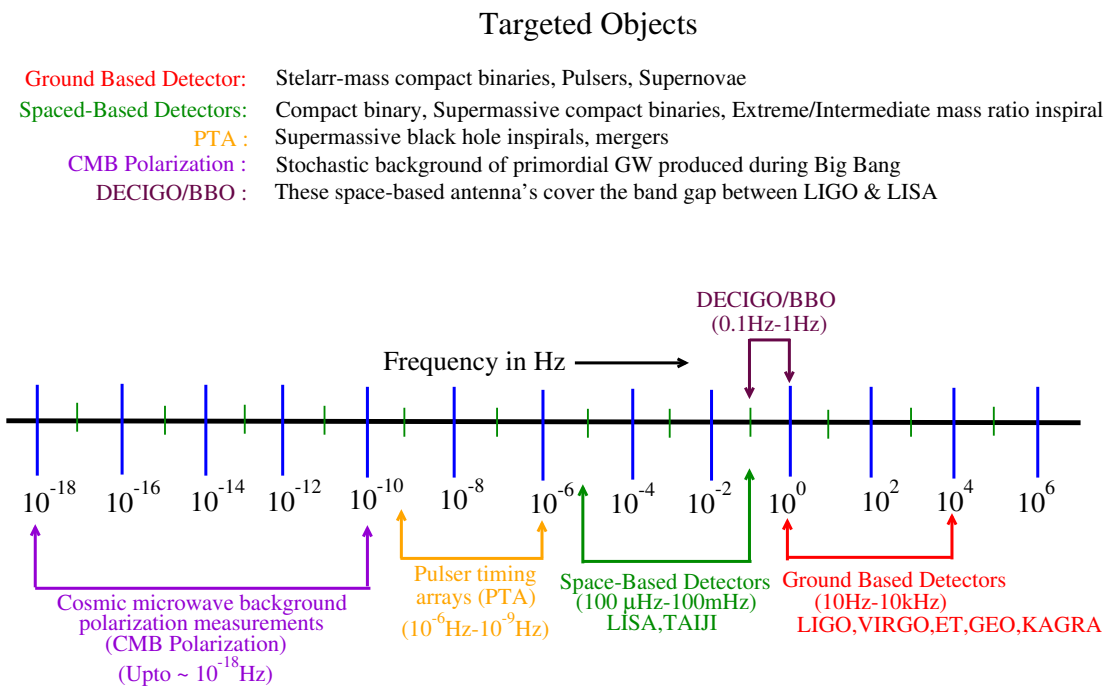


**Figure 1.6:** The GW spectrum and detectors for specified frequency ranges

1. High-frequency band $(1Hz - 10kHz)$
2. Low-frequency band $(100\mu Hz - 1Hz)$
3. Very-low-frequency band $(1nHz - 100nHz)$
4. Extremely-low-frequency band $(1aHz - 1fHz)$.

The detectors accordingly classified as:

1. ground-based GW detectors
2. space-based GW detectors
3. pulsar timing method
4. cosmic microwave background (CMB) methods.

For a more detail classification and associated detectors see Kuroda et al. (2015). Here we discuss different detectors and their working principle in a brief.

#### 1.3.3.1 Ground-Based Detectors

**1.3.3.1.1 Resonant bar detectors** The journey of direct GW detection started with Weber's ground-based resonant-mass detector (Weber, 1969; Ferrari et al., 1982; Weber & Karade, 1986; Weber, 1970) in 1960 while the existence of mere GW was not widely accepted. Weber developed the first resonant detector by using a 2m long cylinder with a diameter of 0.5m, made of Aluminum,

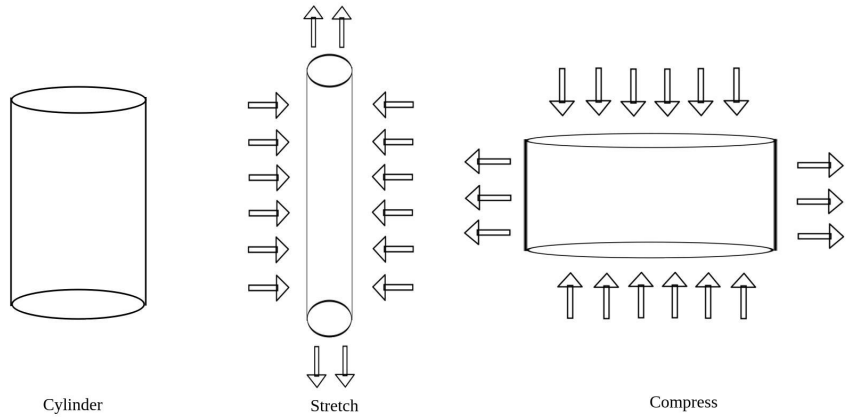


**Figure 1.7:** Resonant bar detector

and placed it in a vacuum at room temperature, in a way that it could be free from the earth's vibration and the acoustic noises. The idea behind this detector is that, as GW is transverse when it travels it manifests itself as a time-dependent strain in space-time. This quadrupole strain is perpendicular to the direction of motion of GW. As a result, when GW travels, it stretches and compresses alternatively the perpendicular axes. Weber uses this idea for a cylinder where any GW passes perpendicular to the cylinder will stretch and compress the length of the cylinder(Figure. 1.7). If the resonant frequency of the cylinder and frequency of GW nearly match, the strain produced by GW on the cylinder would be detectable. Piezoelectric crystals were used here by Weber, when GW causes stretching/compressing, a voltage would develop in the crystal and help to detect the strain caused by GW. This detector developed initially by Weber had a sensitivity of $h \approx 10^{-16}$, where h is the metric perturbation produced by the source. Weber reported several detections but in the meanwhile several independent bar detectors were developed which couldn't reproduce Weber's report thus these detections were not widely accepted. To increase the sensitivity second-generation bar detectors more specifically the cryogenic bar detectors were developed which increase the isolation of the bar and lower the temperature to neglect thermal vibrations and other noises. The dimension of the detectors was also extended to increase the sensitivity. Some of the second generations bar antennas are, given in table 1.1.

These cylindrical bar detectors' geometric design became a disadvantage as they expanded and contracted along their length, making them insensitive to GWs that traveled along their axis. The more convenient shape for bar detectors than is spherical ones. The third generation spherical bar detectors thus proposed namely MiniGRAIL(Netherlands) (Gottardi et al., 2007), TIGA (US) (Merkowitz & Johnson, 1997), SFERA (Italy) (Fafone, 2006), and Mario Schenberg(Sao Paulo, Brazil) (Aguiar & et. al., 2006). The strain sensitivity of these antennas ranges from $4 \times 10^{-21} - 10^{-22}$. These resonant bar detectors are way cheaper than interferometers but can detect only the resonant frequencies, which is a very narrow bandwidth for the detection astronomy. Moreover, the relatively small size of these detectors makes it more prone to get affected by the noises. These difficulties led the researchers to gradually decline these detectors for observations and lead to more focus on the interferometers.

**Table 1.1:** Resonant Bar Detector

| Second Generation Resonant Bar Detectors | | | | | |
|---|---|---|---|---|---|
| Detector's Name | Date | Location | Strain Sensitivity | Materials | Cooled at |
| GEOGRAV / ALTAIR | 1980/1990 | Frascati IFSI-CNR laboratory, Italy | $3 \times 10^{-18}$ | Aluminum bar | $4.2°K$ |
| EXPLORER (Astone et al., 1993) | 1985 | University of Rome, CERN | $7 \times 10^{-19}$ | Aluminum bar | $2°K$ |
| ALLEGRO (Mauceli et al., 1996) | 1991-2008 | Louisiana State University, USA | $7 \times 10^{-19}$ | Aluminum bar | $6°K$ |
| NIOBE (Blair et al., 1995) | 1993 | University of Western Australia at Perth, Australia | $5 \times 10^{-19}$ | Niobium bar | $5°K$ |
| NAUTILUS (Astone et al., 1996) | 1995 | INFN in Frascati, Italy. | $6 \times 10^{-19}$ | Aluminum bar | $0.1°K$ |
| AURIGA (Prodi & et al., 1998) | 1997 | INFN in Legnaro, Italy | $3 \times 10^{-19}$ | Aluminum bar | $0.1°K$ |

**1.3.3.1.2 Interferometers** The advances of laser interferometers over resonant bar detectors come from their gigantic dimension, which helps to observe in a better sensitivity range and from its broad frequency range. Gertsenshtein (Gertsenshteĭn & Pustovoĭt, 1963) first proposed the idea of interferometric detection. After that, in 1973, R. Weiss and collaborators did a detailed study on noise reduction strategies and designed the detector accordingly (Muehlner & Weiss, 1972). A simple diagram for the working GW interferometers with Fabry Perot arms is shown in figure 1.8. Here, the laser source emits light, which gets split at the beam splitter in two paths. After being reflected by the mirrors at the arm ends, the light returns and recombines. The two light rays that return are out of phase and cause destructive interference, as a result, no light got detected by the photo diode. When GW passes through the detector, the two perpendicular arms experience opposite variations in length: one gets compressed, and the other gets stretched, as a result, a small difference in the phase of the light rays occurs. This difference differs from the conditions of destructive interference, and a small fraction of light was detected by the photodiode, which indicates an observation.

Now, a GW with wavelength $\lambda_{GW}$ and magnitude $h$, introduces a change in length of the detectors arm of length $L$, given by $\Delta L = hL$. The most desirable astrophysical sources of GW emit GW of approximate amplitude $10^{-21}$, even for a 5km arm length detectors, the change in length will be of the order of $\Delta L \sim 10^{-19}$. This range is again very small, and sensitive and can be disturbed by several noises like seismic noise, thermal noise, shot noise, or other quantum sources of noise. Thus, the detection using interferometers requires extreme sensitivity and needs

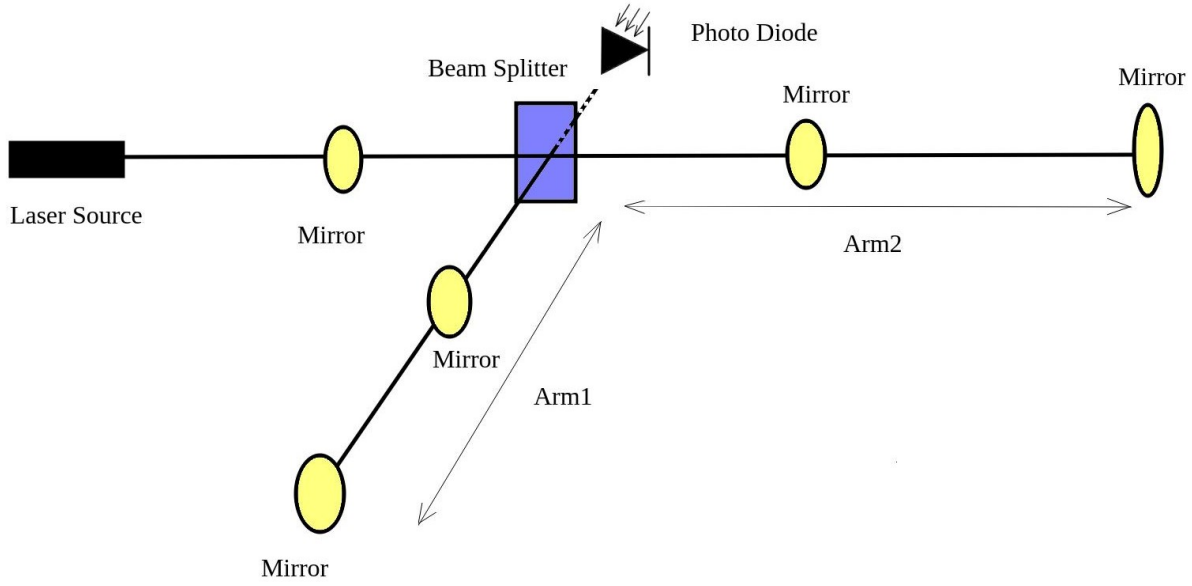


**Figure 1.8:** Gravitational Wave Interferometer

confirmation from more than one detector. With this enthusiasm, several ground-based GW detectors have been built, funded, or proposed in the last 30 years. In the table 1.2, we list some of the ground-based detectors.

#### 1.3.3.2 Pulsar Timing Array(PTA)

PTA covers the nano hertz frequency range from $10^{-9} - 10^{-6} Hz$. Instead of measuring the strain produced by GW in detector length as the ground and spaced-based detectors do, these detectors measure the variation in radio frequency pulse arrival timing from pulsars. Several collaborations work using these detectors e.g.,

- The North American Nanohertz Observatory for Gravitational Waves (NANOGrav)
- The European Pulsar Timing Array (EPTA)
- Parkes Pulsar Timing Array (PPTA)
- Indian Pulsar Timing Array (InPTA)

#### 1.3.3.3 CMB Measurements

The extremely low-frequency GWs up to $10^{-18} Hz$ are coming from the stochastic background produced during the Big Bang. These are too small to be detected by LISA or PTAs. Some of the detectors working in these areas are :

- The Background Imaging of Cosmic Extragalactic Polarization (BICEP1 & 2)
  item Keck Array
- Atacama Cosmology Telescope (ACTpol)

**Table 1.2:** Interferometers

| First Generation Interferometer | | | | |
|---|---|---|---|---|
| Detector's Name | Date | Location | Strain Sensitivity $[1/Hz^{1/2}]$ | Arm Length |
| TAMA 300 | 1995 | Japan | $10^{-21}$ at $1kHz$ | 300 Meter |
| GEO600 | 1995 | Germany | $2.2 \times 10^{-22}$ at 530 Hz | 600 Meter |
| LIGO | 2002 | Hanford & Livingston, US | $2 \times 10^{-23}$ at 200Hz | 4000 Meter |
| CLIO | 2006 | Japan | $10^{-21}$ at 400Hz | 100 Meter |
| Virgo | 2007 | Italy. | $3 \times 10^{-21}$ at $10Hz$ | 3000 Meter |
| Second Generation Interferometer | | | | |
| GEO High Frequency | 2010 | Germany | $2 \times 10^{-22}$ at 600 Hz and slightly above | 600 Meter |
| Advanced LIGO | 2015 | US | $8 \times 10^{-24}$ at 100Hz | 4000 Meter |
| Advanced Virgo | 2011 | Italy | $3 \times 10^{-22}$ at $10Hz$ | 3000 Meter |
| KAGRA | 2020 | Japan | $3 \times 10^{-22}$ at $250Hz$ | 3000Meter |
| IndIGO | 2030 | India | under construction | 4000 Meter |
| Third Generation Interferometer | | | | |
| Einstein Telescope | 2035 | proposed | Proposed | 10000Meter |
| Cosmic Explorar | proposed | proposed | proposed | 40km |

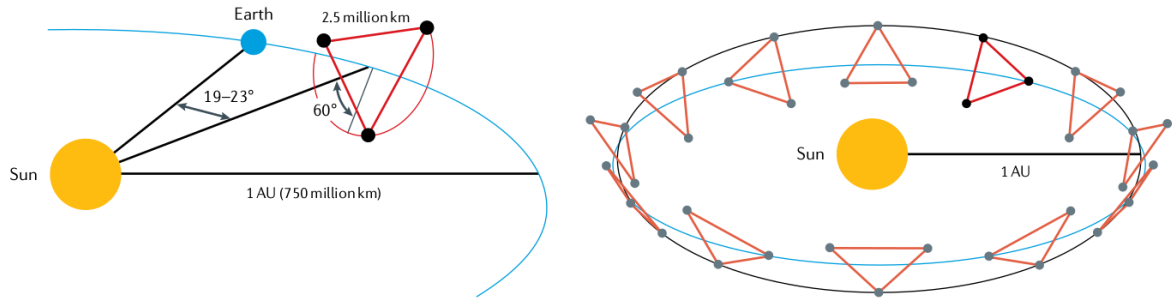


**Figure 1.9:** Figure credit: LISA Consortium.

- POLARization of the Background Radiation (Polarbear)
- The South Pole Telescope (SPTpol)

#### 1.3.3.4 Space-based Detectors-LISA

An upcoming observer of GW and the main motivation of this contribution: Extreme mass ratio inspirals (EMRI) are the targeted source of this Space-based GW detector: Laser Interferometer Space Antenna (LISA) orbiting the sun, which works on similar principles as ground-based interferometers. LISA will be launched by 2035 and help us to do even more precise tests of general relativity by directly mapping the curvature of space time at the event horizons of supermassive black holes. The joint mission of ESA/NASA explores the unknown universe in the milliHertz frequency range $100\mu Hz - 100mHz$. In this range, LISA could observe compact binaries of white dwarfs, neutron stars, and massive black holes. Our target source EMRIs or IMRIs with central black hole mass $M_{SMBH} \equiv 10^4 - 10^6 M_{\odot}$, are lying only in this detector frequency range. The sensitivity to lower frequencies compared to the ground-based detectors becomes possible because these detectors have longer arms and are unaffected by seismic noise. To test noise control abilities and other technical issues before launching LISA, the LISA Pathfinder mission was done successfully in the year 2016 whose outcomes are very optimistic(Armano et al., 2017). In the LISA mission, three spacecraft forming an equilateral triangle of side 2.5 million Km placed in the orbit around the sun (see figure 1.9) are used. LISA sensitivity plot and characteristics strain of a few sources, are shown in figure 1.10, which is taken from (Amaro-Seoane et al., 2017). How long a binary stay in the range of LISA depends on the mass and the mass ratio of the massive black hole binaries. There are some other proposed spaced-based detectors like Taiji(orbiting sun)(Ren et al., 2023), TianQin(orbiting sun) (Ye et al., 2019), DECIGO (orbiting earth) (Yagi & Seto, 2011) which are under construction stage and may start working in the next 10years.

## 1.4 Conclusion

The prospects for modifications to current observatories in this decade and the building or launch of additional observatories in the 2030s provide significant scientific potential for the discipline of GW science in the next decades. There are clear avenues to improving the instruments' sensitivity as well as their frequency range. The network of detectors will both improve and grow in the coming decade, and future planned LISA, DECIGO, ET and CE observatories offer the possibility

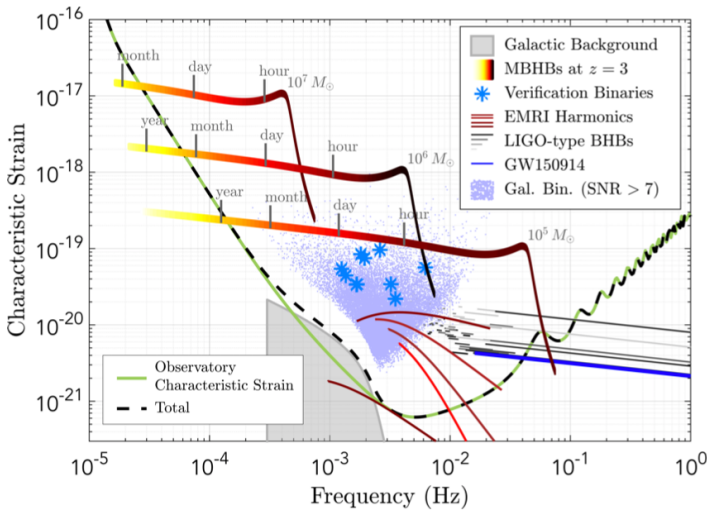


**Figure 1.10:** Characteristic strain of GW signal versus frequency plot. Figure credit: Amaro-Seoane et al. (2017)

of a quieter environment, implementation of detectors of greater complexity, and longer arms. As a result, informations regarding stellar-mass BBH systems, SMBH binaries, dynamics of the galaxies in the Universe will be detectable. These equipment, in conjunction with EM wave and particle detectors, will provide quantitative and qualitative new insights into physics, astrophysics, cosmology, and astronomy. Indeed, GW detectors have offered a new window into the Universe.

# Chapter 2

# Accretion Disk Physics

## 2.1 Introduction

The process via which a gravitational object (such as planets, compact stars, etc.) gathers matter from its surroundings (such as the ambient medium or a binary companion) is known as accretion. It is a highly efficient energy-releasing mechanism, and it is the sole process that allows compact stars to be seen through electromagnetic waves. Recent direct observation of EHT & VLBI provided the first image of black hole (e.g, Sagittarius A$*$ (Akiyama & et. al., 2022)(see figure 2.1), Messier 87 (Event Horizon Telescope Collaboration & Akiyama et. al., 2019)). The bright region around the central black hole of the image is known as a photon ring. This light is certainly emitted from the immediate environment of the black hole which indicates the accumulated matter around it. This evidence helps to support the enormous hard work done by the Astrophysicist

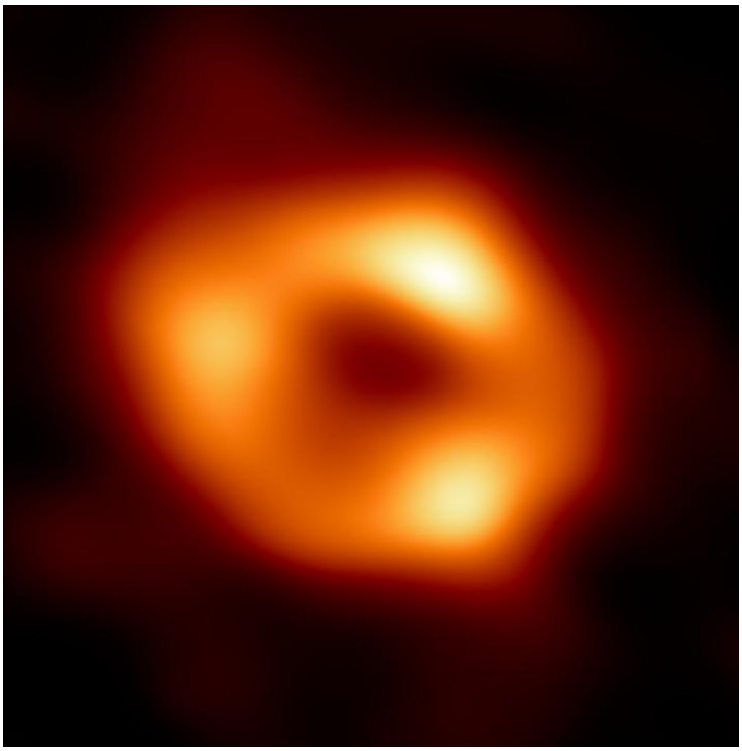

**Figure 2.1:** Sagittarius A$*$ imaged by the Event Horizon Telescope in 2017, released in 2022

to develop various aspects of an accretion disk theory. The ascendancy of accretion flows was proven throughout a range of astronomical phenomena. In nature we can observe several types of accretion disk formation as (figure 2.2),

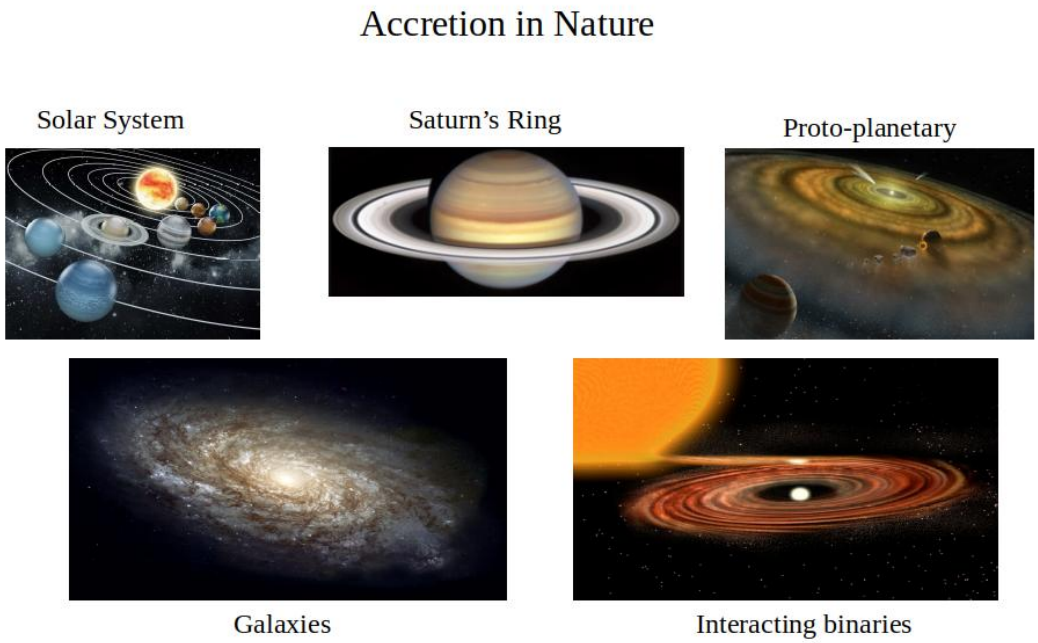


**Figure 2.2:** Astrophysical examples of accretion disk

1. A proto-star (young stellar object) with a gaseous envelope is created when the center region of a dense molecular cloud collapses during star formation, and it eventually settles to a revolving proto-planetary accretion disk (e.g.,NGC 1333, HH30, etc). Within these disks, planets and planetary systems emerge as a result of sedimentation and self-gravity.

2. Cataclysmic variables (CVs) are consisting of a white dwarf and a normal star. When the companion's outer layers overflow the "Roche lobe," the companion loses matter through the spinning binary system's initial Lagrangian point. When the white dwarf is only weakly magnetized, matter forms an accretion disk around it and finally reaches its surface.

3. Most galaxies (e.g., Quasars, Seyfert Galaxies, Radio Galaxies, Blazars) have supermassive (millions to billions of solar masses) black holes at their cores. The black hole accretion in active galactic nuclei (AGN) provides radiative power that generally outshines the host galaxy. The accretion disk is surrounded by a heated corona containing gas clouds. A massive torus of gas and dust partially obscures the core section, affecting the observable appearance of an AGN.

4. The tiny counterpart of a quasar, known as a microquasar, is a compact area that encircles a stellar black hole that has a mass many times greater than that of its companion star. An accretion disk surrounds the black hole, formed by material being drawn from the partner star. Friction can cause this accretion disk to heat up to the point where it starts to release X-rays. These X-ray binaries can be loosely classified into two groups based on the mass of the companion star: low-mass X-ray binaries (LMXBs) and high-mass X-ray binaries (HMXBs), with X-ray pulsars and soft X-ray transients serving as the respective sub-classes.

5. Gamma-ray bursts (GRB) are the universe's most intense explosions. Based on observations, GRBs are cosmic events that are followed by gradually diminishing afterglows. From a few

days to several years, afterglows are seen and tracked. Every piece of information on the inner engines of GRBs is inferred indirectly. Energy requirements, however, point to a similar final product configuration: the creation of a gigantic debris disk with a high rate of accretion surrounding a solar-mass black hole. This disk's accretion time establishes the burst's temporal scale. These time scales indicate that accretion discs in GRBs are probably hyper-accreting.

Prior to making direct observations, Previous research revealed a number of indirect observational signs of an accretion disk, including explanation of strong emissions of about $10^{47} erg/s$, specific radiation like infrared from Be stars, UV, X-ray from the inner core of AGN, and interacting binaries, time variation of a double peak emission line from a CV, Doppler boosting, etc. The most discussed and observed system where accretion plays an important role is a system of double star. An accreting flow's characteristics are determined by the material that was accreted, the source of the accretion, and the flow's geometrical form. When gas or matter infalls on a gravitating object, gravitational energy is released, and matter gets accreted. The rate at which this process took place is known as the mass accretion rate. In this regard, a crucial term is the Eddington rate.

For a given mass, there is a maximum limit for possible luminosity; known as the Eddington luminosity given as,

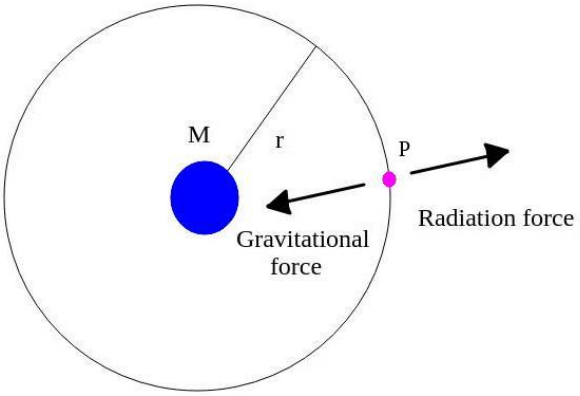


**Figure 2.3:** matter in the vicinity of a gravitating object

$$L_E = \begin{cases} \frac{4\pi cGMm_H}{\sigma_T} \\ \frac{4\pi cGM}{\kappa_{es}} \end{cases} \qquad (\kappa_{es} = \frac{\sigma_T}{m_H}) \tag{2.1}$$

The Eddington luminosity for typical parameters becomes

$$L_E = 1.26 \times 10^{38} \frac{M}{10M_\odot} erg S^{-1} = 3.2 \times 10^4 \frac{M}{10M_\odot} L_\odot \tag{2.2}$$

where $L_\odot = 3.846 \times 10^{33}$erg/s. The maximum possible mass accretion rate associated with this luminosity is known as Eddington mass accretion rate and is given by,

$$\dot{M}_E = \frac{L_E}{c^2} = 1.4 \times 10^{17} \frac{M}{M_\odot} g S^{-1} \tag{2.3}$$

The Wide-field Infrared Survey Explorer (WISE) discovered an extremely luminous infrared galaxy (ELIRG): WISE J224607.57-052635.0 (or W2246-0526 for short) in 2015, which is 12.5 billion light years away from Earth. This was announced as the most luminous known galaxy in the universe (Wu et al., 2015), with a luminosity of $349\times10^{12}L_{\odot}$. The galaxy releases 10,000 times more energy than the Milky Way galaxy, although it is the smaller of the two. With an estimated bolometric luminosity of $1.6 \times 10^{48}$erg/s, SMSS J215728.21-360215.1 ($z = 4.692$) is the most luminous known quasar (Onken et al., 2020). The majority of galactic nuclei exhibit substantially sub-Eddington accretion over the expanse of the cosmos that interests us. While most galaxies are projected to have bolometric luminosities less than the Eddington value (Kollmeier et al., 2006), super-Eddington accretion is also expected in many cases. According to several studies (e.g, (Pounds et al., 1995)), supermassive black holes with accretion rates near or over the Eddington limit, for instance, are thought to be hosted by narrow-line seyfert 1 galaxies (NLS1). It has also been proposed that super-Eddington accretion disks are hosted by the weak emission-line quasars (Luo et al., 2015). According to Mortlock et al. (2011), the existence of $\sim 10^9 M_{\odot}$ black holes around redshift $z = 7$ implies that, for any plausible model of black hole seeds, super-Eddington accretion around supermassive black holes must occur for at least a portion of the time for these black holes to gain so much mass before this redshift.

The flow in accretion theory is made up of discrete particles, and the accretion types are classified into two categories based on the flow geometry. When the flow has no angular momentum, the accretion is spherically symmetric; when the matter has angular momentum, the accretion is disk-shaped. In our work, we analyze an accretion-embedded EMRI system, which consists of an accretion flow encircling the core supermassive Kerr black hole and a companion black hole traveling through it while staying totally submerged within the disk. As a result, the system's two BHs experience two distinct scenarios of accretion dynamics. Next we will discuss these two types of accretion flows in detail.

## 2.2 Importance of accretion disk in binary merger

A significant distinction between Hz and milliHz binary sources of GW is the latter's propensity to be impacted by the surrounding astronomical environment. The presence of astrophysical distractions [see Figure 1.1] can affect the development of the source in the mHz band, confusing predictions made using vacuum templates, decreasing the accuracy of parameter estimation (and hence limiting the utility of tests of general relativity), and introducing biases. In the following comprehensive work, we consider the accretion disk as the perturber among the other surrounding medium (see Chapter 1). Inclusion of the environmental impact offered by an accretion disk in

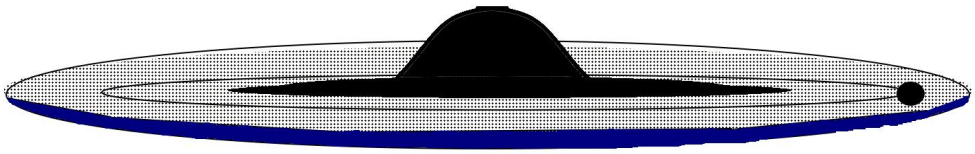

**Figure 2.4:** Test particle (companion BH) moving through an accretion disk around a central black hole

the emitted GW templates would provide a more accurate template for detection. However, this

brings up an excellent and pertinent question: whether the environment-induced change provides such a strong impression that it could be detected by present-day GW detectors? The ground-based LIGO/VIRGO detector has taken credit for the initial GW discovery and made sure to pave the path for new methods of astronomical detection. Therefore, these occurrences have already verified certain general relativity (GR) predictions, but the decade of precision with GWs has only begun. Detectors that have already been introduced will continue to provide detections in the next period at an increasing pace with higher signal-to-noise ratios. This dignified race will be accompanied by the third-generation detectors that are planned, which will aid in more precise detections. Hopefully, the environmental influences on the GW profile can be studied shortly and might help usher in the age of GW accuracy without taking any special restrictions into account. The greatest explanation of gravitation that effectively explains how any kind of matter influences or is affected by space time is Einstein's general relativity (GR). However, GR addresses some of the unanswered questions, such as the bound for graviton mass, dark energy, dark matter, the information loss issue, and the disparity between light speed and the speed of GWs. To solve these problems, a number of theories have been developed, including teleparallel equivalent general relativity, the quantum description of gravity, f(R) gravity, f(T) gravity, scalar-tensor gravity, Gauss-Bonnet gravity, etc. The standard polarizations of GW in GR have two modes; however, the polarization modes in the modified or extended theories have six kinds in four dimensions. The only way to determine which theory of gravity is best characterized is by experimental or observational verification. The most recent and effective approach to confirming these theorems is observation of GW. Several research projects demand direct detection for the information of the deviation from Einstein's GR by observing a GW (as predicted by GR) and analyzing its characterization modes as predicted by other gravity theories. In order to probe these theorems with GW, the sensitivity of the detectors demands that they be more mature and sensitive so that they can be utilized by these relativistic gravity theories (Berti et al., 2018; Capozziello & Bajardi, 2019). Several studies focus on the identification of dark matter densities surrounding compact objects from the associated GW radiation (Coogan et al., 2022; Kavanagh et al., 2020). The presence of dark matter around compact binaries causes dephasing of the emitted GW. The potential of the detector to detect such dephasing must be a next step towards accuracy in astronomy. Interaction among SMBH and bosonic stars, or Q-balls, also leads to changes in the surrounding medium, but this affects the emitted GW waveform by a very small amount compared to the dominant quadrupole term. Therefore, it is highly possible that environmental effects induced by accretion disk, even if small compared to the leading-order effects, will be strong enough to be visible and to modify the higher-order effects significantly. Hence, proper detection of environmental effects is essential to do high-precision science using gravitational waves.

## 2.3 The Accretion Disk & the EMRI formation channels

There are primarily two pathways that comprise the EMRI formation process. Compact objects, e.g., white dwarf (WD), neutron star (NS), or black hole (BH), captured by an SMBH are the typical creation pathway of dry EMRIs (Sigurdsson & Rees, 1997; Amaro-Seoane et al., 2007; Babak et al., 2017; Gair et al., 2017; Amaro-Seoane, 2018). Tidal separation of compact binaries and massive stars that were tidally stripped by an SMBH, i.e., multi-body scattering in the nuclear

star clusters (Miller et al., 2005; Chen & Han, 2018; Wang et al., 2019; Raveh & Perets, 2021) are other approaches. The prerequisite for the generation of EMRI via these processes is that the back-reaction from gravitational wave emission must be the major correction to the orbit relative to relaxation processes such as two-body interactions (i.e., GW emission timescale $t_{GW} < t_R$, the relaxation timescale); otherwise, it might lead to a direct plunge or scatter away from the SMBH. This results in an EMRI that frequently has extremely high eccentricities. Therefore, dry EMRIs are strongly eccentric when they reach the LISA band and are just moderately eccentric at coalescence. Babak et al. (2017); Gair et al. (2017); Fan et al. (2020) predicted that there will be a few to thousands of observable dry EMRIs every year by space-based detectors, taking into account a number of astrophysical uncertainties. The detectability of the dry EMRI rate does, however, decrease in rates by about a factor 3, as calculated in Vázquez-Aceves et al. (2022).

Another EMRI formation channel, a wet formation channel where an already present accretion disk around a supermassive black hole drags into it, aligns the inclined orbit of a stellar black hole by exerting hydrodynamic drag or dynamical friction on the orbiting stars. In-situ star formation within the accretion disk itself may also occur (Sigurdsson & Rees, 1997; Amaro-Seoane et al., 2007; Babak et al., 2017; Gair et al., 2017; Amaro-Seoane, 2018; Miller et al., 2005; Chen & Han, 2018; Wang et al., 2019; Raveh & Perets, 2021; Derdzinski & Mayer, 2023). The addition of a wet channel may increase the EMRI production rate by orders of magnitude (Tagawa et al., 2020; Pan & Yang, 2021; Pan et al., 2021; Vázquez-Aceves et al., 2022). So regardless of the differences between the various disk models taken into account, the existence of disks often increases the EMRI production rate by orders of magnitude (Tagawa et al., 2020; Pan & Yang, 2021; Pan et al., 2021; Vázquez-Aceves et al., 2022). Therefore, these wet EMRIs have a thus far new potential to investigate the fundamental laws of gravity since the disk-environmental impacts could result in an observable phase shift in the EMRI wave-form (Yunes et al., 2011; Kocsis et al., 2011; Barausse et al., 2014). Furthermore, wet EMRIs are expected to be circular in the LISA band due to the effective eccentricity damping by the density waves, whereas dry ones have moderate eccentricity as they approach the merger stage. This makes eccentricity measurements an interesting way to distinguish these wet EMRIs from dry ones. Readers are referred to Pan et al. (2021) : Table I, where LISA detectable rates were tabulated and shown wet EMRI formation is evidently an important or even dominant channel.

## 2.4 Accretion around the companion BH

When an accretion disk is present in a system of binary compact objects on the equatorial plane of the central supermassive black hole (SMBH), the companion black hole, which is entirely immersed in the disk, must travel across it. As a result of this obstruction, the companion's motion is subjected to extra forces known as self-accretion & dynamical friction. Because the companion is entirely immersed in the disk, it will accrete spherically owing to its associated gravitational aspects and suffer momentum loss. Again, as it moves across the disk, the companion black hole interacts gravitationally with the background medium, changing its velocity and hence its momentum. When GW is released from any system, it depletes its momentum. The existence of the disk, on the other hand, adds to additional momentum loss in addition to the loss caused by GW emission [Discussed in details in chapter 3].

As discussed, the companion BH is completely immersed within the accretion disk surrounding the central SMBH, it will start accreting spherically. There are two famous and simplest accretion solutions that describes this category where the accreting material has a net angular momentum zero are given as:

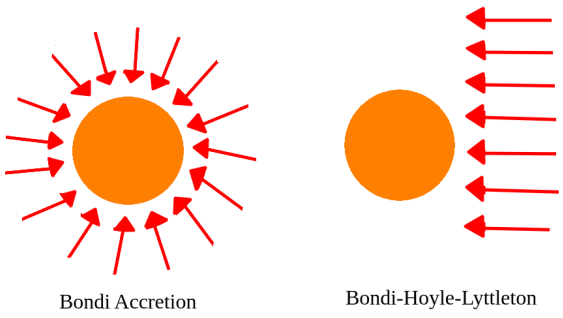


**Figure 2.5:** Momentum-less matter accretion

1. Bondi-Hoyle-Lyttleton Accretion (Hoyle & Lyttleton, 1939): Accreting matter possesses uniform velocity at a large distance. This model is applied to wind accretion in highly massive X-ray binaries, the center of the hot accretion disk, etc.

2. Bondi Accretion Bondi (1952): Matter has pure radially accreting motion. (see figure 2.5). These types of accretion flow models are applied to: the sun, compact objects accreting interstellar matter, accretion on a star, core collapse supernovae, etc.

Here, we briefly discuss this spherical accretion flow or the Bondi flow that the companion BH undergo while moving through the accretion disk.

### 2.4.1 Spherically symmetric flows-Bondi Flow

Hoyle & Lyttleton (1939) performed the first derivation of the accretion rate for a star moving through cold gas and also examined the change in luminosity of a sun-like star due to its passage through an interstellar gas cloud. In this study, the effect of pressure was ignored. Later, Bondi (1952) considered an isolated accreting object in an ambient where matter accreted onto it spherically symmetrically and described the infall of gas onto a gravitating object by a polytropic equation. Bondi's formulation is also relevant in the case of outflows, i.e., for winds. This spherical accretion solution is also known as Bondi accretion.

Let an isolated point object of mass $M$ be surrounded by a spherically symmetric (see figure 2.6) steady ($\frac{d}{dt} = 0$) inviscid and polytropic flow that is one-dimensional in the radial direction. The point object consideration implies no increment in mass of the accreting star (to make no changes in the total gravitating field). The contributions from the fields of magnetics and radiation are ignored. The flow characteristic depends inclusively on the polytropic index, i.e., for $\gamma = 1 \rightarrow$ isothermal flow, for $\gamma = 5/3 \rightarrow$ adiabatic monoatomic, for $\gamma = 4/3 \rightarrow$ adiabatic monoatomic and relativistic, etc. Further, the flow is considered to have uniform density ($\rho_\infty > 0$) and zero velocity ($v_\infty = 0$) at very large distances.

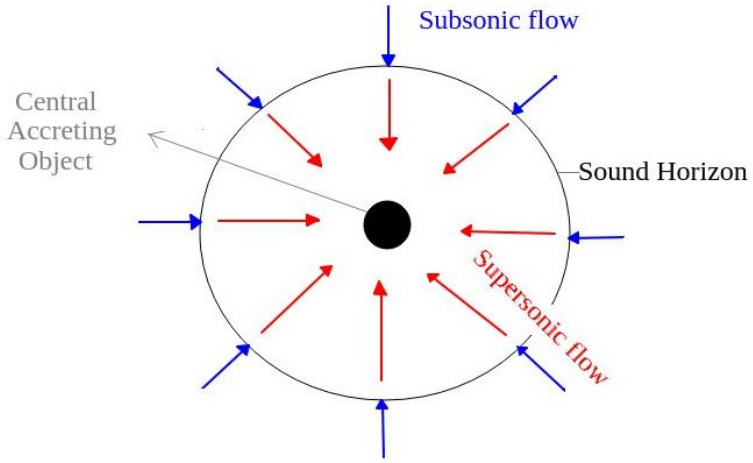


**Figure 2.6:** Bondi accretion

For a steady, spherical accretion of adiabatic gas onto a stationary non rotating black hole, the equation of state is given by,

$$p = K\rho^{\gamma} \tag{2.4}$$

$K\&\gamma$ are adiabatic constant and index. The sound speed is $a_s = \sqrt{\frac{dp}{d\rho}} = \sqrt{\frac{\gamma P}{\rho}}$. The flow then completely governed by the Euler equation

$$u\frac{du}{dr} = -\frac{1}{\rho}\frac{dp}{dr} - \frac{GM}{r^2} \tag{2.5}$$

and the continuity equation,

$$\nabla.(\rho u) = \frac{1}{r^2}\frac{d}{dr}(\rho u r^2) = 0 \tag{2.6}$$

### 2.4.2 Transonic nature of the flow

At a very large distance, i.e., when $r \to \infty$ from the central accreting object, the influence of gravity is very negligible. As a result, the accreting flow would feel a very negligible gravitational pull and would possess a very low, non-zero sound speed. Now, as the matter moves forward toward the central object, the flow velocity increases to be subsonic at a distance $r$. The gravitational pull becomes significant as the flow moves closer to it, and as a result, the flow velocity increases. Near the event horizon, it becomes comparable to light velocity $c$. This indicates that the flow must pass through a sonic point. To find out the location of the sonic point, we rewrite the equation (2.6), as

$$\frac{\rho'}{\rho} + \frac{u'}{u} + \frac{2}{r} = 0 \tag{2.7}$$

The prime denotes the derivative w.r.t. $r$. The Euler equation takes the form,

$$uu' + a_s^2\frac{\rho'}{\rho} + \frac{GM}{r^2} = 0 \tag{2.8}$$

Solving the above two equations we obtain,

$$u' = \frac{D_1}{D} \qquad \& \qquad \rho' = -\frac{D_2}{D} \tag{2.9}$$

where

$$\begin{aligned} D_1 &= \frac{2a^2/r - GM/r^2}{\rho} \\ D_2 &= \frac{2u^2/r - GM/r^2}{u} \\ D &= \frac{u^2 - a^2}{u\rho} \end{aligned} \tag{2.10}$$

As $u'$ is always finite, if the denominator of the above equation at some point is null, the numerator will also disappear at that point. Such points are called critical points, and the condition for the same is given by:

$$u_c^2 = a_{s,c}^2 = \frac{GM}{2r_c} \qquad c \text{ stands for critical points} \tag{2.11}$$

The Mach number ($M = \frac{u}{a_s}$) is unity at these critical points; therefore, these points can be said to be the sonic points ($r_c$). That means, at this point, a sound horizon exists before which the flows are subsonic in nature, and after that, the flow is supersonic. Thus, this flow is transonic in nature. To understand the transonic nature of the flow, the flow variables at the critical points are expressed in terms of the sound speed (Chakrabarti, 1990a).

$$a_{s,c} = \left(\frac{n}{n-3/2}\right)^{\frac{1}{2}} a_{s\infty} \qquad a_{s\infty} \text{ is the sound speed at infinity} \tag{2.12}$$

The above equation shows that the flow is transonic in nature if $n > 3/2$. This correlates the $\mathscr{M}$ and $\mathcal{E}$, and the accretion rate can be written as,

$$\dot{\mathscr{M}}_c = \frac{1}{4}\left(\frac{n a_{s\infty}}{n-3/2}\right)^{n-3/2} \tag{2.13}$$

The figure 2.7 represent mach number vs logarithmic radial distance depicts the integral curves of the flow. The physically significant transonic solutions are those that connects from the star surface to infinity ($ABC\&A'BC'$). The contours have constant accretion rate $\dot{\mathscr{M}}$. The radial velocity for the solution $ABC$ is subsonic at far distances and super sonic near the black hole. On the other hand for the solution $A'BC'$, the radial velocity is subsonic on the surface of the star and supersonic at infinity.

For a more detailed study on Bondi flow at the critical points, see Chakrabarti (1990a).

$$a_s^2 = u_s^2 = \left(\frac{2}{5-3\gamma}\right) a_{s,\infty}^2 \tag{2.14}$$

and

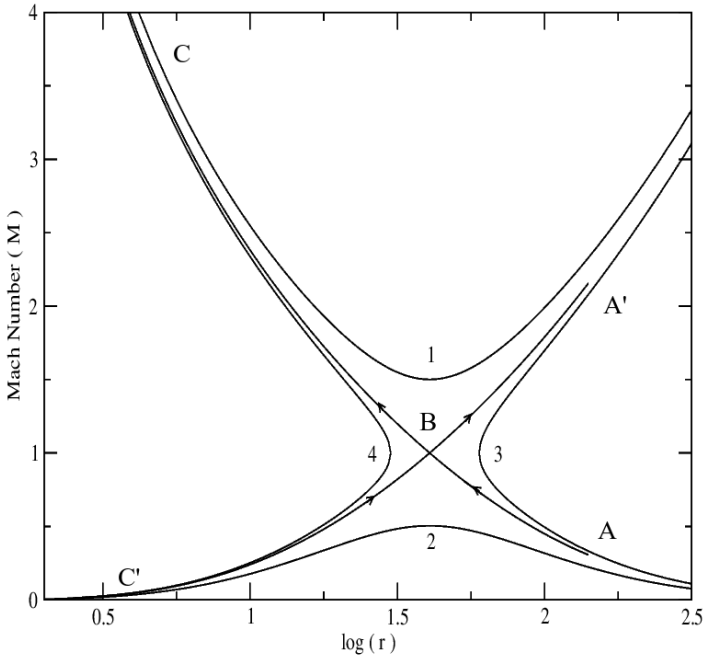


**Figure 2.7:** Phase space trajectory of Bondi flow

$$r_s = \left(\frac{5-3\gamma}{4}\right)\frac{GM}{a_{s,\infty}^2} \tag{2.15}$$

Using

$$\rho = \rho_\infty \left(\frac{a_s}{a_{s,\infty}}\right)^{\frac{2}{(\gamma-1)}} \tag{2.16}$$

one can obtain the mass accretion rate as,

$$\dot{M} = 4\pi\rho_\infty u_s r_s^2 \left(\frac{a_s}{a_{s,\infty}}\right)^{\frac{1}{(\gamma-1)}} = 4\pi\lambda\rho_\infty a_{s,\infty}\left(\frac{GM}{a_{s,\infty}^2}\right)2 \tag{2.17}$$

With some modifications, the Bondi solution may be used to describe the situation of accretion onto a moving black hole in a homogeneous medium. The alterations are negligible if the object is traveling extremely subsonically in the ambient medium at a velocity $V \ll a_{s,\infty}$. The impact of the object's motion is greater if it is traveling at an arbitrary (non relativistic) speed $V > a_{s,\infty}$. The factor $(a_{s,\infty}^2 + v^2)$ must be used instead of the value $a_{s,\infty}^2$, which appears in the Bondi solution for the accretion rate, density, temperature profile, and so forth. The accretion rate thus becomes,

$$\dot{M} = \frac{4\pi\lambda(GM)^2\rho_\infty}{(a_{s,\infty}^2 + v^2)^{\frac{3}{2}}} \tag{2.18}$$

where $\lambda$ is a constant of order of unity and given by,

$$\lambda = \left(\frac{1}{2}\right)^{\frac{(\gamma+1)}{2(\gamma-1)}}\left(\frac{5-3\gamma}{4}\right)^{\frac{-(5-3\gamma)}{2(\gamma-1)}} \tag{2.19}$$

The companion BH accrete with the mass accretion rate given by equation (2.18).

### 2.4.3 Importance of Bondi flows in Gravitational wave Physics

In general, the existence of an accretion disk in a binary system of compact objects is ignored while analyzing its gravity wave emission characteristics. However, the inclusion of the accretion disk around the black hole and the investigation of its impact on GW emissions have already proved their importance. The drag experienced by the companion black hole as a result of its self-accretion is one of the physical processes that is likely to impact the emitted wave amplitude and its detectibility, both for non-equatorial orbits crossing the disk only twice per revolution and for equatorial orbits embedded in the disk. Bondi & Hoyle's study of spherically symmetric solutions (Bondi, 1952) is used to estimate these transfers of energy and momentum from the disk to the companion (Shapiro & Teukolsky, 1983; Karas & Šubr, 2001; Barausse & Rezzolla, 2008; Basu et al., 2008; Kocsis et al., 2011; Derdzinski et al., 2019a). This is also numerically verified in (Petrich et al., 1989; Font et al., 1998; Font & Ibáñez, 1998; Font et al., 1999). In our study of modeling GW emission from EMRIs containing a transonic flow, the companion's self-accretion is also studied using these spherically symmetric flows.

## 2.5 Accretion around the central SMBH

The spherically symmetric accretion obeys the maximum luminosity rules set by the Eddington Luminosity. However, the existence of super-Eddington luminosity cases cannot be explained by this type of accretion solution. The exceed in luminosity can be explained in terms of conversion efficiency, non-spherical accretion, geometric variation, radiation-matter interaction, gas pressure gradient, etc. Research on several binary systems reveals that there are other types of accretion solutions that exist, are based on angular momentum transport. Many studies are devoted to studying the mechanisms responsible for this outward angular momentum transport in accretion disks. In the Newtonian gravity theory, the angular velocity of a particle in a circular orbit of radius r surrounding a point mass $M$ is given by,

$$\Omega_K = \sqrt{\frac{GM}{r^3}} \tag{2.20}$$

Here, $K$ denotes the Keplerian orbit. The specific angular momentum is then

$$l = r^2\Omega_K = \sqrt{GMr} \tag{2.21}$$

This confirms that particles or objects bound to the orbit of any compact object or star possess specific angular momentum, which immediately leads to the central problem of accretion physics. These objects must then lose angular momentum before they can move into an orbit with a smaller radius $r$ and be accreted. There are two paths through which this momentum could be transported. One is exchanging momentum with others so that one losing momentum goes in and the one gaining momentum moves out. The other way is to consider that the whole system is not isolated and could lose momentum as a whole.

The accretion disk formation surrounding binary star when the accreting matter possess angular momentum took place in two ways: (a) Roche lobe overflow and (b) wind-fed accretion. However, the matter accretion surrounding the central SMBH in an active galactic nuclei (AGN)

is our main interest as we consider an EMRI which are expected to form in an AGN. The disk formation mechanism in an AGN is briefly discussed in the next sections.

### 2.5.1 AGN Accretion

Active galactic nuclei (AGN) galaxies are a kind of galaxy distinguished by an excessive brightness emanating from the galaxy's core that cannot be explained by the presence of stars. This extraordinary brightness is commonly acknowledged by the primary source of radiation from SMBH accretion process. Galaxies are divided into distinct categories based on their orientation with regard to the line of sight, commonly known as the AGN unified model. A graphic illustrating our current knowledge of the AGN unified model is presented in figure 2.8. It has a wide line region (BLR), a hot X-ray corona, and an accretion disk around the SMBH. The gas that spins around the SMBH causes the emission lines to undergo a Doppler shift, giving the BLR its name. Depending on the line of sight, a dusty torus enveloping these internal AGN formations farther from the SMBH obstructs their emission. Lastly, the gas in the narrow-line region (NLR) on the periphery is unaffected by the high velocities surrounding the BLR and accretion disk. Bipolar synchrotron jets are occasionally seen in AGN galaxies, particularly in radio-loud galaxies. Different kinds of AGN galaxies will be identified based on their line of sight and emission at various wavelengths. The term "low and high excitation radio galaxies" (LERG/HERG) refers to AGN galaxies that have a bipolar jet. These galaxies can be classified into several types, such as BL Lac, optically violent variables (OVV), narrow-line radio galaxy (NLRG), broad-line radio galaxy (BLRG), steep spectrum radio quasar (SSRQ), and Blazers (BL Lacs). Quasi-stellar objects (QSOs) are another class of AGNs characterized primarily by high accretion rates (EM power). Last but not least, Seyfert galaxies are those with low accretion rates and radio emission levels. Depending on whether the torus inhibits the BLR's emission, Seyfert's can be classified as Type I or Type II. For this reason, narrow emission-line galaxies (NELG) are another classification for Seyfert 2 galaxies. The inner region shown by the red colour is what AGN accretion looks like. In our work we concentrate in this region. Over the past 70 years, accretion surrounding black holes has been thoroughly investigated. When the surrounding medium is initially at rest, accumulation can take place via a spherically symmetric inflow of matter. We have already talked about this process, which is called the classical Bondi flow. On the other hand, matter would spiral inward through a disk-type formation rather than exhibit spherically symmetric flow when the infalling gas possesses initial angular momentum. This is a largely plausible scenario. With a dynamical period far longer than that of Bondi flow, matter in this disk gradually moves toward the Black Hole by transmitting angular momentum outward. In active galactic nuclei, the matter-accretion took place due to wind-fed accretion and tidal disruptions. How matter moves towards the central CO determines whether it will take the form of a disk or directly fall onto center. However, the matter that accreted must be forced down to $\equiv 10pc$ before it becomes subject to the gravitational pull of the central BH due to the significant size gap between the host galaxy and the BH. Angular momentum is the powerful force that must be overcome in order to transport the gas from the host galaxy into the region of the BH: for the gas to go from a stable orbit at $r = 10kpc$ to $r = 10pc$, it must lose almost 99.9% of its angular momentum. Mapping the gas that comes from the host galaxy into the BH's neighborhood and figuring out what triggers AGN activity are

the two main hurdles. Large-scale gravitational torques have the power to remove large quantities of angular momentum and push gas toward the center parts of galaxies. Examples of these torques are galaxy bars, galaxy interactions, and galaxy major mergers. It is anticipated that smaller-scale processes, such as nested bars and nuclear spirals, will push the gas down to around $10 - 100$ pc, whereas the gravitational torques these large-scale processes impose on the gas will have little influence on sub-kpc scales. Consequently, the majority opinion now in place holds that all gas-rich galaxies experience gas intake from kpc that scales down to the core $\sim 10 - 100$ pc area. A sequence of gravitational instabilities pushes the gas into the core region, aiding in the gas's transfer of angular momentum in the process. It may not come as expected that the most distinct AGN activity triggers in the local Universe occur at the smallest scales, since the gas inflow time from the host galaxy to the BH accretion disk's pc-scale is probably greater than or equal to approximately $10^8$ years.

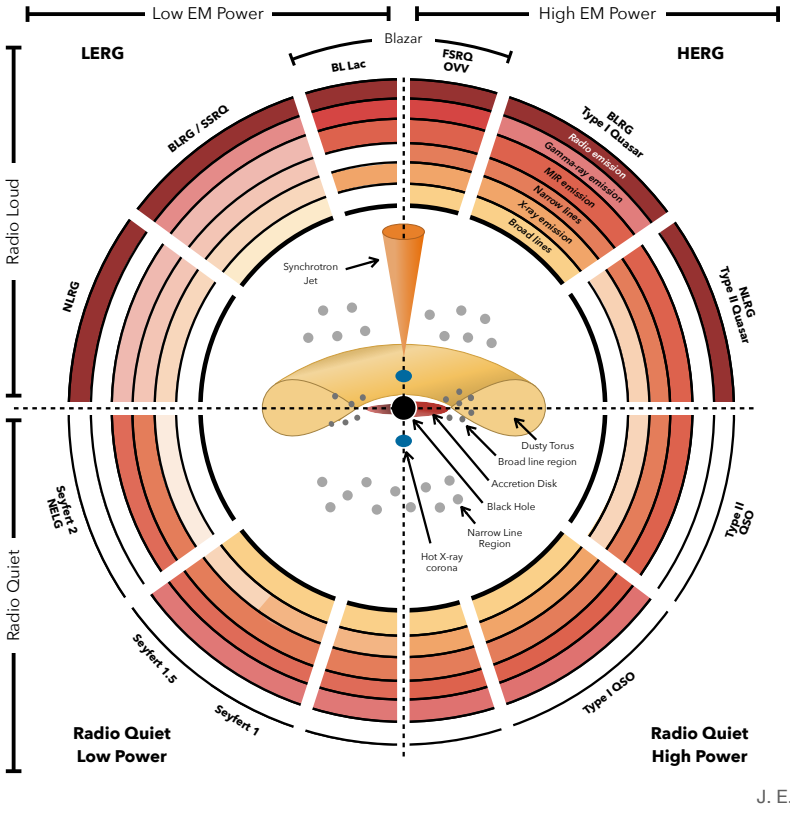


**Figure 2.8:** AGN Unification diagram. Thorne et al. (2022) provided this schematic of AGN unification. The supermassive black hole (SMBH), the accretion disk, the corona, the broad- and narrow-line regions (BLR and NLR, respectively), and a dusty torus are all depicted in the center of the diagram. In Radio Loud galaxies, some of these galaxies exhibit a bipolar synchrotron jet. The concentric circles depict the emission at various wavelengths for the many AGN forms that exist depending on line of sight. The color transparency indicates the strength of the emission for each kind of galaxy. Finally, in terms of the presence of the jet and its SMBH accretion rate (or electromagnetic (EM) power), these kinds may be split into quadrants.

The standard thin disk (Shakura & Sunyaev, 1973; Novikov & Thorne, 1973; Riffert & Herold, 1995), Thick Disk/ Accretion Torus (Kozlowski et al., 1978; Abramowicz et al., 1978; Font & Daigne, 2002; Daigne & Font, 2004; Zanotti et al., 2003, 2005; Qian et al., 2009; Pugliese et al., 2013), the slim disk Abramowicz et al. (1988, 1997); Beloborodov (1998); Sadowski (2009), the

Optically thin advection-dominated accretion flow (Ichimaru, 1977; Narayan & Popham, 1993; Narayan & Yi, 1994, 1995a,b; Abramowicz et al., 1995; Chen, 1995; Chen et al., 1995; Abramowicz et al., 1996; Chen et al., 1997) and TCAF Chakrabarti (1990a); Chakrabarti & Titarchuk (1995); Chakrabarti (1996a); Lu et al. (1997); Mondal (2010) are the five fundamental solutions that best explain the accretion flows. A combination of these solutions is frequently used when applying them to black hole accretion.

In the upcoming sub-sections, we only discuss those accretion flow geometry that were frequently used in GW Astrophysics. However before that we discuss shortly the observability of AGNs and the EMRIs.

### 2.5.2 Observability of AGN through EM radiation

AGN spans the whole electromagnetic spectrum. Based among some of the universe's most extreme objects, it contains intricate physical processes, each of which contributes at a different wavelength. Cold gas accretion via a "dusty torus" is quite prevalent in radio-quiet AGN. Thermal radiation from the bright disk is observable in the UV to visible spectral range. After being ejected from the disk, photons meet the corona encircling the inner part of the disk and emit in X-ray owing to Compton up-scattering (continuum + Compton scattering). Broad Emission Lines (BLR) are apparent in the spectra if the core area is not obscured, as in Type-I AGN. When there is obscuration, such as edge-on view, as is the case with Type-II AGNs, the obscuring structure reemits in the near-to mid-IR wavelength after absorbing the continuum and soft X-Ray from the disk+corona. Hence, a bright disk is involved in the radiatively efficient cold gas flow. AGNs with radio-loud jets exhibit robust non-thermal radio emission. Jennison and Das Gupta (Jennison & Das Gupta, 1953) made the initial detection of bipolar radio emission from Cygnus A. First radio-loud quasar was reported by Schmidt (1963). There are several space-borned and ground based telescopes/observatories that targeted these sources e.g., Hubble Space Telescope, Chandra, XMM-Newton, SUZAKU, NuSTAR, AstroSAT & National Radio Astronomy observatory(NRAO), Event Horizon Telescope, GMRT, Himalayan Chandra Telescope, etc.

The major objective of the upcoming space-borne gravitational-wave (GW) detector LISA is extreme mass ratio inspirals, or EMRIs. A supermassive black hole (SMBH) is orbited by a stellar-mass compact object (SBO) in a typical EMRI. Such systems frequently take place in gas-rich premises. Binaries, such as EMRIs and MBH binaries, can develop and grow more compact through interactions with the ambient gas. It is predicted that $1\% - 10\%$ of the EMRIs seen by LISA will be found in the accretion disk of active galactic nuclei (AGNs), based only on observations of actively accreting MBHs. However, as was previously mentioned, the creation of EMRIs includes a broad variety of dynamical processes and periods of time, thus even in the absence of a gas disk, LISA predictions in the literature still differ by orders of magnitude. Recent evaluations suggested that the number of EMRIs occurring in AGNs may be significantly higher than originally thought, and that LISA may find $10 - 10^4$ EMRIs annually from accretion disks-rich environment, as opposed to just $1 - 10^2$ from configurations that are essentially gas-free (Speri et al., 2023).

### 2.5.3 Thin disk solutions : Standard $\alpha$ disk model of Shakura & Sunyaev

We see that for spherically accreting flows, the velocity of the flow is very high, so the density is low, and it takes little infall time. These imply that the flow is inefficient for energy radiation. As mentioned in the earlier section, when the flow possesses some angular momentum, its velocity decreases, and as a result, density increases, which results in a higher infall time. As a result, this type of flow forms a radiatively efficient disk, which cools down by radiating locally as a black body. The first well-described disk model for this type of standard Keplerian flow was given by Shakura & Sunyaev (1973)(SS73). A relativistic generalization of this solution can be found in Novikov & Thorne (1973); Riffert & Herold (1995). The model assumes that the accretion disk is geometrically thin and optically thick. The inflowing matter follows the Keplerian angular momentum distribution inside the disk, where its radial velocity effectively reduces in comparison to the free-fall velocity. This thin disk model applies when disk luminosity is below Eddington luminosity. An accreting flow residing in Keplerian orbits around a black hole was considered, where the viscous nature of the flow helps to transfer the angular momentum outward and allow the accreting matter to transfer inward. In the derivation of this geometrically thin, optically thick, and non-self gravitating model, a number of simplifications were made, such as: (i) the formed disk is axially symmetric, i.e., $\frac{\partial}{\partial \phi} = 0$, (ii) the disk is stationary, $\frac{\partial}{\partial t} = 0$, (iii) the local height of the disk is $h \ll R$, where $R$ is the radius of the Keplerian orbit on the equatorial plane. This assumption implies that the vertical velocity components are ignorable compared to the radial velocity. The angular velocity of the flow around a central black hole of mass $M$ is given by (inside disk pressure is ignored),

$$\omega = \sqrt{\frac{GM}{R^3}} \tag{2.22}$$

The Keplerian velocity is then,

$$v_\phi = r\omega = \sqrt{\frac{GM}{R}} \tag{2.23}$$

The angular momentum of the flow at a given radius $R$ is

$$L = \sqrt{GMR} \tag{2.24}$$

This implies that at higher radii, the angular momentum is high. In the steady state, the rate of change of angular momentum is given by:

$$\dot{L} = \sqrt{GMR}\dot{M} \tag{2.25}$$

where $\dot{M}$ is the matter accretion rate. The surface density of the disk is denoted by $\Sigma$, which is obtained by integrating the gas density $\rho$ at the equatorial plane($z = 0$) given by,

$$\Sigma = \int_{-H}^{H} \rho dz = 2\rho H \tag{2.26}$$

where $H$ denote the height of the disk.

A more detailed study of these models, considering the conservation of mass, conservation of specific energy, specific angular momentum, and vertical momentum, respectively, was done. For steady state flow, the mass accretion rate ($\dot{M}$) is obtained from the integration of the continuity equation and is given by,

$$\dot{M} = 2\pi R v_R \Sigma \tag{2.27}$$

where $2\pi$ comes from the geometrical shape of the axially symmetric flow. In this model, the turbulent motion of the flow is considered to be the reason behind viscosity, and it is also considered that the turbulent scale height is equal to $H$. The viscous stress tensor for this flow is proportional to the pressure and parameterized as,

$$t_{r\phi} = -\alpha P \tag{2.28}$$

where $\alpha$ is a dimensionless parameter whose value ranges between 0 and 1. The viscous stress acted between the adjacent layers of the flow led to the loss of angular momentum of the flow, which is given by

$$W_{r\phi} = 2\int_0^H t_{r\phi} dz \tag{2.29}$$

The viscous stress and mass accretion rate are related to each other by

$$\dot{M}\omega R^2 = -2\pi W_{r\phi} R^2 + C \tag{2.30}$$

where $C$ is determined from $W_{r\phi} = 0$ at the last stable orbit. Using $C$, we get $W_{r\phi} = -\frac{\dot{M}\omega}{2\pi}\,[1 - \sqrt{R_{in}/R}]$ where $R_{in}$ is the inner radius of the disk. Here in SS73, the turbulent stress is considered to have vanished at the ISCO for the stability of the flow. The existence of finite stress at ISCO led to instability, but that is expected for any flow when it crosses the innermost stable circular orbit (ISCO). Solutions with such a finite stress at the ISCO could be found in Balbus & Mummery (2018); Mummery & Balbus (2019a,b).

The height of the accretion disk in the SS73 model is obtained by using the hydrostatic equilibrium, where radiation pressure is balanced by the component of gravitational force normal to the plane of the disk given by,

$$\frac{1}{\rho}\frac{dP}{dz} = -\frac{GM}{R^3} z. \tag{2.31}$$

The SS73 disk is distinctly divided into three parts based on the dominance of radiation and opacity, namely zone A, zone B, and zone C. In this model, the structure of the disk depends upon some unknown disk variables, which were specified in the three zones separately as follows:

In zone A, the radiation pressure dominates, and the source of opacity is electron scattering. Here, the disk height and the surface density is defined as:

$$H(cm) = 3.2.10^6 \dot{m} m (1 - x^{-1/2}). \tag{2.32}$$

$$\Sigma_0(g/cm^2) = 4.6\alpha^{-1}\dot{m}^{-1} r^{3/2}(1 - r^{-1/2})^{-1} \tag{2.33}$$

Here $\dot{m} = \frac{\dot{M}}{\dot{M}_{cr}}$, $m = \frac{M}{M_\odot}$ and $x = \frac{R}{R_{in}}$, where $\dot{M}_{cr} = 3 \times 10^{-8}(\frac{0.06}{\eta})\frac{M}{M_\odot}M_\odot/year$ and $\eta$ is the efficiency of the gravitational energy release. $M_\odot$ is the sun mass. For Schwarzchild Black Hole, $\eta = 0.06$, and for Kerr BH, $\eta$ can attain 40%.

In zone B, the gas pressure dominates and opacity is still contributed by electron scattering. The disk height here varies as follows:

$$H = 1.2 \times 10^4 \alpha^{-1/10} \dot{m}^{1/5} m^{9/10} x^{21/20} (1 - x^{-1/2})^{1/5}. \tag{2.34}$$

and the surface density,

$$\Sigma_0 = 1.7 \times 10^5 \alpha^{-4/5} \dot{m}^{3/5} m^{1/5} r^{-3/5} (1 - r^{-1/2})^{3/5} \tag{2.35}$$

In zone C, the opacity is contributed by free-free absorption, and gas pressure dominates. The disk height is

$$H = 6.1 \times 10^3 \alpha^{-1/10} \dot{m}^{3/20} m^{9/10} x^{9/8} (1 - x^{-1/2})^{3/20} \tag{2.36}$$

and the surface density,

$$\Sigma_0 = 6.1 \times 10^5 \alpha^{-4/5} \dot{m}^{7/10} m^{1/5} r^{-3/4} (1 - r^{-1/2})^{7/10} \tag{2.37}$$

From the above expressions, we found that the height of the disk depends on the accretion rate but is not always proportional to it. Dependence on the accretion rate of the other variables was also found, such as density, temperature, and radial velocity of the flows.

#### 2.5.3.1 Application of thin disk solutions in Gravitational wave Physics

Binaries of compact objects, specifically massive ones, are likely to contain an accretion disk surrounding the central black hole. The impact of this disk presence on the emitted GW signal was investigated, considering various accretion flow models. Disk torques in disk-embedded EMRIs or IMRIs can accelerate or decelerate an inspiral when it is in the LISA band. The magnitude of the torques will scale with the density of the disk, and the precise amount and direction of the torque will be determined by the mass of the inspiralling compact object and the disk parameters. Although the effect is orders of magnitude weaker than that of gravitational waves (GWs) in this regime, analytical work Yunes et al. (2011); Kocsis et al. (2011); Barausse et al. (2014) and more recent 2D hydrodynamical simulations Derdzinski et al. (2019a, 2021); Garg et al. (2022) have demonstrated that even a slight dephasing over several thousand cycles may accumulate to a detectable phase shift (up to a few radians), depending on the density of the environment. Bright AGN accretion disks are predicted to be thin and dense, but their core regions are hot and dominated by radiation pressure. Simple models anticipate surface densities ranging from 10 to $10^7$ $g/cm2$ based on analytical estimations of densities in the inner regions of such disks. The thin disk solutions by Shakura and Sunyaev (SS) and their relativistic modifications predict the disk density that lies in this range. Many studies focus on this disk model to estimate the environmental impact of the accretion disk on the emitted GW signal, e.g., (Vokrouhlicky & Karas, 1993, 1998; Šubr & Karas, 1999; Karas & Šubr, 2001; Levin, 2007; Yunes et al., 2011; Kocsis et al., 2011; Barausse et al., 2014). A Shakura-Sunyaev $\alpha$-disk with $\Sigma \sim 10^2 g/cm^2$ embedded in an EMRI can accrue a phase shift of up to $\leq 10^{-2}$ radians in 4 years of observation. In contrast, a $\beta$-disk would

**Table 2.1:** EMRI with SS disk (Shakura & Sunyaev, 1973)

| EMRI with SS disk and the phase shift | | | | |
|---|---|---|---|---|
| Work | Mass ratio | Observation time | Phase shift | Source Distance |
| Kocsis et al. (2011) | $(10^{5-6}, 10^{1-2})M_\odot$ | 1 year | $10^{-3}$ | 1MPc |
| Yunes et al. (2011) | $(10^5, 10)M_\odot$ | 1 year | $10^{-3} - 10^{-2}$ | 1MPc |
| Barausse et al. (2015) | $(10^6, 10)M_\odot$ | 1 year | $10^{-2}$ | 1MPc |
| Derdzinski et al. (2021) | $(10^6, 10^3)M_\odot$ | 4 years | $< 10^{-3}$ | z=1 |

dephase over a 4-year period of $10^1 - 10^2$ radians (Derdzinski et al., 2021). These dephasings are significant or not will depend on the higher values of the signal-to-noise ratio (SNR) of the source in the LISA band. They were found to be detectable depending on the disk densities, mass ratio of the disk, and the existence of such systems within the redshift distance $z = 3$. Here we list the foundings of several works where a SS disk is considered around the central SMBH.

Šubr & Karas (1999) examined how a CO's eccentricity and inclination changed when it crossed a thin, radiatively-efficient Sunyaev-Shakura $\alpha$-disk and found that the orbit coincides with the disk's plane at its periphery and circularizes. Karas & Šubr (2001) extend this study to the inner regions of the Shakura-Sunyaev disks, where the density profile is considerably altered by radiation pressure; they also studied the exchange of angular momentum with spiral density waves that are similar to Type I and Type II planetary migration, and hydrodynamic drag during disk crossing. They have found that GW emission drives the interior evolution to around $\sim 100GM/c^2$. They have also supplied formulae for the relative timing of the impacts. Levin (2000) considered models of thin, radiatively-efficient, self-gravitating disks that included thin and optically thick regimes. Like Karas & Šubr (2001), he re-derived order-of-magnitude estimates of the non-relativistic hydrodynamic drag and planetary migration timelines, and he also took azimuthal wind effects into account. Based on these calculations, Levin contended that such disk effects may be significant for LISA EMRIs. Kocsis et al. (2011); Yunes et al. (2011) focus on $\alpha$ & $\beta$ disk of SS model and calculate the phase shift of the emitted GW signal from the vacuum premises. These studies also demonstrates that disk migration has a major impact on the E/IMRI. Barausse et al. (2014); Barausse et al. (2015) noted that environmental disturbances are insignificant for eLISA observation of E/IMRI, with the exception of geometrically thin disks. Simulation by Derdzinski et al. (2019a, 2021) & Garg et al. (2022) in a Newtonian framework around an IMRI found the disk produces a phase shift which is detectable by LISA.

#### 2.5.3.2 Limitations

The Shakura-Sunyaev accretion disk model was the first formulated disk theory that describes the disk presence in any binary system very well. However, the inner region of this disk model suffers from several stability issues. Here we discuss very briefly these issues. For a detailed analysis of

stability on the Shakura-Sunyaev disk model, see Piran (1978); Pringle (1981). A system or disk is said to be in thermal equilibrium when the amount of heating equals the amount of cooling. The inner region of the SS73 disk is radiation pressure-dominated, and opacity is contributed by Thompson scattering. We consider a time scale where mass transfer is insignificant, so that the surface density is considered constant. The viscous heating of the disk when $P \propto H$ can be written as, $Q^{+} \propto H^{2}$ and the radiative cooling is given by $Q^{-} \propto H$. Thus, it can be easily seen that for a slight increase in the thickness of the disk, the rate of increase in heating would be higher than the amount of cooling. On the other hand, a slight thinning in disk height would cause reduced heating compared to cooling. Such thermally unstable behavior, which depends on $\alpha$ may not exist in a realistic accretion disk. In this standard disk model, the mass accretion rate is given by $\dot{M} = \dot{M}(\Sigma)$. Now, a sudden change in accretion rate implies a similar change in density of the disk so that it remains stable and satisfy $\frac{\partial \nu \Sigma}{\partial \Sigma} > 0$.

But if the density does not increase in a similar sense, with the increasing mass accretion rate, the disk will have viscous instability. Another anomaly appears while considering the stress-energy tensor for the disk regarding the choice of pressure type, i.e., whether to choose gas pressure, radiation pressure, or any other. For a highly accreting disk, radiation pressure is preferred, but that leads to thermal instability. This thin disk model also assumes that this disk is radiatively efficient. This assumption means that all the heat generated by viscosity at a given radius is immediately radiated away. In other words, the viscous heating is balanced by the radiative cooling locally, and no other cooling mechanism is needed. This assumption can be satisfied as long as the accretion rate is small. At some luminosity, however, the radial velocity is large and the disk is thick enough to trigger another mechanism of cooling called advection. It results from the fact that the viscosity-generated heat does not have sufficient time to transform into photons and leave the disk before being carried inward by the motion of the gas. The higher the luminosity, the more significant advective cooling is. At the highest luminosities, it becomes comparable to radiative cooling, and the standard thin disk approach can no longer be applied.

Apart from theoretical limitations, observational results are not also fully satisfactory. The Shakura-Sunyaev disk fails to explain the non-thermal component of the emitted disk spectrum.

It is thought that the thermal emission from the typical optically thick, geometrically thin accretion disk i.e. Shakura-Sunyaev disk is responsible for the observed optical and ultraviolet (UV) light from the SMBHs driven active galactic nuclei (AGN) accretion (Ho, 2008). These objects' hard and soft X-ray spectra imply that the X-ray parts of the spectra may include even larger bumps. Space-based studies made it clear that standard accretion disks, which are often the colder ones, could not account for the generation of X-rays.

Instead of such problems, the Shakura-Sunyaev disk model reasonably well explains disks present in binary systems. This disk model describes the high and soft spectral states of the x-ray binaries but fails to describe the other spectral states. We will discuss these in detail in Section §6.0.4.

### 2.5.4 Observational evidences of transonic flows:

The standard model of disks became a popular contender for explaining the "big blue bump" found in the UV region of active galaxies in the early 1980s (Malkan & Sargent (1982); Sun & Malkan (1989) and references therein). The hard and soft X-ray spectra of these objects suggest

that there could be even bigger bumps in the X-ray sections of the spectra. With the advent of space-based investigations, it became evident that the production of X-rays could not be explained by standard accretion disks, which are often the cooler ones. Additional components, such as plasma clouds, hot corona, etc., that are self-consistently constructed and recognized as a hotter post-shock region in transonic flows when flow passes through a shock transition were needed to explain the hard components seen in the spectra of black hole candidates (Chakrabarti & Titarchuk, 1995). Thus, the hot post-shock corona of the accretion disk naturally produced the X-ray continuum emission or the non-thermal component of the power-law spectrum via a scattering mechanism (e.g., Seyfert I & II, Quasar, Blazer, BL Lac). Inverse Compton scattering of thermally produced soft photons from the accretion disk by a corona of hot electrons near the inner edge of the disk is commonly acknowledged as the cause of the power-law (PL) component. There are theories put forth in the literature that define the corona as the region between the ISCO radius and the truncation radius. The reason for the disk's truncation at a particular distance from its central black hole and how it relates to the corona are both unknown. The shock location is the radius of the disk's truncation, which is frequently used to identify the inner boundary of the thin disk solution. According to transonic flows, shock forms at low angular momentum satisfying the Rankine-Hugoniot conditions and naturally produces a hot Comptonizing region by converting the significant kinetic energy of the infalling matter to thermal energy. A typical AGN's X-ray spectrum in the $2-10$ keV range largely displays the signature of the development of the hot Comptonizing zone and offers a weak indication of transonic accretion flows. In particular, an object like M87 does not appear to have the big blue peak in its spectrum (which is a characteristic of the Keplerian disk); additionally, the spectral data of M87 may be satisfactorily well fitted by a sub-Keplerian component alone; therefore, there is little need for a Keplerian component (Mandal & Chakrabarti, 2008). In addition, the same shock site that may account for the spectrum characteristics may also be able to account for the temporal characteristics resulting from its oscillation (Molteni et al., 1996b). In AGN systems, the matter is pushed and puffed up by the extra thermal pressure in the post-shock corona (Le & Becker, 2005; Chattopadhyay & Chakrabarti, 2011). Additionally, in an active galaxy, the entering matter is either wholly sub-Keplerian or a combination of Keplerian and sub-Keplerian flows. This is because, unlike in the case of accreting matter from its companion binary star, where the matter supply is likely to be Keplerian, the infalling matter may come from constantly colliding winds from a large number of stars $\sim$ pc away or from a dusty torus at the outer edge, which may cause the majority of the angular momentum to be lost. The transonic solutions found in this situation are in good agreement with the objects' outer boundaries. The enhanced viscosity on the equatorial plane separates the matter into two components, the equatorial Keplerian component and the sub-Keplerian halo outside, as predicted by Chakrabarti in the TCAF model (Chakrabarti & Titarchuk, 1995), and confirmed by numerical simulations (Giri & Chakrabarti, 2013; Giri et al., 2015). In comparison to other models that are already in the literature, the transonic solution is more advantageous due to its physical characteristics and the dynamics of the flow. Because of this, the canonical thin-disk model is frequently used in the literature (for example, for x-ray binaries) to extract physical parameters of the flow (Chakrabarti, 2017). It should also be applicable to all black hole candidates, ranging from the common quasars and AGNs to nanoquasars or stellar-mass black holes (Chakrabarti & Titarchuk, 1995; Mandal & Chakrabarti, 2008). The observational evidence

for SMBH accretion is also present (Nandi et al., 2019; Nandi et al., 2021; Mondal & Stalin, 2021; Mondal et al., 2022a,b,c,d).

In spite of the observational data mentioned above, as far as we are aware, various models exist, are valid under certain premises, and are capable of describing a particular collection of observable traits. As of right now, none of these models are capable of accurately describing all the traits that have been seen. But there aren't enough observational data to absolutely reject any explanation, either. A consensus has not yet been reached on this open issue and unresolved matter. We make no assertions regarding the superiority of any one disk model over another.

### 2.5.5 Accretion disk theory : Theory of a relativistic perfect fluid

Before discussing the accretion theory, it is necessary to describe the fundamental quantity of a fluid, irrespective of its equations of state, which is its four-velocity. The contravariant components of which are given by,

$$u^{\mu}_{fluid} = \frac{dx^{\mu}}{d\tau} \tag{2.38}$$

where $\tau$ is the proper time of an observer comoving with the flow. These satisfy the normalization condition.

$$u^{\mu}_{fluid}.u^{fluid}_{\mu} = \pm 1 \qquad \pm \text{ depends on the signature of the space time.} \tag{2.39}$$

The next fundamental quantity required to describe a perfect inviscid fluid in a gravitational field is its mass-current and the energy momentum tensor.

The rest-mass density current in the $\mu$ direction is given by,

$$J^{\mu} = \rho u^{\mu}_{fluid} \tag{2.40}$$

and the flux of $\mu$ momentum along $\nu$ direction is given by

the stress-energy tensor which governs the fluid dynamics of a non-self gravitating disk at the low viscosity limit ,

$$T^{\mu\nu} = (\rho + P)u^{\mu}_{fluid}u^{\nu}_{fluid} + Pg^{\mu\nu}, \tag{2.41}$$

Most likely, the accretion flow that is present here in the neighborhood of the AGN has a very high accretion rate and minimal angular momentum. Also, at a great distance from the central SMBH, the matter is thought to be initially subsonic, and near the event horizon, it is supersonic, approaching light velocity $c$ (note that the maximum sound speed in a relativistic regime is $\frac{1}{\sqrt{3}}c$ ). Transonic solutions with multiple sonic points are one of the most intriguing types of solutions for modeling the aforementioned accretion near AGN. Not only is it derived in a mathematically robust way using a relativistic hydrodynamic equation with boundary conditions that are very realistic, but it also accurately describes the non-thermal component of the spectrum because the formation of the shock in the flow produces a hot Comptonizing region naturally in the inner part of the disk that converts soft photons coming from the disk into hard photons, in contrast to other models. Several studies earlier (Abramowicz & Zurek, 1981; Fukue, 1987; Chakrabarti, 1989, 1990a, 1996a; Lu et al., 1997; Mondal, 2010)) have used these steady-state solutions topologies

to describe several observational features (like the existence of hard photons, QPOs, and jets, etc.). An improved time-dependent version of this model (TCAF) has recently been developed, and it is successfully capturing the observational characteristics of black hole binaries as well as of the AGN spectra (Nandi et al., 2019; Nandi et al., 2021; Mondal & Stalin, 2021; Mondal et al., 2022a,b,c,d).

For a viscous flow, the stress-energy tensor has a form,

$$T^{\mu\nu} = (P+\rho)u^{\mu}_{fluid}u^{\nu}_{fluid} + Pg^{\mu\nu} + 2\eta\sigma^{\mu\nu} \tag{2.42}$$

where

$$\sigma^{\mu\nu} = \frac{1}{2}\left(u^{\mu}_{;\beta}P^{\beta\nu} + u^{\nu}_{;\beta}P^{\beta\mu}\right) - \frac{1}{3}\Theta P^{\mu\nu} \tag{2.43}$$

$\Theta = u^{\mu}_{;\mu}$ and $P^{\mu\nu} = u^{\mu}u^{\nu} + g^{\mu\nu}$ is the projection operator.

### 2.5.5.1 Relativistic Euler equation:

The relativistic form of the Euler equation can be obtained from the projected momentum balance equation in a given direction $\alpha$ given by

$$P_{\alpha\mu}T^{\mu\nu}_{;\nu} = 0 \tag{2.44}$$

$$u_{\alpha;\nu}u^{\nu}(P+\rho) + P_{,\nu}u^{\nu}u_{\alpha} + P_{,\alpha} + P_{\alpha\mu}(2\eta\sigma^{\mu\nu})_{;\nu} = 0 \tag{2.45}$$

The comma represents the ordinary derivative, and the semi-colon represents the covariant derivative.

**2.5.5.1.1 Radial Euler Equation:** Using $\alpha = r$ in the equation (2.45) and using the relativistic thermodynamical quantities, we can obtain the radial momentum balance equation for an isentropic flow as,

$$\begin{aligned} g_{rr}u^{r}\frac{\partial u^{r}}{\partial r} + g_{rz}u^{r}\frac{\partial u^{z}}{\partial r} + \frac{2}{\gamma}\left(u^{r}u_{r}+1\right)ha_{s}\frac{\partial a_{s}}{\partial r} + \frac{1}{\gamma}\left(u^{r}u_{r}+1\right)\frac{a_{s}^{2}}{\rho_{o}}\frac{\partial \rho_{o}}{\partial r} = \\ -\left[g_{rr}u^{z}\frac{\partial u^{r}}{\partial z} + g_{rz}u^{z}\frac{\partial u^{z}}{\partial z} + \frac{2}{\gamma}u^{z}u_{r}ha_{s}\frac{\partial a_{s}}{\partial z} + \frac{1}{\gamma}u^{z}u_{r}\frac{a_{s}^{2}}{\rho_{o}}\frac{\partial \rho_{o}}{\partial z}\right] - \left[g_{rr,r}(u^{r})^{2} + \left(g_{rr,z}+g_{rz,r}\right)u^{r}u^{z}\right. \\ \left. + g_{rz,z}(u^{z})^{2} - \Gamma_{kr\nu}u^{k}u^{\nu}\right]. \end{aligned} \tag{2.46}$$

For an adiabatic flow, i.e., $P = k\rho_{0}^{\gamma}$, the above equation has the form,

$$\begin{aligned} g_{rr}u^{r}\frac{\partial u^{r}}{\partial r} + g_{rz}u^{r}\frac{\partial u^{z}}{\partial r} + 2nha_{s}\left(u^{r}u_{r}+1\right)\frac{\partial a_{s}}{\partial r} = \\ -u^{z}\left[g_{rr}\frac{\partial u^{r}}{\partial z} + g_{rz}\frac{\partial u^{z}}{\partial z} + 2nha_{s}u_{r}\frac{\partial a_{s}}{\partial z}\right] \\ -\left[g_{rr,r}(u^{r})^{2} + \left(g_{rr,z}+g_{rz,r}\right)u^{r}u^{z}\right. \\ \left. + g_{rz,z}(u^{z})^{2} - \Gamma_{kr\nu}u^{k}u^{\nu}\right] \end{aligned} \tag{2.47}$$

For a one-dimensional flow, one has to use $u^z = 0$.

**2.5.5.1.2 Vertical Euler Equation :** Vertical momentum balance equation for an isentropic flow can be found by using $\alpha = z$

$$g_{rz}u^r\frac{\partial u^r}{\partial r} + g_{zz}u^r\frac{\partial u^z}{\partial r} + \frac{2}{\gamma}u^r u_z h a_s\frac{\partial a_s}{\partial r} + \frac{1}{\gamma}u^r u_z\frac{a_s^2}{\rho_o}\frac{\partial \rho_o}{\partial r} = - \left[g_{rz}u^z\frac{\partial u^r}{\partial z} + g_{zz}u^z\frac{\partial u^z}{\partial z} + 2bha_s\frac{\partial a_s}{\partial z} + b\frac{a_s^2}{\rho_o}\frac{\partial \rho_o}{\partial z}\right] - \left[\{g_{rz,r}(u^r)^2 + (g_{rz,z} + g_{zz,r})\,u^r u^z + g_{zz,z}(u^z)^2\} - \Gamma_{kz\nu}u^k u^\nu\right] \quad (2.48)$$

where, $b = \frac{1}{\gamma}(u^z u_z + 1)$.
For an adiabatic flow i.e. $P = k\rho_0^\gamma$, equation (2.48) take the form,

$$g_{rz}u^r\frac{\partial u^r}{\partial r} + g_{zz}u^r\frac{\partial u^z}{\partial r} + 2nha_s u^r u_z\frac{\partial a_s}{\partial r} = - \left[g_{rz}u^z\frac{\partial u^r}{\partial z} + g_{zz}u^z\frac{\partial u^z}{\partial z} + 2nha_s\left(u^z u_z + 1\right)\frac{\partial a_s}{\partial z}\right] - \left[\{g_{rz,r}(u^r)^2 + (g_{rz,z} + g_{zz,r})\,u^r u^z + g_{zz,z}(u^z)^2\} - \Gamma_{kz\nu}u^k u^\nu\right] \quad (2.49)$$

This is the vertical momentum balance equation.

### 2.5.5.2 Conserved quantities of the flow :

The symmetry of the space time, i.e., the stationarity and axial symmetry of the chosen metric tensor, provides two killing vectors, $\partial_t$ and $\partial_\phi$. For an ideal inviscid flow, these killing vectors provide two conserved quantities for the flow, viz., energy $\mathcal{E} = hu_t$ and angular momentum $\mathcal{L} = -hu_\phi$. Here $h$ is the specific enthalpy. Interestingly, we can see that for particle dynamics, the conserved quantities are $u_\phi = -\mathcal{L}$ and $u_t = \mathcal{E}$. In the next section, we will discuss the different types of accretion solutions:

### 2.5.5.3 Continuity Equation:

The general relativistic conservation of rest mass gives,

$$\begin{aligned} \nabla_\mu J^\mu &= (\rho_0 u^\mu)_{;\mu} = 0 \\ \frac{1}{\sqrt{-g}}\frac{\partial}{\partial x^\mu}\left(\sqrt{-g}J^\mu\right) &= 0 \end{aligned} \quad (2.50)$$

For a stationary-axisyymetric flow confined in equatorial plane ($\theta = \pi/2$) the above equation reduces to,

$$\begin{aligned} \frac{\partial}{\partial r}(\sqrt{-g}\rho_0 u) &= 0 \\ \sqrt{-g}\rho_0 u &= \dot{M} \\ &= Constant \end{aligned} \tag{2.51}$$

This constant is known as the mass flux of the flow. $\sqrt{-g}$ is known as the geometrical factor. It is the determinant of $g_{\mu\nu}$ and is the measure of the volume element in 4-D space.

#### 2.5.5.4 Conservation of Angular Momentum:

The equation for the conservation of angular momentum is obtained from,

$$\left(\delta^{\mu}_{\phi} T^{\mu\nu}\right)_{;\nu} = 0 \tag{2.52}$$

or,

$$\rho_0 u^{\mu} \left(h u_{\phi}\right)_{,\mu} = \left(\eta \sigma^{\gamma}_{\phi}\right); \gamma \tag{2.53}$$

where $\eta = \nu\rho_0$ is the coefficient of dynamical viscosity and $\nu$ is the kinematic viscosity. The shear tensor component $\sigma^{r}_{\phi}$ when rotation is dominant is,

$$\sigma^{r}_{\phi} = -\frac{A^{3/2}\gamma^3 \Omega_{,r} \Delta^{1/2}}{2r^5} \tag{2.54}$$

The angular momentum equation therefore can be written as,

$$\mathcal{L} - \mathcal{L}_{+} = \frac{1}{u^r r^5} \frac{d\Omega}{dr} \nu A^{3/2} \gamma^3 \Delta^{1/2} \tag{2.55}$$

where $\mathcal{L} = -h u_{\phi}$ is the conserved fluid angular momentum and $h = \frac{P+\rho}{\rho_0}$ is specific enthalpy. For an inviscid flow $\eta = 0$, one obtains $\mathcal{L} = Constant$. The above equation contains the radial velocity, which allows the flow to be non-Keplerian. The term $\mathcal{L}_{+}$ defines the angular momentum on the horizon. For a significant radial velocity, the shear tensor has the form,

$$\sigma^{\mu\nu} = \frac{1}{2}\left(u^{\mu}_{;\beta} P^{\beta\nu} + u^{\nu}_{;\beta} P^{\beta\mu}\right) - \frac{1}{3}\Theta P^{\mu\nu} \tag{2.56}$$

where projection tensor $P^{\mu\nu} = g^{\mu\nu} + u^{\mu}u^{\nu}$ and $\Theta = u^{\mu}_{;\mu}$. For this case, the term $\mathcal{L}_{+}$ is the specific angular momentum at the place where the shear effect vanishes.

#### 2.5.5.5 Equation of Entropy Generation:

$$\begin{aligned} \left(S^{\mu}\right)_{;\mu} &= \frac{Q^{+}}{T} - \frac{Q^{-}}{T} \\ T\left(S^{\mu}\right)_{;\mu} &= Q^{+} - Q^{-} \end{aligned} \tag{2.57}$$

where the four components of entropy are given by $S^{\mu} = \rho_0 s u^{\mu}$, and $Q^{+}$ and $Q^{-}$ are the heat generation and heat loss rates of the system at a given temperature $T$.

In the 1980s, transonic flow solutions were extensively explored in order to generate realistic physical models for black hole accretion (Abramowicz & Zurek, 1981; Fukue, 1987). This transonic solution has made significant progress because of the efforts of Chakrabarti and his coworkers since the late 1980s (Chakrabarti, 1989, 1990a,b) which explains the spectral and timing properties of the accretion disk quite satisfactorily. The next section is dedicated to this accretion flow model.

We solve the relativistic Euler equation, continuity equation, and entropy generation equation to describe a general relativistic geometrically thin transonic accretion flow.

In the steady state, flow transports multiple conserved quantities down the stream line, which are energy ($E_{disk}$), angular momentum ($L_{disk}$), mass flux($\dot{M}$), and entropy ($S$), respectively, given by

$$E_{disk} = hu_t^{fluid} \tag{2.58}$$

$$L_{disk} = -hu_\phi^{fluid} \tag{2.59}$$

$$\dot{M} = 2\pi r u^r_{fluid}\Sigma \tag{2.60}$$

where $h = \frac{P+\rho}{\rho_0}$, is the specific enthalpy of the flow and the integrated surface density of the disk is $\Sigma = \int_{-H}^{H} \rho dz$, $H$ represents the disk height (Novikov & Thorne, 1973; Abramowicz et al., 1997). In terms of the adiabatic sound speed $a_s = \left(\frac{dP}{d\rho}\right)_s$, the specific enthalpy could be expressed as $h = \frac{1}{1-na_s^2}$, where $n$ is the polytropic index, which is related to $\gamma$ as $\gamma = 1 + \frac{1}{n}$(Chakrabarti, 1989). In order to find a hydrodynamic solution in a steady state, one needs to obtain all the 4-velocity $u^\mu_{fluid} = (u^t, u^r, u^\phi, 0)$ components. In terms of the specific angular momentum of the flow, the fluid's 4-velocity components are expressed as

$$l_{disk} = \frac{L_{disk}}{E_{disk}} = -\frac{u_\phi^{fluid}}{u_t^{fluid}} \tag{2.61}$$

which is also conserved. The angular velocity of the flow is,

$$\Omega = \frac{u^\phi_{fluid}}{u^t_{fluid}} = -\frac{g_{t\phi} + l g_{tt}}{g_\phi + l g_{tt}}. \tag{2.62}$$

The radial velocity $v$ in the rotating frame is given by $v = \frac{\mathbb{V}}{\sqrt{1-\Omega l}}$, where $\mathbb{V}^2 = -\frac{u_r^{fluid} u^r_{fluid}}{u_t^{fluid} u^t_{fluid}}$ and $(v_\phi)^2 = -\frac{u_\phi^{fluid} u^\phi_{fluid}}{u_t^{fluid} u^t_{fluid}} = \Omega l$ (Chakrabarti, 1996b,a; Mondal, 2010). Using the condition $u_\mu^{fluid} u^{mu}_{fluid} = 1$, the other components of the 4-velocity are given by,

$$u^r_{fluid} = \frac{1}{\sqrt{g_{rr}}} \frac{v}{\sqrt{(1-v^2)}} \tag{2.63}$$

$$u_t^{fluid} = \sqrt{\frac{(g_{t\phi}^2 - g_{\phi\phi} g_{tt})}{(1-v^2)(g_{\phi\phi} + 2l g_{t\phi} + l^2 g_{tt})}} = \frac{R(r,l)}{\sqrt{(1-v^2)}} \tag{2.64}$$

At this point, one needs to find $v$ in order to obtain the components of $u^\mu_{fluid}$. This can be done when one integrates the gradient of velocity $\frac{dv}{dr}$, obtained by differentiating the energy equation

(equ (2.58)) and the mass flux equation (equ (2.60)) w.r.t. $r$.

$$\frac{dv}{dr} = \frac{\left[a_s^2\left(\frac{2n}{2n+1}\right)\frac{H'}{H} - \frac{R'}{R}\right]v(1-v^2)}{\left[v^2 - \left(\frac{2n}{2n+1}\right)a_s^2\right]} = \frac{N}{D} \tag{2.65}$$

where $(\prime)$ signifies the derivative w.r.t. $r$ and $a_s$ can be eliminated during integration by equation (2.58). The only parameters necessary for the flow are the specific energy ($E_{disk}$) and the specific angular momentum ($l_{disk}$), i.e., $(E_{disk}, l_{disk})$. In order to obtain the solution for accretion flows, the relevant boundary conditions must also be met. Solutions for both accretion and wind (outgoing) types surrounding compact objects, such as black holes and neutron stars, can be obtained (Chakrabarti, 1996b,a; Mondal, 2010; Chakrabarti, 1989; Smith et al., 2002).

### 2.5.6 Boundary conditions and Critical points for Accretion flows

There is a class of solutions that may be produced using different parameter values (e.g., $E_{disk}, l_{disk}$). The boundary conditions are critical and have the potential to change the solutions. Only by analyzing the full parameter space covered by $(E_{disk}, l_{disk})$ can transonic solutions be identified (Chakrabarti, 1996a). The boundary requirements for accretion around a black hole are: $r \to horizon, v \to c$ and for $r \to \infty, v \to 0$. The solution of interest is the one that connects infinity to the horizon with velocity $v = 0 \to c$. The numerical computation of these solutions is difficult, and the simplest method to solve this problem is to analyze the sonic/critical point condition, as mentioned below (Chakrabarti, 1990a, 1989). From the boundary condition, we see that far away from the central object, the velocity of the flow is subsonic, and near the horizon, the flow velocity is supersonic and reaches close to $c$. The critical points exist in this flow when $v = a_s\sqrt{\frac{2n}{2n+1}}$ and the flow passes through the critical points where the $D$ and $N$ of the equation (2.65) vanish simultaneously.

Putting, $D = N = 0$, we get the critical point condition as,

$$v_c = a_{sc}\sqrt{\frac{2n}{2n+1}} \quad \text{and} \quad a_{sc} = \sqrt{\left(\frac{2n+1}{2n}\right)\frac{R'}{R}\frac{H}{H'}} \tag{2.66}$$

Therefore, the Mach number of the flow is $M = \frac{v_c}{a_s|_c} = \sqrt{\frac{2n+1}{2n}}$. The subscript $c$ stands for the quantities calculated at the critical point location $r = r_c$. This critical point condition introduces enormous simplification in obtaining the transonic solution. If one supplies $(E_{disk}, l_{disk})$, then it is possible to integrate the $\frac{dv}{dr} = \frac{N}{D}$ equation from the critical point $r = r_c$, in order to obtain complete hydrodynamical solutions from the outer disk to the horizon for the transonic flows (Abramowicz & Zurek, 1981; Fukue, 1987; Chakrabarti, 1989, 1990a, 1996a; Lu et al., 1997; Mondal, 2010).

The presence and nature of critical points now entirely depend on the parameter $(E_{disk}, l_{disk})$. Also, the precise position and number of physical critical points $r_c$ (could be one, two, or three in the interval from the horizon to the outer boundary in the disk) are completely dependent on $(E_{disk}, l_{disk})$ and can be calculated using equation (2.58) and condition (2.66)(Chakrabarti, 1990a). The accretion solution surrounding SMBHs now boils down to whether comparable values of $(E_{disk}, l_{disk})$ are available in the outer boundary and are realistic or not. In the sub panel of

figure 2.9, we sketch the parameter space corresponding to different values of $(E_{disk}, l_{disk})$ and identify the region corresponding to various forms of transonic solutions. The whole parameter space yields all possible accretion solutions.

The parameter ranges of $(E_{disk}, l_{disk})$ are clearly shown in the sub panel of the figure, where both the quasi-triangular form of the NSA (No-Shock-in-Accretion) and SA (Shock-in-Accretion) regions are significant for the transonic solutions. The sole distinction is that the SA-region meets the requirements for Rankine-Hugoniot shocks, and the flow may contain shocks in accretion flows (Molteni et al., 1999; Chakrabarti et al., 1996). Both areas (SA and NSA) contain three critical point solutions (inner $X-$ types, middle $O-$ types, and outer $X-$ types) that are required for shock generation. The areas NSA or SA, which correspond to transonic solutions, encompass a pretty large amount of parameter space in the sub panel, indicating that these solutions are quite likely to be feasible near SMBH. Second, in the case of AGN systems, accretion happens largely from ambient medium; thus, the matter is very much sub-Keplerian, with favorable energy and angular momentum matching the NSA and SA regions of the parameter space. As a result, the transonic solutions that we employed are reasonable. Although viable, the points other than the NSA or SA-regions accretion solution are not relevant to the current study since there are less than three critical points. In (Chakrabarti, 1996b,a, 1990a), the whole parameter space, subdivisions, and details of all such solutions are presented. Several other groups have separately examined the possibility of standing shocks in sub-Keplerian inviscid, isothermal, and adiabatic accretion flows (Yang & Kafatos, 1995; Caditz & Tsuruta, 1998; Nobuta & Hanawa, 1994). Numerical verification of the solutions is also done (Chakrabarti & Molteni, 1993; Molteni et al., 1996a). Although in this study, we worked at a low viscous limit, similar results were found for viscous flows with and without cooling effects (Chakrabarti & Das, 2004; Mondal et al., 2009; Nagarkoti & Chakrabarti, 2016).

Other solutions, such as thin disk solutions, are also conceivable, and their parameter spaces are likewise included in the figure. The region $I$ corresponds to the Paczynski type thin disk solution (Muchotrzeb & Paczynski, 1982) where the inner sonic point forms close to the horizon. As an example, the Keplerian disk solution lies on the right $l_{kep}$ -curve, the rotationally dominated thin disk solution has significant angular momentum, and it lies close to the $l_{kep}$ -curve. The ADAF is a solution to the Euler equation that has a significant radial velocity advected toward the center and is thus located in the aforementioned region, but unlike the transonic solution, it does not use a critical or sonic point condition for the solution. Recent studies demonstrate that standing shocks can also arise in the ADAF when the equations are solved using the procedures described in Chakrabarti (1989) (Le et al., 2016; Le & Becker, 2005).

Here, we show one such solution that was found in the SA region in Figure 2.9, where we plot Mach no. $\frac{v}{a_s}$ versus radial distances. One of the transonic solutions that we have taken into account as a disk solution in the merger studies is the solid arrow-headed curve. We see that at long distances, the flow is subsonic, crosses the outer critical point $(O)$ at $r = 186.78 r_g$ to become supersonic, and subsequently the supersonic flow approaches the black hole horizon (Kato et al., 1988; Nakayama & Fukue, 1989; Matsumoto et al., 1984). However, before passing the middle sonic point $(M)$ at $r = 10.77 r_g$, the accretion disk may contain a shock in the flow (Fukue, 1987; Nakayama, 1994; Yang & Kafatos, 1995). The shock in the solution is represented by the arrow-headed dotted line, in which the supersonic flow transitions to a subsonic branch and then

back to supersonic at the inner critical point $\mathcal{I}$ at $r = 3.5r_g$(Le et al., 2016; Nagakura & Yamada, 2008; Kato et al., 1988). It is important to notice that the solution fulfills the right boundary conditions $v = 0 \rightarrow c$ as predicted by GTR, and the flow has a significant radial velocity between the outer critical point ($O$) and the horizon, as indicated in the image, which is unusual in earlier research. This distinguishing trait differentiates the other solution. These solutions (Chakrabarti & Titarchuk, 1995; Chakrabarti, 2017; Smith et al., 2002) are thus essential when investigating the net drag force applied onto the companion during its merger.

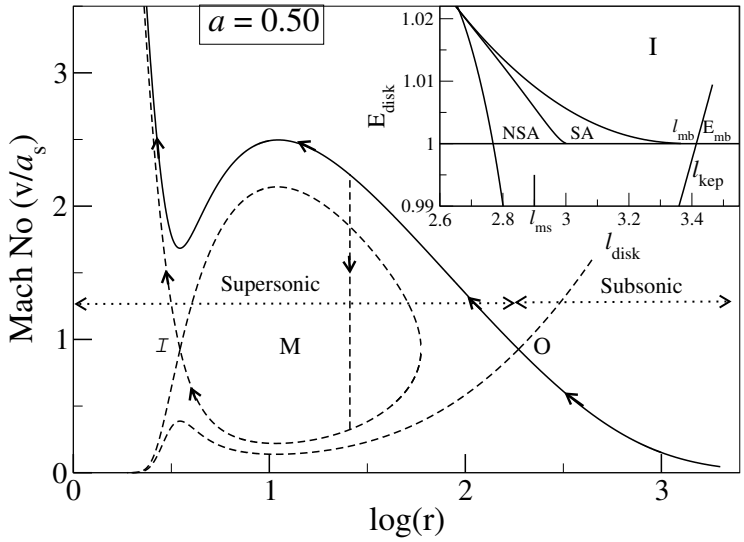


**Figure 2.9:** We illustrate the solution topology (Mach no. vs radial distance $r$) with multiple sonic/critical points. The three critical points are as follows: $inner(\mathcal{I}) = 3.50r_g$(X-type), $middle(M) = 10.77r_g$(O-type), $outer(O) = 186.78r_g$(X-type). The solid arrow-headed line illustrates a transonic solution of the hydrodynamic equation. We can observe that flow is subsonic for a long distance and turns supersonic after reaching the outer critical point O. Flow may experience a shock transition at $r_S = 26.81r_g$ , as indicated by the vertical arrow line. To meet the inner boundary condition at the BH horizon, flow becomes subsonic after the shock, then supersonic again at the inner sonic point ($\mathcal{I}$). The position of the shock, as established by the Rankine-Hugoniot Condition, and the critical points are determined by the flow's specific energy ($E_{disk}$) and specific angular momentum ($l_{disk}$). We display the parameter space of $E_{disk}$ & $l_{disk}$ and its subdivisions against the number of sonic points in the sub panel. The parameters space of our major interest is represented by the NSA (no shock in accretion) and SA (shock in accretion), for which three sonic points exist. The solution for a Keplerian disk is represented by the point $l_{kep}$ on the right curve. Chakrabarti (1996a) discusses the whole parameter space, subdivision, and solutions in depth. Because ambient matter at great distances is sub Keplerian and subsonic, these transonic solutions are ideal for AGN accretion. In our solution, we use $E_{disk} = 1.003$, $l_{disk} = 3.05 < l_{kep}$, $a = 0.50$.

In figure 2.10, we plot the flow parameters, namely sound speed $a_s$, rest mass density $\rho_0$, and the radial component of flow velocity $U^r_{fluid}$ in the upper panel. In the lower panel, we plot the relative velocity of the companion BH while moving through the disk $V_{rel}$, spherically accreting companion BH's accretion rate $\dot{M}_{bondi}$ and the drag due to accretion $\frac{dP^r}{d\tau}$. We compare the results for two cases: when there is a shock in accretion (*dashed line*) and no shock in accretion (*solid line*). We see an increment in the drag force as $r$ decreases. As we see from the figure, the flow has a substantial radial velocity up to the horizon, and the overall hydrodynamic profile of our disk ($a_s$, $\rho_0$, $U^r_{fluid}$, $V_{rel}$, etc.) is different from other standard disk models. As a result, the hydrodynamic drag force is also expected to be different.

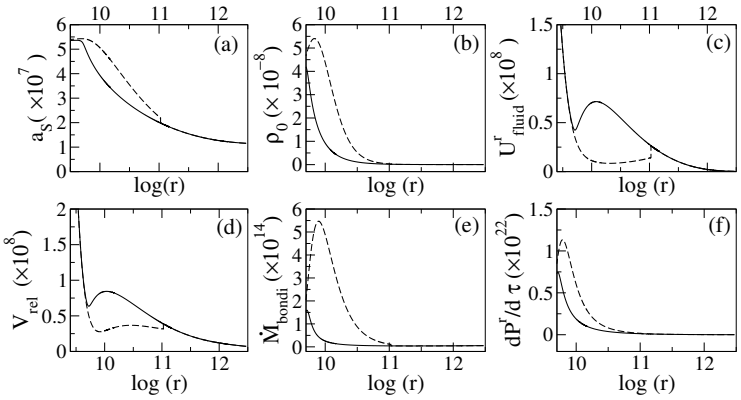


**Figure 2.10:** The transonic solutions for different flow variables are plotted in the figure. For the same flow parameter as in figure 2.9. In the figure, we plot sound speed ($a_s$) of flow in panel (a), disk rest mass density ($\rho_0$) in panel (b), flow velocity ($U^r_{fluid}$) in panel (c), relative velocity $V_{rel}$ in panel (d), Bondi accretion rate $\dot{M}_{bondi}$ in panel (e) and the radial component of the hydrodynamic drag due to accretion in panel (f) w.r.t the radial distance $r$. We choose the SI unit system in this figure. The *solid line* in all the figure represent the no shock accretion and the *dashed line* indicates the shock accretion. The net hydrodynamic drag force acted on the companion BH depends on the disk model i.e. it depends on the variation of the flow variables.

### 2.5.7 Two-Component Advective Flow Solution (TCAF)

This section covers the two-component advective flow (TCAF) model, which was developed by Chakrabarti & Titarchuk (1995) and is considered to be one of the most successful accretion disk models (henceforth, CT95). This model, which consists of two disk components with a low-viscosity sub-Keplerian halo component (CT95) encircling a high-viscosity standard Keplerian disk component located in the disk equatorial plane, was developed based on the theoretical works of Chakrabarti (1990a). This flow, in contrast to the Keplerian disk, has a higher radial velocity that can become supersonic at the black hole's horizon and equal the speed of light $c$. However, the matter is subsonic, far from the black holes. As a result, the nature of black hole accretion is always transonic. The gravitational pull of the black hole's surroundings creates a virtual barrier that inflowing matter must overcome during accretion. Such a virtual barrier may cause the discontinuous transition of the flow variables in the form of shock waves, depending on the flow parameters. Advective accretion flow prefers to pass through the shock because it is thermodynamically advantageous (Fukue, 1987; Chakrabarti, 1989), even though accretion flows that contain shock waves have a high entropy content. However, factors including the flow's specific energy and angular momentum, its heating and cooling processes, the viscosity of the flow, etc. all affect how the shock forms. The matter heats up as a result of this shock, which transforms the kinetic energy of the invading flow into thermal energy. Consequently, a CENtrifugal pressure-dominated BOundary Layer (CENBOL) develops around the black hole (CT95). The density of matter also rises inside the CENBOL. The flow then carries on into the black holes, where it supersonically accretes.

### 2.5.8 Application of TCAF solutions in Gravitational wave Physics

So far, we can see that the transonic flow that we studied in our work is one of the viable choices to represent the accretion flow around SMBH. The observational aspects of this model also provide

evidence of the existence of such flows in nature. Therefore, it is intriguing to take into account this transonic model in the analysis of the disk impact on GW emissions. This thesis intends to determine the impact of this disk model in very detail using general relativistic regime. Whether the impact of the transonic model can be seen in GW observation or not and whether it aids in the resolution of this problem will be discussed in the upcoming chapters.

### 2.5.9 Thick Disk/ Accretion Torus

The features of non-self-gravitating, stable, axisymmetric, and plane-symmetric toroidal fluid configurations in Kerr space times are widely known in astronomy but less so in GW-Astrophysics. The thick disk, also known as the "Polish doughnut", is the most basic analytic model of a black hole accretion disk. It is the simplest in the sense that it simply considers gravity and a perfect fluid, i.e., the most basic description of accretion. We discuss the basic characteristics of this disk here briefly.

The stress energy tensor of a perfect fluid with the four velocity $u^{\mu}_{fluid}$ is given by,

$$T^{\mu\nu} = \rho_0 h u^{\mu}_{fluid} u^{\nu}_{fluid} + p g^{\mu\nu} \tag{2.67}$$

The terms $p, \rho_o, h$ denote the pressure, rest mass density, and specific enthalpy, respectively. The equation of state is given by:

$$p = k\rho_0^{\Gamma} \qquad k \ \& \ \Gamma \text{ are the polytropic constant and index} \tag{2.68}$$

The geodesic is given by the Kerr metric in Boyer-Lindquist coordinates,

$$\begin{aligned} dS^2 &= g_{\mu\nu} dx^{\mu} dx^{\nu} \\ &= (1 - \frac{2Mr}{\Sigma}) dt^2 + (\frac{4Mar\sin^2\theta}{\Sigma}) dt d\phi - \frac{\Sigma}{\Delta} dr^2 - \Sigma d\theta^2 \\ &- (r^2 + a^2 + \frac{2Mra^2\sin^2\theta}{\Sigma})\sin^2\theta d\phi^2 \end{aligned} \tag{2.69}$$

Here $\Delta = r^2 - 2Mr + a^2$ and $\Sigma = r^2 + a^2\cos^2\theta$, $a$ is the Kerr parameter.

The fluid velocity is given by,

$$\vec{u^{\mu}_{fluid}} = U(r,\theta)[-dt + l(r,\theta)d\phi] = A(r,\theta)[\frac{\partial}{\partial t} + \Omega(r,\theta)\frac{\partial}{\partial \phi}] \tag{2.70}$$

The angular velocity $\Omega = \frac{u^{\phi}_{fluid}}{u^{t}_{fluid}}$, $A = u^{t}_{fluid}$, specific energy $U = -u_t^{fluid}$ and specific angular momentum $l = -u_{\phi}^{fluid}/u_t^{fluid}$. The relation between specific angular momentum and angular velocity is given by,

$$\Omega = -\frac{g_{t\phi} + g_{tt} l}{g_{\phi\phi} + g_{t\phi} l}, \qquad l = -\frac{g_{t\phi} + g_{\phi\phi}\Omega}{g_{tt} + g_{t\phi}\Omega} \tag{2.71}$$

The normalization condition of four velocity i.e. $u^{\mu}.u_{\mu} = -1$ provides,

$$AU = \frac{1}{1 - \Omega l} \tag{2.72}$$

The structure of the torus is given by the Euler equation, which has the form,

$$a^{\mu}_{fluid} = -\frac{(g^{\mu\nu} + u^{\mu}_{fluid} u^{\nu}_{fluid})\partial_{\nu} p}{p + \rho} \tag{2.73}$$

$a^{\mu}_{fluid}$ is the four acceleration and can be expressed in terms of the gradient of a scalar potential $W(p) = -\int \frac{dp'}{p' + \rho(p')}$ as,

$$a^{fluid}_{\mu} = \partial_{\mu} W = \partial_{\mu} lnU - \frac{\Omega}{1 - \Omega l}\partial_{\mu} l \tag{2.74}$$

Taking the derivative of the above equation and using $l$ and $\Omega$ to have the same contour levels, one obtains:

$$W - W_{out} = lnU - lnU_{out} - \int_{l_{out}}^{l} \frac{\Omega(l')dl'}{1 - \Omega(l')l'} \tag{2.75}$$

where 'out' stands for the outer edge of the torus. For a torus with constant angular momentum,

$$W - W_{out} = lnU - lnU_{out} \tag{2.76}$$

To have a closed equipotential surface with a cusp, the specific angular momentum $l$ must be between the marginally stable $l_{ms}$ and marginally bound $l_{mb}$ equatorial geodesic (i.e., "Keplerian") orbits. This is easily understood by remembering that the potential $W(r, \theta = \pi/2)$ is just the effective potential characterizing the equatorial motion of a test particle around a Kerr black hole from eq. (2.76). For selecting the class of solutions with a limited radial extent (i.e., with finite inner and outer radii), a negative value for the "potential barrier" at the torus's inner edge must also be chosen. i.e.

$$\nabla W = W_{in} - W_{cusp} = W_{out} - W_{cusp} \leq 0 \tag{2.77}$$

For a polytropic equation of state, eq (2.76) further simplified,

$$\int_0^p \frac{dp'}{p' + \rho(p')} = ln\frac{h}{h_{out}} \tag{2.78}$$

Further the rest mass density is given by,

$$\rho_0(r, \theta) = \left\{ \frac{\Gamma - 1}{\Gamma} \frac{[e^{W_{out} - W(r,\theta)} - 1]}{k} \right\}^{\frac{1}{\Gamma - 1}} \tag{2.79}$$

Therefore the total rest mass of the torus,

$$M_{t,0} = \int \rho_0 \sqrt{-g} u^t d^3x, \qquad \sqrt{-g} = \Sigma sin\theta, d^3x = dr d\theta d\phi \tag{2.80}$$

For more information regarding this disk model, we recommend the interested reader refer to the references (Kozlowski et al., 1978; Abramowicz et al., 1978; Font & Daigne, 2002; Daigne & Font, 2004; Zanotti et al., 2003, 2005; Qian et al., 2009; Pugliese et al., 2013).

### 2.5.10 Application of Thick disk solutions in Gravitational wave Physics

SMBHs are predicted to be enclosed by matter, either in the form of stellar disks, as in "normal" galactic centers, or in the form of gas and dust accretion disks, as in AGNs. Studies for AGN-containing EMRIs, which include an SMBH surrounded by a non-self-gravitating torus, were conducted in order to determine the extent to which the interaction with matter could change the emitted gravitational-wave signal (Barausse & Rezzolla, 2008; Barausse et al., 2015). They show that, when the satellite black hole is sufficiently distanced from its central object, the hydrodynamic drag that the torus exerts on it can have significant impacts that are qualitatively distinct from radiation reaction effects. To be more specific, when the torus is corotating with the SMBH, the radiation reaction always increases the inclination of the orbits with respect to the equatorial retrograde configuration, while the hydrodynamic drag always decreases it (i.e., orbits evolve towards the equatorial prograde configuration).

## 2.6 Conclusion

A crucial role in the creation and development of a variety of astronomical objects, including planets, stars, and black holes, is played by accretion disks. There are several analytical models of accretion disks based on sub-Eddington (thin disks, ADAFs, and TCAFs) and super-Eddington (slim disks, Polish doughnuts) accretion rates. As already discussed, binaries of compact objects, particularly massive ones, are likely to have an accretion disk encircling the center black hole. The influence of this disk on the emitted GW signal was explored in order to probe the accretion disks using GW and to estimate accurate parameters from the observed GW data. So far in GW astronomy, the thin disk model by Shakura & Sunyaev (1973) was extensively used to estimate the environmental impact of the accretion disk on the emitted GW signal, e.g., (Vokrouhlicky & Karas, 1993, 1998; Šubr & Karas, 1999; Karas & Šubr, 2001; Levin, 2007; Yunes et al., 2011; Kocsis et al., 2011; Barausse et al., 2014; Derdzinski et al., 2019a, 2021; Garg et al., 2022). These research findings conclude that dephasing produced by a thin accretion disk imposes significant modifications and also found that, depending on the distances of the source, its mass ratio and the density of the disk, impact of thin accretion disk are observable by the space-based GW detectors. To find out how much matter interaction may alter the emitted GW signal that an EMRI emits, studies (Barausse & Rezzolla, 2008; Barausse et al., 2015) were also carried out on a non-self-gravitating torus/thick disk embedded EMRI (Kozlowski et al., 1978; Abramowicz et al., 1978; Font & Daigne, 2002; Daigne & Font, 2004; Zanotti et al., 2003, 2005; Qian et al., 2009; Pugliese et al., 2013). This demonstrate how the hydrodynamic drag of the torus may have important consequences qualitatively different from radiation response effects on a satellite black hole when it is far enough from its primary object. More specifically, orbits evolve towards the equatorial prograde configuration when the torus is corotating with the SMBH because of the radiation reaction that always increases the orbits' inclination towards the equatorial retrograde configuration while hydrodynamic drag always decreases it. The slim disk model Abramowicz et al. (1988, 1997); Beloborodov (1998); Sadowski (2009) is used to study the GW generated by the precession of the accretion disk in systems like micro-quasars, central engines of gamma-ray bursts, etc. Such emitted GWs are powered by the Bardeen-Petterson effect when the transient stationary state is reached and the accretion rates are in the range $\dot{M} = (0.1-10)M_{\odot}$ ((Alfonso et al., 2015)).

Therein, they find that the precession of slim accretion disks could be observed by upcoming space-borne detectors like DECIGO, Ultimate-DECIGO, and BBO, and this is most likely to occur if the sources in this class are located at distances less than 1 Mpc. Black hole binaries in quiescent nuclei are expected to be surrounded by a thick, radiatively inefficient accretion disk. The optically thin ADAF model (Ichimaru, 1977; Narayan & Popham, 1993; Narayan & Yi, 1994, 1995a,b; Abramowicz et al., 1995; Chen, 1995; Chen et al., 1995; Abramowicz et al., 1996; Chen et al., 1997) best describes the disk around these non-active nuclei. Narayan (2000) investigates the impact of accretion flow-induced dynamical friction force on the orbital decay of stars and supermassive black holes. This study mainly targeted non-active galaxies where the chances of the presence of ADAF flow (less dense than the thin disk model) are quite high, and it was obtained that in the case of ADAF, accretion drag should be completely minimal, and thus the orbital evolution in such galaxies will be totally regulated by the gravitational radiation reaction. The models of accretion flow that have been presented thus far have certain limitations. The hard power law component of the spectra cannot be explained by the thin disk model, for instance, but the multicolor blackbody component can. Likewise, the absence of an advective component renders the thick disk model incomplete. Up to 50 times the Eddington rate of mass accretion is often required in slim disk models, etc. So far, this chapter has shown that the transonic flow is a feasible option for modeling the accretion flow surrounding SMBH. Such fluxes in nature are also supported by the observable components of this model. Thus, including this transonic model in the investigation of the disk influence on GW emissions is rather interesting. Using the general relativistic regime, this thesis aims to ascertain the influence of this disk model in great detail.

# Chapter 3

# Impact of the accretion disk on the geodesic orbits : Comparison between disk & without disk.

## 3.1 Introduction & Previous explorations

The detection of potential milliHz sources, primarily extreme/intermediate mass ratio inspirals (E/IMRIs), is a key scientific goal of upcoming space-borne gravitational wave (GW) detectors such as the LISA ((Bailes et al., 2021; Amaro-Seoane et al., 2017; Babak et al., 2017)), Tian-Qin Project (Luo et al., 2016), and Taiji Program (Hu & Wu, 2017). It is anticipated that the event rate of such visible EMRI within the detectable frequency range of space-based detectors is a few hundred to several thousand per year. However, a range of dynamical relaxation processes-such as binary tidal break-up, chaotic dynamics around a massive black hole (BH) binary, deflecting compact objects on very low angular momentum orbits around the central supermassive black hole (SMBH), etc.-are involved in the formation channels of EMRI at different timescales. A "dry EMRI" refers to EMRIs formed through this pathway (Sigurdsson & Rees, 1997; Amaro-Seoane et al., 2007; Babak et al., 2017; Gair et al., 2017; Amaro-Seoane, 2018; Miller et al., 2005; Chen & Han, 2018; Wang et al., 2019; Raveh & Perets, 2021; Fan et al., 2020). Several new research (Pan & Yang, 2021; Pan et al., 2021), however, indicate that the event rates are higher than previously assumed. The EMRI production rate is often increased by orders of magnitude when an accretion disk surrounds an AGN (wet channel) exist (Tagawa et al., 2020; Pan & Yang, 2021; Pan et al., 2021; Vázquez-Aceves et al., 2022; Zwick et al., 2021). Compared to just $1 - 10^2$ EMRIs per year from the dry channel, LISA could detect $10 - 10^4$ EMRIs per year from the wet channel (accretion embedded) (Speri et al., 2023). The eccentricity of the E/IMRI orbit originates from both the wet and dry E/IMRI formation processes. Since the companion BH is orbiting elliptically around the primary central SMBH, in our work, we will be concentrating on the second type of formation channel for E/IMRI systems, where these systems contain a massive accretion disk (Mayer (2013)) that surrounds the primary BH and the companion BH is enmeshed in it. In this case, hydrodynamical drag provides an additional incentive to eliminate the companion's energy and angular momentum in addition to GW loss. By causing the companion's inspiraling motion to diverge, this speeds up the coalescence process and alters the GW signals that are released. The companion encounters two primary forms of drag forces while the disk is present: self-accretion ((Bondi & Hoyle, 1944; Bondi, 1952)) and dynamic friction ((Chandrasekhar, 1943; Ostriker, 1999; Kim & Kim, 2007)). The main mechanism that progressively lowers the companion's energy and angular momentum is the emission of GW. While the individual disk drag components' contributions to the reduction of those orbital parameters are relatively smaller, the integrated

impact of the disk is however significant (Chakrabarti (1993); Basu et al. (2008); Yunes et al. (2011); Kocsis et al. (2011); Derdzinski et al. (2019a); Garg et al. (2022)).

The influence of a massive accretion disk on the emission process and profile of gravitational signal from E/IMRI is a long-standing topic and was first addressed by Chakrabarti (1993, 1996c); Molteni et al. (1994) where they examined the effect of hydrodynamic drag produced on the companion traveling in a Keplerian orbit. The study reveals that for sub-Keplerian disks, drag force lowers infall time, but for super-Keplerian disks, drag force increases infall time and, in extreme instances, can establish a stationary orbit. Narayan (2000) soon after conducted an order-of-magnitude study for the ADAF model and concluded that there was no significant effect. However, there are significant differences between Chakrabarti's and Narayan's disk models. Considering Newtonian or pseudo-Newtonian framework, Giampieri (1993); Vokrouhlicky & Karas (1993, 1998); Šubr & Karas (1999); Karas & Šubr (2001); Levin (2007); Basu et al. (2008); Basu (2018) have made further advancements in this area by taking into account a variety of physical circumstances, such as on and off equatorial orbital motion, a radiatively efficient self-gravitating disk model, an inefficient advection dominated accretion flow (ADAF) model, etc. All of these studies, available so far, have shown that, the coalescence time delay is small when the companion is embedded in the ambient accretion disk due to the negligible impact on angular momentum exchange of the companion causes by the hydrodynamic drag. However one should note that the effect considerably depends on the choice of the disk model.Barausse & Rezzolla (2008) conducted the first analysis in the general relativistic framework by taking into account a thick torus with zero radial velocity. A similar but more detailed study considering a standard disk has been done by Yunes et al. (2011); Kocsis et al. (2011). This work shows disk migration has a significant influence on the E/IMRI. Barausse et al. (2014); Barausse et al. (2015) pointed out that for eLISA observation of E/IMRI, environmental disturbances are negligible except for a geometrically thin disk. The result of all these studies shows that the effect of the accretion disk crucially depends on the choice of the hydrodynamic model of the accretion disk. Recent simulation work done by Derdzinski et al. (2019a,b, 2021) has considered a $2-D$ viscous accretion disk in a Newtonian framework around an IMRI and found disks produce a phase shift that is detectable by LISA if the surface density is $10^3 gcm^{-2}$. However, in their studies, they considered the hydrodynamical model that represents the accretion flows, which are very unlikely to appear in realistic situations. By altering the flow parameters, they were able to determine the drag magnitude for various disk models, including the Keplerian disk ($\alpha$ & $\beta$ disk) (Shakura & Sunyaev (1973)), accretion tori (Basu et al. (2008)), ADAF (Narayan (2000)), transonic flow (Chatterjee et al. (2023)), and others.

The presence of a massive accretion disk, boson stars, bumpy black holes, spacetime mapping, and other previously ignored non-negligible astrophysical effects on the GW are now expected to be measured more accurately with the increased sensitivity of LISA (Bezares et al., 2022; Baibhav et al., 2021; Guo et al., 2019; Derdzinski et al., 2019a; Kocsis et al., 2011). The likelihood of detection, however, is dependent on the signal's signal-to-noise (SNR)-weighted amplitude (Sesana et al. (2005); Kocsis et al. (2011); Moore et al. (2015); Robson et al. (2019)). As a result, even with sufficiently accurate templates available, the possibility of detection is limited by the detector's sensitivity constraint on the parameter space ((Moore et al., 2015; Robson et al., 2019)), even though there may be potential sources that fall inside the LISA range but are lacking detectable

SNR because they are below the detector's sensitivity curve.

Therefore, the goal would be to determine the ideal E/IMRI orbital parameters that can result in the least SNR needed for detection. Since the accretion flow surrounding a black hole has a very high accretion rate and a low angular momentum, we chose the transonic flow to govern the flow dynamics in this work. This flow also preserves the requirement that matter be primarily subsonic, later supersonic, and finally tend to the light velocity $c$ near the event horizon of the SMBH. The theoretical development and observational evidence are given in Chatterjee et al. (2023) and references therein.

Finding the optimal orbital parameters that display the substantial hydrodynamic drag is the main objective of the current study. Higher hydrodynamic drag would provide the companion with higher torque. The phase shift of the companion (with and without the disk) would be higher at higher torques, increasing the likelihood of a higher SNR value. Considering that the net torque on the companion is highly dependent on the orbital parameters in addition to the flow parameters, one can compare the various values of torque on the companion by retaining the disk parameters (transonic flows in this case) fixed and varying the orbital parameters (eccentricity, semi-major axis, black hole spin, ratio of EMRI, etc.). In this work, we are interested to determine the initial orbital parameters of the EMRIs for which the disk drag has the largest effect on the released GW signal, allowing it to approach the detector's detection threshold and hover just above the sensitivity curve. The majority of current research computes disk drag within a Newtonian framework, focusing on circular orbits. With this approach it is impossible to estimate the magnitude of the disk drag due to changes in orbital parameters. Within the relativistic paradigm, the modification of the orbital parameters around a spinning Kerr BH can be accomplished neatly for general elliptical orbits. Using Ryan's formula (Ryan (1995, 1996)), which includes the leading-order impact of black hole spin, the loss rate owing to the GW emission is computed. This formula is an improved version of Peter & Mathews' (Peters & Mathews (1963); Peters (1964)) equation. As a result, it is a more appropriate approximation to apply in the Kerr black hole scenario (Glampedakis et al. (2002); Gair & Glampedakis (2006)). Finally, the ratio of the loss rates owing to GW emission and disk drag is compared in order to derive the maximum torque. Determining the ideal orbital parameters for which the radiated GW strain stands above the noise sensitivity curve of LISA and, as a result, the SNR is greater than the necessary value for detecting the E/IMRIs is consequently our main goal in our relativistic treatment. In this work, we kept the accretion rate $\dot{M} = 1\dot{M}_E$ in most of the cases and fixed other flow variables to determine the set of optimum orbital parameters for which the strength of disk drag becomes greater and apparent to LISA. By adjusting the orbital parameters and loss rates, the disk drag's magnitude is calculated. In order to determine the greatest effect of disk drag on the produced GW emission, we investigate the elliptic orbits with various initial configurations. Examining GW astronomy with systems that have these sets of initial configurations would provide a more precise investigation of the accretion disk physics as they offer the maximum drag effect.

To proceed further, we first discuss the geodesic motion of the companion black hole in the geodesic of the central supermassive black hole of an EMRI.

## 3.2 Evolutions of EMRIs in the vacuum premises : The standard picture in Newtonian regime

In this section, we very briefly discuss the GW radiation emitted from a binary system of component masses: SMBH mass $M$ and companion mass $m$ in a Keplerian elliptical orbit in the Newtonian framework Peters & Mathews (1963); Peters (1964); Maggiore (2007). The center-of-mass (COM) of this system reduces the problem to a one-body problem. The total mass of the system is therefore $M_T = M + m$ and the reduced mass is $\mu = \frac{Mm}{M+m}$. The COM is under acceleration $\ddot{r} = -\frac{GM}{r^2}\hat{r}$ where relative coordinates $r = r_2 - r_1$, $r_1$ and $r_2$ define the position coordinates of $M$ and $m$. The energy and angular momentum of the system in polar coordinates $(r, \psi)$ are given by

$$L = \mu r^2 \dot{\psi} \qquad \text{and} \qquad E = \frac{1}{2}\mu(\dot{r}^2 + r^2\dot{\psi}^2) - \frac{G\mu M_T}{r} \tag{3.1}$$

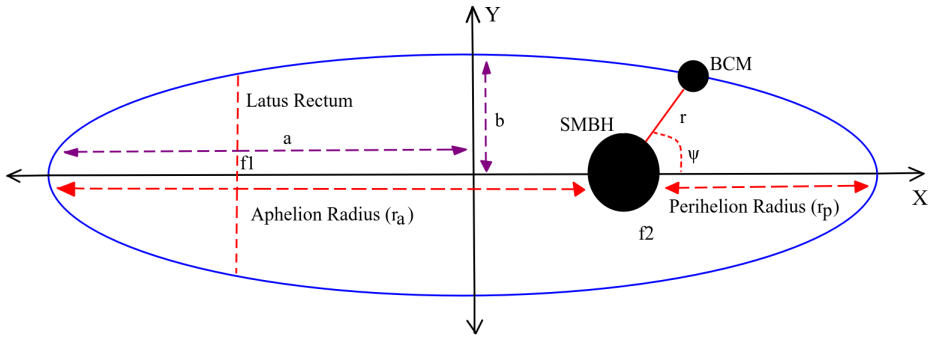


**Figure 3.1:** Schematic diagram of an elliptical orbit. The SMBH is at one of the two foci and the BCM is inspiralling elliptically around it. $\psi$ is measured counter clock wise from the horizontal axis. The aphelion and perihelion radii are defined interms of eccentricity $(e)$ and the semi major axis a.

Combining these two we get,

$$\frac{1}{r} = \frac{1}{R}(1 + e\cos\psi) \tag{3.2}$$

where $R = \frac{L^2}{GM_T\mu^2}$ and $e = 1 + \frac{2EL^2}{G^2M_T^2\mu^3}$.

The eccentricity $e$ for elliptical orbit is $0 \leq e < 1$. Now the semi major axis of the orbit is given by,

$$\mathrm{a} = \frac{R}{(1 - e^2)} \tag{3.3}$$

using a in equation (3.2), we get

$$r = \frac{\mathrm{a}(1 - e^2)}{(1 + e\cos\psi)} \tag{3.4}$$

and interms of $r$, the angular velocity is

$$\dot{\psi} = \frac{\sqrt{GM_T R}}{r^2} \tag{3.5}$$

Now to calculate the power radiated from the system, we need the second mass moment of the system. For that purpose we consider a Cartesian coordinate $(x, y)$ on the focus of the ellipse such that,

$$x = r\cos\psi \qquad \text{and} \qquad y = r\sin\psi \tag{3.6}$$

In this frame the second mass moment is given by,

$$M_{xy} = \mu r^2 \begin{pmatrix} \cos^2\psi & \sin\psi\cos\psi \\ \sin\psi\cos\psi & \sin^2\psi \end{pmatrix}_{xy} \tag{3.7}$$

using this in equation (1.80), we obtain the radiated power as,

$$P = \frac{32G^4\mu^2 M_T^3}{5c^5 \mathrm{a}^5} f(e) \tag{3.8}$$

$$f(e) = \frac{1}{(1-e^2)^{7/2}}\left(1 + \frac{73}{24}e^2 + \frac{37}{96}e^4\right) \tag{3.9}$$

## 3.3 Evolutions of companion of the EMRI in eccentric equatorial orbits around spinning black holes in the vacuum premises : The standard picture in relativistic regime

As previously noted, we take into account an E/IMRI system in which the central SMBH's mass, $M$, controls the background space-time's curvature, whereby the companion black hole's mass, $m(m \ll M)$, travels like a test particle.

The metric of the Kerr space-time in the rest frame of the central black hole's Boyer-Lindquist (B-L) coordinates ($r$, $\theta$, $\phi$, $t$) is given by (Chandrasekhar, 1943),

$$dS^2 = g_{\mu\nu}dx^\mu dx^\nu = (1-\frac{2r}{\Sigma})dt^2 + (\frac{4ar\sin^2\theta}{\Sigma})dtd\phi - \frac{\Sigma}{\Delta}dr^2 - \Sigma d\theta^2 - (r^2+a^2+\frac{2ra^2\sin^2\theta}{\Sigma})\sin^2\theta d\phi^2 \tag{3.10}$$

Here $\Delta = r^2 - 2r + a^2$ and $\Sigma = r^2 + a^2\cos^2\theta$, $a$ is the Kerr parameter. Here we use $M = G = c = 1$ units.

The companion's orbit is thus seen as the geodesic of the background space-time, which develops secularly under gravitational radiation reactions. This is a fair estimate (because $m << M$) that has been embraced as normal practice in EMRI science (Glampedakis & Kennefick, 2002; Glampedakis et al., 2002). The fiducial geodesic of the background space-time can be defined by two scalar constants, viz., the specific energy $E = u_a\left(\frac{\partial}{\partial t}\right)^a$, and the specific angular momentum $L = u_a\left(\frac{\partial}{\partial \phi}\right)^a$, where $\left(\frac{\partial}{\partial t}\right)^a$ and $\left(\frac{\partial}{\partial \phi}\right)^a$ are the two killing vectors corresponding to the stationarity and axisymmetry of the background space-time, respectively. The equation of geodesic then takes the form (Glampedakis et al., 2002),

$$r^4(\frac{dr}{d\tau})^2 = T^2 - \Delta(r^2 + (L - aE)^2) = V_r \tag{3.11}$$

$$r^2\frac{d\phi}{d\tau} = -(aE - L) + \frac{aT}{\Delta} = V_\phi \tag{3.12}$$

$$r^2\frac{dt}{d\tau} = -a(aE - L) + \frac{(r^2 + a^2)T}{\Delta} = V_t \tag{3.13}$$

In our case we are considering equatorial geodesic therefore,

$$\theta(\tau) = \pi/2 \tag{3.14}$$

where $T = E(r^2 + a^2) - La$, $\Delta = r^2 - 2r + a^2$. The eccentricity ($e$) and the semi latus rectum ($p$) are a remapping of $E$ and $L$ as $p = 2\frac{r_a r_p}{r_a + r_p}$ and $e = \frac{r_a - r_p}{r_a + r_p}$, where apastron $r_a$, and the periastron $r_p$ ($r_a > r_p$) are defined as the two turning points of the radial potential, *i.e.*, $V_r(r_a) = V_r(r_p) = 0$. These definitions of $e$ and $p$ coincide with the usual definitions of eccentricity and semi-latus rectum in the Newtonian limit. The energy ($E$) and angular momentum ($L$) can be obtained by solving the equations (Glampedakis & Kennefick, 2002),

$$E = [1 - (1/p)(1 - e^2)1 - \frac{x^2}{p^2}(1 - e^2)]^{1/2} \tag{3.15}$$

$$x = L - aE \tag{3.16}$$

$$x^2 = \frac{-N(p, e) \mp \Delta_x^{1/2}(p, e)}{2F(p, e)} \tag{3.17}$$

The upper sign corresponds to prograde and the lower sign corresponds to retrograde motion. Here, $F(p, e) = \frac{1}{p^3}[p^3 - 2(3 + e^2)p^2 + (3 + e^2)^2 p - 4a^2(1 - e^2)^2]$,
$N(p, e) = \frac{2}{p}[-p^2 + ((3 + e^2) - a^2)p - a^2(1 + 3e^2)]$,
$C(p, e) = (a^2 - p)^2$, $\Delta_x(p, e) = N^2 - 4FC$.

Note that the semi-major axis ($X$) and eccentricity ($e$) are gauge-dependent values, but the gauge is already defined by using the Boyer-Lindquist coordinate system. Furthermore, because $E$ and $L$ are scalar constants, they are gauge invariant under an infinitesimal coordinate shift. Equation (3.11) implies that $r$ executes a periodic motion between $r_a$ and $r_p$ therefore, it can be written as

$$r = \frac{p}{1 + e\cos\chi} \tag{3.18}$$

where $\chi$ is a parameter, varying from $\chi = 0$ at $r = r_p$ to $\chi = \pi$ at $r = r_a$ and finally to $\chi = 2\pi$ back to $r = r_p$ (Glampedakis & Kennefick, 2002). The radial orbital period $T_r$ is defined as

$$T_r = \int_0^{2\pi} \frac{dt}{d\chi} d\chi = \int_0^{2\pi} \frac{dt}{dr}\frac{dr}{d\chi} d\chi. \tag{3.19}$$

The azimuthal coordinate $\phi$ can similarly be expressed as a function of $\chi$ using equations (3.11) (C.3),(C.4),(3.18). $\phi$ is not a strictly periodic function of $\chi$. However, $\phi$ changes by the same amount as $\Delta\phi = \phi(2\pi) - \phi(0)$ as $r$ completes a full period. As a result, we get a precessing orbit.

For a given Kerr parameter ($a$) and eccentricity ($e$), the semi-major axis ($X$) is $X = \frac{p}{(1-e^2)}$. This is different from the gauge choice of Memmesheimer et al. (2004).

## 3.4 Evolution of eccentric orbits around spinning black holes under gravitational radiation reaction

The change in energy and angular momentum i.e the loss rates due to GW emission and the respective changes in orbital parameters are given by

$$\frac{dE}{dt} = -\frac{32G^4\mu^2M_T^3}{5c^5\mathrm{a}^5}\frac{1}{(1-e^2)^{7/2}}\left(1+\frac{73}{24}e^2+\frac{37}{96}e^4\right) \tag{3.20}$$

$$\frac{dL}{dt} = -\frac{32G^{7/2}\mu^2M_T^{5/2}}{c^5\mathrm{a}^{7/2}}\frac{1}{(1-e^2)^2}\left(1+\frac{7}{8}e^2\right) \tag{3.21}$$

Similarly the evolution of semi major axis and eccentricity can be obtained as,

$$\frac{d\mathrm{a}}{dt} = -\frac{64G^3\mu M_T^2}{5c^5\mathrm{a}^3}\frac{1}{(1-e^2)^{7/2}}\left(1+\frac{73}{24}e^2+\frac{37}{96}e^4\right) \tag{3.22}$$

$$\frac{de}{dt} = -\frac{304G^3\mu M_T^2}{15c^5\mathrm{a}^3}\frac{e}{(1-e^2)^{5/2}}\left(1+\frac{121}{304}e^2\right) \tag{3.23}$$

This part is completely based on the work of Peter & Mathews formula (Peters & Mathews, 1963; Peters, 1964). An improved version of this formalism is obtained by Ryan's formula, (Ryan, 1995, 1996) which incorporates the leading order effect of black hole spin. Thus, a better approximation to use in the case of the Kerr black hole (Glampedakis et al., 2002; Gair & Glampedakis, 2006) are the Ryan fluxes, which are given in the weak field approximations Ryan (1996) as,

$$\left.\frac{dE}{dt}\right|_{GW} = -\frac{32}{5}\frac{\mu^2}{M^2}(\frac{M}{p})^5(1-e^2)^{3/2}[f_1(e)- \frac{a}{M}(M/p)^{3/2}f_2(e)] \tag{3.24}$$

$$\left.\frac{dL}{dt}\right|_{GW} = -\frac{32}{5}\frac{\mu^2}{M}(\frac{M}{p})^{7/2}(1-e^2)^{3/2}[f_3(e)+ \frac{a}{M}(M/p)^{3/2}(f_4(e)-f_5(e))] \tag{3.25}$$

where $f_1(e) = 1+\frac{73}{24}e^2+\frac{37}{96}e^4$, $f_2(e) = \frac{73}{12}+\frac{823}{24}e^2+\frac{949}{32}e^4+\frac{491}{192}e^6$, $f_3(e) = 1+\frac{7}{8}e^2$, $f_4(e) = \frac{61}{24}+\frac{63}{8}e^2+\frac{95}{64}e^4$, $f_5(e) = \frac{61}{8}+\frac{91}{4}e^2+\frac{461}{64}e^4$. $M$ is the mass of the central black hole and $\mu = Mm/(M+m)$ is the reduced mass. The semi-latus rectum $p = r_p(1+e)$.

For Schwarzschild space-time (Kerr parameter$a = 0$), this formula reduces to the celebrated Peter & Mathews formula (Peters & Mathews, 1963; Peters, 1964). The Ryan fluxes can also be derived from the rigorous Teukososky formalism in the weak field limit (Glampedakis & Kennefick, 2002). However, in a strong field regime, eqs. 3.24 and 3.25 become increasingly inaccurate in comparison to the fluxes calculated using Teukolsky formalism, and therefore, near the innermost stable circular orbit (ISCO), one needs to incorporate the strong field effects to estimate the radiation reaction more accurately. The inclusion of higher-order post-Newtonian (PN) terms improves the accuracy (Will, 2011; Zwick et al., 2023). But as the total mass of the binary system increases, these higher-order PN corrections are no longer sufficient, and other methods (EOB or phenomenological waveform) are used (Owen et al., 2023; Yunes et al., 2010).

### 3.4.1 Adiabatic approximation and the averaged energy and angular momentum

Under radiation response, the satellite's trajectory deviates from the geodesic one, which is parameterized by energy ($E$) and angular momentum ($L$). The emitted GW gradually modifies the motion of the satellite from the above-mentioned equations (section §3.3). The fundamental issue in computing the trajectories here is due to time scale discrepancies, i.e., the time frame of the orbital period is much shorter than the timescale for the GW radiation reaction. Mino (2003, 2005a,b) address this problem by formulating an assumption that shows the evolution of the parameters, e.g., energy and angular momentum, can be obtained from the GW emission force by evaluating the radiative field instead of the retarded field by subtracting the retarded solution from the advanced perturbative solution, and these solutions are gauge-invariant. Mino also obtained that the total GW energy emitted by a moving body is equal to the total work done by the radiation reaction (Gal'tsov, 1982; Quinn & Wald, 1999). This approximation helps to remove the oscillatory changes of the $E$ and $L$ along the orbital time period and provides the time-averaging changes of the parameters. This assumption of using a radiative field for the calculation of orbital trajectories under GW emission is known as the adiabatic approximation (Pound et al., 2005). We can write the changes in 4-momentum due to GW emission under adiabatic approximation as,

$$\left.\frac{dP_t}{d\tau}\right|_{GW} = \dot{E}_{GW}.u_t^{sat} \tag{3.26}$$

$$\left.\frac{dP_\phi}{d\tau}\right|_{GW} = \dot{L}_{GW}.u_\phi^{sat} \tag{3.27}$$

where the 4-velocity of the companion BH (satellite BH) are $u^\mu_{sat} = \frac{dx^\mu}{d\tau}$. We consider the changes in energy and angular momentum i.e $\dot{E}_{GW}$ and $\dot{L}_{GW}$ for a given orbit due to radiation reaction as given in equations (3.24) & (3.25).

## 3.5 Environmental impact on EMRIs : Modifications of the standard picture

From a generalized view, if we differentiate between the two situations, i.e., when (a) the accretion disk is absent and (b) the accretion disk is present, we see that, in (a), the emitted GW carries

energy and angular momentum due to radiation. As a result, the orbital radius decreases and coalescence takes place. In (b), the presence of the disk offers additional forces exerted on the companion, which result in more energy and angular momentum loss compared to (a). The higher loss rates help to shrink the orbital radius more rapidly, and coalescence takes place comparatively faster than the previous one. The additional forces that act on the companion are mainly of two types: (i) self-accretion and (ii) dynamical friction.

#### 3.5.0.1 Hydrodynamic drag due to Accretion

In the first case, we assume the companion black hole is fully engulfed in the disk. We select Bondi-Hoyle-type self-accretion for the companion. The accretion of matter on stars was first studied and explained by Bondi and Hoyle (Bondi & Hoyle, 1944; Bondi, 1952). The companion black hole, when moving through a gaseous medium (Figure 3.2), matter accreted onto it, leading to a mass gain of the companion. This accretion of matter also alters the angular momentum and energy from the disk to the companion. Thus, the motion of the companion gets modified.

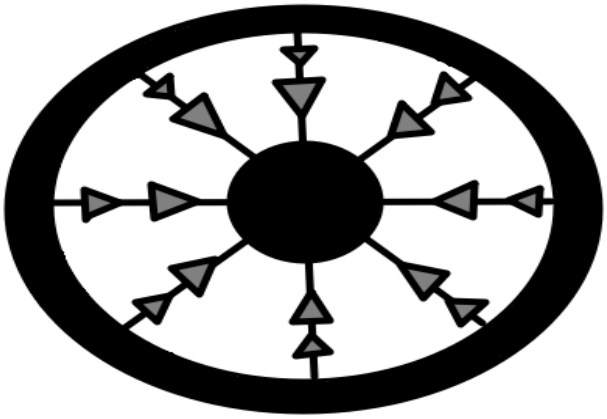

**Figure 3.2:** Zero angular momentum accretion suffered by the companion black hole : Bondi accretion(Bondi & Hoyle, 1944; Bondi, 1952)

The change in 4-momentum of the companion due to its self-accretion is,

$$\left.\frac{dP^{\mu}}{d\tau}\right|_{accr} = h_{enth}\frac{dm}{d\tau}u^{\mu}_{fluid} \tag{3.28}$$

where $h_{enth}$ is the specific enthalpy of the fluid, $u_{fluid}$ is the fluid 4-velocity and the accretion rate

$$\frac{dm}{d\tau} = \frac{4\pi\lambda m^2\rho_0}{(v_{rel}^2 + a_s^2)^{3/2}}. \tag{3.29}$$

Here $m$ is the mass of the companion black hole, $a_s$ is the sound velocity, and $\rho_0$ is the rest-mass density and can be obtained from equation (2.16). $\lambda = \left(\frac{1}{2}\right)^{\frac{(\Gamma+1)}{2(\Gamma-1)}}\left(\frac{5-3\Gamma}{4}\right)^{\frac{-(5-3\Gamma)}{2(\Gamma-1)}}$ is a dimensionless constant that depends on the polytropic index $\Gamma$ for a fluid with the polytropic equation of state(Shapiro & Teukolsky, 1983). Here we have used the relativistic form of $v_{rel}$. The expression

of which is given by [see Appendix A],

$$v_{rel} = \frac{\sqrt{(u^{fluid}.u_{sat})^2 - 1}}{(u^{fluid}.u_{sat})} \tag{3.30}$$

Equation (3.28) may be used to calculate the energy and angular momentum lost as a result of the companion's self-accretion. The quantity of which relies on other flow characteristics, including sound speed ($a_s$), density, etc., as well as the relative velocity $v_{rel}$ between the companion ($u_{sat}$) and the flow ($u_{fluid}$). Since the properties of our disk differ greatly from those of previous disk models, different results are likewise anticipated. Additionally, self-accretion increases the companion's mass. The equation (5.2) may be used to determine the companion's current mass.

#### 3.5.0.2 Hydrodynamic drag due to deflection

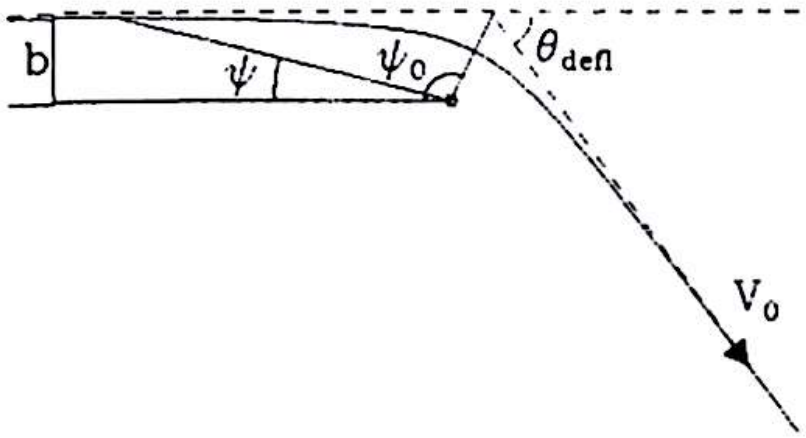


**Figure 3.3:** Encounter of mass with a single star

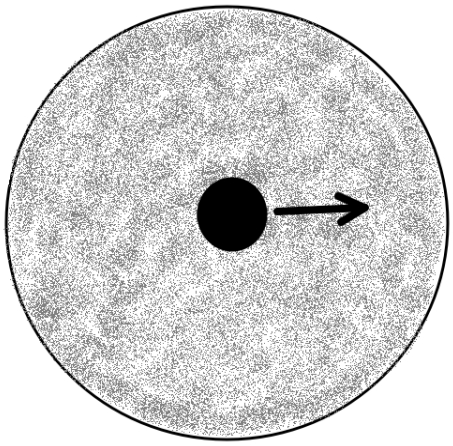

**Figure 3.4:** Satellite moving through a homogeneous sea of stars

When a massive object with significantly larger velocity moves through a background medium, its gravitational interaction with its own gravitationally induced wake exerts a retarding force to decrease the velocity of the fast-moving massive object. The process through which this drag force

removes angular momentum from the object is known as dynamical friction. In a pioneering study, Chandrasekhar (1943) derived the analytic theory for gravitational drag in a uniform collision-less background for a straight-line trajectory (Figure 3.3 & 3.4). This theory has been applied widely to many astronomical systems. Later, for a gaseous (collisional) medium and straight line trajectory, the gravitational drag was obtained by Ostriker (1999). In this work of Ostriker, we see that a subsonic object also experiences drag force for a finite interaction time, contrary to the previous work where the effects of drag on subsonic objects were found to be negligible (Dokuchaev, 1964; Ruderman & Spiegel, 1971; Rephaeli & Salpeter, 1980). For a perturber moving on a circular orbit in a uniform gaseous medium, Kim & Kim (2007) extended the work of Ostriker (1999), using the semi-analytic method. All these derivations are very successful in many astrophysical scenarios within the Newtonian framework. Barausse (2007) generalized this drag force for the relativistic case to study the interaction between compact objects and the accretion disk. Our present work closely follows these results for the calculation of drag exerted on the companion of the EMRI.

The components of the deflection drag can therefore be obtained as a sum of drag forces along the tangential and radial directions. Thus, one can write it as

$$\left.\frac{dP^{\mu}}{d\tau}\right|^{defl} = \left.\frac{dP}{d\tau}\right|^{tang} \sigma^{\mu} + \left.\frac{dP}{d\tau}\right|^{rad} \chi^{\mu} \tag{3.31}$$

where $\sigma^{\mu}$ is a unit space like vector orthogonal to $u_{sat}$ and pointing in the direction of the motion of the fluid, and $\chi^{\mu}$ is also a unit space like vector, orthogonal to both $u_{sat}$ and $\sigma$, and pointing in the radial direction. The expressions of the different components can be obtained from (Kim & Kim, 2007; Barausse, 2007; Barausse & Rezzolla, 2008). $\sigma$ and $\chi$ are given by,

$$\boldsymbol{\sigma} = \frac{\boldsymbol{u_{fluid}} - \gamma \boldsymbol{u_{sat}}}{\sqrt{\gamma^2 - 1}} \tag{3.32}$$

$$\boldsymbol{\chi} = \lambda \boldsymbol{u} + \alpha \boldsymbol{\sigma} + \left(\frac{\boldsymbol{\partial}}{\boldsymbol{\partial r}}\right) \tag{3.33}$$

is a unit space-like vector along the radial direction. $\chi$ is orthogonal to $\boldsymbol{u_{sat}}$ and $\boldsymbol{\sigma}$. Thus $\boldsymbol{\chi . u} = 0$ and $\boldsymbol{\chi . \sigma} = 0$ gives

$$\boldsymbol{\chi} = -u_r \boldsymbol{u} + \sigma_r \boldsymbol{\sigma} + \left(\frac{\boldsymbol{\partial}}{\boldsymbol{\partial r}}\right) \tag{3.34}$$

In our case, $\boldsymbol{u . u} = 1$, $\boldsymbol{\sigma . \sigma} = -1$, and $\boldsymbol{u . \sigma} = 0$.

Therefore

$$\boldsymbol{\chi . \chi} = \frac{u_r^2}{\gamma^2 - 1} + g_{rr} \tag{3.35}$$

which is also of negative amplitude. Thus we can write the unit space like vector $\chi$ as,

$$\boldsymbol{\chi} = \frac{-u_r \boldsymbol{u} + \sigma_r \boldsymbol{\sigma} + \left(\frac{\boldsymbol{\partial}}{\boldsymbol{\partial r}}\right)}{\sqrt{\frac{u_r^2}{\gamma^2 - 1} + g_{rr}}} \tag{3.36}$$

The term $\gamma$ gives the relative motion of companion with respect to the fluid & known as the Lorentz factor. The value of $\gamma$ [see Appendix B] is given by,

$$\gamma = \boldsymbol{U}^{\boldsymbol{fluid}}.\boldsymbol{U}_{\boldsymbol{sat}} \tag{3.37}$$

The tangential and radial drags (Ostriker, 1999; Kim & Kim, 2007; Barausse, 2007) are given by,

$$\left.\frac{dP}{d\tau}\right|^{tang} = \frac{4\pi(P+\rho)m^2\gamma^2(1+v^2)^2}{v^2} I_{tang} \tag{3.38}$$

$$\left.\frac{dP}{d\tau}\right|^{rad} = \frac{4\pi(P+\rho)m^2\gamma^3(1+v^2)^2}{v^2} I_{rad} \tag{3.39}$$

Numerically-computed steady-state values of $I_{tang}$ and $I_{rad}$ are given by[(Kim & Kim, 2007)],

$$\begin{aligned} I_{tang} &= 0.7706 \log\left(\frac{1+M}{1.0004-0.9185M}\right) - 1.4703M, \text{ For } M < 1.0 \\ &= \log\left(330\left(\frac{r}{r_{min}}\right)(M-0.71)^{5.72}M^{-9.58}\right), \text{ For } 1.0 \leq M \leq 4.4 \\ &= \log\left(\frac{\left(\frac{r}{r_{min}}\right)}{0.11M+1.65}\right), \text{ For } M \geq 4.4 \end{aligned} \tag{3.40}$$

$$\begin{aligned} I_{rad} &= M^2 10^{3.51M-4.22}, \text{ For } M < 1.1 \\ &= 0.5 \log\left[9.33M^2(M^2-0.95)\right], \text{ For } 1.1 \leq M \leq 4.4 \\ &= 0.3M^2, \text{ For } M \geq 4.4 \end{aligned} \tag{3.41}$$

where $r$ is the radius of the circular orbit, and $r_{min} = \frac{2m(1+v^2)}{v^2}$ is the capture impact parameter of the satellite black-hole, $\mathcal{M} = \frac{v}{v_s}$ is the Mach number.

Accumulating all the effects, the modified 4-momentum of the companion can therefore be obtained as,

$$P^\mu = P^\mu + \left.\frac{dP^\mu}{d\tau}\right|_{total} d\tau \tag{3.42}$$

where

$$\left.\frac{dP^\mu}{d\tau}\right|_{total} = \left.\frac{dP^\mu}{d\tau}\right|_{GW} + \left.\frac{dP^\mu}{d\tau}\right|_{Accretion} + \left.\frac{dP^\mu}{d\tau}\right|_{Deflection} \tag{3.43}$$

Equation no (3.26), (3.27),(3.28) and (3.31) respectively provides the right hand sides terms. Here $d\tau$ is the proper time interval between two successive orbits of the companion.

## 3.6 Results and Discussions

This section examines the dynamics of the companion BH surrounding a center SMBH while taking into account the impact of an accretion disk. The companion BH's dynamics are controlled by energy and angular momentum loss, which change the orbital parameters. As said, in addition to the gravitational radiation response, the accretion disk's hydrodynamic drag can also affect the motion of the orbiting companion. These impacts are evaluated when a massive accretion disk is present in the EMRI system. We begin with an E/IMRI that has a mass ratio of $q = \frac{M_{SMBH}}{m_{CBH}} = 10^{-2} - 10^{-4}$, where $m = m_{CBH}$ is the companion BH mass and $M = M_{SMBH} = 10^8 - 10^5 M_\odot$ is

the primary SMBH mass, at a large separation during the inspiral stage. A Kerr metric provides the system's background metric. We assume that the combined metric of the binary system is purely attributable to the core supermassive Kerr BH (Equation (3.10)) and that the presence of the companion and disk has no effect on it. For these systems, we compute the fluxes averaged over one period. We employ the quadrupole approximation formula provided by Ryan (1995) to calculate the energy and angular momentum loss rates $\frac{dE}{dt}$ and $\frac{dL}{dt}$ for the GW emission. The disk under consideration in our work is geometrically thin, and the transonic accretion flow solution around the center SMBH is assumed to have an accretion rate of $\dot{m} = \frac{\dot{M}}{\dot{M}_E}$, where $\dot{M}$ is the accretion rate of the companion BH and $\dot{M}_E$ is the Eddington mass accretion rate. We consider the companion's orbital plane to correspond with the disk's; therefore, the companion will constantly be embedded within the disk, allowing us to witness the maximal influence of the disk drag on the companion BH. In order to analyze this orbital motion, we developed a computational (numerical) code for integrating the companion's geodesic equations and calculating the loss rates from the instantaneous 4-momentum ($P^{\mu}$) of the companion during its orbital development, taking all such effects into account. The initial semi-major axis ($X$) and eccentricity ($e$), Kerr parameter ($a$), initial E/IMR ratio, mass accretion rate $\dot{M}$, and the disk parameters (described in section §2.5.5) are the starting parameters that remain necessary for this code.

We presents our results in the following subsections.

### 3.6.1 Satellite orbital degradation crossing through an accretion disk and change in infall time

In this subsection we compares evolution in companion's energy loss during the emission of gravitational waves (GW) in vacuum with the case when the companion BH is under the influences of hydrodynamic drag.

In figure 3.5, we plot the variation of energy in the last 6 years before the coalescence. We plot the results for two cases: (i) GW+Disk (*blue line*) and (ii) GW alone (*red line*), with initial eccentricity and Kerr parameter values of $e = 0.50$ and $a = 0.50$, respectively. In the figure, we see that, in the presence of the disk, the energy loss rate is comparatively higher than in the absence of the disk, indicating that a non-negligible hydrodynamic drag acted on the companion due to the disk. The reduction of coalescence time in the present and absence of the disk is more than 6 months. For high eccentric orbits, this coalescence time further reduces.

We exhibit energy loss in the most recent years of the inspiral in the presence (*solid line*) and absence (*dashed line*) of the disk for $e = 0.30$ in Figure 3.6 to provide additional clarity about the effects of the disk drag. This graph show that while the infall time is shorter for the high eccentric orbit ($e = 0.50$), the disk drag has a greater impact on the lower eccentric orbit ($e = 0.30$). This is because in low eccentric orbits, the companion passes across the disk over a longer period of time, increasing the overall combined impact of disk drag.

The companion's energy loss for a number of eccentric orbits with and without a disk is compared and shown in Figures 3.7. We illustrate the companion's energy loss for four scenarios with eccentricities of $e = 0.15$ (*solid line*), 0.25 (*dotted line*), 0.30 (*dashed line*), and 0.50 (*dot-dashed line*) in Figure 3.7. As we can see, the energy loss rate is very low during the inspiral phase and significantly increases following the inspiral-to-merger phase transition. A highly eccentric

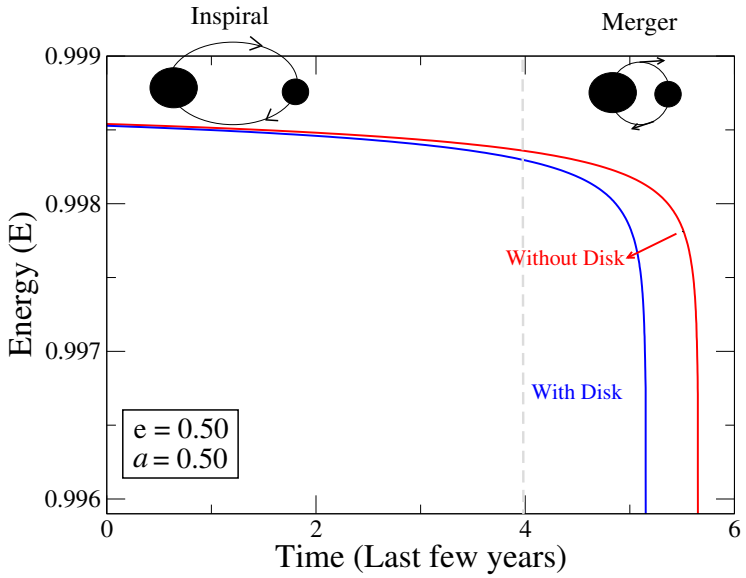


**FIGURE 3.5:** We compare the results of the decrease in the energy ($E$) of the companion black hole when the accretion disk is present (*blue line*) and absent (*red line*). We plot the figure for the last few years before coalescence, where we can see the change of $E$ ( between solid and dashed line), increases when EMRI moves from the inspiral to merger phase. Though the change is small, we see that in the presence of the disk, the companion loses energy faster($\sim$ 6 months) than in the absence of the accretion disk. Initial conditions are as follows:$\dot{m} = 1$, $e = 0.50$, $a = 0.50$, $X = 500r_g$,$M = 10^8 M_\odot$, $m = 10^6 M_\odot$.

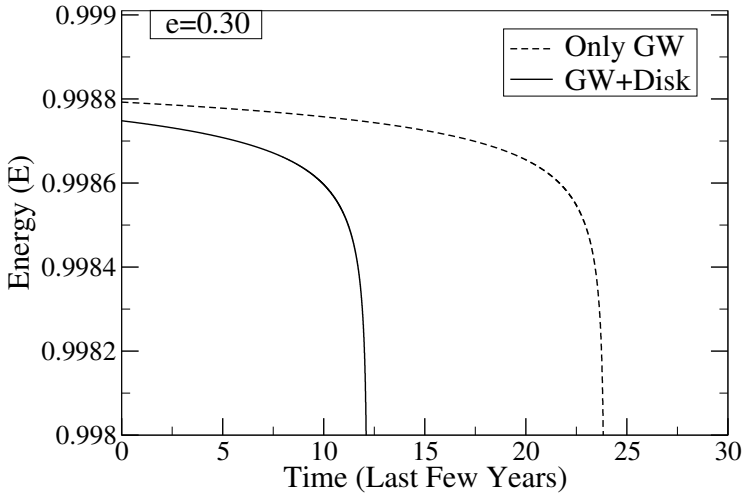


**FIGURE 3.6:** In this Figure we reproduce Figure 3.5 with eccentricity $e = 0.30$ keeping all other parameters same.

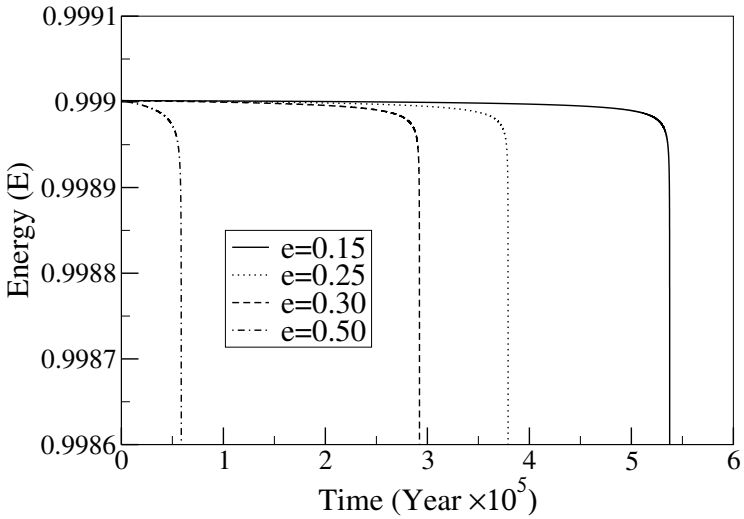


**Figure 3.7:** This Figure illustrates the variation in the companion black hole's energy loss with respect to time ($T$) for orbits with eccentricities of $e = 0.15$(*solid line*) 0.25 (*dotted line*), 0.30(*dashed line*) and 0.50 (*dot-dashed line*). We see that the energy declines initially gradually and then quickly, especially in the final few years prior to the coalescence. A low eccentric orbit loses energy more slowly than one that is relatively high in eccentricity.

orbit ($e = 0.50$) also coalesces much more quickly than a low eccentric orbit ($e = 0.15$). The change with respect to other parameters during the last several years of observation, however, makes it evident from the following figures that it would be better to monitor high eccentric orbits since they are subject to the maximum impact of disk drag.

### 3.6.2 Torque on the companion BH: with & without disk

This subsection compares the emission rate of gravitational waves (GW) with the emission rate resulting in the presence of the hydrodynamic drag on the companion BH. For illustration, we take into account elliptic orbits with various starting eccentricities and various semi-major axes. We show the change in angular momentum ($L$) during the previous six years leading up to the coalescence in Figure 3.8. We give our results for two cases: (i) GW+Disk (*blue line*) and (ii) GW alone (*red line*), with initial eccentricity and Kerr parameter values of $e = 0.50$ and $a = 0.50$, respectively. We see that the angular momentum drops relatively more faster when disk is present. As a result, the coalescence period is almost a year shorter. For high eccentric orbits, the coalescence time is further reduced.

We draw Figure 3.9, where we compare the angular momentum loss in the presence (*solid line*) and absence (*dashed line*) of the disk, to demonstrate the effects of the hydrodynamic drag of the disk on a lower eccentric orbit compare to Figure 3.8. Infall time has changed significantly during the past five years of observation in the presence of disk torque. We can also see that the variations in eccentricity may cause distinct modifications in infall time.

Figure 3.10 illustrates the overall variations of angular momentum with infall time for different elliptic orbits. We select four different elliptic orbits with eccentricities $e = 0.15$(*solid line*) 0.25 (*dotted line*), 0.30(*dashed line*) and 0.50 (*dot-dashed line*) to observe the decay of the angular momentum with eccentricity during the inspiral motion of the companion within the disk. Evidently

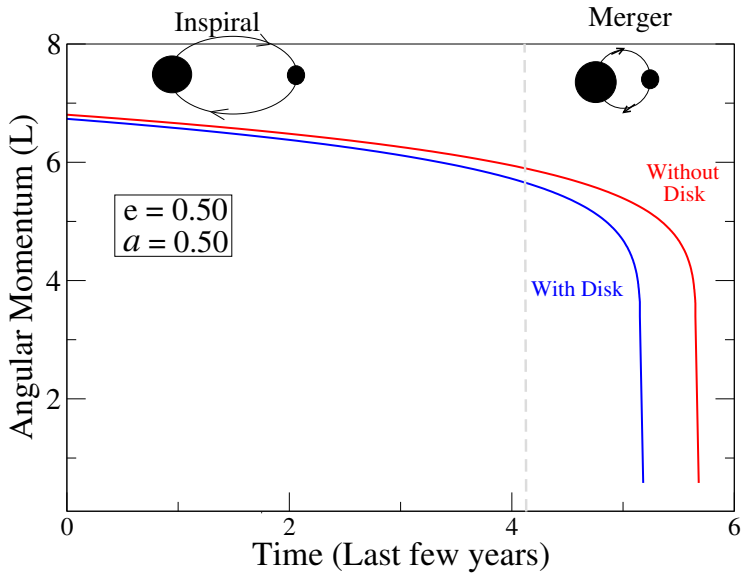


**FIGURE 3.8:** In the graph, we examine the loss of the companion's angular momentum ($L$) as a function of time ($T$) for both the presence (*blue line*) and absence (*red line*) of the accretion disk. We plot the figure for the final few years prior to coalescence, where we can observe how $L$ (between the solid and dotted line) changes as the stage transitions from spiral to merging. We see that coalescence occurs somewhat more quickly ($\sim$ 1 year) when the disk is present than when it is not. Initial conditions are as follows:$\dot{m} = 1$, $e = 0.50$, $a = 0.50$, $X = 500r_g$,$M = 10^8 M_\odot$, $m = 10^6 M_\odot$.

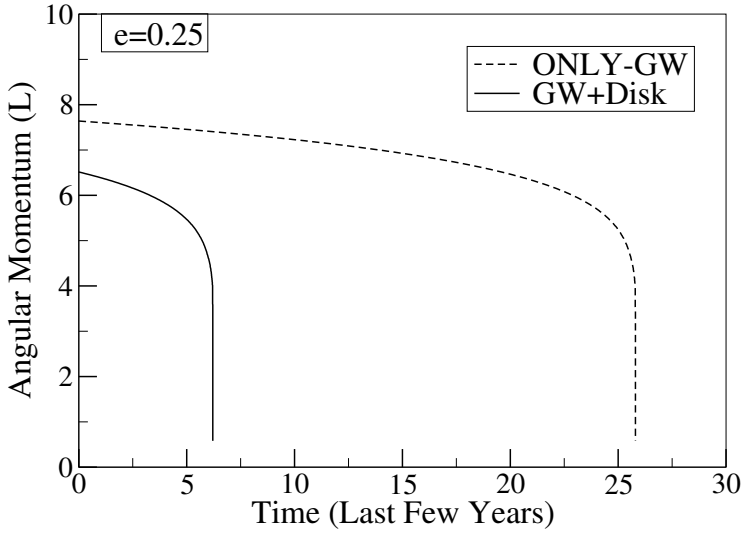


**FIGURE 3.9:** In this Figure, we evaluate the loss rates with and without an accretion disk for the initial eccentricity $e = 0.25$, and find that the incorporation of an accretion disk minimizes infall time.

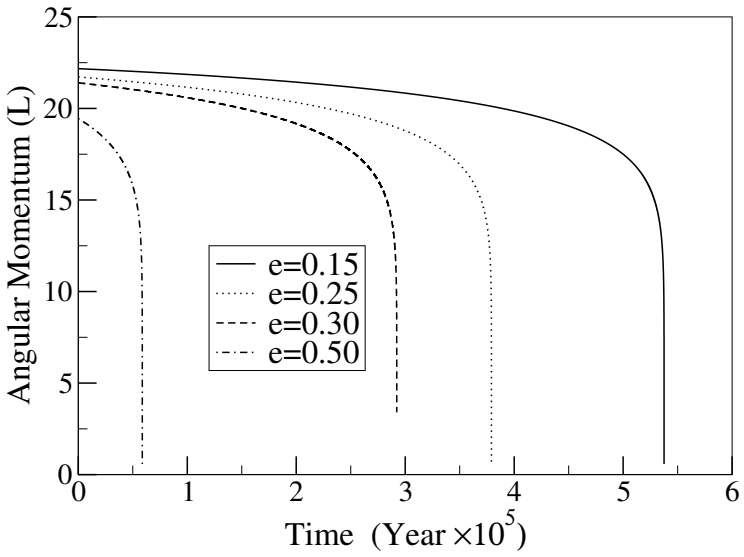


**Figure 3.10:** We plot the angular momentum ($L$) of the companion black hole with time ($T$) in this Figure for four cases with eccentricities $e = 0.15$(*solid line*) 0.25 (*dotted line*), 0.30(*dashed line*) and 0.50 (*dot-dashed line*) in the presence of an accretion disk. We can see that as time passes, the angular momentum diminishes. We can also see that a low eccentric orbit has more angular momentum and takes longer to lose it than a high eccentric orbit.

the loss rate is larger for the high eccentric orbit ($e = 0.50$), which loses angular momentum more rapidly than the low eccentric orbit ($e = 0.15$).

The torque is defined as the rate of angular momentum loss $\frac{dL}{dt}$. We estimated $\frac{dL}{dt}$ in both the presence and absence of the accretion disk. The difference between the two values represents the torque on the companion caused only by the disk. This disk torque is caused by the entire hydrodynamic drag acting on the companion as a result of the disk's self-accretion and deflection. Thus, in the presence of the disk, the companion's angular momentum decays faster with time.

To estimate the net torque acting on the companion, we plot the rate of loss of angular momentum $\left(\frac{dL}{dt}\right)_{\rm disk} = \left(\frac{dL}{dt}\right)_{\rm acc} + \left(\frac{dL}{dt}\right)_{\rm defl}$ for the eccentricities $e = 0.15$(*red line*) and 0.50(*solid line*) respectively in the Figure 3.11. The total estimated torque is presented within the perihelion radius $r_P = 100r_g$ to ISCO. This is because the late inspiral stages are more effective at detecting the accretion disk within the LISA band. The magnitude of the torque $\left(\frac{dL}{dt}\right)_{\rm disk}$ is significantly increased in this observed band for the high eccentric orbit. The results clearly show that high eccentric orbits decay relatively faster due to the significant impact of the disk on the companion, and thus could be one of the preferable orbital parameters for EMRIs in order to observe in the LISA band.

We investigate the angular momentum loss rates for additional orbital parameters. We investigate three unique orbits with semi-major axes of $X = 200r_g$, $500r_g$, and $900r_g$, respectively. The initial eccentricities of the three orbits are similar and equal to $e = 0.50$. Figure 3.12 depicts the angular momentum loss with the perihelion radius $r_P$ for various semi-major axes ($X$). We can observe that the relative change of $\frac{dL}{dr_P}$ is nearly comparable, albeit slightly bigger for $X = 900r_g$.

The evolution of the perihelion radius ($r_P$) of the companions with the infall time for different eccentric orbits with initial $X = 500r_g$ can be seen in Figure 3.13. As expected, the smaller perihelion radius infall time is likewise smaller. Because high eccentric orbits have a smaller $r_P$, their orbital evolution is substantially faster. As a result, the rate of change in perihelion radius,

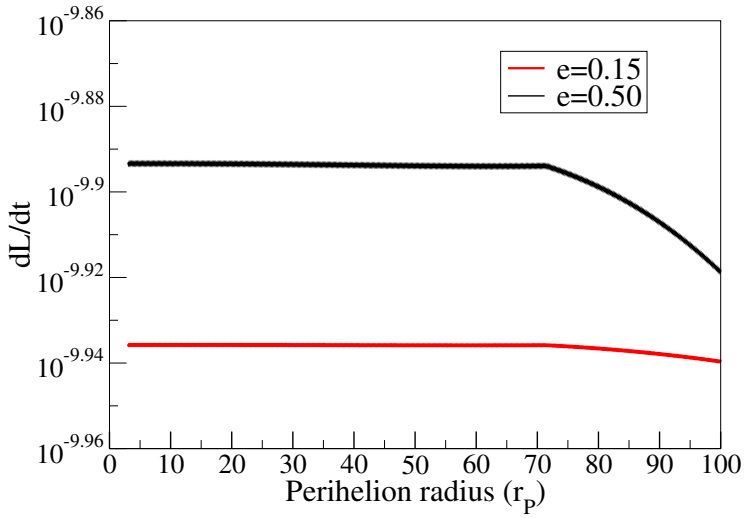


**Figure 3.11:** This Figure depicts the torque due to disk drag. We can see the loss rate, which means that the torque is greater for high eccentric orbits. Initial values: $\dot{m} = 1$, $a = 0.50$ and $X = 500r_g$.

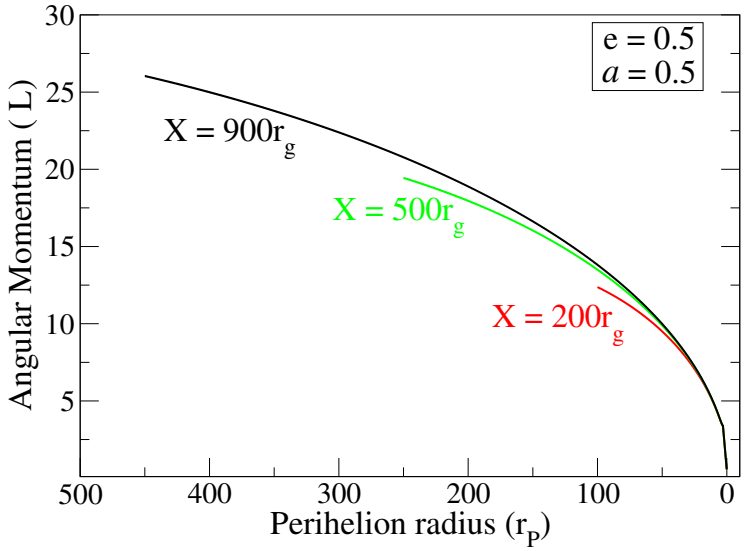


**Figure 3.12:** In this Figure, we analyze three possible orbits with varying semi-major axis. Angular momentum vs perihelion radius is drawn here for $X = 200r_g$ (*red line*), $500r_g$ (*green line*), $900r_g$ (*black line*), respectively. Although slightly greater for $X = 900r_g$, we can see that the relative change of $L$ with respect to $r_P$ is nearly identical.

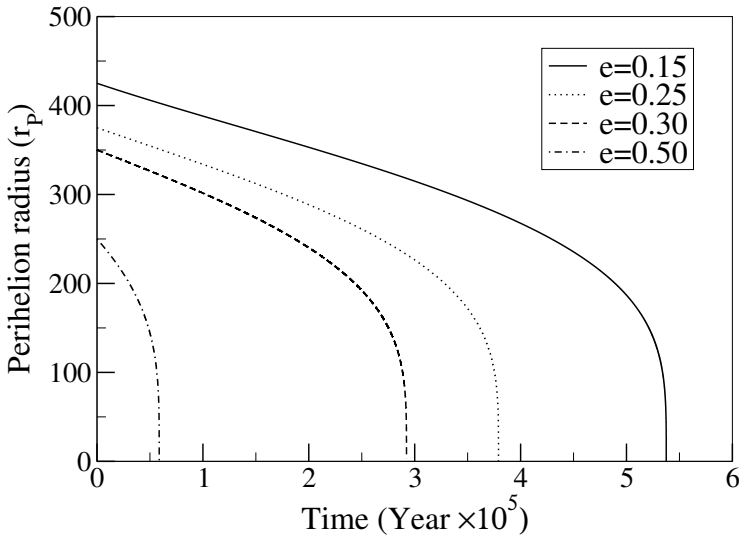


**Figure 3.13:** In this figure we plot the radial distance with time for various eccentric orbits. We see here that the smaller the eccentricity the longer the infall time. Parameters used are $\dot{m} = 1$, $e = 0.50$, $a = 0.50$, $M = 10^8 M_\odot$, $m = 10^6 M_\odot$

$\frac{dr_P}{dt}$, would be even faster for $X = 200r_g$ because initial values of $r_P$ are smaller for $e = 0.50$. Thus, the torque $\left(\frac{dL}{dt}\right) = \left(\frac{dL}{dr_P}\right)\left(\frac{dr_P}{dt}\right)$ will prevail for orbits with $e = 0.50$ and $X = 200r_g$, i.e., for high ecentric and short semi-major axis orbits, this would be an ideal parameter for LISA observation.

The aforementioned conclusion can also be drawn from Figures 3.14 and 3.15 which use the same three orbits to show the loss of angular momentum ($(L)$) with changing eccentricity. Figure 3.14 further examines the eccentric orbit with initial eccentricity ($e = 0.50$) for various initial parameters. As can be seen in Figure 3.15 the bigger orbits often migrate more slowly and have slower decay. As a result, the eccentricity evolves more quickly for $X = 500r_g$(*green line*) and less slowly for $X = 900r_g$(*black line*) in the presence of the disk. Since $\left(\frac{de}{dt}\right)$ is significantly greater even though $\left(\frac{dL}{de}\right)$ is comparatively smaller for this orbit, the torque $\left(\frac{dL}{dt}\right) = \left(\frac{dL}{de}\right)\left(\frac{de}{dt}\right)$ is higher for smaller semi-major axes ($X = 200r_g$).

### 3.6.3 Loss rates & Magnitude comparison : GW vs Disk: Accretion & Deflection

#### 3.6.3.1 Magnitude of energy loses : GW vs Disk

In this subsection, we compare the orders of magnitude of the energy loss rates $\frac{\Delta E}{E}$ brought on by accretion and deflection for the orbits with $a = 0.50$, $e = 0.50$, and $r_P = 500r_g$. We also compare the rates of energy loss for three accretion rates $\dot{m} = 0.1$, 1, and 10 to show how the companion interacts with the accretion disk via the self-accretion and deflection processes distinctly. This is shown in figure 3.16, where we can observe that the loss rates rise with time and that a higher mass accretion rate results in more energy loss. As it gets closer to the core SMBH, the rate of energy loss increases. The (*dash line*) is drawn with $\dot{m} = 0.1$ in panels (a) and (c) and $\dot{m} = 10$ in panels (b) and (d), respectively, while the *solid line* is drawn with the mass accretion rate $\dot{m} = 1$ in each panel.

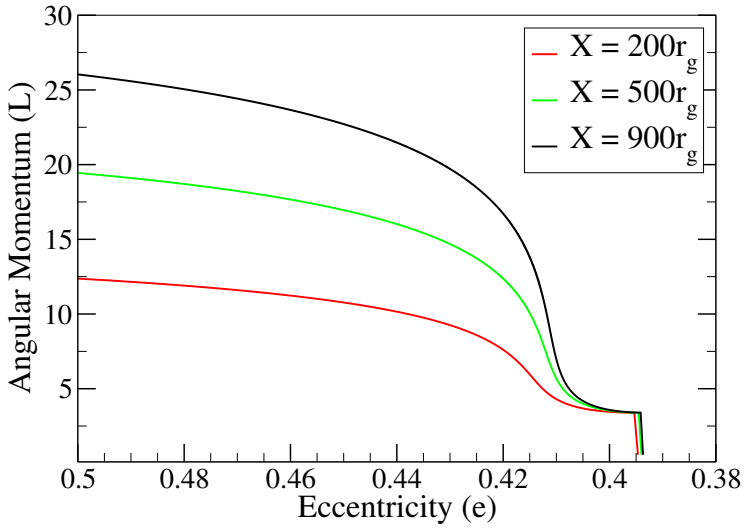


**Figure 3.14:** This Figure show, how angular momentum ($L$) is lost as eccentricity fluctuates and decays. For $X = 900r_g$(*black line*), the eccentricity develops more slowly, while for $X = 500r_g$(*green line*), it develops more quickly. The orbit with much smaller semi-major axis i.e. $X = 200r_g$(*red line*), the development is more quicker. Parameters used are $\dot{m} = 1$, $e = 0.50$, $a = 0.50$, $M = 10^8 M_\odot$, $m = 10^6 M_\odot$.

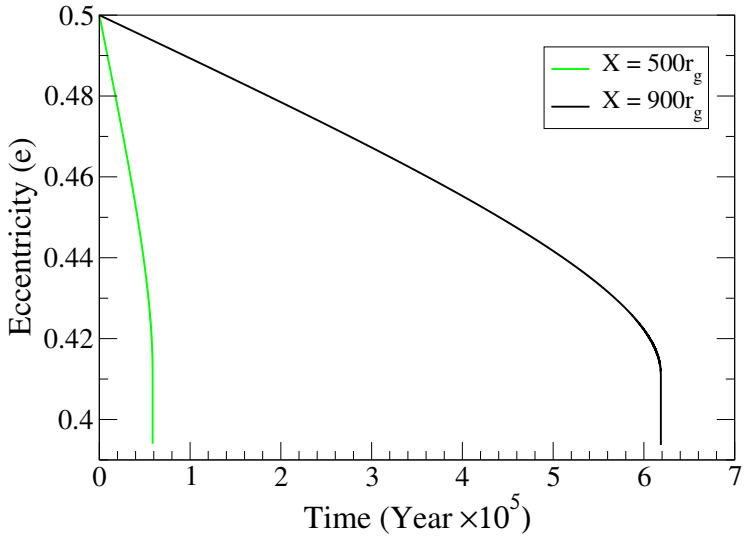


**Figure 3.15:** This Figure shows the variation of eccentricity with time for two orbit with different semi major axis which are $X = 900r_g$(*black line*) and $X = 500r_g$(*green line*), $e$ it develops more quickly for the later one. Parameters used are $\dot{m} = 1$, $e = 0.50$, $a = 0.50$, $M = 10^8 M_\odot$, $m = 10^6 M_\odot$.

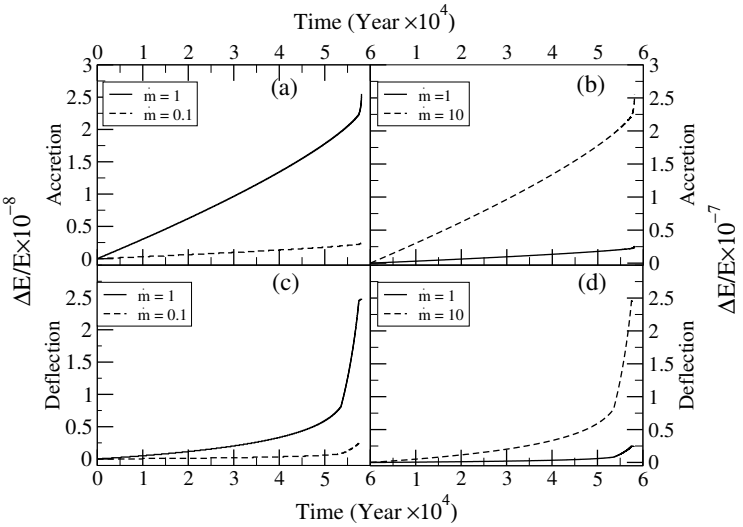


**Figure 3.16:** Initial parameters : $a = 0.50$, $e = 0.50$ and $X = 500r_g$. Variation of Energy loss of companion black hole due to accretion (panel (a) & (b)) and deflection (panel (c) & (d)) are shown. The $\dot{m} = 1$(*solid line*), $\dot{m} = 0.1$( panel (a) & (c) *dash line*) and $\dot{m} = 10$ (*dash line*) in the panel (b) & (d) are shown. With increasing mass accretion rate , the energy loss also increases.

Figure 3.17 shows the energy loss rate for accretion and deflection over time for three orbits with starting eccentricities of $e = 0.15$ (*solid line*), $e = 0.25$(*dotted line*), and $e = 0.50$ (*dashed line*). We can observe that when eccentricity is at its lowest, energy loss is at its highest and takes the longest to occur.

In Figure 3.18, we examine the energy loss from accretion and deflection for two orbits with differing semi-major axes, $X = 500r_g$ (*green line*) and $X = 900r_g$ (*black line*). The fact that energy loss rates are higher for bigger orbits suggests that hydrodynamic drag forces are present and significant for lengthy inspiral cases.

Figure 3.19 shows the energy loss rates against time for various Kerr parameters with the mass accretion rate of $\dot{m} = 1$ and eccentricity $e = 0.50$. The fluctuation of energy loss due to accretion (*solid line*) and deflection (*dash line*) for $a = 0$ is shown in panel (a), and the same is shown for $a = 0.50$ in panel (b). We can observe that in the case of no rotation, the loss rates exceed the $a = 0.50$ condition. For Kerr parameters $a = 0.50$ (*solid line*), $a = 0.75$ (*dash line*), and $a = 0.95$ (*dot line*), respectively, we show energy loss owing to accretion and deflection individually in panels (c) and (d). While the loss rate from deflection reduces for higher spin values, the loss rate from accretion increases with an increasing Kerr parameter.

Figure 3.20's left panel shows the energy emission rates as a result of gravitational wave (*solid line*) and hydrodynamic drag (*dashed line*). In the right panel of the image, the change in the companion's energy $\frac{\Delta E}{E}$ owing to drag (*dashed line*) and GW (*solid line*) is depicted as a result of these loss rates. We can observe that the energy loss rate from hydrodynamic drag is present in both panels but is far less than the GW emission. For a variety of orbits these changes are likewise measured and observed.

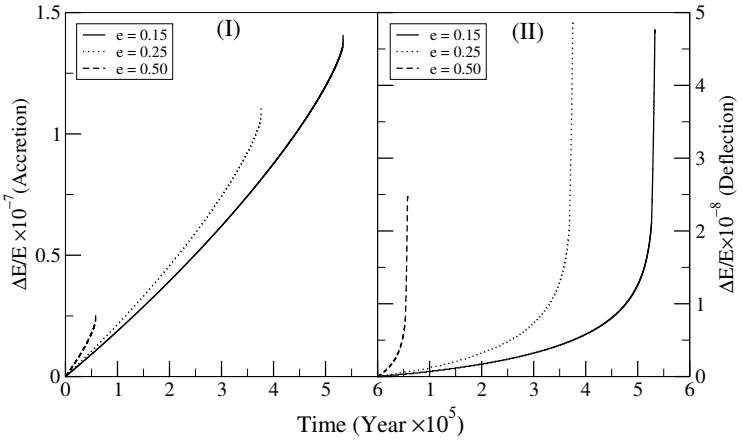


**FIGURE 3.17:** Initial parameters : $a = 0.50$, $\dot{m} = 1$ and $X = 500r_g$. We plot the energy loss due to accretion (panel (I)) and deflection (panel (II)). We consider three orbit with eccentricities $e = 0.15$ (*solid line*), $e = 0.25$(*dotted line*) and $e = 0.50$ (*dashed line*). We see that lower eccentric orbit took greater time to loss energy but the loss is greater than the other cases.

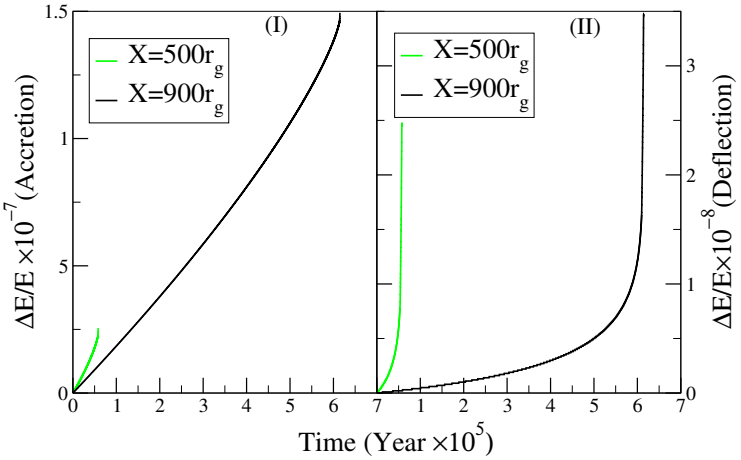


**FIGURE 3.18:** Initial parameters : $a = 0.50$, $\dot{m} = 1$ and $e = 0.50$. We compare the energy loss with time due to accretion (panel (I)) and deflection (panel (II)) for two orbits with semi major axis $X = 500r_g$ (*green line*) and $X = 900r_g$ (*black line*). The energy loss is higher for a bigger orbit.

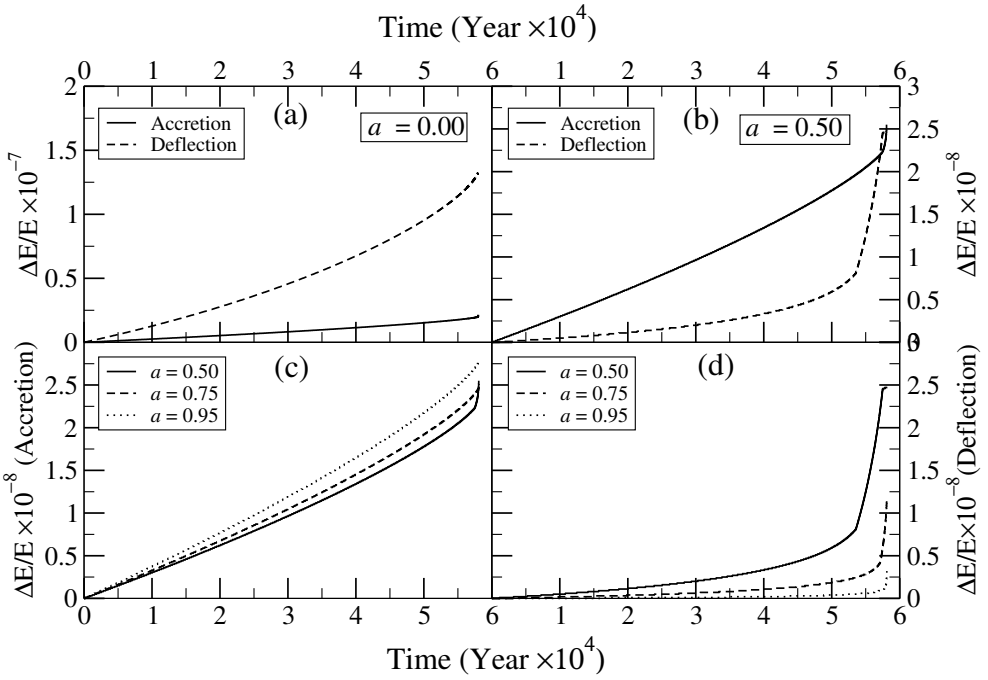


**FIGURE 3.19:** Initial parameters : $\dot{m} = 1$ and $e = 0.50$ and $X = 500r_g$. We compare the energy loss with time in the four panel. In the upper panels (a) & (b), we plot the energy loss due to accretion (*solid line*) and deflection(*dash line*) for $a = 0.0$ (panel (a)) and $a = 0.50$ (panel (b)). In the lower panel a comparison of loss rate for various Kerr parameters $a = 0.50$ (*solid line*), $a = 0.75$ (*dash line*) and $a = 0.95$ (*dot line*) are shown for accretion (panel (c)) and deflection (panel (d)). We see that the loss rates are more for no spin case comparing to a spinning black hole. We also see that the with increasing Kerr parameter the loss rate due to accretion increases but for deflection the loss rate decreases for higher spin values. The physical origin of both the forces might lead to this opposite nature.

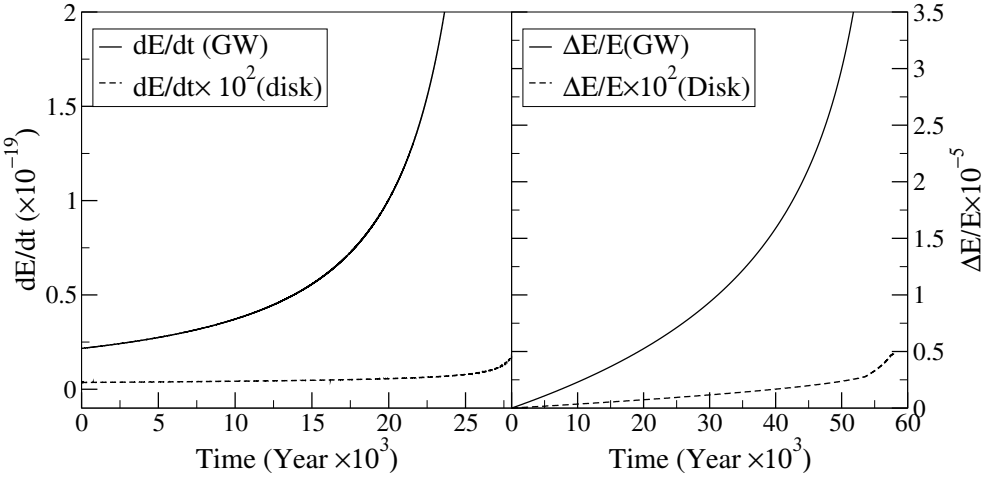


**FIGURE 3.20:** In the left panel we plot $\dot{E}$ vs time for the system with central BH mass $10^5 M_\odot$ and $EMR = 10^{-4}$ and in the right panel we plot $\frac{\Delta E}{E}$ for a system with companions mass $10^8 M_\odot$ and $10^6 M_\odot$. In both panels of the figure, we present a comparison of the energy loss of companion black holes between the loss rates due to the emission of GW(*solid line*) and due to the disk drag(*dash line*) while companion BH($m$) moves through the accretion disk. Here again, it clearly shows that the energy loss is small but non-negligible in the presence of the disk. $\dot{m} = 1$, $a = 0.50$, $e = 0.30(left)$ $e = 0.50(right)$ and $X = 500r_g$ are additional parameters.

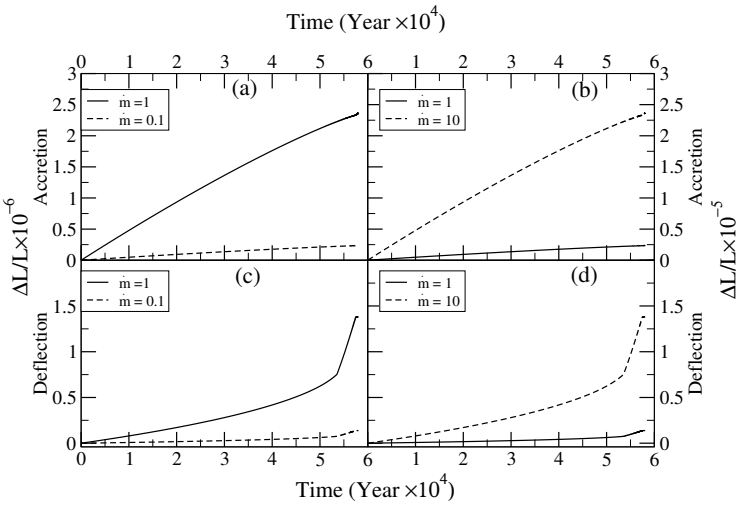


**FIGURE 3.21:** Initial parameters : $a = 0.50$, $e = 0.50$ and $X = 500r_g$. Variation of angular momentum loss of companion black hole due to accretion (upper panel) and deflection (lower panel) are shown. The $\dot{m} = 1$(*solid line*), $\dot{m} = 0.1$( upper and lower left panel *dash line*) and $\dot{m} = 10$ (*dash line*) in the upper and lower right panel are shown. With increasing mass accretion rate, the loss also increases.

#### 3.6.3.2 Magnitude of Angular momentum loses of the companion BH : GW vs Disk

The system loses angular momentum when a gravitational wave is emitted. The disk's presence allows for a momentum exchange with the system. Here, we talk about how companion self-accretion and deflection affect angular momentum loss over time. In Figure 3.21, we depict the change in momentum loss rates ($\frac{\Delta L}{L}$) owing to accretion and deflection with time ($T$) for two examples, with starting eccentricity and Kerr parameter at $e = 0.50$ and $a = 0.50$. In each panel of the figure, the *dash line* is drawn when $\dot{m} = 0.1$ and $\dot{m} = 10$, respectively, and the *solid line* is drawn when the mass accretion rate $\dot{m} = 1$. As time passes, we see that the loss rates rise and that a greater mass accretion rate results in a bigger loss of momentum.

Figure 3.22 shows the angular momentum loss rate for accretion and deflection over time for three orbits with starting eccentricities of $e = 0.15$ (*dash line*), $e = 0.25$(*dot line*), and $e = 0.50$ (*solid line*). We can observe that the loss rates are higher when the eccentricity is at its lowest. We can also see that for low eccentric orbits, the infall time is higher than for high eccentric orbits.

In figures 3.23 (I) & (II), we examine the angular momentum loss resulting from accretion and deflection for two orbits with semi-major axes of $X = 500r_g$ (*green line*) and $X = 900r_g$ (*black line*), respectively. We can observe that the orbit with $X = 900r_g$ has a larger rate of momentum loss.

Figure 3.24 shows the momentum loss rates vs. time for various Kerr values where the mass accretion rate is assumed to be $\dot{m} = 1$ and the eccentricity is assumed to be $e = 0.50$. In the first picture (a), the variation in momentum loss due to accretion is shown by *solid line* and due to deflection is shown by *dash line* for $a = 0$, and in the second figure (b), the same is shown for $e = 0.50$. We can observe that loss rates are higher for $a = 0$ case than the prograde spin $a = 0.50$. We depict momentum loss resulting from accretion and deflection individually for $a = 0.50$ (*solid line*), $a = 0.75$ (*dot line*), and $a = 0.95$ (*dash line*) in the third and fourth panels (c) & (d), respectively. We see that the loss rate for accretion grows with increasing $a$, but the loss rate for deflection reduces with increasing spin.

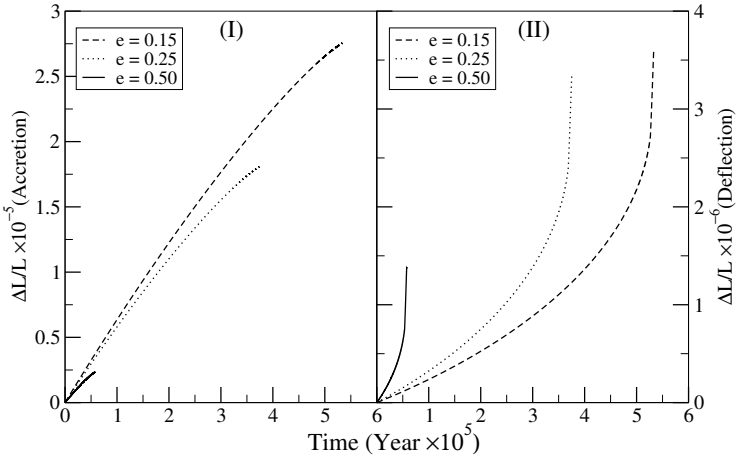


**FIGURE 3.22:** Initial parameters : $a = 0.50$, $\dot{m} = 1$ and $X = 500r_g$. We plot the angular momentum loss due to accretion (left panel) and deflection (right panel). We consider three orbit with eccentricities $e = 0.15$ (*dash line*), $e = 0.25$(*dot line*) and $e = 0.50$ (*solid line*). We see that lower eccentric orbit took greater time to loss momentum but the loss is greater than the other cases.

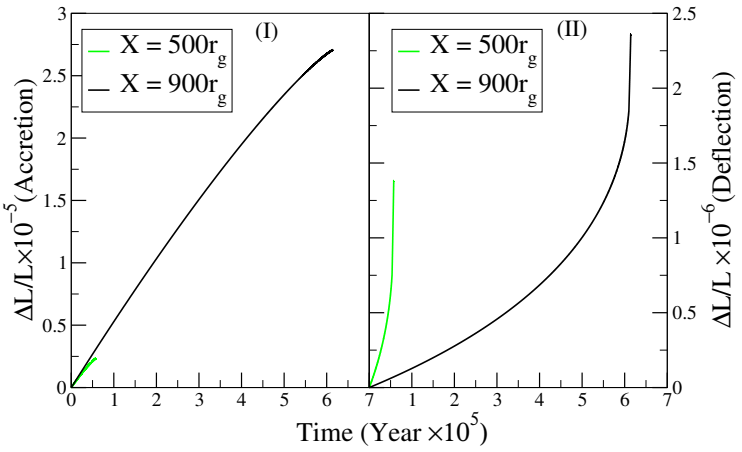


**FIGURE 3.23:** Initial parameters : $a = 0.50$, $\dot{m} = 1$ and $e = 0.50$. We compare the momentum loss with time due to accretion (left panel) and deflection (right panel) for two orbits with semi major axis $X = 500r_g$ (*green line*) and $X = 900r_g$ (*black line*). The momentum loss is higher for a bigger orbit.

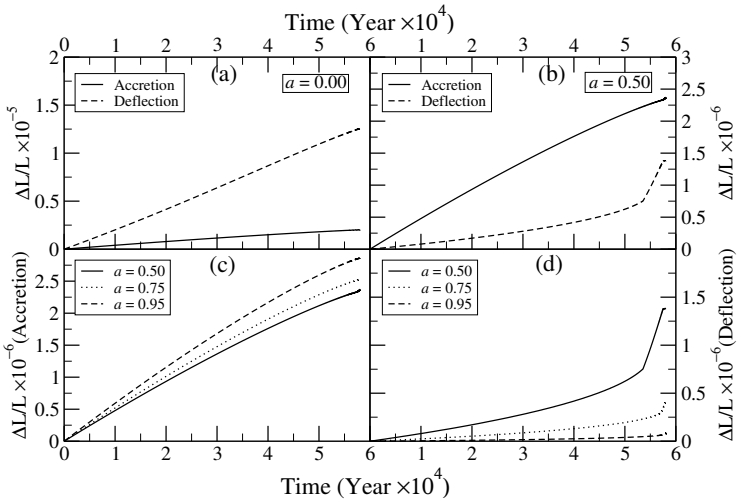


**FIGURE 3.24:** Initial parameters : $\dot{m} = 1$ and $e = 0.50$ and $X = 500r_g$. We compare the momentum loss with time in the four panel. In the upper panel we plot the momentum loss due to accretion (*solid line*) and deflection(*dash line*) for $a = 0.0$ (panel (a)) and $a = 0.50$(panel (b)). In the lower panel a comparison of loss rate for various Kerr parameters $a = 0.50$ (*solid line*), $a = 0.75$ (*dot line*) and $a = 0.95$ (*dash line*) are shown for accretion (panel (c)) and deflection (panel (d)). We see that the loss rates are more for no spin case comparing to a spinning black hole. We also see that the with increasing Kerr parameter the loss rate due to accretion increases but for deflection the loss rate decreases for higher spin values. The physical origin of both the forces might lead to this opposite nature.

The angular momentum emission rates owing to GW (*blue line*) and due to hydrodynamic drag (*red line*) are shown in the left panel of figure 3.25. During its orbital motion, the companion BH's angular momentum is altered by these emission rates. As a result, during this motion, the right panel of Figure 3.25 shows the change in instantaneous angular momentum $\frac{\Delta L}{L}$ owing to GW (*blue line*) and due to drag (*red line*).

For different kinds of orbits, these modifications are seen. Based on the aforementioned numerical findings, we can now say that the disk exerts an additional torque on the companion, which alters the companion's orbital motion and causes a greater loss of energy and angular momentum. This extra torque shortens the infall period. The cumulative phase of the signal was the last place where this shift in infall time could be seen. The cumulative phase shift would be small since the contribution of disk effects is small compared to the GW emission but not insignificant. The detectability of the dephasing of the transmitted GW signal in the LISA band determines whether or not the net cumulative effect is significant.

### 3.6.4 Impact on the orbital parameters : Evolution with & without disk

Continuous loss of the orbital parameters $E$ and $L$ leads to a gradual reduction in the companion's orbital radius and propel the inspiral motion. As a result, the orbit evolves with time, and the current trajectory is determined by the current values of $E$ and $L$. The perihelion and aphelion radius are therefore reduced in the case of an elliptical orbit or inspiral. Figure 3.26 shows the reduction in perihelion ($r_P$) and aphelion ($r_a$) radii with time ($T$) in both the presence (*solid line*) and absence (*dash line*) of the disk. We begin at $r_a = 750r_g$ and $r_P = 250r_g$ at the beginning of the inspiral stage, but special emphasis is put on in the final few years before coalescence, when the companion goes from the inspiral to the merger stage. This is due to the possibility that such a system may have been detectable during recent LISA band observations. The graphic includes the

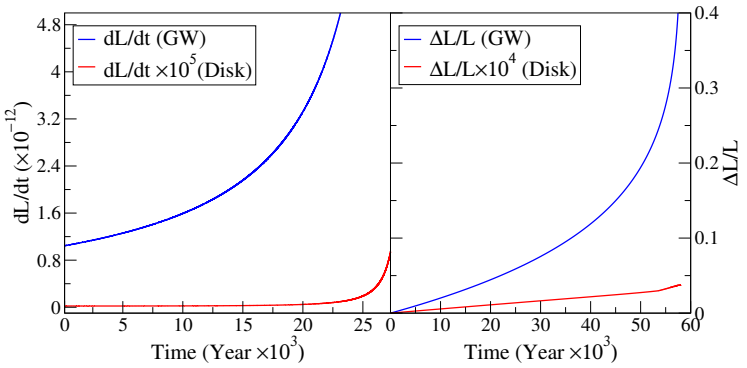


**FIGURE 3.25:** We show the angular momentum ($L$) emission rate of the companion black hole (left panel) as a function of the GW emission (*blue line*) and disk drag (*red line*) as the companion travels across the accretion disk. We depict the instantaneous change in angular momentum of the companion BH $\frac{\Delta L}{L}$ owing to the GW emission (*blue line*) and due to disk drag (*red line*) in the right panel. EMRI with masses of $M = 10^5 M_\odot$ $m = 10 M_\odot$, and $M = 10^8 M_\odot$ $m = 10^6 M_\odot$ are selected for the left panel, respectively. $\dot{m} = 1$, $a = 0.50$, $e = 0.30(left)$ $e = 0.50(right)$ and $X = 500 r_g$ are additional parameters. The disk introduces a tiny but not insignificant contribution to the GW loss rates, as can be seen from both panels.

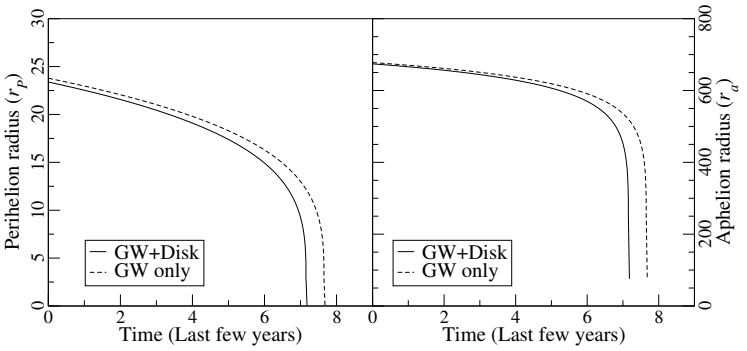


**FIGURE 3.26:** In the following plot, we contrast the reduction in perihelion ($r_P$) and aphelion ($r_a$) radius with time ($T$) under the two scenarios of an accretion disk existing (*solid line*) and an absence of the disk (*dash line*). Before the coalescence, we track the developments during the last several years. We see that both the orbit's $r_P$ and $r_a$ decrease more quickly (by about a year) in the presence of an accretion disk than in the absence of one. The initial parameters taken into consideration for this plot are as follows:$\dot{m} = 1$, $e = 0.50$, $a = 0.50$, $X = 500 r_g$, $M = 10^8 M_\odot$, $m = 10^6 M_\odot$.

initial orbital radii values as well as further orbital characteristics. The aphelion and perihelion distances both steadily decrease over time, but there are variations between them i.e., for the cases of with and without a disk. Additionally, we see that both radii drop at a comparatively higher pace when the disk is present.

The total infall time before the coalescence is shown in Figure 3.27. Here we consider two different orbits with initial values $X = 500 r_g$ ($r_P$ (*solid line*) and $r_a$ (*dot-dash line*)) and $X = 900 r_g$ ($r_P$ (*dash line*) and $r_a$ (*dot-dot-dash line*)) and observe the decrease in perihelion ($r_P$) and aphelion ($r_a$) radius. The $r_p$ decreases at a faster rate; however, the $r_a$ slowly increases in the inspiral stage. The orbit evolves in such a way that the eccentricity of the orbit decreases very slowly with time to make it circular. In the final merging stage before the coalescence, both radii sharply fall.

To learn more about these elliptical inspiral orbits of the E/IMRIs, we take the instantaneous values of $r_a$& $r_P$ and represent them in terms of orbital eccentricity as $e(T) = \frac{r_a - r_p}{r_a + r_p}$. As is well known, an elliptic orbit tends to become circular by decreasing its eccentricity ($e$) during GW

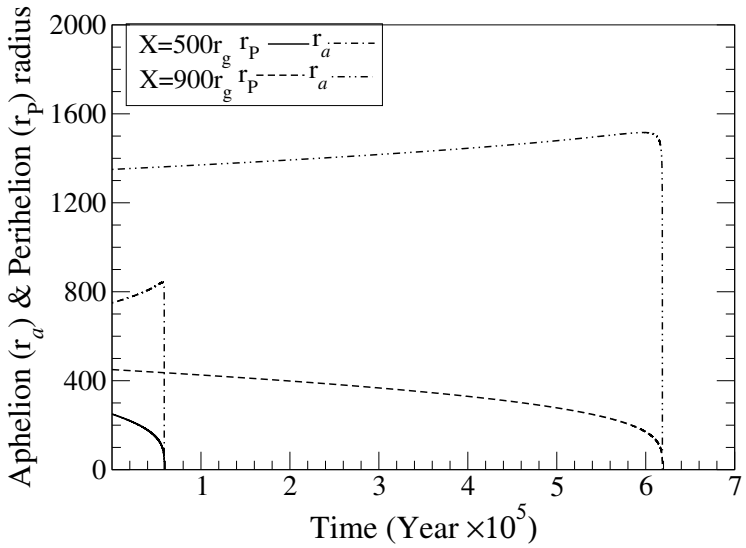


**Figure 3.27:** A comparison of the perihelion ($r_P$) and aphelion ($r_a$) radius with time ($T$) for two orbits with semi-major axis $X = 500r_g$ and $X = 900r_g$ is shown in this figure. The $r_P$ and $r_a$ for $X = 500r_g$ are shown by *solid line* and *dot-dash line*. For $X = 900r_g$, the $r_P$ and $r_a$ are shown by *dash line* and *dot-dot-dash line*. As expected, from the figure we see that the $X = 900r_g$ orbit takes a larger time for circularization ($\sim$ 0.5 million years). Initial parameters used here are : $\dot{m} = 1$, $e = 0.50$, $a = 0.50$, $M = 10^8 M_\odot$, $m = 10^6 M_\odot$.

emission, whereas a circular orbit stays circular. For high elliptic orbits, the degradation rate ($\dot{e} = \frac{de}{dT}$) is greater. We explored numerous elliptical orbits in our numerical analyses, and two such instances with starting eccentricities of $e = 0.50$ and $e = 0.25$ are shown in Figure 3.28. For $a = 0.50$, when the accretion disk is absent, a solid line is depicted, and when the disk is present, a dash line is shown. Again, the progression is shown in the years preceding the coalescence. The existence of the accretion disk decreases eccentricity more effectively, causing the orbit to become a circle more quickly. In contrast to high eccentric orbits, low eccentric orbits spare more time; as a result, the hydrodynamic drag's cumulative impact is greater. The solid and dotted lines are separated more widely at $e = 0.25$ than at $e = 0.50$. In particular, we can observe from the figure that for $e = 0.25$, the disk coalescence period is reduced to about 20 years, while for $e = 0.50$, it is reduced to 0.5 years.

The eccentric orbit with initial eccentricity $e = 0.50$ was earlier investigated for different initial parameters having semi-major axis $X = 500r_g$(*dash line*) and $X = 900r_g$(*solid line*) in presence of the disk in Figure 3.15. We can see from that, as usual the larger orbit decay slower and takes a longer time for migration. Therefore the eccentricity evolves slower for $X = 900r_g$ and faster for $X = 500r_g$. However, the amount of change of eccentricity is the same for both cases even though the inspiralling stages are different.

The total infall time for different eccentric orbits has been investigated in Figure 3.29. Here we plot the change of the perihelion ($r_P$) and aphelion ($r_a$) radius with time for different eccentric orbits having the same initial value of the semi-major axis $X = 500r_g$. We compare the result for three orbits with low, moderate, and high eccentricities, e.g., $e = 0.15$, $e = 0.25$, and $e = 0.50$. As already mentioned, the low eccentric orbit took a longer time to become circular before coalescence. Therefore, the rate of change of $r_a$ and $r_P$ is smaller in this case. The infall time decreases for moderate orbits and is significantly lower for high eccentric orbits. The total orbital impact

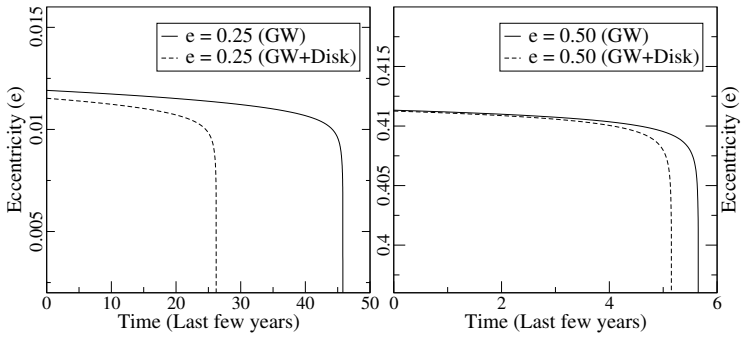


**FIGURE 3.28:** This graph displays the decline in the orbit's eccentricity ($e$) over the most recent observational years. We contrast two eccentric orbits with starting eccentricities of $e = 0.50$ (high) and $e = 0.25$ (moderate). In both scenarios, the accretion disk is absent (shown by a *solid line*)) and present (represented by a *dash line*). We notice that the companion's orbit loses eccentricity relative to more quickly for $e = 0.25$ than for $e = 0.50$ in the presence of the disk. This is because the companion has a longer inspiral for $e = 0.25$. The starting parameters utilized for these figures are $\dot{m} = 1$, $a = 0.50$, $X = 500r_g$, $M = 10^8 M_\odot$, $m = 10^6 M_\odot$.

of hydrodynamic drag is much greater (as it takes longer) for low eccentric orbits; however, coalescence takes place faster for high eccentric orbits. The decay of the orbits can be understood from the variation of the $r_P$ values for three cases, as shown in Figure 3.29.

So far in the literature, circular orbits have been primarily examined (Giampieri (1993); Vokrouhlicky & Karas (1993, 1998); Šubr & Karas (1999); Karas & Šubr (2001); Levin (2007); Basu et al. (2008)). However, it should be noted that the circular orbit is a specific case for studying EMRI dynamics. Both of the E/IMRI formation routes (dry and wet, already addressed) contribute to the eccentricity of the E/IMRI orbit. As a result, it is crucial to research the various elliptical orbits of the E/IMRIs for the LISA observation. As a result, we looked at how e changed for high eccentric orbits with various beginning configurations. The fluctuation of the perihelion ($r_P$) and aphelion ($r_a$) radii with the eccentricity ($e$) is plotted in Figure 3.30 for three distinct values of the initial inspiral radius (high, moderate, and low) of the binary mergers with semi-major axes $X = 900r_g$, $X = 500r_g$, $X = 200r_g$. We choose the initial eccentricity $e = 0.50$ in three of these situations. The coalescence time is greater for $X = 900r_g$ and moderate for $X = 500r_g$, as predicted. When $X = 200r_g$, the coalescence period is significantly shorter. Despite the fact that the starting separations are significantly varied, the figure shows an approximately identical shift in eccentricity for all three examples (with the same initial ($e$)). It's possible that the inner portion of the disk closest to the primary accreting SMBH is where the disk drag is most effective. However, because low and moderately eccentric orbits spend more time in the inspiral, the effect of disk drag is greater. Such orbits tend to be circular and have a bigger fluctuation in eccentricity (see Figure 3.28). One may witness the eccentricity of these orbits changing from these estimates (Figures 3.28 and 3.30), and in a few situations, it could be feasible to distinguish between the low and high eccentric orbits during merging. Due to the fact that moist EMRIs tend to agglomerate more quickly and have a greater tendency to be eccentric than dry EMRIs. Therefore, this research may be crucial for figuring out the many wet and dry creation paths of EMRIs during observations.

We present Figure 3.31 specifically at the late inspiral stage (the perihelion radius $r_P = 70r_g$ to ISCO), where detectability is predominant to assess the size of the torque owing to disk. When

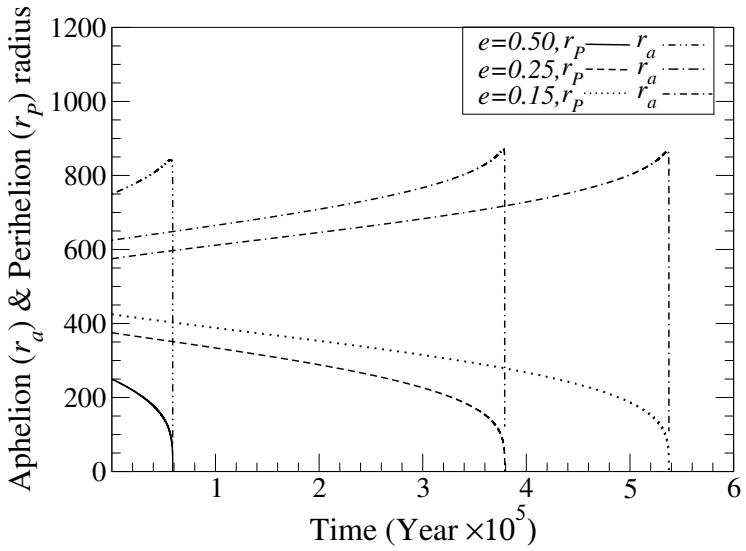


**FIGURE 3.29:** In this figure we plot the perihelion ($r_P$) and aphelion ($r_a$) radius of the companion black hole's orbit with time ($T$) for the three cases with eccentricities $e = 0.15[r_P \rightarrow$ *dot line*,$r_a \rightarrow$ *dot dash dash line*], $e = 0.25[r_P \rightarrow$ *dash line*,$r_a \rightarrow$ *dot dash line*] and $e = 0.50[r_P \rightarrow$ *solid line*,$r_a \rightarrow$ *dot dot dash line*]. From the figure, we see that $r_a$ initially increases and after a while decreases toward $r_P$. The circularization takes place faster for the comparatively high eccentric orbit. The initial parameters are $\dot{m} = 1$, $a = 0.50$, $X = 500r_g$.

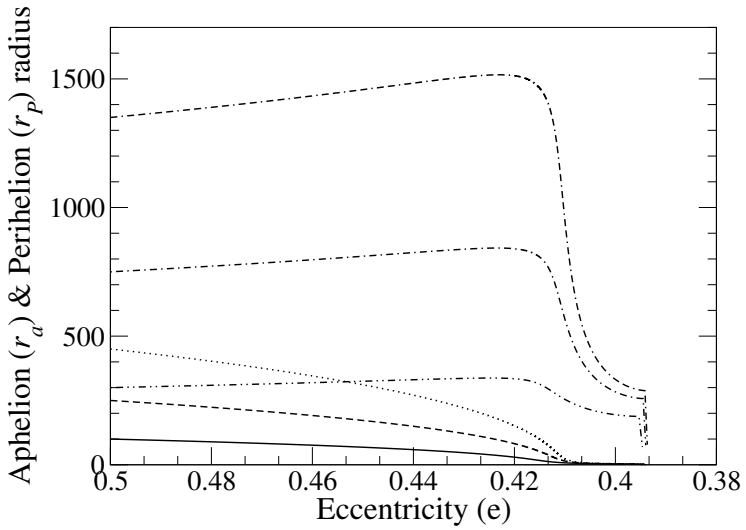


**FIGURE 3.30:** The illustration shows a comparison of the orbit's eccentricity (e) and the perihelion and aphelion radii ($r_P$ and $r_a$). For each of them, initial eccentricity $e = 0.50$ is taken into account. The different semi-major axes are correspondingly depicted at $X = 200r_g(r_P \rightarrow$ *solid line*,$r_a \rightarrow$ *dot dot dash line*), $X = 500r_g$ ($r_P \rightarrow$ *dash line*,$r_a \rightarrow$ *dot dash line*), and X = $X = 900_g$ ($r_P \rightarrow$ *dot line*,$r_a \rightarrow$ *dot dash dash line*). Eccentricity is decreased to about the same levels in all three scenarios.

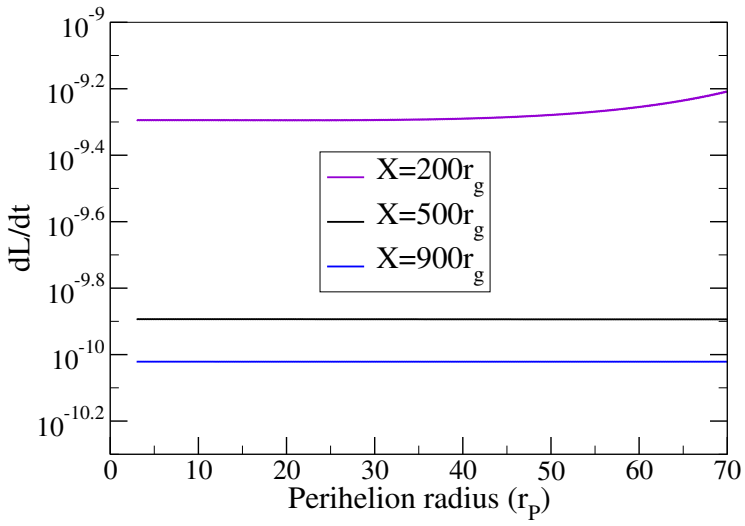


**Figure 3.31:** In the Figure, we present the torque $\left(\frac{dL}{dt}\right)_{\rm disk}$ caused by disk-drag in all three orbits and can see that it is larger for the orbit with $X = 200r_g$ than the others.

we change the semi-major axis of the orbits while holding all other orbital parameters constant, we can clearly see that the $\left(\frac{dL}{dt}\right)_{\rm disk}$ is significantly greater for $X = 200r_g$ than it is for the other orbits. Therefore, all of the aforementioned data point to high eccentric orbits with lower semi-major axis orbits as having a more pronounced accretion drag effect on companion dynamics. As a result, a system with high eccentricity and a lower semi-major axis would have a significant influence on the amount of GW radiation it emits.

### 3.6.5 Orbital Evolution : Impact of spin of the central SMBH

Next, we have a look at figure 3.32 to observe how the energy loss changes over time for two sharply opposing spin parameters, $a = 0.50$(*dash line*) and $a = -0.50$ (*solid line*), respectively. It demonstrates that the prograde spin took around 0.0256 million years longer than the retrograde spin. Therefore, compared to a direct spin, a retrograde spin loses energy far more quickly in the presence of an accretion disk due to both GW emission and hydrodynamic drag. In figure 3.33, we compare the outcome to other retrograde spins for Kerr values $a = 0.0$ (*solid line*), $-0.50$ (*dot line*), and $-0.999$ (*dash line*). The figure shows that the loss of energy is slower and that the infall time is longer for a non-spinning BH. In contrast to the other orbits, the retrograde orbit with the high Kerr value $a = -0.999$ takes the shortest amount of time (0.0142 & 0.0398 million years compared to $a = -0.50$ and $a = 0.0$), demonstrating unequivocally that coalescence is accelerated in the presence of an accretion disk. A direct orbit enters the merger stage far more slowly than a retrograde orbit. We also compare the energy loss of the companion for $a = 0.5, -0.5$ and $a = 0.999, -0.999$, respectively, and plot them with regard to GW energy loss in the presence of disk in figures 3.34 and 3.35. We can observe from both figures that the value of $\Delta E$ is higher for retrograde orbits. The figures show that retrograde orbits are always preferable to prograde orbits when comparing the relative loss rates of energy and angular momentum of the orbits.

We show a constant decline of the companion BH's elliptical inspiral motion in figures 3.36 and 3.37, and we present a continuous decay of the elliptical inspiral motion of the companion. Here, the perihelion ($r_P$) and aphelion ($r_a$) radius decrease with infall time ($T$) and orbital eccentricity

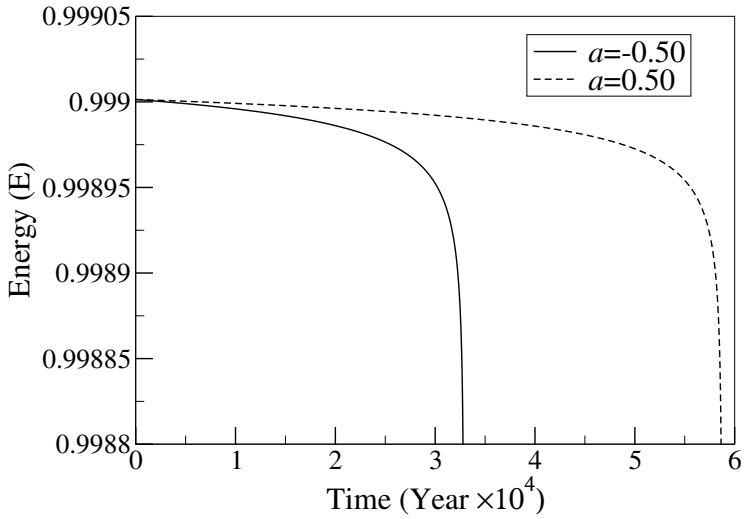


**Figure 3.32:** For two exactly opposite Kerr parameters, $a = 0.50$(*dash line*) and $a = -0.50$ (*solid line*) variations are shown in this figure. The orbits' initial eccentricity is $e = 0.50$. This Figure shows that the retrograde orbit required less time than the prograde orbit (approximately 0.0256 million years).

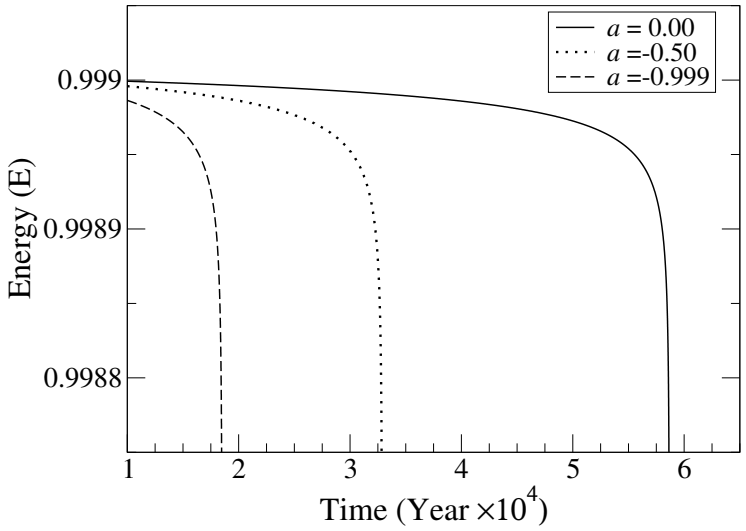


**Figure 3.33:** Variation of energy and its comparisons for the Kerr parameters $a = 0.0$ (*solid line*),$a = -0.50$ (*dot line*) and $a = -0.999$ (*dash line*), are shown in this figure. The orbits' initial eccentricity is $e = 0.50$. In comparison to other orbits, the one with the most extreme negative Kerr value expends the least time and loses energy. The figure revealed that non-spinning BH lost energy slowly and took longer to reach the merger stage.

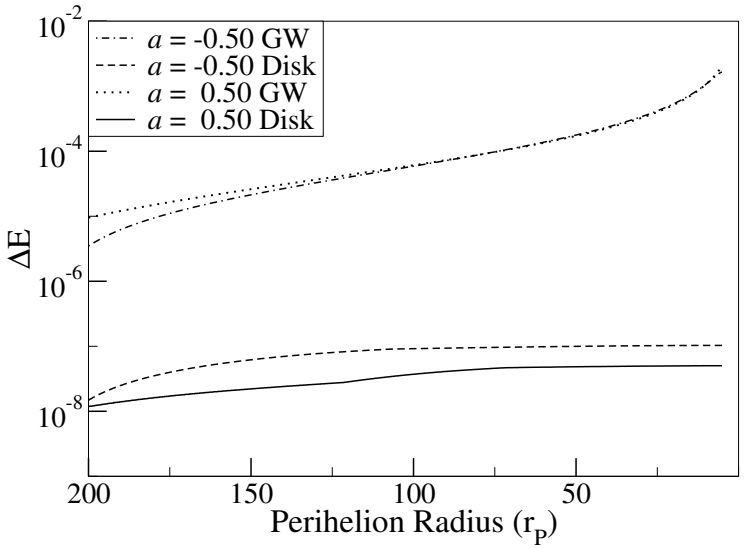


**Figure 3.34:** For two exactly opposite Kerr parameters, $a = 0.50$ and $a = -0.50$ we compare $\Delta E$ and plot them with respect to GW energy loss in the presence of disk in this figure. We see that disk contribution to energy loss is more for retrograde orbit

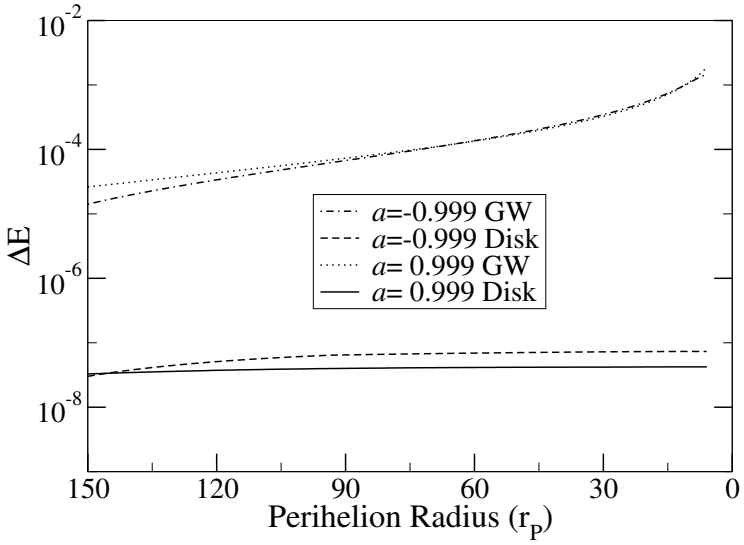


**Figure 3.35:** Figure 3.34 is reproduced for the extreme Kerr value $a = \pm 0.999$. As earlier we here also obtained that energy loss due to disk contribution is more for retrograde orbit.

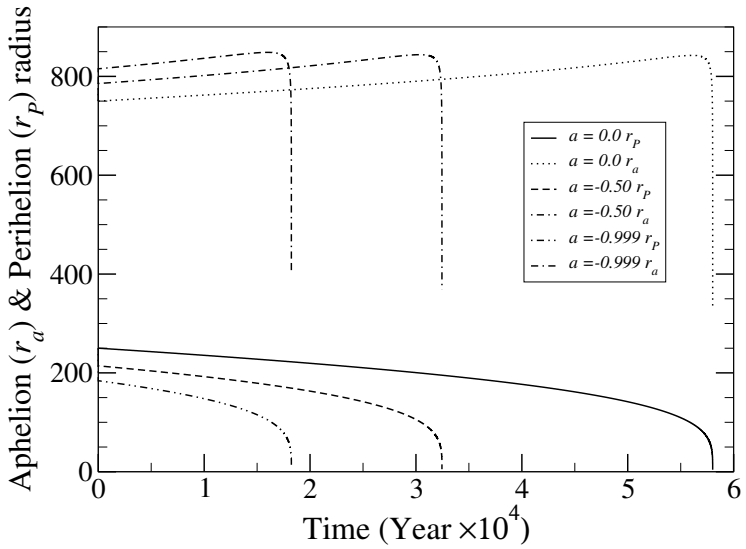


**Figure 3.36:** Initial parameters : $\dot{m} = 1$, $e = 0.50$ and $X = 500r_g$. We compare the perihelion ($r_P$) and aphelion ($r_a$) radius with the time($T$). We show the variation for three orbits with Kerr parameters $a = 0.0[r_P \rightarrow$ *solid line*, $r_a \rightarrow$ *dot line*$]$, $a = -0.50[r_P \rightarrow$ *dash line*, $r_a \rightarrow$ *dot dash line*$]$ and $a = -0.999[r_P \rightarrow$ *dot dot dash line*, $r_a \rightarrow$ *dot dash dash line*$]$. We see that the orbit with no spin took greater time comparing to others.

($e$). We show the variation for three orbits with the following Kerr parameters: $a = 0.0[r_P \rightarrow$ *solid line*, $r_a \rightarrow$ *dot line*$]$, $a = -0.50[r_P \rightarrow$ *dash line*, $r_a \rightarrow$ *dot dash line*$]$ and $a = -0.999[r_P \rightarrow$ *dot dot dash line*, $r_a \rightarrow$ *dot dash dash line*$]$. As can be seen, compared to other high-spin orbits, the orbit with no spin took longer and lost more eccentricity.

### 3.6.6 Torque on the companion due to co- & contra-rotating spin of SMBH

The companion motion is affected differently by the disk drag depending on whether the BH is spinning progradely or retrogradely. We look into how the loss rates are impacted by the central BH's spin. We calculate the hydrodynamic drag and torque for a range of elliptical orbits by examining numerous values of the co- and contra-rotating BH spins. For three different Kerr parameters, $a = 0.0$ (*solid line*), 0.50 (*dash line*), and $-0.50$ (*dot line*), we exhibit the decay of angular momentum ($L$) in Figure 3.38. Each orbit has an eccentricity of 0.50. The graph demonstrates how different angular momentum losses by the system are caused by changing the central black hole's spin. We can also observe that the retrograde spin with $a = -0.50$ loses angular momentum much more quickly than other spins, suggesting that larger disk drag may be present on these orbits. We compare the time taken for the orbits to lose angular momentum using the two extreme Kerr values, direct orbit and retrograde orbit, with $a = 0.999$ (*solid line*) and $a = -0.999$ (*dot-dot-dash line*), respectively, while holding all other orbital parameters constant. Figure 3.39 is plotted in the late stage of the inspiral, where the middle curve is drawn to the central black hole spin $a = -0.50$ (*dash line*). We see that the orbit takes the least amount of time when the black hole spin parameter is $a = -0.999$ and takes more time for $a = 0.999$ indicating the disk-drag is more for a retrograde orbit than a prograde one. The graphs in Figures 3.40 and 3.41 show the precise spin dependency of the angular momentum loss rate. Here, we examine the hydrodynamic drag torques for two spins that are polar opposites of one another: (i) $a = 0.5$ vs. $a = -0.5$ and (ii) $a = 0.999$ vs. $a = -0.999$. Although the order of magnitude also varies

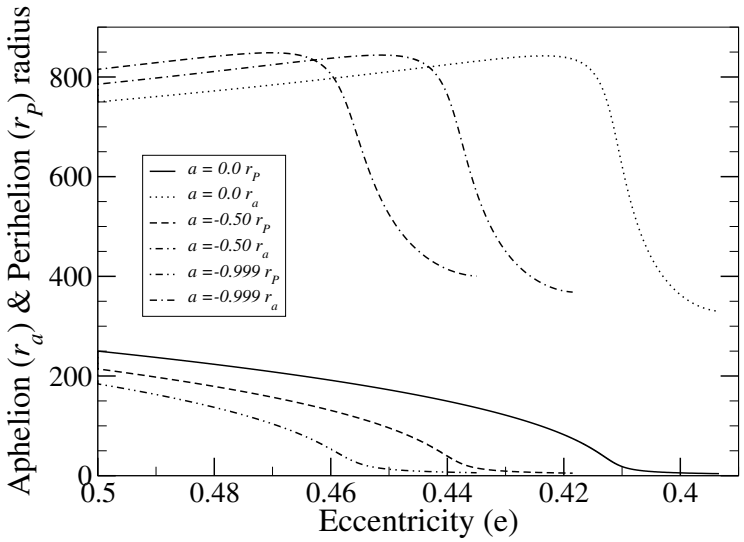


**FIGURE 3.37:** Initial parameters : $\dot{m} = 1$, $e = 0.50$ and $X = 500r_g$. We compare the perihelion ($r_P$) and aphelion ($r_a$) radius with the eccentricity($e$)of the orbit. We show the variation for three orbits with Kerr parameters $a = 0.0[r_P \rightarrow$ *solid line*, $r_a \rightarrow$ *dot line*$]$, $a = -0.50[r_P \rightarrow$ *dash line*, $r_a \rightarrow$ *dot dash line*$]$ and $a = -0.999[r_P \rightarrow$ *dot dot dash line*, $r_a \rightarrow$ *dot dash dash line*$]$. We see that the orbit with no spin, losses more eccentricity comparing to others.

depending on disk parameters, we can observe in both situations that a retrograde orbit has a magnitude that is almost an order higher than a prograde orbit. Here, the torque's strength GW vs disk is plotted. All the figures shows that retrograde orbits have faster coalescence times and higher disk torque than direct orbits.

### 3.6.7 Torque on the companion due to change in accretion rate of Primary BH

We investigate the effect of accretion rate of the central SMBH on the motion of the companion BH. We calculate the torque on the companion due to hydrodynamic drag for various cases by varying the accretion rate and present the obtained result in the figure 3.42. Each color in the figure represent different accretion rate as mentioned in the figure and its caption. We vary the accretion rate from very sub-Eddington to super-Eddington limits and obtained, with the increasing accretion rate the torque on the companion increases. Super Eddington accretion though very contradictory however the development of supermassive black holes from seed stellar mass black holes in the early era will be better understood if there is a super Eddington accretion flow. Super-Eddington accretion flow is generally predicted by a number of semi-analytic and numerical models (Jiang et al., 2014, 2019; Wang & Zhou, 1999; Wang et al., 2013). Radiation efficiency for such an accretion model is less than $5-7\%$ (Jiang et al., 2014, 2019). Consequently, at the optical wavelength, a disk with a super-Eddington accretion rate might seem as a sub-Eddington or low luminous object due to its low efficiency. The brightness does not rise proportionally even at extremely high accretion rates ($>$ 100 Eddington); instead, a logarithmic connection between the accretion rate and the disk's saturated luminosity is present (Wang et al., 2013). As we obtained that the torque provided by the disk drag is directly impacted by the accretion rate, it may be possible to determine the accretion rate directly from GW observation, which will be helpful in confirming the previously stated connection. Super Eddington accretion rate is enabled by our

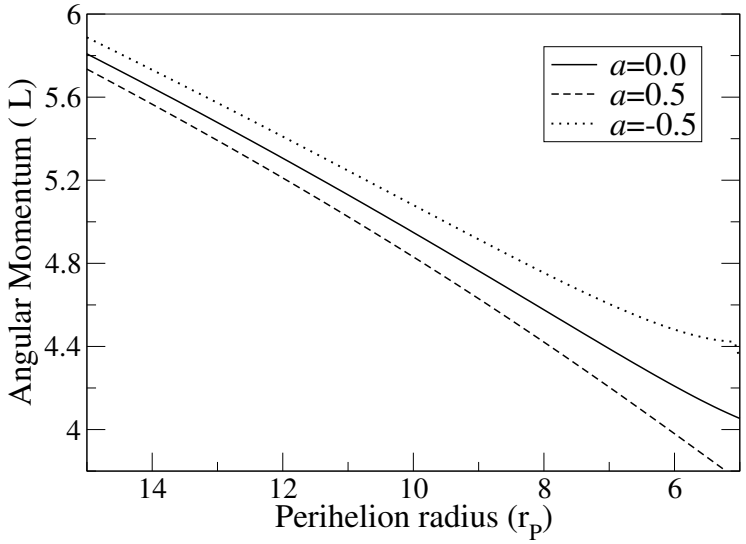


**FIGURE 3.38:** Comparison of angular momentum ($L$) with the perihelion radius ($r_p$) for three different Kerr parameters $a = 0.0$(*solid line*), $a = 0.50$(*dash line*) and $a = -0.50$ (*dot line*) is shown here.

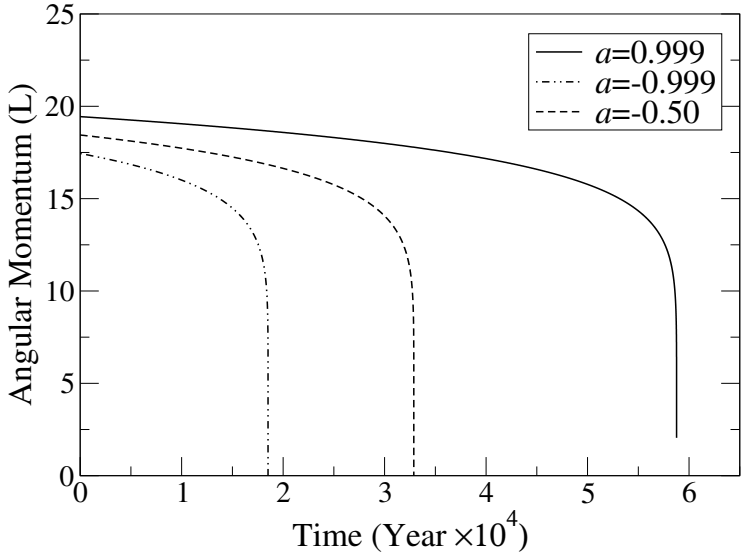


**FIGURE 3.39:** We compare the loss of angular momentum ($L$) with time ($T$) for two extreme Kerr values $a = 0.999$ (*solid line*) and $a = -0.999$ (*dot-dot-dash line*) with middle curve $a = -0.50$ (*dash line*). The eccentricity for the three cases is equal to $e = 0.50$. We noticed that extreme positive Kerr value orbits required a longer time as compared to $a = -0.50$ or $a = -0.999$ orbits to lose angular momentum.

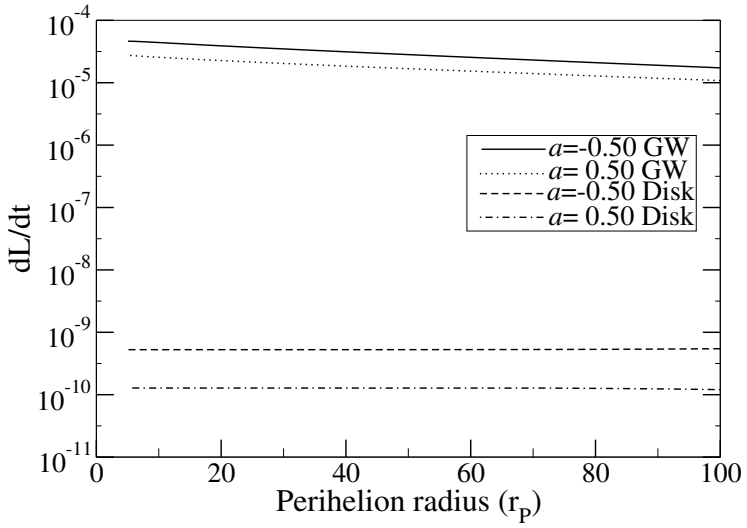


**Figure 3.40:** The spin dependency of the torque due to hydrodynamics drag is compared in this for two exactly opposite spins (i) $a = 0.5$ vs. $a = -0.5$. The magnitude of the torque is plotted with respect to GW torque. The figures show that the retrograde orbits experience greater disk-torque and have shorter coalescence times than direct orbits.

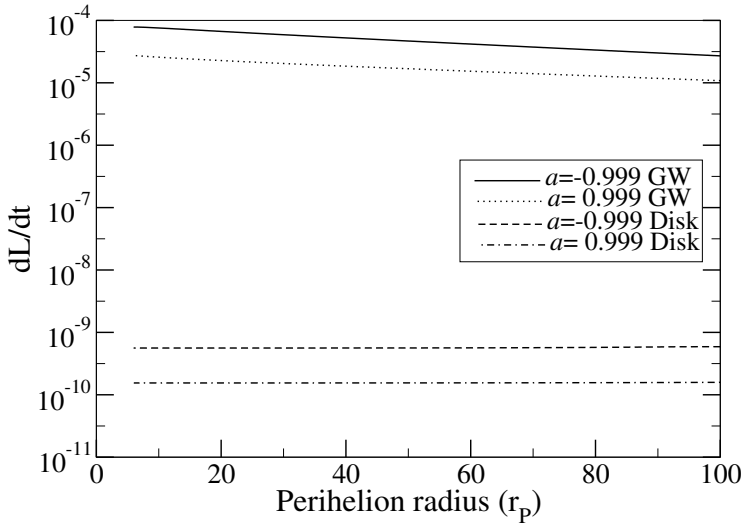


**Figure 3.41:** The spin dependency of the torque due to hydrodynamics drag is compared in this figure for two exactly opposite spins $a = 0.999$ vs. $a = -0.999$ respectively. The magnitude of the torque is plotted with respect to GW torque. The result resembles Figure 3.40.

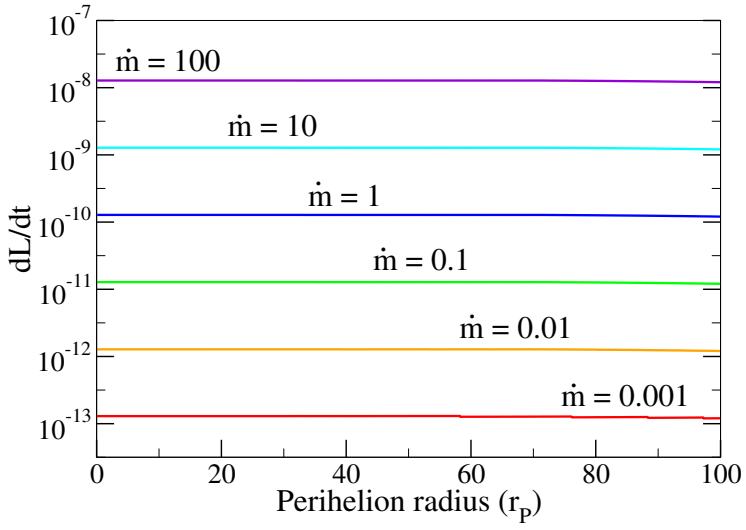


**Figure 3.42:** Initial parameters are $a = 0.50$, $e = 0.50$ and $X = 500r_g$. Here is a comparison of the $\frac{dL}{dt}|_{disk}$ of the companion black hole with perihelion radius ($r_P$) for various disk accretion rates is presented. In the figure the *violet line* represent the torque due to disk when the accretion rate $\dot{m} = 100$. The *cyan line, blue line, green line, orange line & the red line* respectively represents the accretion rate of $\dot{m} = 10, 1, 0.1, 0.01$ and $0.001$. We can see from the figure that with the increasing accretion rate the torque on the companion due to hydrodynamic drag increases. As can be seen from the figure that an orbit with a higher accretion rate will posses a smaller infall time.

accretion model. This, however, can be done elsewhere and is outside the purview of our current investigation.

Next we concentrate on the current values of the orbital parameters, which vary with the mass accretion rate $\dot{m} = \frac{\dot{M}}{\dot{M}_E}$ of the primary SMBH and investigate the influences on the infall time. $\dot{M}_E$ is the Eddington mass accretion rate, in order to analyze the dynamics of the companion BH. For various eccentric orbits, we select $\dot{m} = 0.1, 1, 10, 100$, and we depict the differences in the orbital parameters in various figures.

Figure 3.43 shows the decline of eccentricity for three distinct accretion rates, $\dot{m} = 0.1$ (*solid line*), 1 (*dot line*) and 10 (*dash line*), over time. When compared to the results we receive when the accretion rate $\dot{m}$ is raised, an orbit with a high accretion rate has a lower infall time and a faster decay in eccentricity.

### 3.6.8 Torque on the companion due to change of mass ratio of EMRIs

By altering the mass ratio of the EMRIs, we compare the torque on the companion black hole. We compare the energy and angular momentum loss rates for mass ratios of $10^{-4}$ and $10^{-3}$. The energy loss rate owing to GW emission and disk drag is compared in Figure 3.44 for two scenarios with mass ratios of $10^{-4}$ and $10^{-3}$, and the relative change of torque is examined in Figure 3.45 for the same orbital configuration. The statistics show that for $10^{-3}$ EMRIs, the energy loss rates are two orders greater, and the torque exerted by the disk is one order higher than for $10^{-4}$ EMRIs.

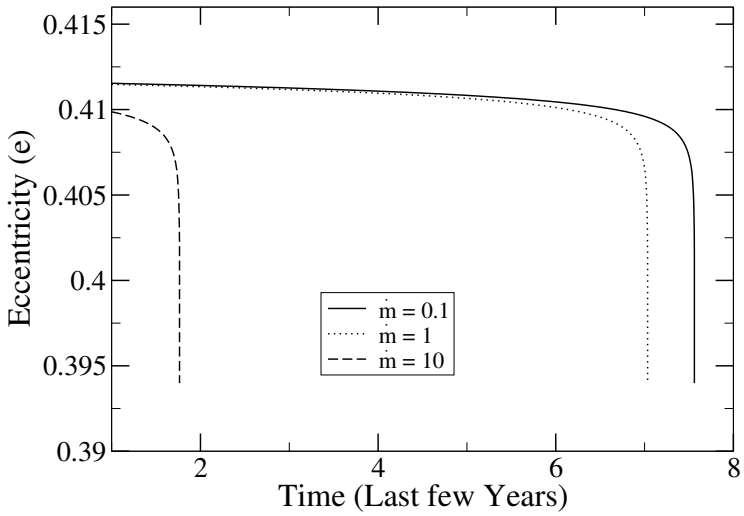


**FIGURE 3.43:** Initial parameters are $a = 0.50$, $e = 0.50$ and $X = 500r_g$. Here is a comparison of the eccentricity ($e$) of the companion black hole's orbit with time ($T$) for various disk accretion rates. The figure is displayed as a *solid line* when the accretion rate $\dot{m} = 0.1$. The eccentricity vs. time is depicted as a *dot line* for $\dot{m} = 1$. A *dash line* represents the plot when $\dot{m} = 10$. As can be seen from this picture, an orbit with a higher accretion rate has a smaller infall time and loses eccentricity more quickly.

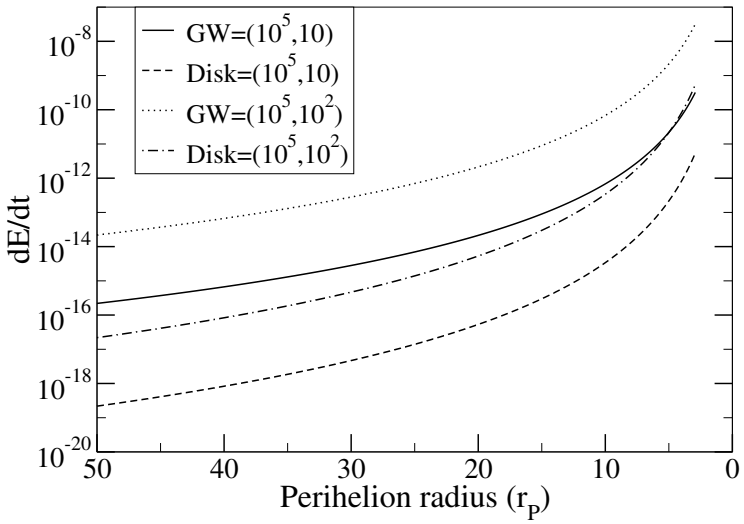


**FIGURE 3.44:** In this figure we compare the variation of $E$ due to different EMRI's mass ratio of $10^{-4}$ and $10^{-3}$, and plot the energy loss rate owing to GW emission and disk-drag. The results show that the energy loss rates owing to disk are two orders higher for mass ratio $10^{-3}$ than for mass ratio $10^{-4}$.

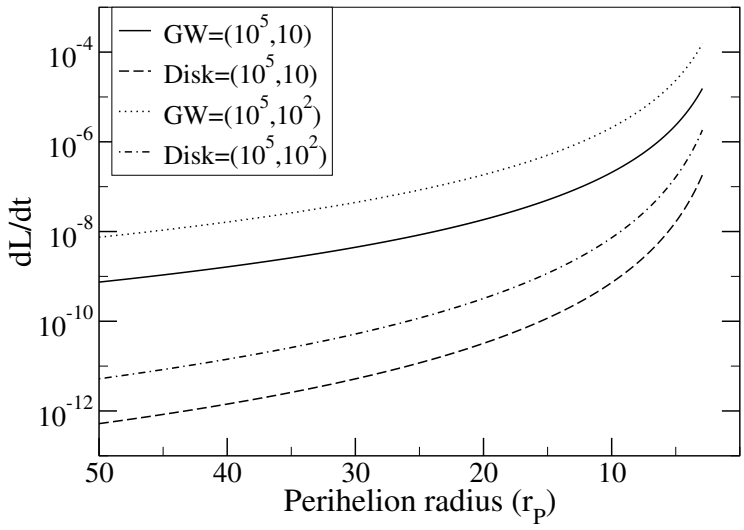


**Figure 3.45:** We compare the fluctuation angular momentum loss rates with respect to the EMRIs mass ratio. We chose two mass ratios of $10^{-4}$ and $10^{-3}$, and plot the relative fluctuation of torque. The results show that the disk torque is one order greater for mass ratio $10^{-3}$ than for mass ratio $10^{-4}$.

## 3.7 Conclusion : Tracing the preferable orbits with the greatest disk drag impact

In the case of an accretion disk-containing EMRI system, we examined the total change in energy and angular momentum of a companion black hole (BH) in an eccentric orbit around a rotating central supermassive black hole (SMBH) due to gravitational wave emission. Our research yields the most accurately fitted orbital parameters that LISA can detect with the desired precision/range. Our methodology was semi-relativistic; that is, we used Ryan's formula (Ryan, 1995, 1996) to calculate radiation fluxes and considered the geodesic motion of the background space-time to examine particle motion. This allows for a more exact evaluation of disk-companion interaction than previous Newtonian predictions. Furthermore, we investigate E/IMRIs embedded in transonic flows, which provide the maximum disk drag compared to other models (Abramowicz & Zurek (1981); Chakrabarti (1990a, 1996a); Lu et al. (1997); Chakrabarti (1993); Yunes et al. (2011); Kocsis et al. (2011); Derdzinski et al. (2019a); Garg et al. (2022)).

The approach we used to achieve the most suitable orbital parameters is to identify the maximum hydrodynamic disk drag offered for a particular orbital configuration of the EMRIs positioned at a detectable distance. The significance of disk drag varies with system characteristics such as eccentricity($e$), semi major axis($X$) of the orbit as well as mass ratio of EMRI, spin($a$) of SMBH, and so on. Therefore, we analyze these variables in order to identify the elliptical orbit with the most disk drag. The initial orbital parameters influence the imprint of disk drag. Depending on the system configuration, we see that different torques are offered. Taking a look at a variety of eccentric orbits and calculating the drag produced by them in the presence of an accretion disk, we identify that a high eccentric orbit yields the most disk drag and is thus more likely to be detected. We also evaluate the variation of drag impact by considering several orbits with semi major axes $(200r_g, 500r_g, 900r_g)$. We discovered that orbits with a lower semi-major axis have the highest drag influence. For our study, the maximum value of semi-major axis is $X = 1000r_g$ to obtain the least significant drag impact. The equivalent semi-latus rectum ($p$) value can be

acquired from here in order to describe an elliptical orbit with $(e, p)$. The torque on the companion BH, is then compared by altering the companions' mass as well. For a central SMBH mass of $10^5 M_\odot$ and two mass ratios, $10^{-3}$&$10^{-4}$, we can see that the more torque exerted by the $10^{-3}$ system, the magnitude increases by one order of magnitude. In comparison, the detectability of the system with mass ratio $10^{-3}$ is greater. Finally, the torque is compared by altering the rotation of the central SMBH. We discover that retrograde spins provide one order of magnitude more disk torque than prograde spins, making them more likely to be detected.

The criteria for a proper parameter estimate include thorough knowledge concerning the nature of the accretion disk and the accretion rate. Electromagnetic observations may be able to resolve the limitations raised above. To improve the accuracy of the calculated orbital parameters, the disk parameters can be varied, which is outside the scope of our present work and will be addressed afterward.

# Chapter 4

# Dephasing & the detectable SNR of gas-rich E/IMRI's in LISA band : Observable signature of transonic accretion flow.

## 4.1 Introduction

Astronomy has undergone a revolution over the last eight years. On September 14, 2015, the Advanced Laser Interferometer Gravitational-Wave Observatory (LIGO) detector directly detected gravitational waves (GW) emanating from the binary black hole (BBH) merger GW150914 (Fig. 4.1). This was a revolutionary discovery that not only proved that GWs could be observable but also, more importantly, provided new knowledge about these systems and the nature of the cosmos. The ground-based detectors LIGO and VIRGO worked together to conduct various observation runs, such as "O1, O2,...," etc., which span many months of duration. During such runs, an impressive amount of GWs was detected coming from sources of binaries of compact objects Abbott et al. (2019); Nitz et al. (2019).

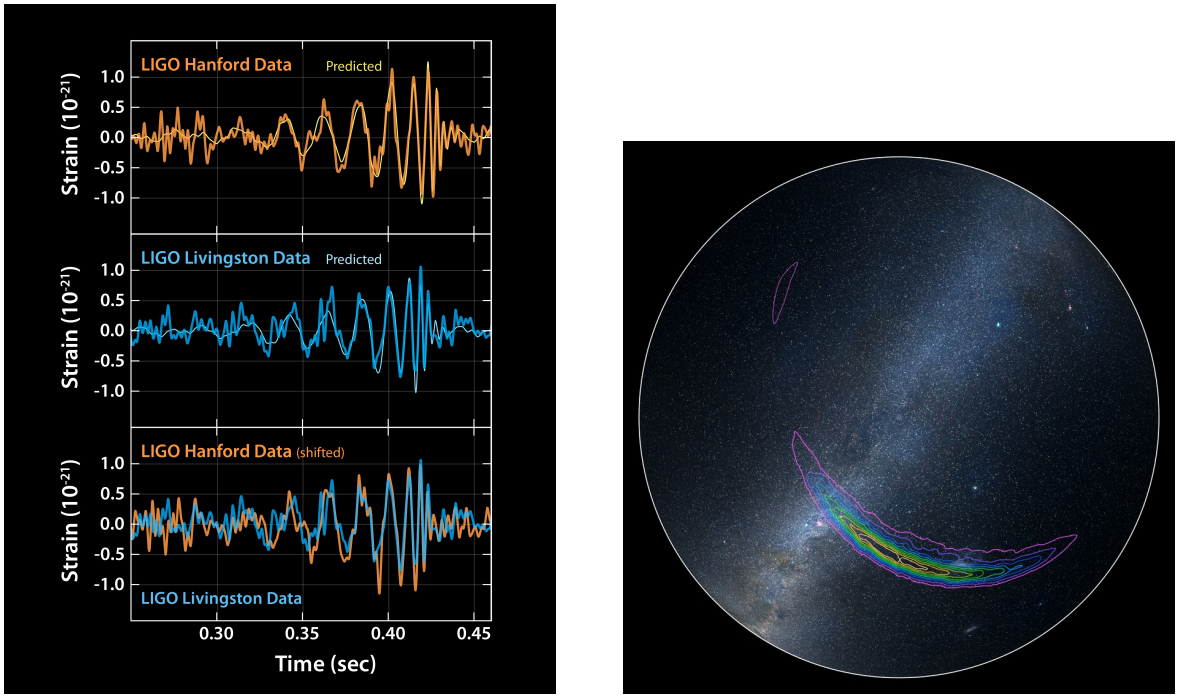


**Figure 4.1:** Observation of the gravitational wave signal GW150914 by the LIGO detector and the approximate location of GW150914 on southern hemisphere. Image credit : left : Caltech/MIT/LIGO Lab, right : LIGO/Axel Mellinger.

The analysis of all the detected GW signals provides very basic information regarding the sources. We show here a few of them in Table 4.1.

| List of few GW Detections | | | | | |
|---|---|---|---|---|---|
| Source | $M$ $(M_\odot)$ | $m$ $(M_\odot)$ | Remnant$(M_\odot)$ | Spin | Distance(MPc) |
| GW200115 | BH(5.7) | NS(1.5) | BH(7.8) | 0.38 | 300 |
| GW200105 | BH(8.9) | NS(1.9) | BH(10.4) | 0.43 | 280 |
| GW190814 | BH(23.2) | BH/NS(2.59) | BH(25.6) | 0.28 | 241 |
| GW190521 | BH(85) | BH(66) | BH(142) | 0.72 | 5300 |
| GW170817 | NS(1.46) | NS(1.27) | BH(2.8) | 0.89 | $40 \pm 10$ |
| GW150914 | BH(35.6) | BH(30.6) | BH(63.1) | 0.69 | 430 |

**Table 4.1:** List of detected GW and the predicted source parameters Abbott et al. (2019); Nitz et al. (2019). Here $M$ and $m$ respectively denotes the masses of the primary and secondary companions of the system.

The parameter estimations shown in Table 4.1, are done by using the matched filtering technique, which is based on the derivations of theoretically calculated signals in a vacuum scenario. The faraway sources of GWs are considered as there is no other environmental impact on them, and the binaries are evolving only due to the emission of gravitational waves. The realistic astrophysical environments surrounding the sources, such as electromagnetic fields, accretion disks, and dark matter (DM), are typically not taken into account in estimates of the accuracy of GW detectors in measuring the source parameters because it is assumed or hoped that their impact will be minimal. However, if precision GW physics is feasible, then it is necessary to take into account the environment's influence on GW observables. Tests of gravity theories and astrophysical models may be in jeopardy if unmodeled deviations (caused by environmental influences) from the pure "vacuum" gravitational waves expected by general relativity reduce the signal-to-noise ratio and the parameter estimate accuracy. On the other hand, if these impacts can be predicted and are not insignificant, they may reveal vital details about the surroundings of GW sources.

The most potent source of mHz GWs (targeted sources of LISA-the spaced-based detector) are the inspiral of massive BH binaries. In this current contribution, we examined both intermediate and extreme mass ratios (E/IMR) to see how environmental factors may affect them. A system known as an E/IMRI occurs when a compact object of relatively lower mass—a white dwarf, neutron star, or black hole—orbits or spirals around a supermassive black hole (SMBH). Thus, the companion behaves essentially like a test particle in the central SMBH's background spacetime. As a result, the system's generated GW signal offers a map of the background metric of the primary supermassive object. In order to test the viability of various paradigms in a strong gravity regime, such as the existence of naked singularities, exotic stars, the prediction of alternative theories of gravity, deformed BH space time, etc., this opens up the possibility of exploring physics in the near-horizon region of the supermassive object.

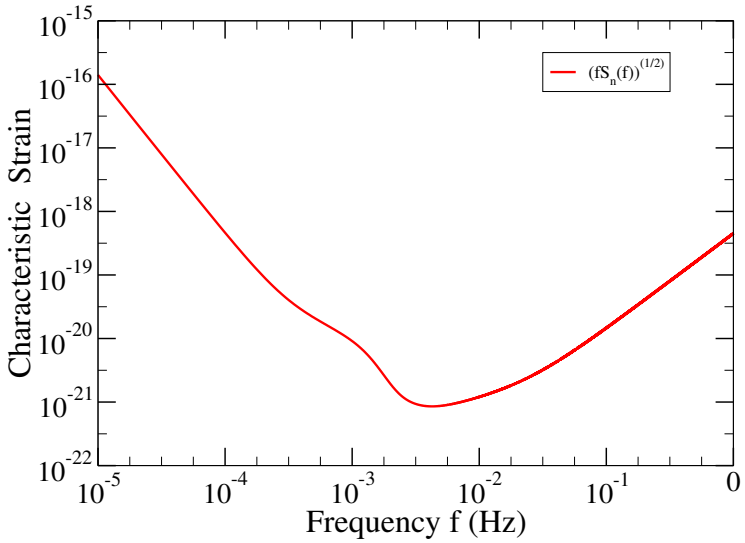


**FIGURE 4.2:** Characteristic strain of LISA using 4years parameter for confusion noise

## 4.2 Sensitivity Curves

The sensitivity curve of LISA can be obtained by using the equation (Robson et al., 2019),

$$S_n(f) = \frac{10}{3L^2}\left(P_{OMS}(f) + \frac{4P_{acc}(f)}{(2\pi f)^4}\right)\left(1 + \frac{6}{10}\left(\frac{f}{f_*}\right)^2\right) + S_c(f) \tag{4.1}$$

where $L = 2.5Gm$, $f_* = 19.09mHz$. The single-link optical metrology noise is,

$$P_{OMS} = (1.5 \times 10^{-11}m)^2\left(1 + \left(\frac{2mHz}{f}\right)^4\right)Hz^{-1} \tag{4.2}$$

Single test mass acceleration noise is,

$$P_{acc} = (3 \times 10^{-15}ms^{-2})^2\left(1 + \left(\frac{0.4mHz}{f}\right)^2\right)\left(1 + \left(\frac{f}{0.8mHz}\right)^4\right)Hz^{-1} \tag{4.3}$$

The confusion noise is estimated by,

$$S_c(f) = Af^{-7/3}e^{-f^\alpha + \beta f\sin(kf)}[1 + \tanh(\gamma(f_k - f))]Hz^{-1} \tag{4.4}$$

where $A = 9 \times 10^{-45}$, $\alpha = 0.138$, $\beta = -221$, $k = 521$, $\gamma = 1680$,$f_k = 0.00113$. Using equation (4.1), we plot figure 4.2. In this figure, the characteristic noise strain of the detector LISA using 4 years parameters for confusion noise is plotted with the detectors frequency sensitivity range that lies between $10^{-5}$Hz to $10^{-1}$Hz. GW strain of any source in this frequency range, if lies above the noise strain is detectable by the LISA detector.

## 4.3 Preludes of signal detection : Expression for SNR

As we discussed earlier, a GW signal is composed of its two polarization modes in a linear combination, i.e., $h_{\mu\nu} = A_+h^+ + A_\times h^\times$. Now, a detector's sensitivity to this signal depends on

the alignment of the source and detector. The output signal at the detector's end provides a combination of noise and the GW signal.

$$s(t) = n(t) + h(t) \tag{4.5}$$

Therefore, the challenge is to extract the signal from this combination. Wiener (1949) provides a solution to this problem by constructing a Wiener optimal filter, also known as a matched filter. In this technique, if $K(t)$ be a real filter function with its Fourier transform $\tilde{K}(f)$, then convolving this with detectors output $s(t)$ provides:

$$(s * K)(\tau) \approx \mathscr{S} + \mathscr{N} \tag{4.6}$$

The SNR i.e signal-to-noise ratio then given by,

$$\rho^2 = \frac{\mathscr{S}^2}{\mathscr{N}^2} = \frac{\left(\frac{1}{2}S_n(f)\tilde{K}(f)\middle|\tilde{h}(f)\right)^2}{\left(\frac{1}{2}S_n(f)\tilde{K}(f)\middle|\frac{1}{2}S_n(f)\tilde{K}(f)\right)} \tag{4.7}$$

Now using Cauchy-Schwarz inequality, the Wiener filter

$$\tilde{K}(f) = \frac{\tilde{h}(f)}{S_n(f)} \tag{4.8}$$

using this we can write the SNR as,

$$\rho^2 = \int_0^\infty df \frac{4\left|\tilde{h}(f)\right|^2}{S_n(f)} \tag{4.9}$$

### 4.3.1 Signal Strain & Power Spectral Density(PSD)

To calculate the SNR we need the Fourier transform of the signal strain $h_c$ and noise amplitude $h_n$. These are defined as (Moore et al., 2015),

$$[h_c(f)]^2 = 4f^2|\tilde{h}(f)|^2 \tag{4.10}$$

$$[h_n(f)]^2 = fS_n(f) \tag{4.11}$$

Therefore the equation (4.9) can be written as,

$$\rho^2 = \int_{-\infty}^{\infty} d(\log f)\left[\frac{h_c(f)}{h_n(f)}\right]^2 \tag{4.12}$$

Another important quantity in sensitivity curves is the power spectral density of noise which is given by,

$$\sqrt{S_n(f)} = \frac{h_n(f)}{\sqrt{f}} \tag{4.13}$$

Similarly for the source signal amplitudes,

$$\sqrt{S_h(f)} = \frac{h_c(f)}{\sqrt{f}} = 2\sqrt{f}|\tilde{h}(f)| \tag{4.14}$$

The power spectral density provides the mean square amplitude of the noise in the corresponding detector. For a GW source of inspiralling compact objects, it spends a longer time in the frequency band of the detectors. To calculate the number of cycles it spent at a particular frequency ($f$) we use,

$$N_{cycle} = \frac{f}{2\pi}\dot{\phi} = \frac{f^2}{\dot{f}} \tag{4.15}$$

where $\phi$ is the orbital phase of the companion BH and . represents the derivative w.r.t. time. Now to calculate the characteristic strain $h_c$ from the Fourier transform of the emitted GW signal $\tilde{h}(f)$, one use,

$$h_c(f) \approx \sqrt{N_{cycle}}|\tilde{h}(f)| \tag{4.16}$$

where this $\tilde{h}(f)$ can be obtained as,

$$\tilde{h}(f) \approx \frac{h_0}{\sqrt{\dot{f}}} \tag{4.17}$$

Therefore the characteristic strain,

$$h_c(f) = \sqrt{\frac{2f^2}{\dot{f}}}h_0 \qquad \text{(Finn \& Thorne, 2000)} \tag{4.18}$$

where we consider the source signal as

$$h(t) = \sqrt{2}h_0 \cos\phi(t) \tag{4.19}$$

where $h_0$ is the instantaneous root-mean square amplitude

In general, among the number of GW cycles generated, one could observe for which the frequency $f > f_{knee} \equiv \frac{n_{cycle}}{\tau}$ where $\tau$ is the LISA mission lifetime. The characteristic strain of the emitted GW can be defined as (Garg et al., 2022),

$$\begin{aligned} h_c &= h\sqrt{f\tau}, && f \leq f_{knee} \\ &= h\sqrt{n}, && f_{knee} < f \leq f_{ISCO} \\ &= 0, && f_{ISCO} < f \end{aligned} \tag{4.20}$$

where $f_{ISCO}$ defined the observed frequency when the companion BH reaches the primary BH's innermost stable circular orbit(ISCO). $h$ is the signal amplitude.

The SNR is then calculated for GW signal emitted from an EMRI between $f_{min}$ and $f_{max}$ by using (Garg et al., 2022),

$$SNR = \sqrt{2.4\int_{f_{min}}^{f_{max}} df \frac{h_c^2(f)}{S_n(f)f^2}} \tag{4.21}$$

Now in the presence of the disk a phase shift is introduced and to observe this phase shift, we compute the detectability of the dephasing by using Kocsis et al. (2011); Garg et al. (2022),

$$SNR = \sqrt{2.4 \int_{f_{min}}^{f_{max}} df \frac{2h_c^2(f)(1-\cos(\delta\phi))}{S_n(f)f^2}} \tag{4.22}$$

where $f_{min}$ and $f_{max}$ are the initial and final frequencies of the source during the observation within LISA frequency band. $S_n(f)$ is the instrumental noise of the detector at frequency $f$ given by equation (4.1). The characteristic strain $h_c$ can be found by using equation (4.18) where the details regarding the calculation of GW strain is discussed in Chapter 5 : §5.3. The phase develop when GW emitted in the presence of an accretion disk is different than that develop in the vacuum premises. We find this difference by calculating $\phi_{\text{with-disk}} - \phi_{\text{no-disk}} = \delta\phi$ and discuss this in the next section. With the definition of eqn (4.22), the signal-to-noise ratio (SNR) of an event is obtained, assuming ideal signal processing. In our study, we use the SNR to have a detectability threshold larger than 8. Less than that the event is undetectable. Using this value one can fix a critical value of a parameter above which it would be detectable in LISA. However before implementing it, we note that the definition of eqn (4.22) usd here is more of an intuitive expression than a formal derivation. A rigorous derivation is obtained in (Yunes et al., 2009) using stationary phase approximation that corresponds well with the results presented here.

## 4.4 Drift in the accumulated GW phase

As we can see from Chapter 3, the companion's trajectory is shaped by the ambient medium owing to hydrodynamic drag. As a result, the infall time and orbital frequency gets altered. The entire cumulative phase is different when the companion is not encased inside the disk. The slight variance in orbital parameters affects the GW signal's overall phase. Therefore, in the presence of the disk, it is possible to determine the phase difference and use the result to determine the features of the massive accretion disk encircling the center of the supermassive black hole. At any time, the orbital frequency of the moving companion $\omega$ is given by,

$$\omega = \dot{\phi} = \frac{d\phi}{dt} = \frac{d\phi}{d\tau}\frac{d\tau}{dt} = \frac{-(aE-L) + \frac{aT}{\Delta}}{-a(aE-L) + \frac{(r^2+a^2)T}{\Delta}} \tag{4.23}$$

$\frac{d\phi}{d\tau}$ & $\frac{dt}{d\tau}$ are obtained from equations (C.3) & (C.4). Here $T = E(r^2+a^2) - La$. The frequency of the emitted gravitational wave is, therefore, $\omega_{GW} = 2\omega = 2\dot{\phi}$.

Thus, by integrating the geodesic equations (C.3) and (C.4), it is possible to determine the total phase that accumulated throughout the decrease in orbital radius from $r_0$ to $r_1$. This total phase can be expressed as follows.

$$\phi = \int_{\tau_0(r_0)}^{\tau(r_1)} \frac{d\phi}{d\tau} d\tau \tag{4.24}$$

In this investigation, $r = r(\tau)$ is already known because the orbit is parameterized by $\tau$. Hence, the phase difference between the disk present and absent would be,

$$\delta\phi = \phi_{\text{with-disk}} - \phi_{\text{no-disk}} = \int_{\tau_0(r_0)}^{\tau(r_1)} \left[\frac{d\phi}{d\tau}\right]_{\text{with-disk}} d\tau - \int_{\tau_0'(r_0)}^{\tau_1'(r_1)} \left[\frac{d\phi}{d\tau'}\right]_{\text{no-disk}} d\tau'. \tag{4.25}$$

Thus, by applying the aforementioned method, one may determine the acquired phase as well as the companion's degree of dephasing.

## 4.5 Results & Discussion

### 4.5.1 Observability of EMRIs in LISA band

LISA will monitor SMBH binaries in the final hours to years of their lives. The SMBH binary merger rate is in fact unlimited based on observations. However, the rates predicted by theoretical models vary greatly based on the assumptions used. As a result, with a mission duration of 4.0 years and a potential extension of up to 10 years, the anticipated number of LISA detections varies from $\mathcal{O}(1)$ to $\mathcal{O}(100)$ each year. A key factor in defining LISA's capability to identify and characterize SMBH binaries is its low-frequency sensitivity. Specifically, it contributes in two major ways that together define the LISA scientific performance for the SMBH parameter space. First of all, it establishes the upper limit on the mass and redshift of the observable binaries. The low-frequency cut-off, on the other hand, regulates how long the signal will be in the detecting band. Therefore, to check the observability of our chosen EMRI systems within LISA frequency band, we plot the relevant characteristic strain for the EMRI ($10^6 M_\odot$, $10^2 M_\odot$) at a distance of 1 GPc in the LISA frequency band in Figure 4.3 and with central BH mass $10^5 M_\odot$ and companion mass $10 M_\odot$ in Figure 4.4. The LISA noise strain is represented by a *dashed line* and was taken from Robson et al. (2019). The figure shows that the characteristic strain is substantially above the LISA noise strain, implying that such EMRIs could be detected. The impact of any accretion disk is only quantified if the EMRI is observable in the first place. As a result, we plotted the previous 5 years of observations before arriving at the ISCO. We use different symbols to locate the positions of the companions when they are one month, six months, and a year apart from ISCO. The LISA mission lifetime is 4 years; within this interval, how long our system remains within the frequency band is shown by using these symbols. As the companion travels closer to the primary, the frequency of the transmitted GW signals increases $10^{-4} - 10^{-2}$Hz monotonically with time, increasing the dephasing and thereby increasing the detection potential of the EMRI's gas-rich environment. Dephasing, on the other hand, is extremely dependent on the hydrodynamic disk model used and is quite sensitive to the gas-rich environment. Our study makes use of transonic flow, which has the potential to generate enough dephasing to be seen in the LISA observation window. By identifying the type of embedded accretion disk by the dephasing of the emitted signals, one can constrain the disk parameters from the observation and also determine the nature of the disk.

### 4.5.2 Accumulated Phase shift due to accretion disk

The loss of $E$ and $L$ due to disk drag is less than that caused by GW radiation, as can be observed from the preceding chapter 3's graphs (Figure 3.25-3.20), but for some EMRI systems, the overall cumulative impact of the disk drag at the culmination of a long-term inspiral may be finite. In addition, we can observe in chapter 3, Figures 3.8 3.26 and 3.28 that the infall time has a whole time lag. The cumulative effect of this time lag during the late inspiral stage creates a definite phase lag that may be detectable during LISA observation, even though this time lag is

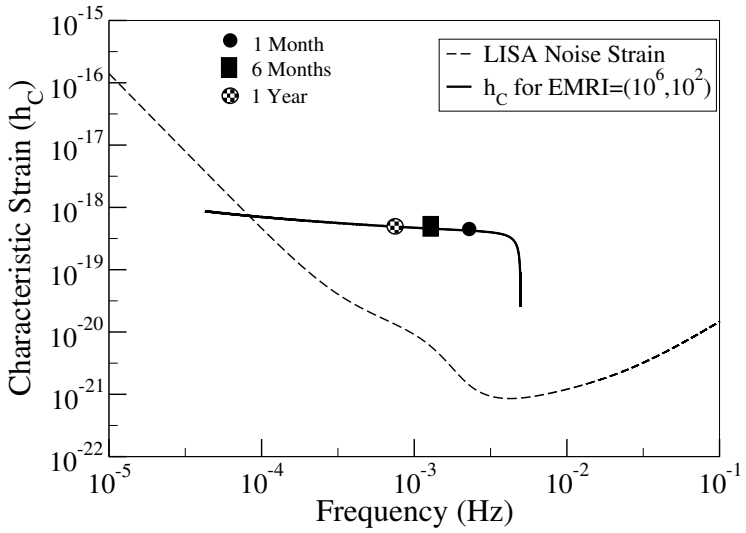


**FIGURE 4.3:** Regarding the observed frequency of GW, the *dashed line* depicts the LISA noise sensitivity curve. Before merging, the last five years of observation were used to plot the characteristic strain hc of the EMRI ($M = 10^6 M_\odot$,$m = 10^2 M_\odot$) at a distance of 1 Gpc (solid line). For an orbit with $a = 0.50$, the strain is estimated up to a marginally stable orbit ($r_{ms} = 4.23 r_g$). As seen by the EMRI's solid line, the orbital radius decreases over time while the frequency of the wave that is released increases. In this figure, we indicated (using various symbols as shown in the image) the companion BH's distance from coalescence at 1 year, 6 months, and 1 month. The graphic shows that the strain is extremely bright within the LISA window for an extended period of time. This increases the likelihood that our transonic disk model will successfully exhibit the impact of disk drag. As a result, the presence of the accretion disk may be detectable in E/IMRIs, and one may constrain the disk parameters using the observed GW data.

small compared to the total journey time starting from the early inspiral stage (Derdzinski et al., 2019a,b, 2021; Speri et al., 2022). To quantify the phase difference ($\delta\phi$), we consequently use equation (4.25) to compute the phase that the companion acquired either with or without the disk. In Figure 4.5, we display this phase shift ($\delta\phi$) with radius for various binary separations. The figure provides an estimate of the phase difference that the companion would have gained over the final five years before coalescence, when their separation was typically approximately $50 r_g$, where $r_g$ is the Schwarzchild radius. From $50 r_g$ onward, we can observe that the phase difference grows monotonically as the orbital decays. The curve depicts a plateau during the inspiral's last stage. When the separation is less, this plateau is typical; however, at the initial separations of $40 r_g$, $30 r_g$, $20 r_g$, and $10 r_g$ the phase shift steadily decreases. As a result, the degree of phase shift would mostly depend on the EMRI's starting separations, which in turn depended on how long the observation period was. Calculating the signal-to-noise ratio (SNR) (equation (4.22)) will reveal whether or not this accumulated phase shift within this radial separation is discernible. The SNR must be greater than the detectable range (SNR $\geq 8$) in order for the EMRIs to be detected by the detector. Our investigation identifies a number of E/IMRI systems whose estimated SNR is above the detectable range and could be observed. The findings of these E/IMRIs are intriguing since the cumulative phase shift throughout GW monitoring would then make it possible to determine if the gas-rich disk environment and the formation channel existed.

As previously indicated, the dephasing of the companion black hole is affected by the observation period (see figure 4.5). We analyze two alternative systems with mass ratios $q = EMR = \frac{m}{M} = 10^{-4}$ & $10^{-3}$ with center BH mass $M = 10^6 M_\odot$ at a distance of 1 GPc from the detector to determine its detectability during different phases of observation. In figure 4.6, we calculate the

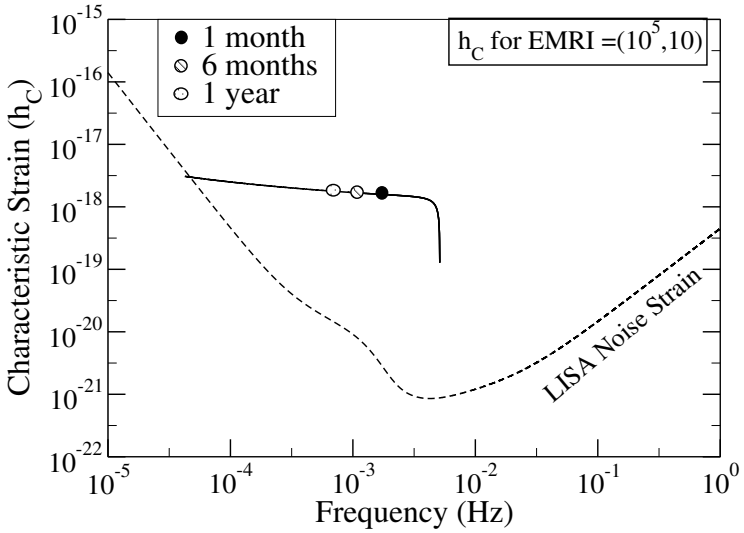


**Figure 4.4:** In the figure, the *dashed line* shows the LISA noise sensitivity curve with respect to the observed frequency of GW. The characteristic strain $h_c$ of EMRI ($M = 10^5 M_\odot$, $m = 10 M_\odot$) at a distance of 1 Gpc is plotted (*solid line*) in the last five years of observation before merging. The strain is calculated up to ISCO ($r = 4.23 r_g$) for $a = 0.50$. With time the orbital radius shrinks and the frequency of the emitted wave enhances gradually as indicated by the *solid line* of the EMRI. We marked the locations when the companion BH is at 1 year, 6 months, and 1 month away before coalescence (denoted by different symbols as shown in the figure). From the figure, we see that the strain is bright within the LISA window and ensures a greater chance of observing the effect of disk drag produced by our transonic disk model. Thus the influences of the accretion disk may constrain the orbital parameters from the observed GW data.

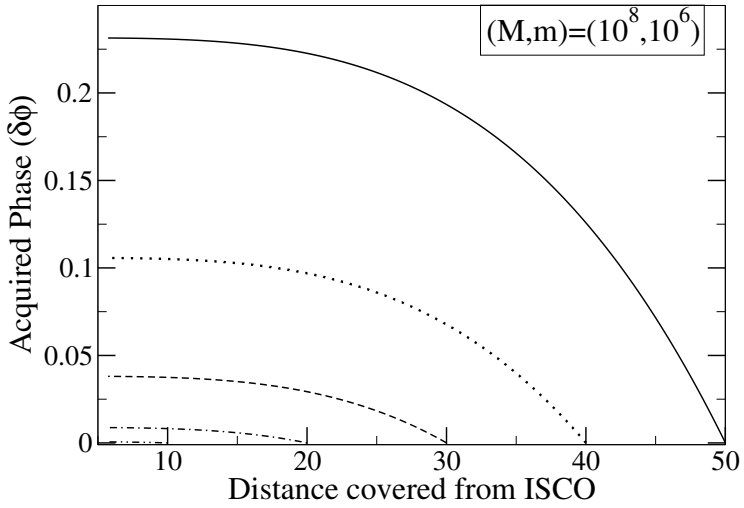


**Figure 4.5:** We show the overall phase difference that the companion BH collected while traversing the disk in this figure. The companion's $\delta\phi$ gain over the previous five years before to merging is shown as a solid line. For lower separations covered by ISCO, the corresponding phase accumulation is displayed, for example, $40 r_g$(*dotted line*), $30 r_g$(*dashed line*), $20_g$(*dot-dashed line*), $10 r_g$(*dot-dot-dashed line*). We observe a monotonic rise in the phase difference $\delta\phi$ throughout orbital decline. Even when the spacing is less, the curve displays a plateau during the late stage of the inspiral. The plateau's magnitude does, however, eventually diminish. By calculating the signal-to-noise ratio (SNR) of the sources, it would be possible to determine whether these phase changes were observable and consequently whether they could be detected by the LISA GW detector or not.

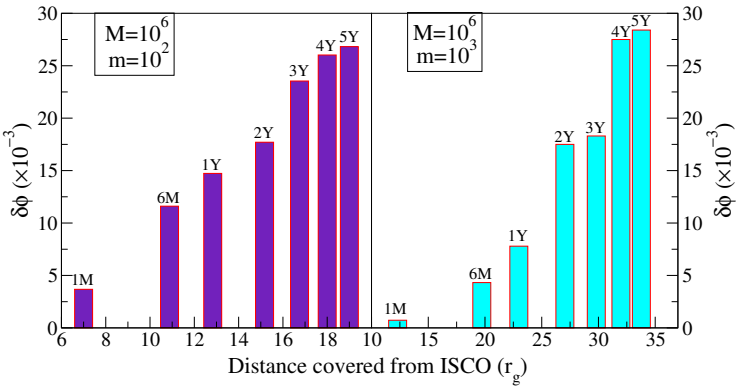


**Figure 4.6:** The distinct histograms of the acquired phase shift $\delta\phi$ for different times of observation are plotted in this figure. The observed period is computed for various separations measured from ISCO. In panels (a) and (b), we plotted two separate E/IMRI cases. Both panels show that when the observation time or orbital radius diminishes, so does the accumulated phase shift owing to disk drag. Again, the detectability of these phase shifts within a single observation period would be determined by SNR quantities (equation (4.22)).

dephasing of the companion when the disk is present or absent. We calculate the accumulated phase shift from the innermost stable orbit (ISCO) for various observation times (5 years, 4 years, 3 years, 2 years, 1 year, 6 months, 1 month, etc.) for both systems $(10^6, 10^2)$ and $(10^6, 10^3)$. The outcomes are shown as a histogram. Again, we notice that the accumulated phase shift varies depending on the initial separation of E/IMRIs for each observed interval. Furthermore, we can see that the dephasing is affected by the mass ratio of the E/IMRIs. We discovered that the accumulated phase shift is detectable up to 6 months ($SNR(\delta\phi) \sim 17$) for $EMR = 10^{-4}$ (left panel), but it is less noticeable and requires a longer observation time (about 1 year or more) for $EMR = 10^{-3}$ (right panel).

Further in figure 4.7, we calculate the dephasing of the companion when the disk is present and absent from the ISCO for various observation times for both the systems $(10^5, 10)$ & $(10^5, 10^2)$. We can see that the accumulated phase shift is different for different observed periods as it depends on the initial separation of E/IMRIs. As we obtained earlier in Figure 4.6, here also we can see that the dephasing also depends on the mass ratio of the E/IMRIs.

### 4.5.3 Detectability of the phase shift through the estimation of SNR

In Chapter 3, Figures 3.5-3.13, 3.33-3.35 &, 3.38-3.41, shows that there is a noticeable time lag in the infall time caused by the additional hydrodynamic drag forces applied on the companion motion.Although it is small in comparison to the entire travel duration, the time lag causes a phase shift in the output GW signal. As a result, we first compute the phase obtained by the companion with and without the disk independently and then calculate the phase difference ($\delta\phi$). The acquired dephasing, whether minor or inconsequential, may be understood by calculating the SNR from the equation (4.22) during a certain period of observation. Because the SNR is affected by the period of observation, source distance, mass ratio, and so on, we varied them one by one and analyzed the dephasing and SNR for each of them for our provided hydrodynamics disk to assure the detectability (SNR$\geq$ 8) of the orbits. A histogram graphic depicts the results. When the SNR is less than 8, we use a black bar to indicate non-detectable EMRIs and disregard them. The blue cylindrical bar represents detectable (SNR$\geq$ 8) EMRIs.

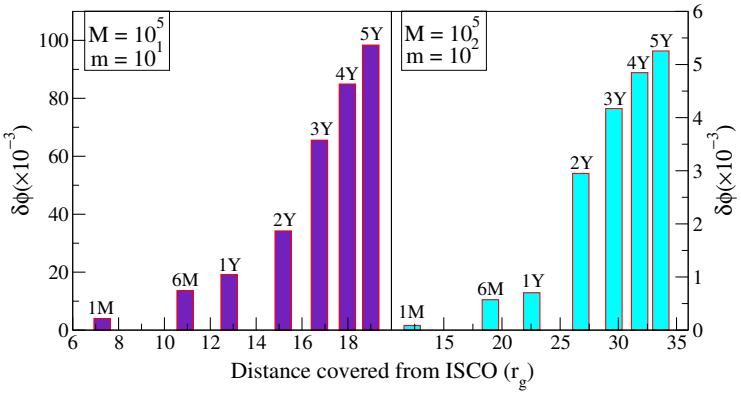


**Figure 4.7:** We plot the various histograms of the acquired phase shift $\delta\phi$ for various observation periods in this figure. For different separations calculated from ISCO, the observed period is computed. In panels (a) & (b), we have plotted two distinct E/IMRI cases. We can see from both panels that the accumulated phase shift caused by disk drag decreases with a decrease in either the orbital radius or the observation period. Once again, SNR values (equation (4.22)) would indicate the detectability of these phase shifts during a specific observation period.

#### 4.5.3.1 Critical observable range & SNR variation with source distance

Figure 4.8 shows the SNR of phase shift derived for different observational times before merging for an EMRI of $M = 10^6 M_\odot$ and $m = 10^2 M_\odot$ situated at a distance of 1 GPc. The figure shows that the SNR of phase shift monotonically falls with the length of observation and becomes non-detectable from the final month ($1 month = 0.083 year$) before merging. Prior to it, SNR was $\geq 8$, and the system was observable.

Figure 4.9 shows the variation in estimated SNR with the distance of the source. Here we consider a duration of 4 years from ISCO as the observing period, and other system details are as follows: masses of the companions are $(10^5 M_\odot, 10 M_\odot)$, the initial eccentricity is $e = 0.30$, and the Kerr parameter is $a = 0.50$.

Another figure with a different mass ratio $(10^6 M_\odot, 10^3 M_\odot)$ depicting the SNR variation with the source distance is shown in Figure 4.10. Here, the observation period is taken as 5 years from the ISCO.

We see that with increasing source distance, the SNR of the signal decreases. Detectors capability to detect sources beyond $D = 1.4$ GPc decreases significantly for sources with masses $(10^6 M_\odot, 10^3 M_\odot)$ and $(10^5 M_\odot, 10 M_\odot)$ respectively. However, it precisely measured the SNR of dephasing within the range of $D = 1.4$ GPc.

#### 4.5.3.2 Minimum duration of observability & SNR variation with LISA observation period

In figure 4.11, we adjust the EMRI with the source distance and determine the SNR of the phase shift. When the source distance is 1 GPc, it is well inside the LISA observational window; however, when the source distance is increased to 2 GPc, it is just observable by LISA and stays undetectable when the distance is 3 GPc or above.

In the figure 4.12, for the EMRI $(10^5 M_\odot, 10 M_\odot)$, the SNR histogram of the accumulated phase shift is plotted at a distance of 1 GPc away during the various observation periods. The figure shows that, as the observing period decreases, SNR decreases monotonically. This is due to the

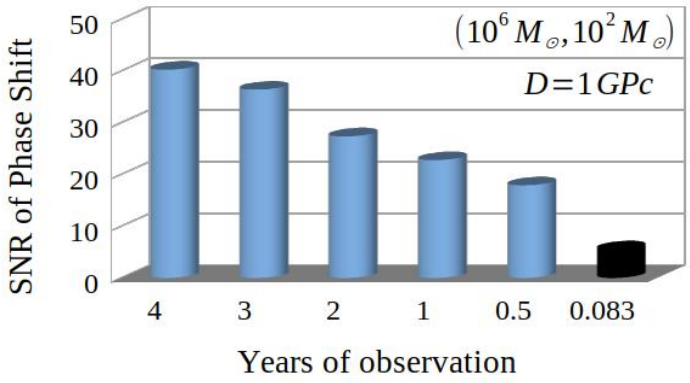


**Figure 4.8:** Histogram of SNR of the accumulated phase shift is plotted for the EMRI $(10^6 M_\odot, 10^2 M_\odot)$ at a distance of 1 GPc. In the Figure 4.8 histogram of SNR of the accumulated phase shift is plotted for the EMRI $(10^6 M_\odot, 10^2 M_\odot)$ at a distance of 1 GPc away during the different observation period. From the figure, we see that SNR monotonically decreases as the observing period of LISA decreases. This is due to the fact that the accumulated phase shift is more for long-term observation (or for large separation). The blue cylindrical bars show a detectable SNR and the black bar represents non-detectability (SNR $< 8$). The SNR is calculated upto the ISCO at $r = 4.23 r_g$.

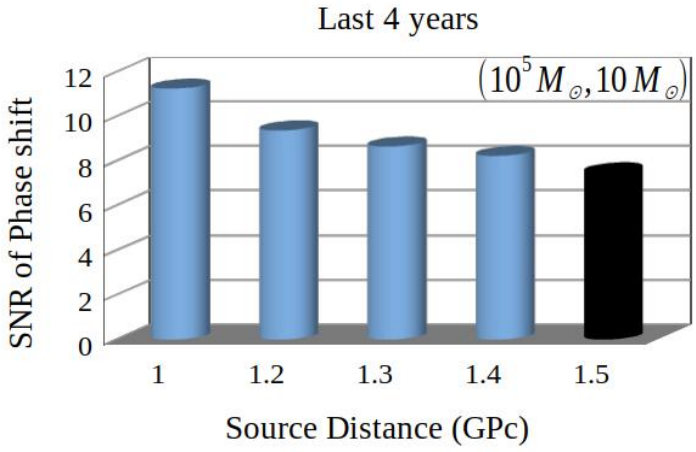


**Figure 4.9:** The SNR of the accumulated phase shift is plotted with the source distance D (GPc) for the last 4 year of observation.

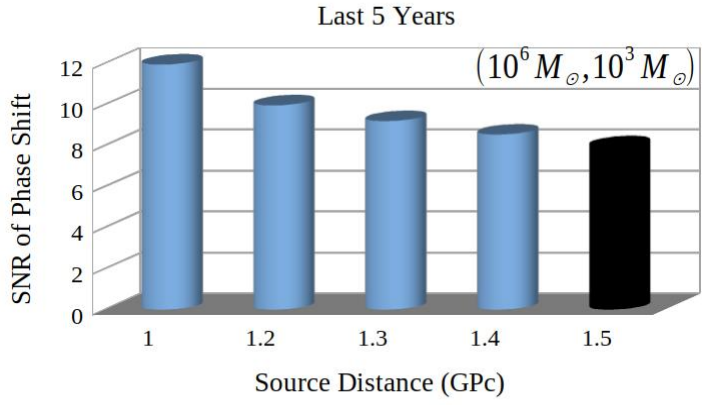


**Figure 4.10:** The SNR of the accumulated phase shift is plotted for the EMRI $(10^6 M_\odot, 10^3 M_\odot)$ with the source distance D (GPc) for the last 5 year of observation..

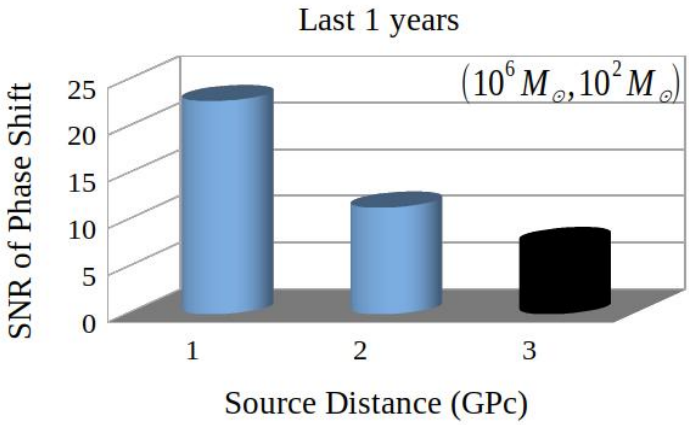


**Figure 4.11:** Histogram of SNR of the accumulated phase shift is plotted for the EMRI $(10^6 M_\odot, 10^2 M_\odot)$. In the Figure 4.11 the SNR of the accumulated phase shift is plotted with the source distance D (GPc) for the last 1 year of observation. From the figure we see that as the EMRI to detector distance increases, the SNR inversely decreases with distance D. We also see that detectability decreases for far distance EMRI represented by the black cylindrical bar

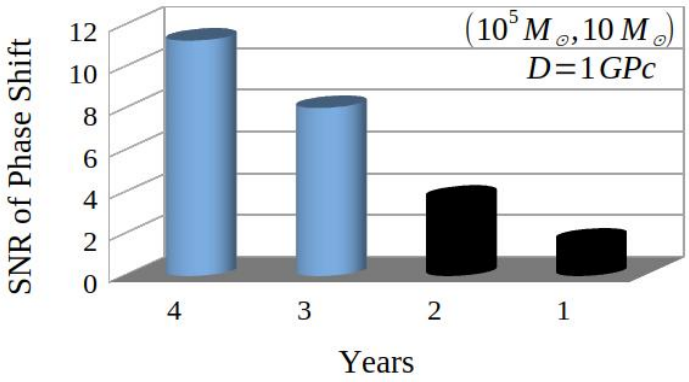


**Figure 4.12:** The histogram of SNR of the accumulated phase shift is plotted for the EMRI $(10^5 M_\odot, 10 M_\odot)$ at a distance of 1 GPc away during the different observation period. From the figure, we see that SNR monotonically decreases as the observing period of LISA decreases.

fact that the accumulated phase shift is more for long-term observation (or for large separation). The gray cylindrical bars show a detectable SNR, and the black bar represents non-detectability ($SNR < 8$). The SNR is calculated up to the ISCO at $r = 4.23 r_g$ ($a = 0.50$) where $r_g$ is the Schwarzchild radius.

It is evident that the companion's motion in the presence of a transonic flow in this type of EMRI would result in enough dephasing to be seen during LISA observation windows. Furthermore, the hydrodynamic disk's chosen parameters have an impact on the dephasing as well. The disk parameters were left unchanged when we performed SNR on these observations.

### 4.5.4 Dependency of the dephasing and SNR on various disk parameters

We've already shown that the disk parameters vary across a wide range, and the sub-panel of Figure 2.9 displays the parameter space accessible for transonic solutions. The dephasing of the EMRIs is affected by the disk parameters, such as the energy and angular momentum of the flow.

Altering the accretion rate also results in a change in dephasing. This is due to the fact that the dephasing and corresponding SNR values are affected by disk torque during the companion inspiral motion. According to equations (3.28), (3.29), the magnitude of the disk drag is affected by flow variables such as velocity, sound speed/temperature, and the density profile of the disk, which in turn is affected by disk parameters such as the flow's energy and angular momentum and the accretion rate at the outer boundary. Thus, the disk's hydrodynamic properties are extremely sensitive, and the selection of disk parameters is critical in determining dephasing and SNR values. As a result, in this subsection, we focus on the dephasing and the estimated SNR values from the equation (4.22) with the disk parameters. The SNR can then be used to judge if the acquired dephasing is visible or not during different observations. Furthermore, the SNR is affected by mass ratio, source distance, and observation period, among other factors; therefore, we chose an EMRI system with a mass ratio of $(M, m) = (10^6 M_\odot, 10^2 M_\odot)$ and a distance of 1 GPc. We also take into account the last four years of EMRI observations from the ISCO and modify the transonic disk characteristics and accretion rate. Changing the outer boundary conditions, namely initial velocity($v$) and temperature($T$) at the outer disk (see Figure 2.9), yields three alternative disk solution profiles for three disk parameters, which are then used to calculate dephasing and SNR. Figures 4.13,4.14 & 4.15 display the findings. For the three solutions $(v_1, T_1), (v_2, T_2)$ and $(v_3, T_3)$, respectively, we take into consideration the disk parameters (energy and angular momentum) $(E_1, L_1) = (1.01, 2.85)$, $(E_2, L_2) = (1.004, 3.05)$, and $(E_3, L_3) = (1.001, 3.2)$. We can observe from the figure that the three solutions have different estimated dephasing in the produced GW signal. As we can also observe, the equivalent SNR values that are shown in the histogram (right panel) are analogously dissimilar. The plot shows how the accretion rate affects both the phase shift and the SNR's magnitude. As a consequence, we change the rate of accretion and present Figures 4.13, 4.14 and 4.15 for $\dot{M} = 0.01, 0.1$, and $1.0\dot{M}_E$, respectively. On the right panel, we can also observe that the phase shift and its detectability, or SNR, both increase with increasing accretion rate and are over the detectability threshold of SNR $\geq 8$. The investigation may also provide a potential range for that, which the EM observations might confirm. In order to more precisely restrict the accretion parameters, both the GW and EM-wave observations will be useful.

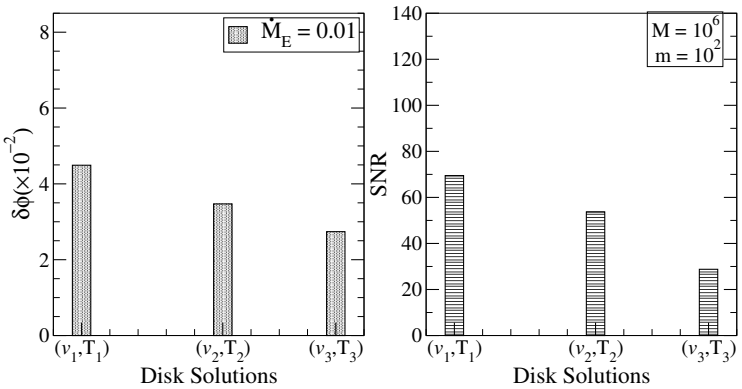


**Figure 4.13:** In the figure, we compare the phase shift (left panel) and SNR values (right panel, calculated from equation (4.22)) for the variation of the disk parameters and accretion rate. We consider three different disk profile solutions $v = v(r)$ and $T = T(r)$ (matter infall velocity $v$ and temperature $T$ are obtained for different outer boundary conditions) and compare the dephasing and SNR values in terms of disk parameters (e.g., energy and angular momentum) of the flow for a mass accretion rate $\dot{M} = 0.01\dot{M}_{Edd}$. The EMR configuration for these plots are as follows: mass ratio $(M, m) = (10^6 M_\odot, 10^2 M_\odot)$ at a distance 1 GPc. We consider the last 4 years before coalescence as our observing window.

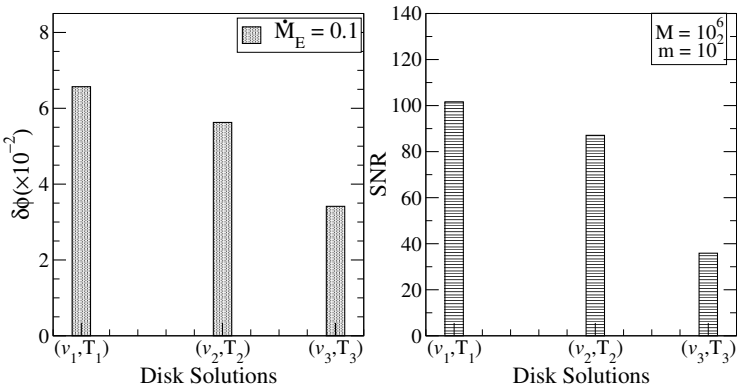


**Figure 4.14:** For the mass accretion rate $\dot{M} = 0.1\dot{M}_{Edd}$, Figure 4.13 is reproduced here.

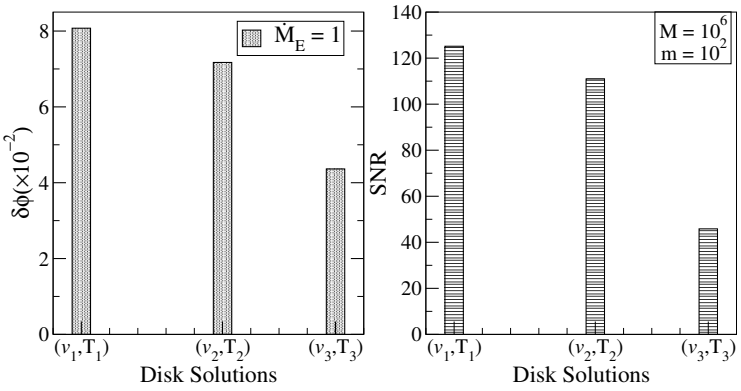


**Figure 4.15:** For the mass accretion rate $\dot{M} = 1\dot{M}_{Edd}$, Figure 4.13 is reproduced here. For each of these solutions $(v_1, T_1), (v_2, T_2), (v_3, T_3)$, we see that with the increasing accretion rate dephasing and its detectability increases (see Figure 4.13 & 4.14 for the comparison).

### 4.5.5 Detectable E/IMRIs at the largest possible separation in the LISA band

So far, in the preceding sections (see Figures 4.5 to 4.15), we have taken into consideration the distance from the ISCO as the observation intervals and calculated the dephasing of the E/IMRIs. However, as one gets closer to the ISCO, the strong field effects become more substantial, and the equations become progressively erroneous. Furthermore, the position of the ISCO is dependent on the spin of the SMBH; the greater the spin, the closer the final stable orbit is to the event horizon. As a result, the decision is fairly arbitrary and would be better justifiable for EMRIs produced via dynamical relaxation channels. The spin of the central SMBH can also affect the accuracy of the event rate in such E/IMRIs in the LISA band (Pan et al., 2021; Vázquez-Aceves et al., 2022). As a result, an equally obvious approach would be to begin developing the EMRI at the greatest feasible distance from LISA. Therefore, the dephasing is estimated from the furthest visible separation, and then we calculate the variation by taking the different initial positions of the evolving E/IMRIs as it proceeds in the LISA band. In all such observations, we take an equal portion of the four-year observation period, and the results are shown in Figure 4.16.For instance, we chose three separations, A, B, and C, which represent the system's strain at radial distances of $(40 - 35.15r_g)$, $(35.14 - 26.28r_g)$ and $(31.8 - 4.23r_g)$, respectively. As the E/IMRIs combine for coalescence, these ranges become visible to LISA because the predicted strain is much above the detector's noise strain (obtained from Robson et al. (2019) and depicted by the long solid

line). In the left panel, we use the mass ratio $EMR = 10^{-3}$ with a main mass of $10^6 M_\odot$ and a source distance of 1 GPc to illustrate the usual strain of an E/IMRI. In the right panel of Figure 4.16, the relative phase shift and SNR values obtained for the three observation sets A, B, and C are also presented using a histogram. As the E/IMRIs progress from the maximum feasible visual separation towards ISCO, the phase shift and hence the SNR/detectability rise ($A < B < C$).

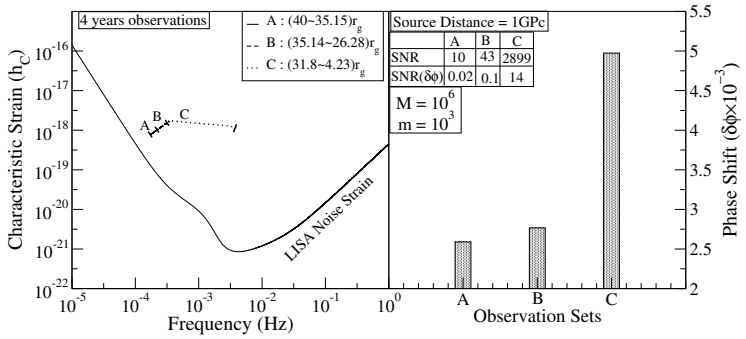


**Figure 4.16:** The LISA noise strain is plotted in terms of the measured frequency (Hz) in the left panel, as illustrated by the *solid line* and acquired from Robson et al. (2019). The cumulative phase shift of a binary inspiral with masses $M = 10^6 M_\odot$ and $m = 10^3 M_\odot$ at a distance of 1GPc is plotted in the right panels of this picture. The left panel shows the strain for three separate observation periods, A, B, and C, which vary from $40 - 35.15 r_g (solid\ line)$, $35.14 - 26.28 r_g (dash\ line)$ and $31.8 - 4.23 r_g$(ISCO for $a = 0.50$)$(dot\ line)$, respectively. Each of these observation periods is identical and equivalent to four years, and A is calculated from the furthest first observable separation in LISA. The phase shift accumulated throughout those intervals, as well as the SNR values, are presented in the right panel. The phase shift and SNR rise from A to B to C as the EMRIs go from the longest observable separation towards the ISCO.

Now, we contrast the findings from the two different EMRI systems and the two distinct observational periods. We assume that the source is at a redshift of $z = 1$, and the primary mass is assumed to be $M = 10^6 M_\odot$ with $EMR = 10^{-3}\&10^{-4}$. We also take into account two different frequency zones for each of the four years of observation: the first observation (A) starting radius $31.9 r_g/18.53 r_g$ which ends up at $10 r_g$, and the second observation (B) from $31.7 r_g/17.98 r_g$ to the final inner most stable orbit at $4.23 r_g$ ($a = 0.50$) for the EMRIs $(10^6, 10^3)/(10^6, 10^2)$ respectively. We compare our predicted results for two observation periods in the left panel of Figure 4.17, where the slightly shorter solid lines correspond to observation (A) and the dotted lines to observation (B) for both EMRIs. Additionally, we record the GW-SNR of each of these individual observations in the legend box of the corresponding figure. The figure demonstrates that the GW-strain is greater for the EMRI $(10^6, 10^3)$ than for the $(10^6, 10^2)$, resulting in the total separability of the two EMRIs. Since B integrates the higher frequency domain closest to ISCO, it has a greater GW-SNR than A.

By changing the accretion rate, we depict the dephasing of the $EMR = 10^{-3}$ in the right panel of Figure 4.17. We employ the identical transonic solution with the accretion rates set to 0.1, 1.0, and 10 Eddington rates for both observations A and B. All other flow parameters were left constant. We can observe that for the EMRI $(10^6, 10^3)$ the dephasing grows monotonically for both observations A and B with increasing accretion rate. The picture and Table 4.2 also show the equivalent shift in SNR values as the accretion rate increases.

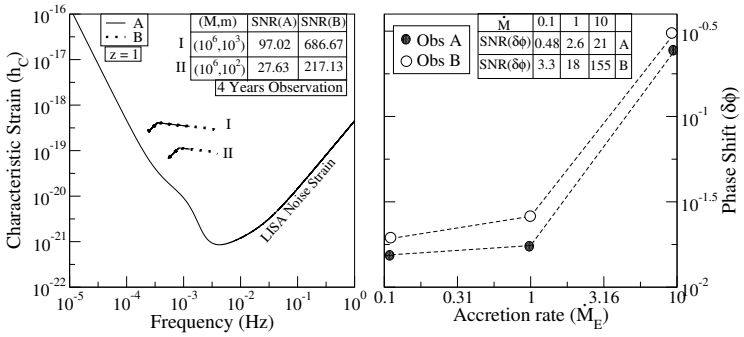


**Figure 4.17:** The typical strain as a function of frequency for two EMRI systems with black hole masses of $(10^6, 10^3)$ and $(10^6, 10^2)$ at redshift $z = 1$ is shown in the left panel of the image. There are two separate 4-year-long observations conducted for each system. The first observation (A) starts at a radius of $31.9r_g/18.53r_g$ and finishes at $10r_g$(solid line), and the second observation (B) starts at a radius of $31.7r_g/17.98r_g$ and ends at final inner most stable orbit $4.23r_g$ $(a = 0.50)$(dot line), respectively, for the EMRIs $(10^6, 10^3)$ and $(10^6, 10^2)$. We can observe that the GW-strain is greater for the EMRI $(10^6, 10^3)$ than for the $(10^6, 10^2)$, indicating that the two EMRIs can be distinguished fully. In the legend box are the corresponding SNR values (derived using equation (4.21)). Because B integrates up to ISCO in the high frequency domain more than A does, the observation (B) has a higher GW-SNR than A. We plot the acquired phase shift $\delta\phi$ for the EMRIs $(10^6, 10^3)$ in the right panel while taking into account the various accretion rates depicted in the figure. We see that the phase shift and corresponding SNR values rise with increasing accretion rate.

### 4.5.6 Comparison of the detectability with other accretion disk models.

To compare the dephasing with other accretion disk models, we used two EMRI systems $(10^6, 10^2)$ and $(10^6, 10^3)$ with accretion rates of 0.1, 1.0 and 10 Eddington. The phase shift and GW-SNR values for the transonic accretion flow are already described in Figure 4.17. For various disk models, we gathered data from recent simulation studies Derdzinski et al. (2019a); Kocsis et al. (2011) (SS-disk model (Shakura & Sunyaev, 1973)). In Table 4.2, we compare and tabulate each sets of data autonomously. The companion's dephasing is solely determined by the accretion disk model used. We've previously established that our model has more relative disk drag/torque, hence the dephasing and detectability of such E/IMRIs is better for the transonic disk model. In other words, when the gas-riched E/IMRI systems are identified in the LISA range, Table 4.2 clearly predicts a detectable signature of the transonic disk.

### 4.5.7 Estimation of Optimal Orbital parameters using SNR

We estimated the SNR for several orbits while keeping the period of observation fixed for an EMRI situated at 1GPc distance. We set the detectability threshold of SNR $\geq 8$ here once again. This suggests that the orbits with higher disk drag are capable of causing substantial dephasing in the signal, and the SNR is predicted to be higher than the threshold value. The non-detectability here alludes to inadequate dephasing and negligible disk-drag torque on certain orbits. We depict the variation of estimated dephasing-SNR in terms of eccentricity $(e)$, semi-major axis $(X)$, and SMBH spin $(a)$ in the figures 4.18, 4.19 & 4.20.Other parameters are kept constant for each modification. The projected SNR fluctuations are consistent with the previous findings. Figure 4.18 shows that the SNR of dephasing grows with increasing eccentricity because disk torque increases for high eccentric orbits. The ideal orbital eccentricity is $e \geq 0.2$, as shown in the figure. SNR falls with increasing semi-major axis in 4.19 because disk torque is greater for smaller $X$.

| Comparison of phase shift & SNR in last 4 year for sources at $z = 1$ | | | | | | |
|---|---|---|---|---|---|---|
| $EMR$ | $\dot{M}$ | Other Model | | Transonic Disk | | |
| | | $\delta\phi$ | SNR(GW) | $\delta\phi$ | SNR(GW) | SNR($\delta\phi$) |
| $(10^6, 10^2)$ | $0.1\dot{M}_E$ | – | 160 | $> 10^{-2}$ | 217.13 | 4.13 |
| $(10^6, 10^2)$ | $1.0\dot{M}_E$ | $\leq 10^{-3}$ | 160 | $10^{-2} - 10^{-1}$ | 217.13 | 5.64 |
| $(10^6, 10^2)$ | $10\dot{M}_E$ | $10^{-3} - 10^{-2}$ | 160 | $> 10^{-1}$ | 217.13 | 69.50 |
| $(10^6, 10^3)$ | $0.1\dot{M}_E$ | – | 508 | $> 10^{-3}$ | 686.6 | 3.38 |
| $(10^6, 10^3)$ | $1.0\dot{M}_E$ | $< 10^{-3}$ | 508 | $> 10^{-2}$ | 686.6 | 18.86 |
| $(10^6, 10^3)$ | $10\dot{M}_E$ | $10^{-3} - 10^{-2}$ | 508 | $\geq 10^{-1}$ | 686.6 | 155.90 |

**Table 4.2:** The table compares the dephasing generated by transonic accretion disk to the other model (SS-disk) (Derdzinski et al., 2019a). The various SNRs are computed and compared using equations (4.21) and (4.22). We observe that the dephasing in transonic flows is much larger than that calculated in recent research Derdzinski et al. (2019a); Kocsis et al. (2011).

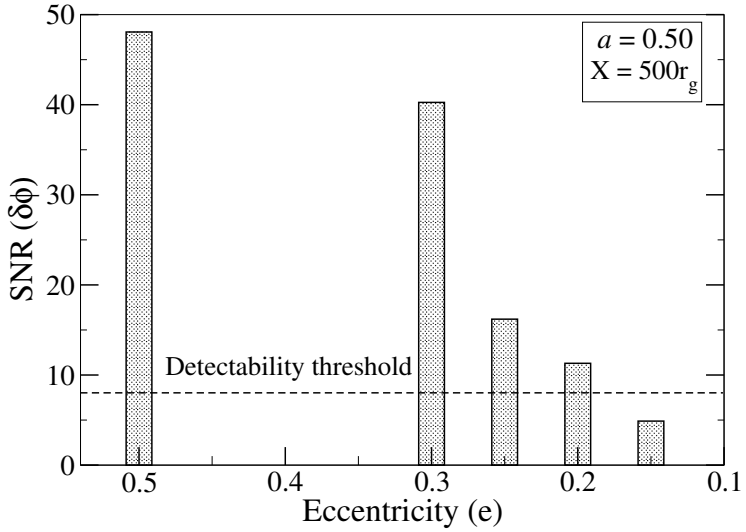


**Figure 4.18:** We depict the variation of the estimated dephasing-SNR in terms of eccentricity ($e$) in the this figure for several eccentric orbits. We see that the likelihood of detection rises with increasing eccentricity. Additionally, the minimal threshold in this setup, where spin $a = 0.50$ and semi-major axis is $X = 500$ are similar and larger than 0.15. The minimal SNR necessary for determining the ideal values of the orbital parameters is provided by the threshold line displayed by *dash line*

The graphic shows the best value of $X < 1000r_g$. In addition, in Figure 4.20, we examine the SNR by modifying the spin of the central SMBH for two sets of data, namely $X = 500r_g$ and $X = 900r_g$. We see that higher SNR values are obtained for slowly spinning SMBH. We can see that the detectability of dephasing increases for retrograde orbits. The minimal SNR necessary for determining the optimal values of the orbital parameters is provided by the threshold line displayed by *dash line*. However, the choice of the disk characteristics, the nature of the disk, and the accretion rate determine these best parameter values. For our investigation, we settled on an accretion rate of the 1 Eddington rate. We calculated the optimal parameters for a system with a companion mass of $10^6 M_\odot$ and a central SMBH mass of $10^2 M_\odot$ that is 1 GPc away from the detector.

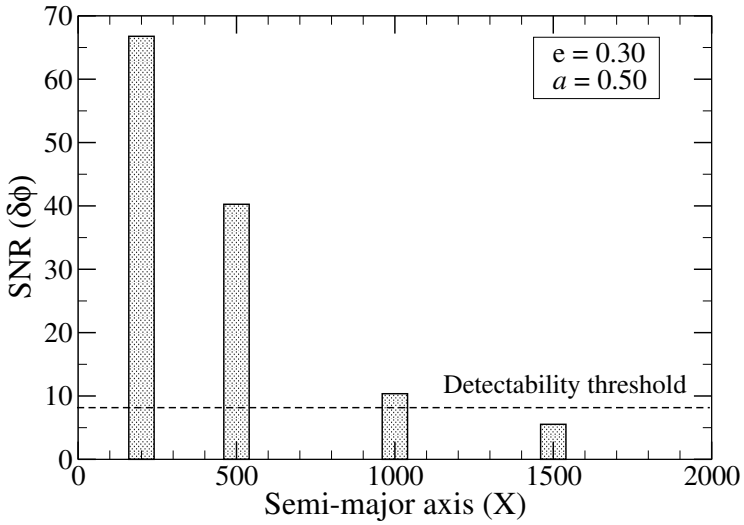


**Figure 4.19:** We depict the variation of the estimated dephasing-SNR in terms of semi-major axis ($X$) in this figure. We alter the semi-major axis ($X$) to depict the SNR($\delta\phi$) (other parameters are shown in the legend box). We can observe that the possibility of detection is decreased with increasing $X$. We can observe that the degree of detectability of dephasing depends on the choice of semi-major axis. The minimal SNR necessary for determining the ideal values of the orbital parameters is provided by the threshold line displayed by *dash line*

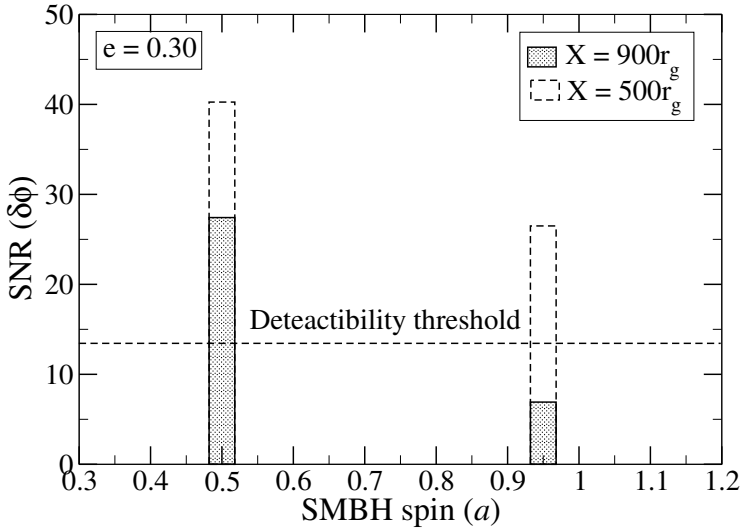


**Figure 4.20:** We depict the variation of the estimated dephasing-SNR in terms of SMBH spin ($a$), respectively, in this figure. We examine the SNR for two sets of data, $X = 500r_g$ and $X = 900r_g$, by changing the spin of the central SMBH. We can observe that slowly spinning SMBHs provide greater SNR values. We can observe that the degree of detectability of dephasing depends on the choice of spin and semi-major axis. The minimal SNR necessary for determining the ideal values of the orbital parameters is provided by the threshold line displayed by *dash line*

## 4.6 Conclusion

EMRIs have acquired recognition as extremely fascinating systems since their frequency range fits the detectability range of the space-based GW detector LISA. The entire momentum exchange between the disk and its companion black hole indicates a change in infall time and, thus, in coalescence time. This suggests that the GW templates must be modified in the presence of disks. In this work, we adopt a semi-relativistic formalism in the Kerr background to describe transonic accretion flow, which is a promising candidate for describing accretion flows near AGN to evaluate the respective changes in the GW waveform in the presence of disk. The hydrodynamic drag of the disks changed the motion of the companion, resulting in amplitude and phase modifications in the generated wave. We discovered that these changes are discernible throughout the previous few years of LISA observations (in some cases as little as six months) for EMRIs located within $z = 1$ of the detector and for the accretion rate of the primary black hole of the order of $\dot{M} = 1\dot{M}_{Edd}$. The drag effect, and therefore, the detectability of the emitted GW, is affected by the disk's hydrodynamical model. Therefore, we change the disk parameters, accretion rate, and period of observation of E/IMRIs and find that, when compared to alternative disk models, the transonic solution offers relatively better visible signatures in detecting gas-rich E/IMRIs inside the LISA range. Such observations will aid in probing the nature of the accretion flow and verifying various accretion physics hypotheses.

# Chapter 5

# Error in EMRIs mass estimation and Constraining the BH parameters from the detected GW strain emitted from accretion embedded EMRIs

## 5.1 Introduction

EMRIs are one of the most interesting mHz-frequency potential sources of gravitational radiation for the space-based detector LISA. EMRIs start when a stellar-origin compact object (CO) with mass $m = 10^{(1-3)}M_{\odot}$ becomes gravitationally bound to the primary black hole with mass $M = 10^{(5-8)}M_{\odot}$ as a result of scattering processes in the stellar cluster surrounding the massive black hole. The subsequent inspiral of CO towards the primary horizon is driven by a radiation reaction. EMRIs can be present in the LISA frequency band for several years prior to the plunge, so modeling the entire observable signal is a difficult task. Even in the final few cycles before collapsing into the central black hole, EMRI orbits are expected to be both eccentric and tilted, and for these reasons, they provide a challenge for both waveform modelers and observed data analysts (Amaro-Seoane et al., 2015; Barack & Cutler, 2004b; Chua et al., 2017). This similar intricacy also makes EMRIs one of the richest sources of gravitational waves. Typically, an EMRI will be visible for $1/(massratio) \sim 10^{5-8}$ cycles before collapse, and the generated gravitational waves will offer an excellent representation of the space time geometry of the primary black hole. General relativity tests may be carried out with great precision prior to accurate detection and parameter inference (Yunes et al., 2012; Gair et al., 2013). The information about the source is widely known to be carried through the time development of the phase of a gravitational wave (Cutler et al., 1993; Finn & Thorne, 2000). Because EMRIs evolve slowly, a significant number of cycles may be seen during the inspiral, providing amazing precise constraints on the source's parameters, e.g., the mass of the companions of EMRIs, spin of the central BH, etc. (Amaro-Seoane et al., 2007, 2012). There are many supermassive black holes (SMBH) with large spin parameters in our universe. Observations show that massive black holes (BHs) reside in the centers of most galaxies, where they are known to accrete matter (Mayer, 2013; Trakhtenbrot, 2014). The inspiralling dynamics of the companion compact object into a supermassive black hole through the accretion disk is different from the CO solo traveling, and these differences are reflected in the emitted gravitational waves. As a result, in order to detect and accurately estimate parameters from these near-extremal sources, our set of waveform models developed in vacuum must be updated to accommodate these environmental aspects. We present throughout this chapter the changes in several parameters of the companions of EMRI embedded in a transonic accretion flow in Kerr space time so that

constraints on parameter estimations offer significant precision. With the present-day increased sensitivity, LISA will have the capability to successfully conclude whether the central object in an EMRI system possesses an accretion disk or not (Chatterjee et al., 2023; Chatterjee et al., 2023; Garg et al., 2022; Derdzinski et al., 2021, 2019b). Thus, constraining the black hole parameters in the presence of an accretion disk is required. Recent works on semi-analytical and analytical studies estimated a few observable aspects that are most probably detectable with present-day detector sensitivity.

The first study to examine the astrophysical imprint caused by an accretion disk on GW radiated from EMRI was Chakrabarti (1993, 1996c); Molteni et al. (1994). Giampieri (1993) carried out the evolution of an equal mass binary system in the presence of mass accretion almost simultaneously. Several methods have been developed by Vokrouhlicky & Karas (1993, 1998); Šubr & Karas (1999); Karas & Šubr (2001); Narayan (2000); Levin (2007) for further development in this field. The general consensus on the accretion disk's effect on GW signals is that it has very tiny effect on the LIGO/LISA frequency range. Barausse & Rezzolla (2008) has developed a more convenient study to address the impacts of hydrodynamic drag on EMRI caused by a thick torus. Relativistic formalism was applied in this study; however, with an accretion flow having zero radial velocity, the accretion rate was calculated without considering the relative velocity of the companion BH. Basu et al. (2008) makes another effort to relativistically generalize the study in a pseudo-Newtonian framework, taking into account non-Keplerian accreting disks. The disk's drag causes a significant reduction in the companion's infall time. Yunes et al. (2011); Kocsis et al. (2011) studies this problem using the standard disk model as the EMRI environment. The effects of mass accretion, hydrodynamic drag, torques, and migrations on emitted GW were examined, and it is concluded that disk migration in particular has a major impact on the EMRI. According to the studies (Barausse et al., 2014; Barausse et al., 2015), astrophysical disturbances are insignificant for eLISA observations of EMRI, with the exception of geometrically thin disks. Additionally, they conclude that if the disk is thin and the drag from accretion and hydrodynamic drag predominates over self-force effects, i.e., the effect of the disk may be larger than or comparable to second-order self-force corrections for a typical EMRI. If the disk is not thin, the disk's effect will be negligible when compared to GW emission for binaries of comparable mass. Furthermore, according to the authors, EMRIs that are detectable by eLISA are more likely to have thick disks than thin ones. However, the Hubble Space Telescope has found a thin disk around a supermassive black hole in a spiral galaxy $NGC$ 3147 (**?**). According to recent simulation work on hydrodynamical flow, disk imprint information has an impact on GW (Derdzinski et al. (2019a,b, 2021)). In order to measure the torques exerted by gravitational interaction and accretion on the secondary BH, Derdzinski considers a 2-D viscous accretion disk in a Newtonian framework around an IMRI and finds that in the presence of the disk, the imprint on the IMRI can be detected by LISA in the final five years of the inspiral if the surface density is $10^3 gcm^{-2}$, and predicts that higher densities of gas disk produce a detectable phase shift. From all of the developments on the impacts of disks on GW, we identified that the impact of an accretion disk on the emitted GW signal from the EMRI can occasionally provide major modifications, ignorable impressions, or no relevant impressions at all, depending on the choice of the accretion disk model.

In this work, following the analytical treatment of Rezzolla, we calculate the deviation in the measurement of energy, angular momentum, and mass of the companions in a general relativistic

framework. We consider relativistically realistic accretion flows having significant radial velocity, e.g., transonic flows in the Eddington and sub-Eddington limits. We already discuss the numerical result obtained in Chapter 3 where a non-negligible imprint of the disk and the phase shift acquired by the companion are detectable. The analytical calculation was thus performed to see the observable aspects more accurately. This once again may boost the renewed interest in this field. In this work, we will consider only EMRIs where the companion is in eccentric and equatorial orbits around the primary black holes, and the central SMBH (mass $M$) determines the curvature of the background space-time in which the companion black hole of mass $m(m \ll M)$ moves like a test particle. It is interesting to see that the variation in the parameter estimation results in distinct orbital variation, and the error estimation of mass parameters lie within the sensitivity range of present-day space-based detectors.

## 5.2 Mass increase of the companion BH during accretion

The nonlinear acceleration of the companion is contributed by the changes in the four-momentum of the companion black hole in the presence of an accretion disk.

$$\frac{du^{\mu}}{d\tau} = \frac{d}{d\tau}(\frac{P^{\mu}}{m}) = \frac{1}{m}\frac{dP^{\mu}}{d\tau} - \frac{P^{\mu}}{m^2}\frac{dm}{d\tau} \tag{5.1}$$

where the four-momentum of the companion can be obtained from the Lagrangian $P_{\mu} = \frac{\partial \mathcal{L}}{\partial \dot{x}^{\mu}}$ that satisfies,

$$P^{\mu}P_{\mu} = m^2. \tag{5.2}$$

The canonical momentum of the companion BH per unit mass, $P_{\mu} = (P_t, P_r, P_{\theta}, P_{\phi})$ are,

$$P_t = E, \ , P_r = -\frac{r^2}{\Delta}\dot{r}, \ P_{\theta} = 0, \ P_{\phi} = -L \tag{5.3}$$

The overdot above represents the differentiation with respect to $\tau$, the proper time. The Lagrangian for the companion BH deduced from the metric of the central Kerr BH in the spherical polar coordinate $(t, r, \theta, \phi)$ and equatorial plane $(\dot{\theta} = 0)$ is given by,

$$\mathcal{L} = \frac{1}{2}\left[(1 - \frac{2M}{r})\dot{t}^2 + \frac{4aM}{r}\dot{t}\dot{\phi} - \frac{r^2}{\Delta}\dot{r}^2 - (r^2 + a^2 + \frac{2a^2M}{r})\dot{\phi}^2\right] \tag{5.4}$$

where $\Delta = r^2 - 2Mr + a^2$, $a$ is the Kerr parameter and $M$ denote the mass of the central BH. The Lagrangian is cyclic in $\phi$ and $t$, therefore we get the two constants of motion as, $E = (1 - \frac{2M}{r})\dot{t} + \frac{2aM}{r}\dot{\phi}$ & $L = -\frac{2aM}{r}\dot{t} + \left[r^2 + a^2 + \frac{2a^2M}{r}\right]\dot{\phi}$. Using the fact that $u^{\mu}u_{\mu} = 1$ with our choice of coordinate, we get the radial equation in terms of $\dot{t}$ and $\dot{\phi}$ as, $\dot{r}^2 = \frac{E\dot{t} - L\dot{\phi}}{r^2/\Delta} - \Delta/r^2$.

The term $\frac{dm}{d\tau}$ can be found from equation (5.2) as,

$$\begin{aligned} m^2 &= -P^\sigma P_\sigma \\ m^2 &= -g_{\sigma\nu}P^\sigma P^\nu \\ 2m\frac{dm}{d\tau} &= -\frac{d}{d\tau}[g_{\sigma\nu}P^\sigma P^\nu] \\ &= -[\frac{dg_{\sigma\nu}}{d\tau}P^\sigma P^\nu + g_{\sigma\nu}\frac{dP^\sigma}{d\tau}P^\nu + g_{\sigma\nu}P^\sigma\frac{dP^\nu}{d\tau}] \\ \frac{dm}{d\tau} &= -\frac{1}{2m}[\frac{dg_{\sigma\nu}}{d\tau}P^\sigma P^\nu + g_{\sigma\nu}\frac{dP^\sigma}{d\tau}P^\nu + g_{\sigma\nu}P^\sigma\frac{dP^\nu}{d\tau}] \end{aligned} \tag{5.5}$$

Now

$$\frac{dg_{\sigma\nu}}{d\tau} = \frac{\partial g_{\sigma\nu}}{\partial X^\lambda}.\frac{dX^\lambda}{d\tau} = g_{\sigma\nu,\lambda}u^\lambda \tag{5.6}$$

$\therefore$

$$\frac{dm}{d\tau} = -\frac{1}{2m}[g_{\sigma\nu,\lambda}u^\lambda P^\sigma P^\nu + 2g_{\sigma\nu}P^\nu\frac{dP^\sigma}{d\tau}] \tag{5.7}$$

So the acceleration is

$$\begin{aligned} \frac{du^\mu}{d\tau} &= \frac{1}{m}\frac{dp^\mu}{d\tau} + \frac{P^\mu}{m^2}\frac{1}{2m}[g_{\sigma\nu,\lambda}u^\lambda P^\sigma P^\nu + 2g_{\sigma\nu}P^\nu\frac{dP^\sigma}{d\tau}] \\ &= \frac{1}{m}\frac{dp^\mu}{d\tau} + \frac{P^\mu}{2m^3}[g_{\sigma\nu,\lambda}u^\lambda P^\sigma P^\nu] + \frac{1}{m^3}P^\mu P_\sigma\frac{dp^\sigma}{d\tau} \end{aligned} \tag{5.8}$$

$\therefore$

$$\frac{du^\mu}{d\tau} = \frac{1}{m}\frac{dp^\mu}{d\tau} + \frac{1}{m^3}P^\mu P_\sigma\frac{dp^\sigma}{d\tau} + \frac{P^\mu}{2m^3}[(g_{\sigma\nu,\lambda}u^\lambda)P^\sigma P^\nu] \tag{5.9}$$

The change in energy and angular momentum due to accretion can be obtained from the equation (3.28) which is,

$$\left.\frac{dP^\mu}{d\tau}\right|_{accr} = h_{enth}\frac{dm}{d\tau}u^\mu_{fluid} \tag{5.10}$$

From here we can write,

$$dP^\mu = \left.\frac{dP^\mu}{d\tau}\right|_{accr} \times d\tau \tag{5.11}$$

The new momentum after accreting then can be written as,

$$P'^\mu = P^\mu + dP^\mu \tag{5.12}$$

The normalization of 4-momentum gives $P^\mu.P_\mu = m^2$ then for the new momentum $P'^\mu.P'_\mu = m^2_{new}$. Here $m_{new} = m + dm$ denotes the new mass of the companion BH. From here, the new 4-velocity components can be found as follows:

$$u'^\mu = \frac{P'^\mu}{m_{new}} \tag{5.13}$$

Therefore, new specific energy is $E'_{sp} = u'_t$ and specific angular momentum $L'_{sp} = -u'_\phi$. The changes in energy and angular momentum then can be calculated as,

$$dE_{Accr} = E'_{sp} - E_{sp} \qquad dL_{Accr} = L'_{sp} - L_{sp}. \tag{5.14}$$

For the change in energy,

$$\begin{aligned}
dE_{Accr} &= E'_{sp} - E_{sp} \\
&= \frac{P_t}{m_{new}} - E_{sp} \\
&= \frac{1}{m_{new}} \left( g_{tt} P^t + g_{t\phi} P^\phi \right) - E_{sp} \\
&= \frac{1}{m_{new}} \left[ g_{tt} (P^t + h_{enth} \dot{m}_b u^t_{fluid} d\tau) + g_{t\phi} (P^\phi + h_{enth} \dot{m}_b u^\phi_{fluid} d\tau) \right] - E_{sp} \\
&= \frac{1}{m_{new}} \left[ g_{tt} (m u^t_{sat} + h_{enth} \dot{m}_b u^t_{fluid} d\tau) + g_{t\phi} (m u^\phi_{sat} + h_{enth} \dot{m}_b u^\phi_{fluid} d\tau) \right] - E_{sp} \\
&= \frac{1}{m_{new}} \left[ m u^{sat}_t + h_{enth} \dot{m}_b u^{fluid}_t d\tau \right] - E_{sp} \\
&= \frac{m}{m_{new}} E_{sp} + \frac{h_{enth} \dot{m}_b}{m_{new}} u^{fluid}_t d\tau - E_{sp} \\
&= E_{sp} \left[ \frac{m}{m_{new}} - 1 \right] + \frac{h_{enth} \dot{m}_b}{m_{new}} u^{fluid}_t d\tau \\
&= -\frac{dm}{m_{new}} E_{sp} + \frac{h_{enth} \dot{m}_b}{m_{new}} u^{fluid}_t d\tau
\end{aligned} \tag{5.15}$$

That gives,

$$dE_{Accr} = -\frac{dm}{m + dm} E + \frac{h_{enth} \left( \frac{dm}{d\tau} \right)}{m + dm} u^{fluid}_t d\tau \tag{5.16}$$

where $\dot{m}_b = \frac{dm}{d\tau}$ is obtained from equation (3.29). Similarly for the change in angular momentum for accretion is obtained as,

$$dL_{Accr} = -\left[ \frac{dm}{m + dm} L + \frac{h_{enth} \left( \frac{dm}{d\tau} \right)}{m + dm} u^{fluid}_\phi d\tau \right] \tag{5.17}$$

Rate of change of energy and angular momentum due to disk therefore can be found as,

$$
\begin{aligned}
\frac{dE}{dt} &= \frac{dE}{d\tau}.\frac{d\tau}{dt} \\
&= \frac{1}{u^t_{sat}}\frac{dE}{d\tau} \\
&= \frac{1}{u^t_{sat}}[\frac{dE}{d\tau}\Big|_{Acc} + \frac{dE}{d\tau}\Big|_{Def}] \\
&= \frac{1}{u^t_{sat}}[\frac{\partial E}{\partial u^\mu}\frac{\partial u^\mu}{\partial \tau}\Big|_{Acc} + \frac{\partial E}{\partial u^\mu}\frac{\partial u^\mu}{\partial \tau}\Big|_{Def}] \\
&= \frac{1}{u^t_{sat}}[\frac{\partial E}{\partial u^\mu}\frac{\partial}{\partial \tau}(\frac{P^\mu}{m})\Big|_{Acc} + \frac{\partial E}{\partial u^\mu}\frac{\partial}{\partial \tau}(\frac{P^\mu}{m})\Big|_{Def}] \\
&= \frac{1}{u^t_{sat}}[\frac{\partial E}{\partial u^\mu}(\frac{1}{m}\frac{dP^\mu}{d\tau} - \frac{P^\mu}{m^2}\frac{dm}{d\tau})\Big|_{Acc} + \frac{\partial E}{\partial u^\mu}(\frac{1}{m}\frac{dP^\mu}{d\tau})\Big|_{Def}] \\
&= \frac{1}{u^t_{sat}}[\frac{\partial E}{\partial u^\mu}(\frac{1}{m}\frac{dP^\mu}{d\tau}\Big|_{Acc} + \frac{1}{m}\frac{dP^\mu}{d\tau}\Big|_{Def}) - \frac{\partial E}{\partial u^\mu}\,(\frac{P^\mu}{m^2}\frac{dm}{d\tau})\Big|_{Acc}]
\end{aligned}
\tag{5.18}
$$

Therefore the final equation for rate of change of energy for disk effect is given by

$$
\frac{dE}{dt} = \frac{1}{u^t_{sat}}[\frac{\partial E}{\partial u^\mu}(\frac{1}{m}\frac{dP^\mu}{d\tau}\Big|_{Acc} + \frac{1}{m}\frac{dP^\mu}{d\tau}\Big|_{Def}) - \frac{\partial E}{\partial u^\mu}\,(\frac{P^\mu}{m^2}\frac{dm}{d\tau})\Big|_{Acc}] \tag{5.19}
$$

In similar way rate of change of angular momentum given by,

$$
\frac{dL}{dt} = \frac{1}{u^t_{sat}}[\frac{\partial L}{\partial u^\mu}(\frac{1}{m}\frac{dP^\mu}{d\tau}\Big|_{Acc} + \frac{1}{m}\frac{dP^\mu}{d\tau}\Big|_{Def}) - \frac{\partial L}{\partial u^\mu}\,(\frac{P^\mu}{m^2}\frac{dm}{d\tau})\Big|_{Acc}] \tag{5.20}
$$

We can calculate the mass of the companion BH exploiting the relation $P^\mu P_\mu = m^2$. As $P^\mu$ changes to $P'^\mu$, then the modified new momentum modifies the mass of the companion.

We can write,

$$
\begin{aligned}
m^2_{new} &= P'^\mu.P'_\mu \\
&= \left(P^t P_t + P^\phi P_\phi + P^r P_r\right) + 2h_{enth}\dot{m}_b\left(u^{fluid}_t P^t + u^{fluid}_\phi P^\phi + u^{fluid}_r P^r\right)d\tau \\
&+ h^2_{enth}\dot{m}_b\left(u^t_{fluid}u^{fluid}_t + u^\phi_{fluid}u^{fluid}_\phi + u^r_{fluid}u^{fluid}_r\right)(d\tau)^2 \\
&= m^2 + 2h_{enth}\dot{m}_b\left(u^{fluid}_t P^t + u^{fluid}_\phi P^\phi + u^{fluid}_r P^r\right)d\tau \\
&+ h^2_{enth}\dot{m}_b\left(u^t_{fluid}u^{fluid}_t + u^\phi_{fluid}u^{fluid}_\phi + u^r_{fluid}u^{fluid}_r\right)(d\tau)^2
\end{aligned}
$$

$$
\begin{aligned}
m_{new}^2 - m^2 &= 2h_{enth}\dot{m}_b \left(u_t^{fluid}u_{sat}^t + u_\phi^{fluid}u_{sat}^\phi + u_r^{fluid}u_{sat}^r\right) d\tau \\
&\quad + h_{enth}^2 \dot{m}_b (d\tau)^2, \quad \text{using } u^\mu.u_\mu = 1 \\
m_{new}^2 - m^2 &= 2h_{enth}\dot{m}_b\gamma d\tau + h_{enth}^2\dot{m}_b(d\tau)^2, \qquad \because \gamma = u_{fluid}.u_{sat} \\
(m_{new}+m)(m_{new}-m) &= 2h_{enth}\dot{m}_b\gamma d\tau + h_{enth}^2\dot{m}_b(d\tau)^2 \\
(2m+dm)dm &= 2h_{enth}\dot{m}_b\gamma d\tau + h_{enth}^2\dot{m}_b(d\tau)^2 \\
(dm)^2 + 2mdm - 2h_{enth}\dot{m}_b\gamma d\tau + h_{enth}^2\dot{m}_b(d\tau)^2 &= 0
\end{aligned}
\tag{5.21}
$$

This yields the estimated error in mass measurement of the companion BH if disk effect is neglected in the following from,

$$
dm = -m + \sqrt{m^2 + \left[2h_{enth}\left(\frac{dm}{d\tau}\right)\gamma d\tau + h_{enth}^2\left(\frac{dm}{d\tau}\right)^2 (d\tau)^2\right]}. \tag{5.22}
$$

Equation (5.22) provides the error in mass estimation of the companion BH. The term $\left(\frac{dm}{d\tau}\right)$ is the Bondi accretion rate and can be obtained from the equation (3.29) and $h_{enth}$ is the specific enthalpy of the accretion flow. In the presence of the accretion disk the four momentum of the companion BH decreases more rapidly compared to the cases when no environmental impact taken into consideration. The impact of the accretion disk drives the momentum loss faster and as a result the infall time becomes comparatively faster. This results in a different estimation of mass of the companion BH (eqn (5.2)). To accurately measure the companion BH mass in the presence of an accretion disk, the total momentum loss should be calculated using eqn (3.43) and then using the eqn (5.22).

Next we calculate the emitted gravitational wave strain and its amplitude. The estimation of the strain is required to calculate the error in mass estimation of the central SMBH.

## 5.3 Gravitational Wave Strain

The two gravitational wave polarization components may be stated as follows under the weak field approximation (source distance $D$ from us is on the order of Mpc) and low velocity limit (companion's velocity $v \ll c$) (see §1.3.1.8, equation (1.77)),

$$
h_+ = \frac{1}{D}\frac{G}{c^4}(\ddot{M}_{11} - \ddot{M}_{22}) \tag{5.23}
$$

$$
h_\times = \frac{1}{D}\frac{2G}{c^4}\ddot{M}_{12} \tag{5.24}
$$

where $\ddot{M}_{ij}$ is the double derivative w.r.t $t$ of the second mass moment (Maggiore, 2007). Here we didn't set $G = c = M = 1$ instead use explicitly the Newton Constant $G$, light speed $c$ and central black hole mass $M$.

which is given by,

$$
M_{ij} = \mu r^2 \begin{pmatrix} \cos^2\phi & \sin\phi\cos\phi \\ \sin\phi\cos\phi & \sin^2\phi \end{pmatrix} = \mu R(r)\Phi(\phi) \tag{5.25}
$$

for the GW propagating along $z$ axis, where $\mu = mM/(m+M)$ is the reduced mass of the binary black hole system.

Thus we have,

$$\begin{aligned} M_{11} &= \mu r^2 \cos^2\phi \\ M_{12} &= \mu r^2 \sin\phi\cos\phi \\ M_{22} &= \mu r^2 \sin^2\phi \end{aligned} \tag{5.26}$$

In general we can write the above equation as,

$$M_{ij} = \mu R(r)\Phi(\phi) \tag{5.27}$$

and

$$\ddot{M} = \mu\left[\ddot{R}\Phi + 2\dot{R}\Phi'\dot{\phi} + R\Phi''\dot{\phi}^2 + R\Phi'\ddot{\phi}\right] \tag{5.28}$$

where $\Phi' = \frac{d\Phi}{d\phi}, \dot{\phi} = \frac{d\phi}{dt}$ and $\dot{R} = \frac{dR}{dt}$ Using these we get,

$$\begin{aligned} (\ddot{M}_{11} - \ddot{M}_{22}) &= \mu\left[(\ddot{R} - 4R\dot{\phi}^2)\cos 2\phi - (4\dot{R}\dot{\phi} + 2R\ddot{\phi})\sin 2\phi\right] \\ &= \mu\left[A\cos 2\phi - B\sin 2\phi\right] \end{aligned} \tag{5.29}$$

and

$$\begin{aligned} 2\ddot{M}_{12} &= \mu\left[(\ddot{R} - 4R\dot{\phi}^2)\sin 2\phi + (4\dot{R}\dot{\phi} + 2R\ddot{\phi})\cos 2\phi\right] \\ &= \mu\left[A\sin 2\phi + B\cos 2\phi\right] \end{aligned} \tag{5.30}$$

Using values of $\ddot{M}_{ij}$ and using the geodesic equations for $\dot{r}$, $\dot{t}$, $\dot{\phi}$ we get,

$$h_+ = \frac{\mu}{D}\frac{G}{c^4}(A\cos 2\phi - B\sin 2\phi) \tag{5.31}$$

$$h_\times = \frac{\mu}{D}\frac{G}{c^4}(A\sin 2\phi + B\cos 2\phi) \tag{5.32}$$

Here $A = (\ddot{R} - 4R\dot{\Phi}^2)$ and $B = 4\dot{R}\dot{\Phi} + 2R\ddot{\Phi}$. The maximum amplitude ($h$) can therefore be obtained from equations (5.31) and (5.32) in the form given by,

$$h = \mu\sqrt{A^2 + B^2} \tag{5.33}$$

Equations (5.23) & (5.24) are the leading order formulation of the GW waveform (up to the order of $\frac{v^2}{c^2}$) and are appropriate for long distances. Higher-order correction terms are required to provide a more precise waveform in the strong-field limit (especially close to ISCO). But the factors are at least one order of magnitude less than the leading order terms, and they are probably

far weaker than the disk's influence, as shown by a few recent studies (Zwick et al., 2023). We just focus on the leading-order analysis in this instance.

## 5.4 Error in estimation of central BH mass

In the presence of a disk, the total momentum loss changes. In this situation, the orbital radius decays more quickly than in the absence of an accretion disk because the companion black hole is losing more energy. The infall time consequently drops significantly. Therefore, the presence of the accretion disk in the EMRI system changes the strain amplitude of the emitted GW signal. The amount of change $dh$ depends on the hydrodynamic choice of the model of the disk, i.e., different accretion disk models induce different amounts of changes in strain- sometimes within the detectable range and sometimes insignificant to detect. If this change in strain is detectable but not taken into account, the estimate of the BH mass will be incorrect. Till now, the GW template has been developed in vacuum, that is, without taking into account any accretion disk surrounding the central compact object, and the observed GW data are compared with it. As a result, the mass parameters calculated from the observed data will be measured incorrectly. The error in the estimation of central BH mass can be obtained from

$$dh = \frac{\partial h}{\partial M} dM \tag{5.34}$$

One can determine the inaccuracy in the mass measurement $\frac{dM}{M}$ for the central BH by estimating the dimensionless parameter $\frac{dh}{h}$ that results from the accretion disk. In section §5.2, the secondary BH mass change with disk is already estimated. This therefore enables us to precisely restrict the BH parameters and explore the accretion disk using the GW signal. To calculate the $\frac{dh}{h}$, and therefore the error estimation in the central black hole mass, let us consider the equation (5.33) here,

$$h = \mu\sqrt{A^2 + B^2}$$

$\mu$ is the reduced mass of the EMRI system which is given by,

$$\begin{aligned} \mu &= \frac{Mm}{M+m} \\ \frac{d\mu}{\mu} &= (\frac{1}{M} - \frac{1}{M+m})dM \\ \frac{d\mu}{\mu} &= \frac{m}{M+m} dM \end{aligned} \tag{5.35}$$

$$
\begin{aligned}
\frac{dh}{h} &= \frac{d\mu}{\mu} + \frac{AdA + BdB}{A^2 + B^2} \\
\frac{dh}{h} &= (\frac{1}{M} - \frac{1}{M+m})dM + \frac{A.A_M + B.B_M}{A^2 + B^2}dM \qquad \text{Using eqn (5.35)} \\
dM &= \frac{(\frac{dh}{h})}{[(\frac{m}{M+m}) + \frac{A.A_M + B.B_M}{A^2+B^2}]} \\
dM &= \frac{dh}{\mu[\sqrt{A^2+B^2}(\frac{m}{M+m}) + \frac{A.A_M + B.B_M}{\sqrt{A^2+B^2}}]}
\end{aligned}
\tag{5.36}
$$

Here suffix $M$ denote derivative w.r.t M. The derivatives of the variables $A$ and $B$ are given by,

$$
\begin{aligned}
A &= \ddot{R} - 4R\dot{\phi}^2 \\
A_M &= \ddot{R}_M - 8R\dot{\phi}\dot{\phi}_M \\
&= 2[r\ddot{r}_M + 2\dot{r}\dot{r}_M - 4r^2\dot{\phi}\dot{\phi}_M]
\end{aligned}
\tag{5.37}
$$

$$
\begin{aligned}
B &= 4\dot{R}\dot{\phi} + 2R\ddot{\phi} \\
B_M &= 4\dot{R}_M\dot{\phi} + 4\dot{R}\dot{\phi}_M + 2R\ddot{\phi}_M \\
&= 2[4r\dot{r}_M\dot{\phi} + 4r\dot{r}\dot{\phi}_M + r^2\ddot{\phi}_M]
\end{aligned}
\tag{5.38}
$$

We have $R = r^2$, $\dot{R} = 2r\dot{r}$, $\ddot{R} = 2r\ddot{r} + 2\dot{r}^2$. The derivatives are given in Appendix C. The gravitational wave strain released by a system with an accretion disk is not the same as the strain released by a system that stays in the vacuum domain. Since the companion's orbital motion get modified in the presence of an accretion disk, the values of $\dot{r}$, $\ddot{r}$, $\dot{\phi}$ & $\ddot{\phi}$ also get modified. Therefore the values defined in eqns (5.37) & (5.38) are different in the presence of an accretion disk. The respective value of GW strain (eqn (5.33)) therefore also get modified. The differences could be estimated by calculating the differences in the strain amplitudes i.e., $|h_{\text{No-disk}}| - |h_{\text{With-disk}}|$ and the phase differences i.e., $\delta\phi$ (§4.4). Once the differences in strain is obtained, by estimating the reduced mass of the system one could obtain the error in mass estimation of the central SMBH from the equation (5.36).

Estimation of the characteristics strain of the emitted GW can be used to estimate the error in the chirp mass calculation and can be obtained from the signal-to-noise-ratio (SNR) of the chirp mass of the EMRIs. We discuss these in the following section.

## 5.5 Error estimation in chirp mass using SNR

The presence of an accretion disk alters the frequency evolution rate of the binary system, which in turn affects the chirp mass. In the scenario where disks exist, the apparent chirp mass can be written as,

$$\mathcal{M}_{disk} = \mathcal{M}_{vac}\left(1 + \frac{\dot{r}_{disk}}{\dot{r}_{GW}}\right)^{\frac{3}{5}} \tag{5.39}$$

where $\mathcal{M}_{vac} = \frac{(M^2 q)^{3/5}}{M_{total}^{1/5}}$ is the chirp mass for the binary system in vacuum, $\dot{r}_{disk}$ & $\dot{r}_{GW}$ are the respective inspiral rates. $q = \frac{m}{M}$ is the mass ratio, $M$ denote the central black hole mass, $m$ companion mass and $M_{total} = m + M$

The SNR-weighted apparent chirp mass between two frequencies is given by (Cutler & Vallisneri, 2007; Garg et al., 2022),

$$\mathcal{M}_{disk} = \sqrt{\frac{2.4\int_{f_{min}}^{f_{max}} df \frac{h_c^2(f)}{S_n(f)f^2}\mathcal{M}_{disk}^2(f)}{2.4\int_{f_{min}}^{f_{max}} df \frac{h_c^2(f)}{S_n(f)f^2}}} \tag{5.40}$$

and the respective bias in chirp mass can be obtained by using,

$$\Delta M = \frac{\mathcal{M}_{disk} - \mathcal{M}_{vac}}{\sigma_M} \tag{5.41}$$

where

$$\sigma_M^{-2} = 2.4\int_{f_{min}}^{f_{max}} df \left(\frac{5}{3}\right)^2 \frac{h_c^2(f)}{S_n(f)f^2}\frac{1}{\mathcal{M}_{vac}^2} \tag{5.42}$$

For a significant value of the bias i.e. detectable imprint is only be found in the presence of an accretion disk if the $\mathcal{M}_{disk}$ is $2\sigma_M$ away from $\mathcal{M}_{vac}$ (Garg et al., 2022).

## 5.6 Results and Discussions

The extreme mass ratio inspiral (EMR) has been identified by scientists as one of the major objectives for the planned launch of the space-based gravitational wave detector LISA, whose frequency range is low (between $0.1mHz - 1Hz$). In this study, we investigate an EMRI in which the companion Kerr black hole of mass $m = 10^{2-6}M_\odot$ is moving through the central Kerr black hole of mass $M = 10^{6-8}M_\odot$, which is surrounded by an accretion disk. In the presence of an accretion disk in an EMRI, we examine the change in mass rate with various parameters while taking into account the pure Kerr potential and applying general relativity. We take into account various elliptical orbits and alter the mass accretion rate to determine whether the disk has any discernible impact on such systems. We further alter the central Kerr BH's spin while examining the development of various orbits with regard to eccentricity, perihelion, and aphelion radii. The comparison of different accretion disk effects, e.g., self-accretion and deflection, is also done for different orbital parameters and spin parameters. We also examine the companion black hole's change in mass as a result of its own self-accretion, and we display this data for various primary accretion rates. It's interesting to note that the GW signals carry a signature of the hydrodynamic characteristics of the accretion disk through the companion's motion. In the precisional era, future space-based detector LISA with greater sensitivity will be able to identify the disk's systematic impact on EMRI. Thus, we conclude by talking about the strain (amplitude) of the GW produced by this EMRI system. The signal-to-noise ratio (SNR) of the emitted GW strain from such

systems is also discussed, along with their detection probability within the specified frequency range of the LISA.

### 5.6.1 Error estimation of companions BH mass

As we consider that an accretion disk is embedded in an EMRI, surrounding the central SMBH, the companion black hole, which is totally engulfed in the accretion disk, begins spherically accreting in its presence, as discussed in §5.2. The mass of the companion black hole grows due to self-accretion. Figure 5.1 depicts the change in mass with time and orbital radius for various orbits with different parameters. The upper panel of the picture depicts the variation with regard to time ($T$), while the lower panel depicts the variation with respect to the perihelion radius ($r_P$). Change in mass vs. time for three distinct orbits with eccentricities $e = 0.50$ (*dash line*), $e = 0.25$ (*dot line*), and $e = 0.15$ (*solid line*) are depicted in panel (a). Panel (e) shows a similar figure but with the perihelion radius changed. Both panels show that the change in mass is greater for lower eccentric orbits. According to much research, extremely eccentric EMRIs have a higher event rate than low-eccentric EMRIs. We show the change for several Kerr parameters relative to time and $r_P$ in panels (b) & (f), respectively. Plots for $a = 0.0$ (*solid line*), $a = 0.50$ (*dot line*), $a = 0.75$ (*dash line*), $a = 0.95$ (*dot-dash line*), and $a = 0.999$ (*dot dot dash line*) are each displayed in a separate panel. The change in mass rate increases along with the rising rotational parameters ($a$). We plot the change in mass with respect to time and $r_P$ for the mass accretion rates $\dot{m} = 0.1$ (*solid line*) and $\dot{m} = 1$ (*dash line*) in panels (c) and (g). The variation of change in mass with respect to time for mass accretion rates $\dot{m} = 1$ (*solid line*) and $\dot{m} = 10$ (*dot line*) is displayed in panel (d). We plot the change in mass vs. $r_P$ for the $\dot{m} = 10$ (*solid line*) and $\dot{m} = 100$ (*dash line*) variables, respectively, in panel (h). We can observe from this entire graphic that a high accretion rate implies a companion black hole's mass will vary more with increasing time and decreasing $r_P$. The rate of change in mass of the companion black hole owing to the accretion disk varies with the accretion rate. A thin accretion disk accretes at 1 Eddington rate, an optically thin ADAF accretes at sub-Eddington rate, and a slim disk model accretes at super-Eddington rate. As a result, the change in mass of the companion black hole may likewise be utilized to identify the accretion disk model. Despite the fact that we acquire stronger impacts of hydrodynamic drag on EMRIs with lower eccentricity, numerous studies have demonstrated that the event rate of highly eccentric EMRIs is greater than that of low eccentric EMRIs (Amaro-Seoane et al., 2015).

### 5.6.2 Modified GW-Strain

Figure 5.2 depicts the GW strain, including disk effects. Our findings show that over time, the effect of the accretion disk becomes strong enough to be recognized. We depict the GW strains in terms of $D/\mu$, where $D$ is the source's distance and $\mu$ is the binary system's reduced mass. We display the GW polarization amplitudes $h_+$ (*red line*) and $h_\times$ (*blue line*) with $\chi$ (panel (a)) in the presence of an accretion disk in the first panel. The amplitude of GW strain put out from an E/IMRI system in the presence and absence of the disk is displayed in panel (b). In this figure, the two appear to lie on top of each other; therefore, we plot $dh$ to examine the differences with $\chi$, as shown in panel (c). This graph demonstrates that the difference in strain amplitudes is sinusoidal. The maximum strain amplitude ($|h|$) for disk and no disk with orbital radius $r_P$ is illustrated in

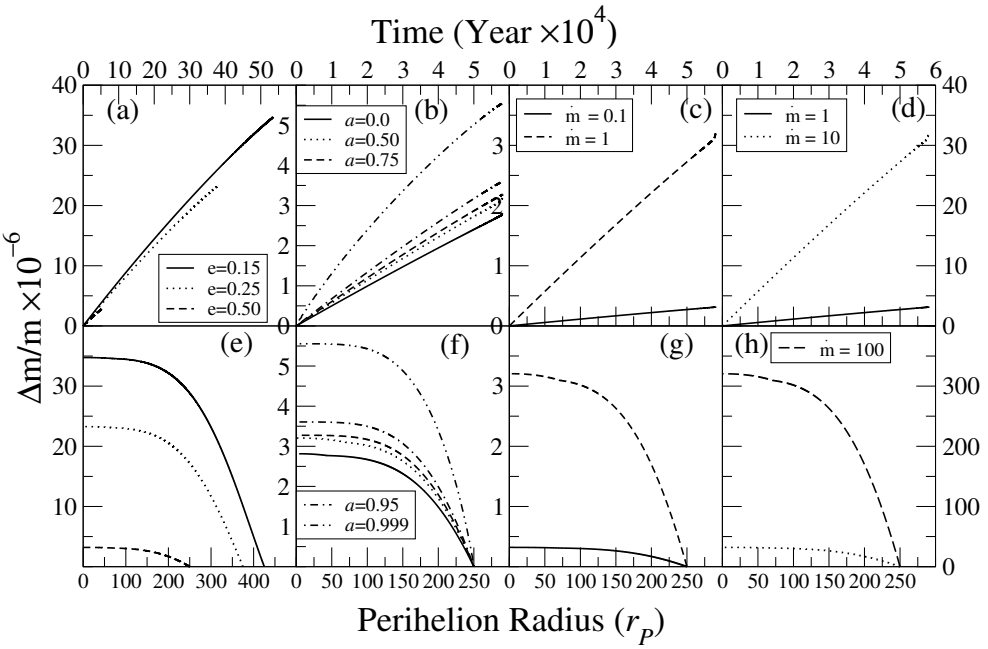


**Figure 5.1:** Initial parameters : $X = 500r_g$. We display the change in mass of a companion black hole as it moves through an accretion disk against time ($T$) and perihelion radius ($r_P$) (upper and bottom panels). The rate of change in mass rises as it approaches the horizon. We compare three orbits with initial eccentricities of $e = 0.15$ (*solid line*), $e = 0.25$ (*dot line*) and $e = 0.50$ (*dash line*) in the extreme left two panels (upper and lower). A low eccentric orbit has a greater change in mass rate. Following that, in the top and bottom panels, we display mass rate versus time and $r_P$ for various Kerr values. The plot is given in both panels for $a = 0.0$ *solid line*, $a = 0.50$ (*dot line*), $a = 0.75$ (*dash line*), $a = 0.95$ (*dot-dash line*), $a = 0.999$ (*dot dot dash line*). The change in mass rate rises as the rotation parameters ($a$) increase. We depict the change in mass vs. time and $r_P$ for the mass accretion rates $\dot{m} = 0.1$ (*solid line*) and $\dot{m} = 1$ (*dash line*) in the upper and lower third panels. The variation of change in mass w.r.t time for mass accretion rates $\dot{m} = 1$ (*solid line*) and $\dot{m} = 10$ (*dot line*) is depicted in the uppermost right panel. In the lower rightmost panel, we depict change in mass versus $r_P$ for $\dot{m} = 10$ (*solid line*) and $\dot{m} = 100$ (*dash line*), respectively. We can observe from this image that a high accretion rate implies a greater change in the mass of the companion black hole with rising time and decreasing $r_P$.

panel (d), where initial $r_P = 100r_g$. We zoomed in to observe the differences and plotted the same thing in panel (e). There are noticeable variations in the strain released by a system with and without a disk. The strain amplitude emitted by a system with a disk is indicated by a *magenta line*, while that of a system without a disk is illustrated by a *green line*. $r_P = 50r_g$, where $r_g$ is the Schwarzchild radius, is the parameter used to plot the GW strain in panels (a), (b), and (c).

#### 5.6.2.1 Error Estimation of central BH mass

Figure 5.3 depicts the change in GW strain $dh/h$ (lower panel) and the accompanying change in the calculation of central black hole mass $\Delta M/M$ (upper panel) with $\chi$. We discovered that the GW strain differs from the strain emitted by a diskless system in the presence of an accretion disk (see figure 5.2). We discover that the discrepancy in the strain signal is large enough to change the mass estimation of the central BH. The graphic shows that the estimated inaccuracy of central BH mass changes sinusoidally with a sinusoidal change in strain. Considering an E/IMRI system with no environmental impact leads to a different mass calculation of the component BHs. The error $\Delta M$ or $\Delta m$, which emerges as a result of disk existence, can be spread throughout the

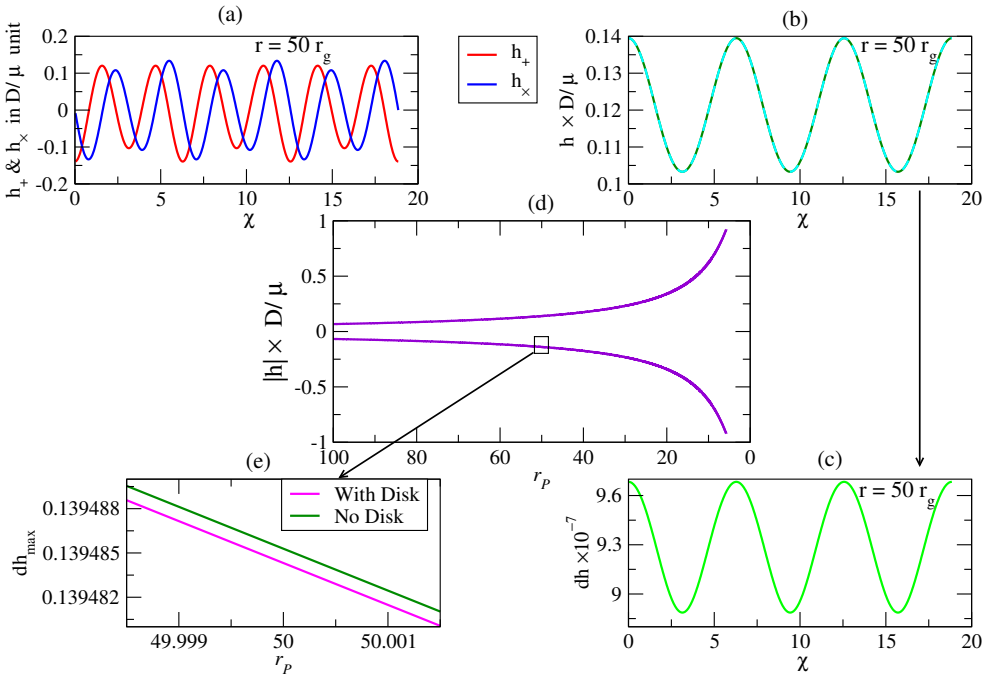


**Figure 5.2:** In this figure, we present the amplitude of the emitted GW as well as the $h_+$ and $h_\times$ polarizations, as well as the strain differences in terms of $\frac{D}{\mu}$ for the two instances of disk and no disk. Here, $D$ is the source distance and $\mu$ is the system's reduced mass. The GW polarization amplitudes $h_+$ (*red line*) and $h_\times$ (*blue line*) with $\chi$ are displayed in panel (a). The GW amplitude is shown in panel (b) for disk and no disk scenarios. Panel (c) depicts the variations between the two examples depicted in panel (b). This graph demonstrates that the difference in strain amplitudes is sinusoidal. We plot (a), (b), and (c) with $r_P = 50r_g$ where $r_g$ is the Schwarzchild radius. The maximum strain amplitude ($|h|$) for disk and no disk with orbital radius $r_P$ is plotted in panel (d). Panel (e) is a zoomed-in version of panel (d), with a clear distinction between disk and no disk. The strain amplitude with disk is shown by a *magenta line*, and the strain amplitude without disk is represented by a *green line*.

BH's mass, regardless of whether their original mass is something else. To remove these errors in parameter estimation, the impact of the environment, namely the effect of the accretion disk, must be considered.

## 5.7 Conclusion

For the space-based detector LISA, we have seen so far that Extreme mass ratio inspiral (EMRIs) are among the most intriguing potential sources of gravitational radiation. For an accretion disk embedded EMRI system, using the space time of a spinning BH, our work has demonstrated how the impact of accretion provides a mass measurement constraints on the BH companions of the EMRIs from the observation of GW. The normalizing condition of the four momentum yields the constraint on the companion BH mass. This estimate is dependent on the initial mass of the companion black hole, its specific enthalpy, accretion rates, and the time in its rest frame. The companion black hole had more energy and angular momentum losses and subsequently experienced a faster coalescence in the presence of an accretion disk (Chapter 3). As a result, the momentum loss rates from the vacuum premises are modified. The study investigates the mass error estimation of companion BHs by adjusting factors like eccentricity, Kerr parameters, and accretion rate. Lower eccentric orbits lose more energy and angular momentum, leading to higher

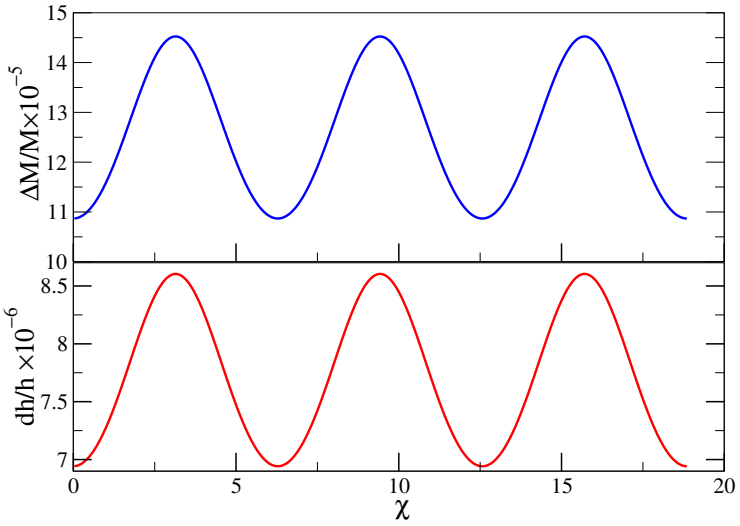


**Figure 5.3:** In this graph, we demonstrate the variation of $\frac{dh}{h}$ and $\frac{\Delta M}{M}$ with $\chi$. The upper panel depicts the variation in strain, while the lower panel depicts the related variations in the central black hole's mass.

mass rate changes. Higher spin values of the central SMBH also result in greater mass estimate changes. The reliance on mass accretion rate varies proportionately, increasing the error in the companion's mass assessment with increasing $\dot{m}$.

Modifications in the infall time results in a modification to the emitted GW strain in the presence of the disk. We estimate this 'new' strain of the GW in this modified scenario. The differences appears in the amplitude of the 'new' strain modifies the estimation of the central SMBH mass. We found that the discrepancy in the strain signal is large enough in the presence of the disk, to change the mass estimation of the central BH. In our work we obtain that the estimated inaccuracy of central BH mass changes sinusoidally with a sinusoidal changes in the estimated GW strain.

The error estimation of the companion BH also get impacted by the choice of the orbital parameters. For an optimal set of orbital parameters, the constrain on masses can be obtained more accurately as these set of parameters would offered the maximal SNR required for observations. We see through SNR calculations that these changes are detectable, and hence these results need to be incorporated into the modified GW waveform to constrain the black hole mass parameters accurately.

# Chapter 6

# Vertical Equilibrium Model for Accretion flow

### 6.0.1 Motivation

Accretion disks are common in astrophysical systems, and in addition to that, the accretion process is also the primary source of electromagnetic radiation observed in some circumstances, making it an essential component of astrophysics. The disk is typically viewed as a flattened two-dimensional object in accretion flow studies, which imply the suppression of the vertical degrees of freedom (direction perpendicular to the disk plane). Furthermore, due to the presence of axisymmetry, the flow variables eventually become a function of only radial and time coordinates, resulting in massive simplifications of the fluid dynamical equations. The detected radiation, however, interacts closely with the disk atmosphere in a vertical direction before it reaches the observer since it is all emitted perpendicular to the disk's plane. As a result, understanding the 2D structure alone is insufficient to properly extract spectroscopic data from the detected radiation (Hubeny, 1990; Hubeny & Hubeny, 1997, 1998; Fukue, 2020). Solving the general relativistic fluid dynamical equations in the background metric of the compact object in $3+1$ dimensions is the best strategy for tackling this issue. This is a challenging endeavor, and there is still a lot to be performed in this area through analytical and numerical investigations. However, an effective approximation method, called the vertical equilibrium model, may be used to represent the 3-D structure of the disk when the vertical expansion of the disk is considerably lower than its radial size and when the outflow rate is minimal in comparison to the overall accretion rate. In the model of vertical equilibrium, it is assumed that the disk has a finite thickness and that the flow is constrained to the area between $-H \;\; to \;\; +H$ in the vertical direction, where $H(r) << r$ is referred to as the local disk height. As a result, the total mass flux $\dot{M}$ may be expressed as a function of $H$, $r$, and the flow variables. Considering a suitable flow model for the vertical direction (a static or dynamic equilibrium), one can then find another relation of $H$ as a function of $r$ and flow variables. It is possible to reduce the $z$-degree of freedom and change the $3D$ problem to $2D$ by using these two equations.

We found that the renowned mass flow formula $\dot{M} = 2\pi r H \rho u^r$, employed in the usual study of the accretion process around compact objects ((Sądowski et al., 2011; Beloborodov, 1998; Peitz & Appl, 1997; Chakrabarti, 1996a)), is not compatible with the continuity equation, and numerous attempts ((Novikov & Thorne, 1973; Abramowicz et al., 1996)) to modify it have been attempted. However, as previously noted, various research (Shakura & Sunyaev, 1973; Novikov & Thorne, 1973; Riffert & Herold, 1995; Abramowicz et al., 1997; Gammie & Popham, 1998; Peitz & Appl, 1997; Kim et al., 2019) have attempted to solve this problem, but a comprehensive general relativistic formulation of the accretion rate is still not available, which might be used

when solving the hydrodynamical equations of the accretion flows.

In these circumstances, we revisit this issue. We present a new relativistic way of obtaining the mass flow formula in the context of curved space-time. We begin with the fluid's total general relativistic energy-momentum tensor. By contracting the energy-momentum tensor with the Killing vectors, we discovered two conserved quantities by utilizing the Killing symmetry of space-time. We use an integral equation to relate the vertical height to the accretion rate by integrating the four-divergence of the conserved quantities. The result is then represented in terms of the accretion rate and flow parameters. Numerous observations show that the spectral states vary with the accretion rate, and it has been discovered that the disk height is directly dependent on the accretion rate. Compared to other thin and slim disk techniques, our analysis is self-consistent and mathematically rigorous. It is worth noting that previous observational investigations of BH/NS binaries have shown a time-dependent cyclic variation of spectral parameter known as accretion hysteresis (Esin et al., 1997; Homan & Belloni, 2005; McClintock & Remillard, 2006; Remillard & McClintock, 2006), and no single model can explain all of the observed spectral states. Therefore, it is crucial to understand the relationship between vertical height and accretion rates in order to deduce information about the observed spectral features.

### 6.0.2 Importance of proper modeling of disk vertical structure in Gravitational wave Physics

As previously stated, knowing the vertical structure of the accretion disk is of the utmost importance for solving the entire hydrodynamical solution. Aside from that, the companion travels vertically across the disk in the context of an inclined orbit of the companion in a binary black hole system embedded in an accretion disk. Therefore, in such a scenario, one also has to know the accurate vertical structure of the accretion disk model and the variation of other flow variables in the vertical direction in order to determine the appropriate hydrodynamical drag impact on the companion. This precision would lead to a more accurate assessment of the drag effect on the emitted GW signal.

### 6.0.3 Previous study on vertical height of the accretion disk

To describe the accretion flow around the black hole in the vertical direction, the flow is considered to be in hydrostatic equilibrium in the vertical direction. We already discussed various accretion disk models in the earlier section with details. Several developments have been made using the vertical Euler equation (equation (2.49)). Here we briefly discuss only the vertical height of those renowned results. Shakura and Sunyaev presented the classic model of accretion flow for geometrically thin and optically thick accretion disks in 1973 (SS73) ((Shakura & Sunyaev, 1973)). The disk is frequently used for defining the high or soft state. This radiatively efficient disk cools down by emitting as a black body locally. The angular momentum of such a flow is locally Keplerian, and the flow's accretion rate ($\dot{M}$) is determined by the position of the innermost stable circular orbit and is given by,

$$\dot{M}\omega R^2 = -2\pi W_{r\phi} R^2 + C \tag{6.1}$$

Here, the stress $W_{r\phi} = 0$ in the last stable orbit is utilized to get the constant $C$. Vertical changes of quantities have been neglected in the SS73 disk model, and the formula for disk height in terms of the $\dot{M}$ is given. This yields a height expression for the disk's inner region, which is dominated by radiation pressure, and $\dot{m} = \frac{\dot{M}}{\dot{M}_{cr}}$ and $m = \frac{M}{M_\odot}$ are used in this case to obtain,

$$H[cm] = 3.2.10^6 \dot{m} m (1 - r^{-1/2}). \tag{6.2}$$

In the middle region, gas pressure dominates, and the variation of the disk height is given by:

$$H = 1.2 \times 10^4 \alpha^{-1/10} \dot{m}^{1/5} m^{9/10} r^{21/20} (1 - r^{-1/2})^{1/5} \tag{6.3}$$

In contrast, the disk height in the outer region is

$$H = 6.1 \times 10^3 \alpha^{-1/10} \dot{m}^{3/20} m^{9/10} r^{9/8} (1 - r^{-1/2})^{3/20} \tag{6.4}$$

We find that, although not always proportionate, the vertical height is dependent on the accretion rate. Together with the temperature, density, and radial velocity of the flows, the vertical height likewise varies with those factors. The SS73 disk effectively characterizes the high/soft state but fails short of representing the other spectral states. Other flow models exist to explain spectral states other than high/soft; for example, the optically thin ADAF model may well characterize low/hard and quiescence states. However, in the case of these accretion disk models, no unique height prescription is applied. In the literature, there are numerous models for estimating disk height. Among them, two prescriptions are commonly used: the NT73 height prescription, which is applied to thin accretion disks and is used to study the soft state of Cyg X-1, GRO J1655-40, GRS 1915+105 (Zhang et al., 1997), transient X-ray sources H1743-322 and XTE J1550-564 (Li et al., 2005), etc.; and the ALP height prescription for the slim disk, which is used to describe binary black holes such as LMC X-3 (Straub et al., 2011), low mass X-ray binary 4U 1630-47 (Abe et al., 2004), black hole binary with super-luminal jet, XTE J1550-564 (Kubota & Makishima, 2004), etc. in order to explain the high luminous spectral states. Novikov and Thorne gave the first relativistic method of determining disk height after SS73. In the vertical direction, NT73 took into account disk materials in hydrostatic equilibrium. The influence of centrifugal and Coriolis forces on the vertical structure is zero in a frame that is co-rotating locally with the disk, which is represented by the tetrad $e_{\hat{t}}$, $e_{\hat{r}}$, $e_{\hat{z}}$, $e_{\hat{\phi}}$. As a result, the frame operates as an orbiting inertial frame. In this frame, the tidal gravitational acceleration is given as $g \equiv R^{\hat{z}}_{\hat{o}_{\hat{z}}\hat{o}^z}$, where $R^{\hat{z}}_{\hat{o}_{\hat{z}}\hat{o}^z}$ can be obtained by transformation of the local non-inertial frame components $R^{(\alpha)}_{(\beta)(\gamma)(\delta)}$ of the Riemann tensor (Bardeen et al., 1972; Fishbone, 1973). The vertical equilibrium equation can be found by taking into account the balance of gravity and pressure forces in the vertical direction as follows:

$$\frac{dp}{dz} = \rho_0 g \tag{6.5}$$

It should be noted that while the pressure force in the non-relativistic Newtonian framework is given by the LHS of the equation, $g$ in the RHS of the equation does not represent the Newtonian gravitational acceleration. This method is therefore semi-relativistic. Disk height is given from

this as

$$H = \sqrt{P/\rho_0}\sqrt{r^3/M}\sqrt{\frac{(r^2+a^2)^2-\Delta a^2}{\gamma^2((r^2+a^2)^2+2\Delta a^2)}} \tag{6.6}$$

where $\gamma = \frac{r^2-2Mr\pm a(Mr)^{1/2}}{r[r^2-3Mr\pm 2a(Mr)^{1/2}]^{1/2}}$. The model has been widely used by several authors even though $\gamma$ diverges when $[r^2-3Mr\pm 2a(Mr)^{1/2}]=0$, i.e., at ISCO. In this approach, the relation between the vertical height and mass flux for a geometrically thin disk is given by:

$$\dot{M}_0 = -2\pi r\Sigma\overline{v}^{\hat{r}}\mathcal{D}^{1/2} \tag{6.7}$$

where $\mathcal{D} = 1-\frac{2}{r_*}+\frac{a_*^2}{r_*^2}$, $r_* = \frac{r}{M}$ and $a_* = \frac{a}{M}$, surface density $\Sigma = \int_{-H}^{H}\rho_0 dz = 2\langle\rho_0\rangle H$ and mass-average radial velocity $\overline{v}^{\hat{r}} = \frac{1}{\Sigma}\int_{-h}^{h}\langle v^{\hat{r}}\rho_0\rangle dz$. Here, height is directly proportional to the mass flux. The effect of the geometry of the curved space-time is included in the term $\mathcal{D}$.

Several authors have addressed the practical problem of NT73, which is that $\gamma$ diverges at ISCO (Riffert & Herold (1995) (RH) Lasota (1994) and Abramowicz et al. (1996)(ACGL)). RH uses the hydrostatic equilibrium to obtain a correction for the thin disk model of NT73, expanding the metric coefficient up to the second-order of $(\frac{z}{r})^2$ in order to prevent the divergent character of height. The outcome yields a lowered disk height, which is expressed as,

$$H \equiv 2\sqrt{\frac{P(0)}{\rho(0)}}\sqrt{\frac{r^3}{M}}\sqrt{\frac{B}{C}} \tag{6.8}$$

where $B = 1-\frac{3M}{r}+\frac{2a\sqrt{M}}{r^{3/2}}$, $C = 1-\frac{4a\sqrt{M}}{r^{3/2}}+\frac{3a^2}{r^2}$, and the associated mass accretion rate is found as $\dot{M} = -4\pi Hr\rho U^2$ where $\mathbf{U} = (U^0, U^1, U^2, 0)$ and $\rho$ is the rest mass density.

The divergent nature of the height expression is preserved at ISCO despite the fact that this vertical height of the thin disk model is applied to numerous quasars, AGN for the soft-X-ray spectra (Brunner et al., 1997; Hubeny & Hubeny, 1997), and eruptions of X-ray novae Monocerotis 1975 (A 0620-00) and X-ray nova Muscae 1991 (GRS 1124-68) (Suleimanov et al., 2008). To avoid this issue, users typically truncate the disk's inner edge at ISCO. The fundamental issue with NT73 is that it is a hybrid model, meaning that gravity is replaced by a geodesic deviation force in place of a relativistic framework when discussing fluid dynamics. Consequently, no mathematically sound approximation scheme can be used to obtain the pressure balance equation of NT73 from the original relativistic fluid dynamical equation. Therefore, a complete general relativistic fluid dynamical method with physically meaningful and mathematically consistent approximation techniques is required to identify the real solution to the problem. Many authors have attempted to find the same along these lines. ALP has performed the first thorough derivation utilizing a full fluid dynamical approach. With the assumption of a quasi-spherical coordinate and the series expansion of relativistic hydrodynamic equations, ALP computed the vertical structure of the thin and slim disk surrounding a Kerr black hole as,

$$-2\frac{P_0}{\rho}+(\frac{H}{R})^2(\frac{1}{R^2})(\mathcal{L}_*^2+u_1^2-\Delta V_0\frac{du_1}{dR}) = 0 \tag{6.9}$$

where, $\mathcal{L}_*^2 = \mathcal{L}^2-a^2(\mathcal{E}^2-1)$, $\mathcal{L}$ and $\mathcal{E}$ are respectively the conserved angular momentum and conserved energy. Using the expression for $H$, the mass accretion rate is considered as Abramowicz

et al. (1996),

$$\dot{M} = -2\pi\Delta^{1/2}\Sigma\frac{V}{\sqrt{1-V^2}} = -2\pi\Delta^{1/2}(2H\rho)\frac{V}{\sqrt{1-V^2}} \tag{6.10}$$

The solution up to the black hole horizon is given by this disk model. According to this solution, the disk thickness is supposed to rise with increasing accretion rate, and $\frac{H}{R} \ll 1$ is likewise satisfied everywhere. For relativistic thin and slim accretion processes, the ALP finding is commonly used since it is universally recognized.

The major assumption considered in the ALP and subsequent authors (Beloborodov, 1998; Sadowski, 2009) is that they considered the energy ($\mathcal{E}$) and angular momentum ($\mathcal{L}$) are constant along the stream-line, i.e., $\mathcal{E} = u_t$ and $\mathcal{L} = -u_\phi$ are conserved. From the thermodynamic point of view of a non-relativistic flow, this is true. However, for a relativistic fluid, the conserved quantities are $\mathcal{E} = hu_t$ and $\mathcal{L} = -hu_\phi$. This implies that ALP and successive authors considered enthalpy ($h$) to be equal to 1 and constant. This assumption mathematically describes dust, or, better yet, pressure-less dust instead of a fluid. The consequences of this assumption (constant enthalpy) are explained as follows:

As mentioned earlier the energy-momentum tensor of a perfect fluid is

$$T^{ab} = (P+\rho)u^a u^b + g^{ab}P = \rho_0 h u^a u^b + g^{ab}P \tag{6.11}$$

where the symbols in the equations are as follows :$\rho = \rho_0 + \epsilon$, $\rho_0$ is the rest mass density, $\epsilon$ is the energy density and thus enthalpy $h = 1 + \frac{P+\epsilon}{\rho_0}$. The metric tensor represented by, $g^{ab}$.

Using the energy-momentum conservation equation, $\nabla_a T^{ab} = 0$ and the particle number conservation equation $\nabla_a(\rho_0 u^a) = 0$, we obtain,

$$dh = \frac{1}{\rho_0}dP \tag{6.12}$$

The above equation implies that the flow is isoentropic ($ds = 0$) i.e. if $h$ stand constant then $P$ too remains constant along the flow lines, i.e., gradient of pressure is zero. In addition if $\mathcal{E} = u_t$ and $\mathcal{L} = -u_\phi$ then the normalization condition of four velocity $u^a u_a = 1$ provides,

$$\pm\left(\sqrt{-g_{rr}}\right)u^r = (A-1)^{1/2}\left[1 + \frac{g_{\theta\theta}}{2(A-1)}(u^\theta)^2\right] + \mathcal{O}\left(u^\theta\right)^4 \tag{6.13}$$

where, $A(r,\mathcal{L},\mathcal{E}) = g^{tt}\mathcal{E}^2 - 2g^{t\phi}\mathcal{E}\mathcal{L} + g^{\phi\phi}\mathcal{L}^2$.

Now back to the ALP prescription, we can see that ALP's assumption for $u^\theta$ is only important up to first order, i.e., $u^r = \frac{\pm(A-1)^{1/2}}{(\sqrt{-g_{rr}})}$, which is then a solution for particle geodesic. Because of that, accreting flow follows here the particle geodesic, which is the characteristic of a pressure-less dust particle. Additionally, another important point is that an accretion disk does not end abruptly at a certain altitude. When dealing with a real accretion flow, one should keep in mind that the flow continuously merges with the environment. Therefore, the variation of all the fluid variables along the vertical direction $z$ should be in such a way that it sustains the real scenario. In the thin disk model, the flow variables vary more rapidly and never diverge at any value of $z$. However, the series expansion of ALP does not monotonically go to zero with increasing $z$ and as a matter of fact, it does not even guarantee convergence for $z > r$. ALP circumvents this problem

by truncating the full series up to the first order of $z/r$. In other words, in this model, the disk abruptly ends at a certain vertical height.

Peitz & Appl (1997) created the vertical structure for hydrostatic flows, which includes relativistic enthalpy almost simultaneously. In the cylindrical coordinate system $(t, \phi, r, z)$, the vertical height for a four-velocity flow $\mathbf{u} = (u^t, u^\phi, u^r, 0)$ is found as

$$\frac{H^2}{r^2} = \frac{c_{ad}^2 r}{M\tilde{\mathcal{R}} + c_{ad}^2 r^2 \mathcal{L}(\frac{\mathcal{N}}{\mathcal{D}} + \frac{1}{r})} \tag{6.14}$$

in which $H$ denotes the disk's height. Under the height integrated density $\Sigma_0 = 2\rho_0 H$, the mass accretion rate is computed as $\dot{M} = -2\pi r u \Sigma_0$ (Peitz & Appl, 1997).

Gammie & Popham (1998); Kim et al. (2019); Popham & Gammie (1998) carried out more disk model development. In order to create an ADAF structure, Gammie and Popham take into account a relativistic equation of state and turbulent shear stress. They then apply ALP's method to construct the vertical structure.

$$H_\theta^2 = \frac{p}{\rho h r^2 v_z^2}. \tag{6.15}$$

In this approach the particle-number conservation equation reduced to the form

$$\dot{M} = -4\pi H_\theta r^2 \rho u^r \tag{6.16}$$

In this case, $v_z$ is extracted from ALP ((Abramowicz et al., 1997)). Nonetheless, the precise enthalpy variation has not been appropriately integrated into any of these explorations. Apart from these methods, several research studies have also been conducted on the vertical equilibrium model within the Newtonian framework. Kim, Jang, and Yi Kim et al. (2019) have recently provided the radiation pressure and vertical equilibrium condition.

$$\frac{1}{\rho}\frac{dp}{dz} = -(\frac{z}{r^3})(GM - \frac{\sigma_{Thompson}}{4\pi m_p c} L). \tag{6.17}$$

Using the above condition, the vertical structure of the flow is thus obtained as,

$$h \equiv H/R = c_s/\Omega_A = \sqrt{\frac{p}{\rho}}(\frac{GM}{r^3} - \frac{\sigma_{Thompson}}{4\pi m_p c} L)^{-1/2}, \tag{6.18}$$

and the mass accretion rate is,

$$\dot{M} = 2\pi r v_r \Sigma \tag{6.19}$$

where $\Sigma = \int_{-h}^{h} \rho(z) dz$ is the surface mass density and the vertical mass density is Gaussian given by,

$$\rho(z) = \rho_0 \exp -\frac{z^2}{2h^2} \tag{6.20}$$

From all the above studies, we see that no where complete general relativistic and self-consistent study is used to derive a relation connecting the disk height $H$ with mass flux $\dot{M}$. Some developments used a semi-relativistic hybrid approach; others used a full general relativistic fluid dynamical approach; however, they made several assumptions and approximations. Furthermore, the general relativistic derivations of the relation between $\dot{M}$ and $H$ are derived assuming

a $1D$ flow structure, i.e., the flow variables are assumed to depend on the radial coordinate $r$ only. As a result of that, $\dot{M}$ becomes linearly related to $H$ for a given value of $\rho$ and $v$. After a short review of the spectral states of x-ray binaries, we present here a complete general relativistic derivation of the mass-flux and relate it to the vertical height of the accretion flow using the first principle.

### 6.0.4 A brief discussion on the spectral state of X-ray binaries

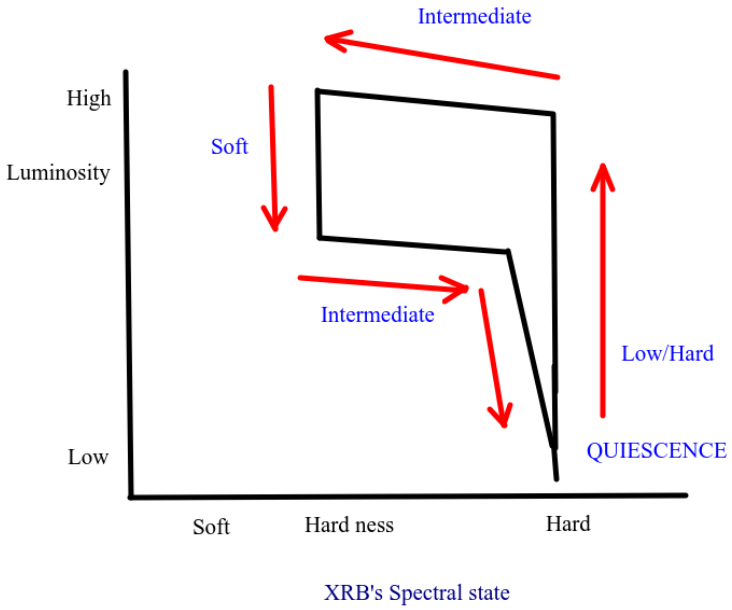


**Figure 6.1:** Spectral states of X-ray binaries

The X-ray observations of black hole binaries made us aware of the wide range of emission properties of accreting black holes. With the increasing order of the accretion rate, spectral states change in succession, and the vertical structure of the disk changes as well. Nowadays, according to present findings, the whole emission range is classified by five distinct spectral states (see figure 6.1) :(a) quiescence state; (b) low/hard state; (c) intermediate state; (d) high/soft state; and (e) very high state (Chen & Taam, 1996; Esin et al., 1997; Fender et al., 2004; Homan & Belloni, 2005; McClintock & Remillard, 2006; Remillard & McClintock, 2006; Done et al., 2007; Belloni, 2010). Observationally, the spectral state changes in the order of (a)→ (e) with increasing accretion rate and then come back again to the quiescence state (a) as the mass accretion rate falls back to a low value again (Nowak, 1995; van der Klis, 1995). A high-luminous, high-soft state has a high accretion rate. On the other hand, the accretion rate is small in comparatively low luminous states, and the morphology of the thin disk changes accordingly. As the matter is accreted into the black hole, gravitational energy is converted to the thermal energy that is being released. This is the source of luminosity for the different spectral states. The angular momentum transfer leads the accreting matter to form a disk-like configuration whose structure depends on the accretion rate and some of the internal parameters. When one considers the full outburst cycle of an X-ray binary (e.g., Cygnus X-1 (Zdziarski & Gierliński, 2004), GX339-4, GS1124-683 (Miyamoto et al., 1995), Nova Muscae (Gilfanov et al., 1993), a neutron star X-ray binary Aql

X-1 (Maccarone & Coppi, 2003), XTE J1650-500 (Rossi et al., 2004), Microquasar XTEJ1550-564 (Kubota & Done, 2004; Rodriguez et al., 2003), MAXI J1820+070 (Chakraborty et al., 2020)), a cyclic evolution of the spectral states is observed(see (Homan & Belloni, 2005; Dunn et al., 2010)) and in the process of hysteresis, the mass accretion rate varies accordingly. For example (a), the quiescence state, observed mainly in the soft X-ray variant of black hole X-ray binaries, is the lowest luminosity state; the accretion rate (expressed in Eddington units) is of the order of $\dot{M} \leq 10^{-3}$. (b) Low-luminosity hard X-ray (low/hard) state with $0.05 \leq \dot{M} \leq 0.1$, which is totally dominated by non-thermal components associated with strong radio emissions. The next (c) high luminosity high/soft state is dominated by thermal emission having an accretion rate comparable to $\dot{M} \sim 0.4$. Some non-thermal components were also found in this state. The transitional state between low and high states is known as (d) the intermediate state ($0.11 \leq \dot{M} \leq 0.12$). The spectrum of this state can be described by a combination of thermal and non-thermal emission and observed over a wide range of luminosities. Finally, in the (e) very high state, the flows exhibit hot temperature properties, and the accretion rate approaches the Eddington limit (Esin et al., 1998). The reason behind different accretion rate modes is explained by several authors in terms of Compton cooling and heating, two-component flow models (Keplerian and Sub-Keplerian (Chakrabarti & Titarchuk, 1995) (see Meyer-Hofmeister et al. (2005) and references therein), disk magnetization (Petrucci et al., 2008), etc. Interestingly, different models of vertical structure predict different emission properties and hence give rise to different spectral states. Now, different vertical geometry is also associated with the different spectral states. It is found that spectral transitions involve the redesign of the vertical structure of accretion flows, thus analyzing the dynamics of disk structure to probe different spectral states. The thin disk model (radiatively efficient) developed by SS73, NT73, Lynden-Bell & Pringle (1974); for more details, see reviews by Pringle (1981), Frank et al. (2002), Kato et al. (2008), Abramowicz & Fragile (2013), Blaes (2014) is utilized in different accreting black hole systems e.g. luminous active galactic nuclei (Koratkar & Blaes (1999)) and in various black hole binaries in thermal state (Remillard & McClintock (2006); McClintock et al. (2014)). The Slim disk or Optically thick Advection-Dominated Accretion Flow (ADAF) model ( Katz (1977); Begelman (1978); Abramowicz et al. (1988); see also Begelman & Meier (1982); Eggum et al. (1988)) is applied to Seyfert galaxies (Mineshige et al., 2000), ultraluminous X-ray sources (Watarai et al., 2001). Optically thin ADAF or a two-temperature ADAF (Ichimaru (1977); Rees et al. (1982); Narayan & Yi (1994, 1995a,b); Abramowicz et al. (1995)) has been applied to several black hole systems, including the supermassive black hole in our own Galactic center, Sagittarius A* (Sgr A*), low-luminosity active galactic nuclei, and black hole binaries in the hard and quiescent states. To describe the spectral properties of a full outburst cycle, one required a combination of different accretion disk models. For example, the thermal emission from the high/soft state is believed to be from a standard accretion disk (SS73); the properties of low/hard, quiescent states imply the existence of an optically thin ADAF; and the very high state implies the presence of a slim disk. As the spectral state changes, the thin and slim disk morphology changes as well, which is eventually responsible for the change in radiation properties. Till now, not a single accretion disk model has described the full outburst cycle of the whole spectral state. So only a combination of different accretion disk models describes the entire spectral range. Now every disk model corresponds to a different vertical geometry. Thus, a theoretical model is required to find out the vertical structure associated with the different

spectral states of the black hole candidates from the very basic principal, which encompasses all the variable structures attributed to different spectral states.

The first astronomical object from which gravitational waves (GWs) and light have been detected is the binary neutron star (BNS) merger GW 170817 ((Abbott & et. al., 2017)). Gravitational-wave (GW) detection confirms the existence of massive merging black holes (BBHs), despite the fact that there are few high-mass X-ray binaries (HMXBs) known to host BHs and none of them are expected to produce a binary black hole (BBH) that merges within a Hubble period. The emission properties of HMXB are closely related to the spectral state transition, as discussed earlier. As far as is known, no single accretion flow model can describe the full outburst cycle of the hysteresis loop of these radiations. A proper modeling of a general relativistic accretion flow model is thus required to predict the flow characteristics from the observational data emitted from the accretion disk around massive BH. With these motivations, we look for a vertical structure around a Kerr black hole using four divergences of the energy-momentum tensor. The relativistic continuity equation is integrated with minimum axioms for this purpose, and we derive a fully relativistic version of mass accretion rate.

### 6.0.5 Flow variables and the thermodynamics

In the presence of a gravitational field, the physical expressions of the thermodynamic variables also change accordingly. They reduce to their usual form in the non-relativistic regime. In the gravitational field, the relativistic definition of specific enthalpy ($h$) is given by $h = \frac{P+\rho}{\rho_o}$, where $P$ is the isotropic thermal pressure, $\rho$ is the total mass density (related to the rest mass density $\rho_o$ via, $\rho = \rho_o\,(1+U)$, $U = \frac{P}{(\gamma-1)\rho_o}$ being the specific internal energy which yields

$$\rho = \rho_o[1 + \frac{P}{(\gamma-1)\rho_o}] = \rho_o + \frac{P}{(\gamma-1)} \tag{6.21}$$

where $\gamma = \frac{c_P}{c_v}$ connected to the polytropic index($n$) by $n = \frac{1}{(\gamma-1)}$. Therefore,

$$\frac{d\rho}{d\rho_o} = 1 + n\frac{dP}{d\rho_o} = 1 + \frac{1}{(\gamma-1)}\frac{dP}{d\rho_o} \tag{6.22}$$

The relativistic definition of the adiabatic sound speed ($a_s$) is given by

$$a_s^2 = \left(\frac{\partial P}{\partial \rho}\right)_s = \left(\frac{dP}{d\rho_o}\right) / \left(\frac{d\rho}{d\rho_o}\right) = \left(\frac{dP}{d\rho_o}\right) / \left(1 + n\frac{dP}{d\rho_o}\right) \tag{6.23}$$

which gives,

$$\frac{dP}{d\rho_o} = \frac{{a_s}^2}{1 - n{a_s}^2} \quad \text{and} \quad \frac{d\rho}{d\rho_o} = \frac{1}{a_s^2}\frac{dP}{d\rho_o} = \frac{1}{1 - na_s^2} \tag{6.24}$$

Now, if $\mathbf{ds = 0}$ then, $Tds = 0 = dU + Pd(\frac{1}{\rho_o})$

$$\text{i.e.,} \qquad \frac{d\rho}{d\rho_o} = \frac{(P+\rho)}{\rho_0} = h. \tag{6.25}$$

Thus, the relativistic form of specific enthalpy in terms of the sound speed ($a_s$) is

$$h = \frac{P+\rho}{\rho_o} = \frac{1}{1-na_s^2}. \tag{6.26}$$

The relativistic form of the pressure ($P$) and the total mass density ($\rho$) in terms of the sound speed ($a_s$) and the rest mass density $\rho_o$ are respectively given by,

$$P = \frac{1}{(n+1)}\frac{na_s^2}{(1-na_s^2)}\rho_o, \tag{6.27}$$

$$\rho = \rho_o + nP = \frac{1}{\gamma}\left[\frac{1}{(1-na_s^2)} + \frac{1}{n}\right]\rho_o. \tag{6.28}$$

Consider the adiabatic equation of state, i.e., $P = K\rho_o^{\gamma}$ where $\gamma = 1 + \frac{1}{n}$ and $n$ is the polytropic index. Substituting the adiabatic equation of state, it is very easy to calculate the form of the above thermodynamical variables in terms of the sound speed $a_s = \left(\frac{\partial P}{\partial \rho}\right)_s$ of an ideal fluid.

$$\rho_o = \left[\frac{na_s^2}{K\,(n+1)\,(1-na_s^2)}\right]^n, \tag{6.29}$$

$$P = \frac{1}{K^n\gamma^{n+1}}\left[\frac{a_s^2}{1-na_s^2}\right]^{n+1}, \tag{6.30}$$

$$\rho = \frac{1}{\gamma}\left[\frac{1}{(1-na_s^2)} + \frac{1}{n}\right]\left[\frac{na_s^2}{K\,(n+1)\,(1-na_s^2)}\right]^n. \tag{6.31}$$

### 6.0.6 Relativistic accretion rate in curved space-time

We take into account the energy momentum tensor of a perfect fluid $T^{ab} = (P+\rho)u^a u^b + g^{ab}P$ in an axisymmetric, stationary vacuum space time. The metric of such space time, disregarding the fluid's own gravity, may be represented as

$$\begin{aligned} dS^2 &= g_{\mu\nu}dx^\mu dx^\nu \\ &= \left(1-\frac{2r}{\Sigma}\right)dt^2 + \left(\frac{4ar\sin^2\theta}{\Sigma}\right)dtd\phi - \frac{\Sigma}{\Delta}dr^2 - \Sigma d\theta^2 \\ &- \left(r^2+a^2+\frac{2ra^2\sin^2\theta}{\Sigma}\right)\sin^2\theta d\phi^2 \end{aligned} \tag{6.32}$$

Here, $\Delta = r^2 - 2r + a^2$ and $\Sigma = r^2 + a^2\cos^2\theta$, $a$ is the Kerr parameter and ($r$, $\theta$, $\phi$, $t$) are Boyer-Lindquist (B-L) coordinates and we have used system of unit in which $c = G = M = 1$. Here $c$ and $G$ are the velocity of light, gravitational constant, and mass of the black hole respectively.

Owing to the time translation and axial symmetry, two killing vectors $\xi^a = \left(\frac{\partial}{\partial t}\right)^a$ and $\chi^a = \left(\frac{\partial}{\partial \phi}\right)^a$ satisfying $\nabla_{(a}\xi_{b)} = \nabla_{(a}\chi_{b)} = 0$ exist in this space-time. Since $T^{ab}$ satisfies continuity equation

$$\nabla_a T^{ab} = 0 \tag{6.33}$$

there exist a conserve current $J^a = T^{ab}\xi_b$ satisfying

$$\nabla_a J^a = 0. \tag{6.34}$$

where $J^t$ is the total energy density of the fluid (relativistic mass density of the fluid in $c = 1$ unit) and$J^i$ is the flux of the energy (relativistic mass flux of the fluid in $c = 1$ unit). Note that the four current densities $N^a = \rho_0 u^a$ appearing in the particle number conservation equation $\nabla_a N^a = 0$, give the density and flux of kinetic energy only. However, $J^a$ gives the density and flux of total energy (kinetic and internal). Therefore, in the case of fluid flow, $J^a$ is true density and flux.

By using Gauss's theorem, we get

$$\int_{Space-time-Volume} \nabla_a J^a d^4x = \int_{boundary} n_a J^a dS \tag{6.35}$$

where $d^4x = \sqrt{g}dx^0dx^1dx^2dx^3$, $g = det(g_{\mu\nu})$ and $dS = d^3x$ is the volume element in the 3-D hypersurface and $n^a$ is the unit normal ( $|n^a n_a| = 1$) to the $3-D$ boundary of the $4-D$ integration region.

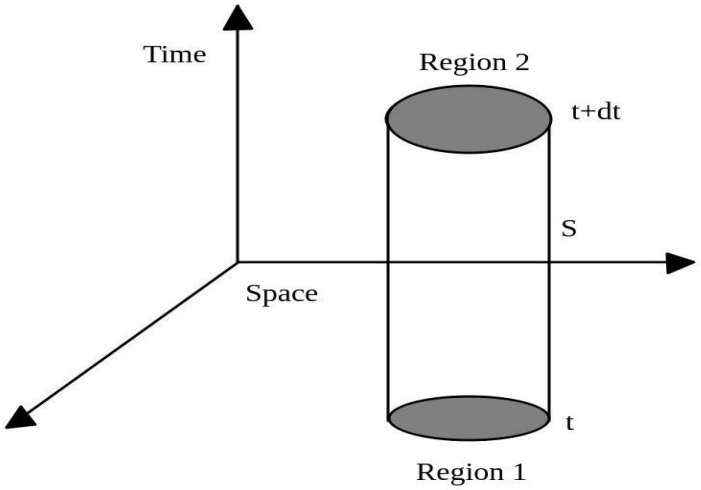


**Figure 6.2:** In this illustration, the top and bottom of the cylinders, Regions 2 and 1, respectively, depict the $3-D$ space area at constant time $t$ and $t+dt$. The $3-D$area that the boundary of the $3-D$ space-like region spans is represented by the side surface $S$.

To get the familiar form of the mass accretion rate, we choose the region of integration as shown in the figure 6.2 (Wald, 1984; Poisson, 2004). Here, the top and bottom parts of the cylinder (Region 2 and Region 1) represent the $3-D$ space region at constant time $t$ and $t+dt$, respectively. The side surface $S$ represents the $3-D$ region spanned by the boundary of the $3-D$ space-like region and the vector along $t$ direction. The R.H.S. of the above equation

$$\int_{boundary} n_a J^a dS = \int_{R_2} n_a J^a dS + \int_{R_1} n_a J^a dS + \int_{S} n_a J^a dS = 0. \tag{6.36}$$

Since Region 2 and Region 1 are spanned by the space like basis vector $\partial_i (i = 1, 2, 3)$ and $n^a$ is perpendicular to that region therefore $n_a(\partial_i)^a = 0$ which gives $n_\mu = \frac{1}{\sqrt{-g^{00}}}\delta^0_\mu$ (see figure 6.3) Now

the orientation of Region 1 and Region 2 are opposite ($n^a|_{R_1} = -n^a|_{R_2}$) and thus

$$\int_{R_2} n_a J^a dS + \int_{R_1} n_a J^a dS = \int n_0 J^0 d^3x \Big|_{t+dt} - \int n_0 J^0 d^3x \Big|_t$$
$$= dt.\frac{d}{dt}\left[\int n_0 J^0 d^3x\right] \tag{6.37}$$

We investigate the particular case of the accretion disk in order to estimate the integral over the curved hypersurface $S$. To do that let us consider a $3-D$ subspace at the constant value of the radial coordinate $R$ and $(R+dR)$ within $z = (-H, H)$ respectively (figure 6.3) where $R$, $\phi$, $z$ are cylindrical coordinates related with the spherical polar coordinates by the transformation : $R = r\sin\theta$ and $z = r\cos\theta$.

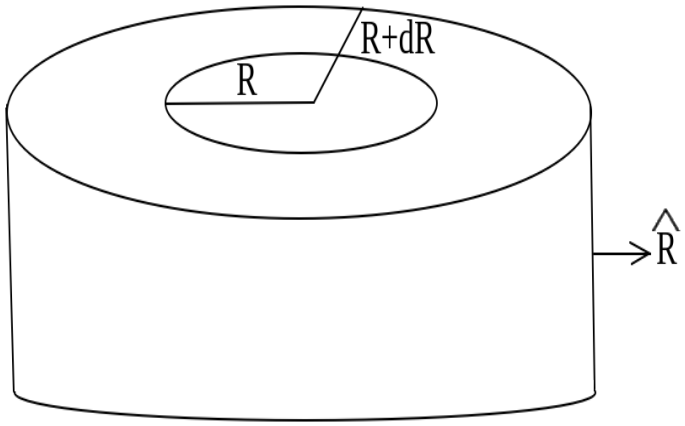


**Figure 6.3:** Closed spatial 2D surface $S_1$ bounding the volume of region 1 and region 2. The side surface S in figure is the 3D hypersurface generated by S during $t$ and $t+dt$. The unit normal to S is $n^a$. It is shown that $n^a = \frac{1}{\sqrt{g^{RR}}}\delta^a_R$.

This corresponds to space-time region generated by the side surface of the $3-D$ cylindrical region at $R$ from $t$ to $t+dt$ which is spanned by the vector $\partial_t$, $\partial_\phi$ and $\partial_z$. Therefore if $n^a$ is the outward normal to this hyper surface (figure 6.3)then,

$$n_a(\partial_t)^a = n_a(\partial_\phi)^a = n_a(\partial_z)^a = 0 \tag{6.38}$$

$$n_\mu = n_R\delta^1_\mu \implies n_R = \frac{1}{\sqrt{g^{RR}}} \tag{6.39}$$

and the magnitude of the hypersurface element generated by coordinate differentials $dt$, $d\phi$, $dz$ is

$$dS = \sqrt{|g_P|}dtd\phi dz \tag{6.40}$$

$$\text{where,} \quad g_P = \begin{vmatrix} g_{tt} & g_{t\phi} & g_{tz} \\ g_{\phi t} & g_{\phi\phi} & g_{\phi z} \\ g_{zt} & g_{z\phi} & g_{zz} \end{vmatrix} \tag{6.41}$$

is the induced metric in the hypersurface.

$$\begin{aligned} \therefore \int_S n_a J^a dS &= \int_S n_R J^R \sqrt{g_P} dt d\phi dz \\ &= \int n_R J^R \sqrt{g_P} dt d\phi dz \Big|_{R+dR} - \int n_R J^R \sqrt{g_P} dt d\phi dz \Big|_R , \end{aligned} \tag{6.42}$$

where $J^R = T^{Rb}\xi_b = \rho_0 h u_t u^R = \rho_0 u^R \mathcal{E}$ and $hu_t = \frac{P+\rho}{\rho_0} u_t = \mathcal{E}$ is the conserved quantity for the fluid flow.

For accretion processes with negligible out flows the contribution to the integral from the vertical boundary is zero and due to axisymmetry $\partial_\phi J^\mu = 0$. In the choice of such boundary conditions, the vertical motion $u^z$ is not essentially zero at the interior points and at the surface.

$$\begin{aligned} dt.\frac{d}{dt}\left[\int J^t n_t d^3x\right] = dt.\Bigg[ &\int n_R J^R \sqrt{g_\phi} dt d\phi dz \Big|_{R+dR} \\ &- \int n_R J^R \sqrt{g_P} dt d\phi dz \Big|_R \Bigg] \end{aligned} \tag{6.43}$$

For time independent flow, left hand side of above equation is zero. Therefore,

$$\int n_R J^R \sqrt{g_P} dt d\phi dz \Big|_{R+dR} = \int n_R J^R \sqrt{g_P} dt d\phi dz \Big|_R \tag{6.44}$$

Thus the general formula for mass accretion rate is,

$$\dot{M} = 2\pi \int n_R J^R dz \sqrt{g_P} \tag{6.45}$$

Now we consider two special cases, one for spherically symmetric and axisymmetric space time.

#### 6.0.6.1 Schwarzschild black hole

For non-rotating black hole, $g_{t\phi} = g_{tz} = g_{\phi z} = 0$, Therefore

$$g_P = \begin{vmatrix} g_{tt} & 0 & 0 \\ 0 & g_{\phi\phi} & 0 \\ 0 & 0 & g_{zz} \end{vmatrix} = g_{tt} g_{\phi\phi} g_{zz} \tag{6.46}$$

$$dS = \sqrt{|g_{tt} g_{\phi\phi} g_{zz}|} dt d\phi dz \tag{6.47}$$

Thus mass accretion rate for Schwarzschild geometry is,

$$\dot{M} = 2\pi \int n_R J^R dz \sqrt{|g_{tt} g_{\phi\phi} g_{zz}|} \tag{6.48}$$

$$\dot{M} = 2\pi \mathcal{E} \int (\rho_0 u^R) \sqrt{\frac{g_{tt} g_{\phi\phi} g_{zz}}{g^{RR}}} dz = 2\pi R \mathcal{E} \int \rho_0 u^R dz, \tag{6.49}$$

which is a very standard expression of the accretion rate (discussed in §2) for spherically symmetric accretion flows.

#### 6.0.6.2 Kerr Black hole

For a rotating black hole, the metric co-efficients $g_{\mu\nu}$ in cylindrical co-ordinate is given by

$$g_{\mu\nu} = \begin{pmatrix} g_{tt} & g_{t\phi} & 0 & 0 \\ g_{t\phi} & g_{\phi\phi} & 0 & 0 \\ 0 & 0 & g_{RR} & g_{Rz} \\ 0 & 0 & g_{Rz} & g_{zz} \end{pmatrix} \tag{6.50}$$

where

$$\begin{aligned} g_{tt} &= 1 - \frac{2(R^2+z^2)^{3/2}}{(R^2+z^2)^2 + a^2 z^2} \\ g_{t\phi} &= \frac{2aR^2\sqrt{R^2+z^2}}{(R^2+z^2)^2 + a^2 z^2} \\ g_{\phi\phi} &= -\left[\left(R^2 + z^2 + a^2 + \frac{2a^2R^2\sqrt{R^2+z^2}}{(R^2+z^2)^2 + a^2z^2}\right)\frac{R^2}{R^2+z^2}\right] \\ g_{RR} &= -\left[\frac{(R^2+z^2)^2 + a^2z^2}{(R^2+z^2)^2}\left(\frac{R^2}{\Delta} + \frac{z^2}{R^2+z^2}\right)\right] \\ g_{zz} &= -\left[\frac{(R^2+z^2)^2 + a^2z^2}{(R^2+z^2)^2}\left(\frac{z^2}{\Delta} + \frac{R^2}{R^2+z^2}\right)\right] \\ g_{Rz} &= -\left[Rz\frac{(R^2+z^2)^2 + a^2z^2}{(R^2+z^2)^2}\left(\frac{1}{\Delta} - \frac{1}{R^2+z^2}\right)\right] \end{aligned} \tag{6.51}$$

The determinant $g$ value for the $g_{\mu\nu}$ matrix is,

$$\begin{aligned} g = det(g_{\mu\nu}) &= (g_{RR}g_{zz} - g_{Rz}^2)(g_{tt}g_{\phi\phi} - g_{t\phi}^2) = \Delta_2 \times \Delta_1 \\ &= R^2\left[1 + \frac{2a^2z^2}{(R^2+z^2)^2} + \frac{a^4z^4}{(R^2+z^2)^4}\right]. \end{aligned} \tag{6.52}$$

and the induced metric $g_P$ is

$$g_P = \begin{vmatrix} g_{tt} & g_{t\phi} & 0 \\ g_{\phi t} & g_{\phi\phi} & 0 \\ 0 & 0 & g_{zz} \end{vmatrix} = g_{zz}(g_{\phi\phi}g_{tt} - g_{t\phi}^2). \tag{6.53}$$

The accretion rate for a rotating black hole is given by,

$$\begin{aligned}\dot{M} &= 2\pi \int n_R J^R \sqrt{g_P} dz \\ &= 2\pi \int \frac{1}{\sqrt{g^{RR}}} (\rho_0 u^R) \mathcal{E} \sqrt{g_P} dz \\ &= 2\pi \mathcal{E} \int (\rho_0 u^R) \sqrt{\frac{1}{\frac{g_{zz}}{\Delta_2}}} \sqrt{g_{zz}(g_{tt} g_{\phi\phi} - g_{t\phi}^2)} dz\end{aligned}$$

Simplifying the above expression, the final form of the relativistic accretion rate in the Kerr space-time is given by (Chatterjee et al., 2022),

$$\dot{M} = 2\pi \mathcal{E} \int (\rho_0 u^R) \sqrt{g} dz \tag{6.54}$$

It is a precise equation for relativistic accretion flows in curved space-time with non-constant enthalpy. The formula given in the cylindrical polar co-ordinate, therefore in the Newtonian limit, $d\tau \to dt$, $g_{\mu\nu} \to \eta_{\mu\nu}$, and $g$ is calculated in the equation (6.52), is different from $R^4$ for the Minkowski metric. It should be noted that the direct fluctuation of accretion rate with the Kerr parameter has not yet been incorporated in the accretion physics. In that regard, our approach is novel and might be useful in distinguishing the various accretion processes surrounding spinning black holes since the spin dependency of the accretion flow directly effects the creation of thin or thick disks around a rotating black hole. The explicit spin dependency is provided by the determinant of the metric tensor $|g|$, which appears in the under root quantities of the formula (6.54). As a result, for small $R$, the dependency on spin is evident. The flow variable $u^R$ indirectly depends on spin, which has a non-negligible influence. Thus, expression is indeed affected by spin. Furthermore, because $\sqrt{g}$ is a function of $a^2$ but $u^R$ is not, the final formula is not symmetric in terms of co-rotation and contra-rotation spin. Here we develop a Schwarzchild black hole solution with spin $a = 0$.

### 6.0.7 Height of the accretion disk

Following (Pringle, 1981; Smak, 1992; Dominik, 2015; Mishra et al., 2019; Hubeny, 1990; Kim et al., 2019; Fukue, 2020), we assume the Gaussian variation of the flow variables namely $\rho_0$ and $u^R$ along the vertical direction, and express them with respect to the values at equatorial plane($z = 0$) as $\rho_0(z) = \rho_0(z = 0)e^{-\frac{z^2}{2H^2}}$ and $u^R(z) = u^R(z = 0)e^{-\frac{z^2}{2H^2}}$.

**Gaussian nature explanation :**

$$\frac{1}{\rho}\frac{dP}{dz} = -(\frac{z}{r^3})(GM) \tag{6.55}$$

Sound Speed $a_s^2 = \frac{dP}{d\rho}$ therefore $dP = a_s^2 d\rho$

$$\frac{a_s^2}{\rho}\frac{d\rho}{dz} = -\frac{z}{r^3}GM \tag{6.56}$$

$$\int \frac{d\rho}{\rho} = -\frac{GM}{r^3}\frac{1}{a_s^2}\int z dz + Constant \tag{6.57}$$

$$\ln \rho = -\frac{1}{a_s^2}(\frac{GM}{r^3})\frac{z^2}{2} + \ln \rho_0 \tag{6.58}$$

$$\frac{\rho(z)}{\rho_0} = \exp\left[-(\frac{GM}{2r^3 a_s^2})z^2\right] = \exp\left[-\frac{z^2}{2h^2}\right] \tag{6.59}$$

$$\rho(z) = \rho_0(z=0)\exp\left[-\frac{z^2}{2h^2}\right] \tag{6.60}$$

Hence we obtain,

$$\begin{aligned}\dot{M} &= 2\pi\mathcal{E}(\rho_0 u^R)_0 \int_{-\infty}^{\infty} e^{-z^2/H^2}\left[R + \frac{a^2}{R}\frac{\frac{z^2}{R^2}}{(1+\frac{z^2}{R^2})^2}\right]dz \\ &= 2\pi(\rho_0 u^R)_0\left[HR + \frac{a^2}{2}\frac{H^3}{R^3} - \frac{3a^2}{2}\frac{H^5}{R^5}\right]\sqrt{\pi}\mathcal{E}\end{aligned} \tag{6.61}$$

where $(\rho_0 u^R)_0 = \rho_0(z=0)u^R(z=0)$ and

$$u^R = \sqrt{\frac{\Delta + \left(\frac{\mathcal{E}}{\hbar}\right)^2\left[g_{\phi\phi} + 2g_{t\phi}l + g_{tt}l^2\right]}{\Delta g_{RR}}} \tag{6.62}$$

is obtained from the $u^\mu u_\mu = 1$. The above equation gives the expression of mass flux $\dot{M}$ in terms of disk height. We see that the expression is not linear in $H$, which is different from the $\dot{M} - H$ relations existing in other models ((Novikov & Thorne, 1973; Riffert & Herold, 1995; Abramowicz et al., 1997) etc.). The non-linear dependence arises as a natural consequence of the curved geometry of space-time, and this feature cannot be simulated just by modifying the geometrical factor $\Delta$ or $\mathcal{D}$ used in Abramowicz et al. (1996); Novikov & Thorne (1973). We further see that the first term is identical with the expression of mass flux in Newtonian and Schwarzschild gravity. The second and higher-order terms give the general relativistic correction due to the rotation of the black hole. Thus, the difference arises solely due to the rotation of space-time. However, this effect has not been taken into account by many authors while studying accretion processes around Kerr black holes ((Sądowski et al., 2011; Beloborodov, 1998; Peitz & Appl, 1997; Chakrabarti, 1996a), reference therein). The effect is small for the slowly rotating black hole; however, for the rapidly spinning black hole or for the thick disk, this effect should be taken into account. Despite the explicit appearance of $a^2$ in the equation (6.61) the total mass-flux depends on the first order of $a$ because of the presence of the term $u^R$ (equation (6.62)).Now from equation (6.61) we get,

$$\frac{H}{R} = x_\rho - \frac{1}{C}x_\rho^3 - x_\rho^5\left(\frac{1}{D} - \frac{3}{C^2}\right) \tag{6.63}$$

where $x_\rho = \frac{\dot{M}}{2\pi^{3/2}\mathcal{E}(\rho_0 u^R)_0 R^2}$, $\frac{1}{C} = \frac{a^2}{2R^2}$, $\frac{1}{D} = \frac{-3a^2}{2R^2}$. The value of the $(\rho_0 u^R)_0$, at the equatorial plane, now can be found by fully solving the radial hydrodynamical equations as done in

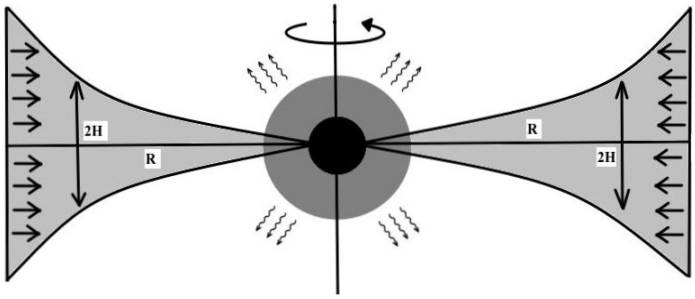


**Figure 6.4:** Schematic diagram of an accreting disk representing disk height with radial distance.

(Chakrabarti, 1996b,a; Mondal, 2010; Mondal & Choi, 2013; Fukue, 1987) but with the corrected expression of Mass flux (equation (6.61)).

### 6.0.8 Results & Discussions

To demonstrate the fluctuation in disk height with regard to radial distances, Kerr parameters, and so on, and therefore to create the disk profile, the values of $(\rho_0 u^R)_0$, at the equatorial plane $z = 0$ for the equation (6.63). The values and the expression of $(\rho_0 u^R)_0$ can only be obtained by solving the relativistic hydrodynamical equations in the full $R - z$ plane completely and then substituting $z = 0$ in the expression. The thorough examination of the $R - z$ plane solution is too extensive to be covered in the current work, and as far as we are aware, no such formulation exists in the literature. We utilize the equatorial solution to get around this issue by resolving the radial hydrodynamical equations as in (Chakrabarti, 1996b,a; Mondal, 2010; Mondal & Choi, 2013; Fukue, 1987) and substituting the result into the equation (6.63) to make it simple to investigate the different characteristics of the equations (6.54) and (6.63). The fundamental premise is that radiation pressure is ignored and sub-Keplerian flows are solved in the low viscosity limit with no dissipation. The solutions are transonic in nature, which means they are subsonic at first and become supersonic after passing the sonic point. The results provided are thus valid for the radial distance from the infinite to the horizon. Using these findings, we show how disk height varies with respect to radial distances and Kerr parameters. The formula shows that the vertical height of the disk explicitly relies on (i) the accretion rate, (ii) the black hole's spin ($a$), and (iii) the internal flow parameters. As a result, the scale height changes as the accretion rate changes. This is significant because the emission parameters and spectral states change as the accretion rate changes. The vertical structure of the disk also depends on the black hole spin, and spin plays an important role in determining the shape of the disk. The effect of the spin comes through the metric coefficients of space-time and also from the flow variables, which indeed depend on the spin explicitly. The metric coefficients vary slowly with black hole spin, and its contribution is thus negligible at larger radii; however, spin influences flow variables. We demonstrate a systematic change of disk height with spin and show that the variation of $H$ changes differently for different spin factors. Figures

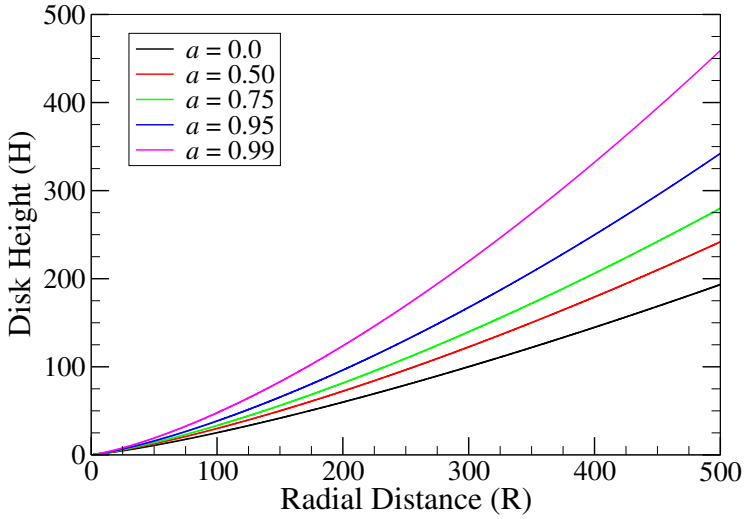


**Figure 6.5:** We plot accretion disk height $H$ with radius $r$ for different Kerr parameters $a$.

6.5 show the spin fluctuation. We are employing the $G = c = M = 1$ unit throughout our study, and the units of velocity, distance, and time are $c, GM/c^2$, and $GM/c^3$, respectively, where $c, G$, and $M$ are the velocity of light, gravitational constant, and compact object mass, respectively. We consider the accretion rate $\dot{\mathcal{M}}_E = \frac{\dot{M}}{\dot{M}_E} = 1$ where $\dot{M}_E$ is the Eddington accretion rate. In the figure, the height of the disk $H$ is plotted for Kerr parameter $a = 0.0, 0.50, 0.75, 0.95, 0.999$ as a function of radial distance $(r)$. The fact that the curves differ for various black hole spins as the black hole spin varies from $-1 \leq a \leq 1$ shows that the disk height does, in fact, depend on the black hole's spin. Additionally, because it does not expressly depend on $a$ alone, the expression of the disk height does not change significantly on the contra-rotating spin (see (6.54)).

#### 6.0.8.1 Comparison with different disk model

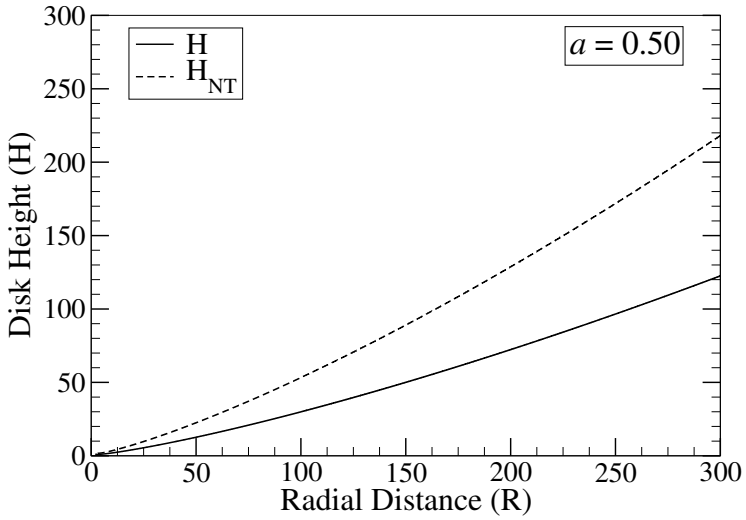


**Figure 6.6:** The variation of accretion disk height with the radial distance is drawn for Kerr parameter $a = 0.50$, mass accretion rate $\dot{\mathcal{M}}_E = 1$ Eddington rate. We compare the disk height with the Novikov & Thorne (1973). The *solid curve* is drawn for our case $(H)$. The *dotted curve* shows the variation for the NT73's model. We consider the same internal flow parameter for the two cases. We see that NT73's disk height is greater than $H$.

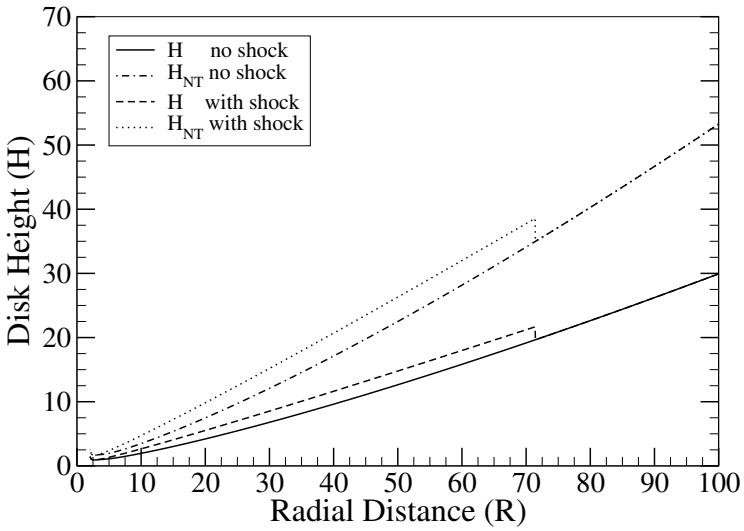


**Figure 6.7:** The disk height $H$ and NT73's disk height in the TCAF shock model is presented for the Kerr parameter $a = 0.50$. We compare disk height in the presence and absence of shock. In the presence of shock, a discontinuity is found in disk height. At the position of the notch, disk height increases suddenly as the post-shock flow is much hotter. In the absence of the shock, disk height remains the same as in figure 6.6.

We contrast the disk height with other recognized recommendations as well. Figure 6.4 shows a typical illustration of an accretion disk surrounding a compact item. Figure 6.6 depicts the precise functional change of the disk height with radial distance. We examine and plot the vertical height of the disk for the black hole spin $a = 0.50$ for the accretion rate $\dot{\mathcal{M}}_E = 1$ Eddington rate. We now compare our disk height with the height (equation (6.6)) of the thin disk model of NT73's disk. We first fix the required parameters to obtain the disk height and plot the results in figure 6.6 for the same parameters. Our disk height $H$ (equation(6.63)) is shown by the solid curve, and NT73's disk height is shown by the dashed curve. The Kerr parameter and the accretion rate, in this case, are considered as $a = 0.5$ and $\dot{\mathcal{M}}_E = 1$ Eddington rate, respectively. Furthermore, we investigate the height prescription of NT73's in the presence of a shock in the accretion flow. Because shock causes a discontinuity, the disk height becomes discontinuous throughout the shock and sharply increases at the post-shock boundary. Figure 6.7 depicts one such plot of disk height with shock. A notch in the graphic denotes a shock transition, which is characterized by a sharp rise in disk height at a certain radius. The height resembles the figure 6.6 if there is no shock in the flow. As a result, the heavy solid line represents the scenario when shock is present in the flow, while the dashed line represents the case when shock is absent in the flow. The TCAF model developed by Chakrabarti and colleagues exploits shock in accretion flow to explain the spectral variance of binaries. We use NT73 to calculate the fluctuation of disk height in TCAF (Chakrabarti, 1996b) and present our results in the figure.

#### 6.0.8.2 Variation of Vertical Thickness with Spectral states

Some analyses assume that the accretion rate varies in order to explain the hysteresis loop of the spectral structure (Liu et al., 2005; Meyer et al., 2007; Bradley & Frank, 2009; Smith et al., 2007; Belloni, 2010; Debnath et al., 2018; Chakrabarti, 2018). It is crucial to remember that black spin and accretion rate both affect the disk's vertical height; as a result, any change in either

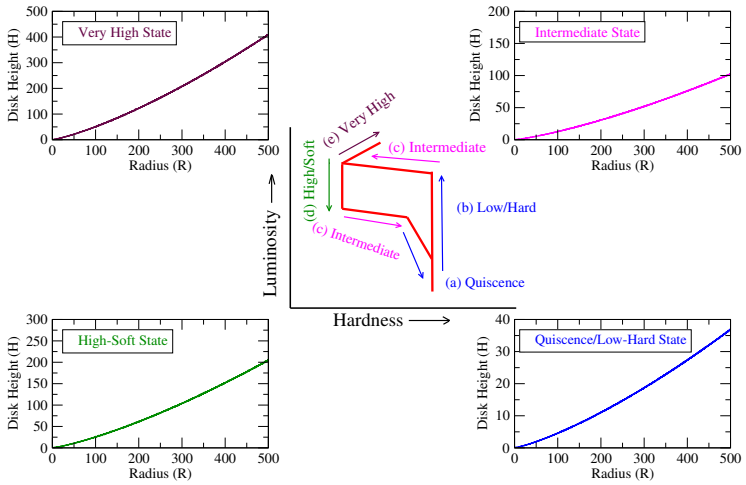


**Figure 6.8:** An evolution of accretion disk height with the spectral state is presented for the Kerr parameter $a = 0.50$. For the quiescence/low-hard state accretion rate is low ($\dot{\mathcal{M}}_E = 0.09$), thus the disk height is also very low (lower right panel). The disk height for the intermediate state where $\dot{\mathcal{M}}_E = 0.25$ is shown in the upper right panel. In the two left panels, the height is plotted for high/soft and very high states where the accretion rate is $\dot{\mathcal{M}}_E = 0.5$ and 1 Eddington rate. We see that disk height increases in each panel with an increasing accretion rate.

of these two parameters will cause the disk height to change, which suggests that this variation may be related to the characteristics of the flow parameters that determine the luminosity state. The alteration of flow characteristics, however, is not caused only by the modification of $H$. The actual fluctuation of the flow parameters is determined by the inherent qualities of the flow matter, such as viscosity and opacity, and the nature of the hydrodynamical equation's time-dependent solution. As an illustration, the center panel of the figure 6.8 shows a typical hysteresis of spectral hardness-intensity diagram, in which the evolution of the five distinct spectral states is displayed in accordance with their growing luminosity from Quiescence (a)→ Low/Hard (b)→ Intermediate (c)→ High/Soft (d)→ Very High (e) for the full outburst cycle. The figure shows that luminosity is lowest in the quiescence state, rises for high/soft state, and reaches its highest level for extremely high state. In full hysteresis of the outburst cycle, this order preserves the sequence as the accretion rate increases. As mentioned for the quiescence state, luminosity is low, thus the accretion rate is also low and is of the order of $\dot{\mathcal{M}}_E \leq 10^{-3}$ Eddington. The luminosity increases from the low/hard state to the intermediate state, and the accretion rate varies as $0.05 \leq \dot{\mathcal{M}}_E \leq 0.3$. The luminosity becomes maximum in the high/soft state or very high state, and the accretion rate is comparable to the $\dot{\mathcal{M}}_E \sim 0.4$ to 1 Eddington rate (Esin et al., 1998). The vertical thickness of the disk gradually varies as the XRB passes through each of the five unique spectral classes over a whole outburst cycle. Figure 6.9 illustrates these variances. The plot displays the spectral states together with their corresponding disk heights. We observe that the disk height decreases in the quiescence/low-hard state (QS/LS), rises through the high luminous spectral states, and reaches its maximum in the very high luminous state (VHS). We discovered that when the spectral state changes, so does the disk's shape. An evolution of accretion disk height with the spectral state is presented in figure 6.8 for the Kerr parameter $a = 0.50$. For the quiescence/low-hard state accretion rate is low ($\dot{\mathcal{M}}_E = 0.09$), thus the disk height is also very low (lower right panel). The disk height for the intermediate state, where $\dot{\mathcal{M}}_E = 0.25$ is shown in the upper right panel. In the two left panels, the height is plotted for high/soft and very high states, where the accretion

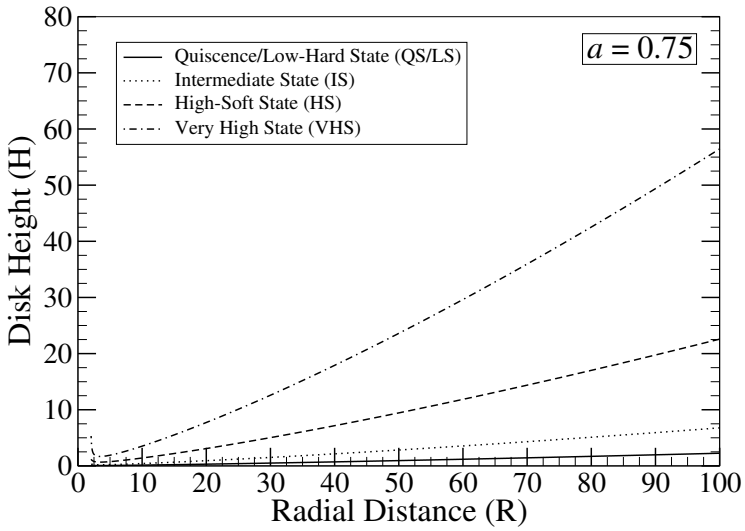


**FIGURE 6.9:** The variation of accretion disk height for different spectral states is shown. We plot disk height $H$ for the spin parameter $a = 0.75$. We use the accretion rate for QS/LS, IS, HS, VHS states as $\dot{\mathcal{M}}_E = 0.04$, 0.12, 0.4, 1 Eddington rate (Esin et al., 1998) respectively. We see that with the increase of accretion rate, disk height increases successively. The QS/LS has the minimum disk height and HS and VHS possess the maximum disk height.

rate is $\dot{\mathcal{M}}_E = 0.5$ and 1 Eddington rate. We see that disk height increases in each panel with an increasing accretion rate. Interestingly, there are several pioneering disk models. Each model closely describes a particular spectral state of XRBs. The well-known thin SS disk best describes the high/soft state. The optically thin ADAF well-demonstrates the under-luminous sources in hard and quiescent states. The disk luminosity in a very high state (e.g., XTE J1550-564), the slim disk, or the optically thick ADAF are important. The TCAF model explains the transition from hard to soft states for a number of sources and for their spectral fitting. The TCAF solution is based on NT73, the disk height prescription, or an equivalent pseudo-Newtonian potential formulation. We thus consider the flow variables of SS-disk, TCAF-disk, and ADAF-disk and compare the vertical thickness in soft, intermediate, hard, and quiescent states. The figure 6.10 shows the vertical height in various spectral states as predicted by associated disk models.

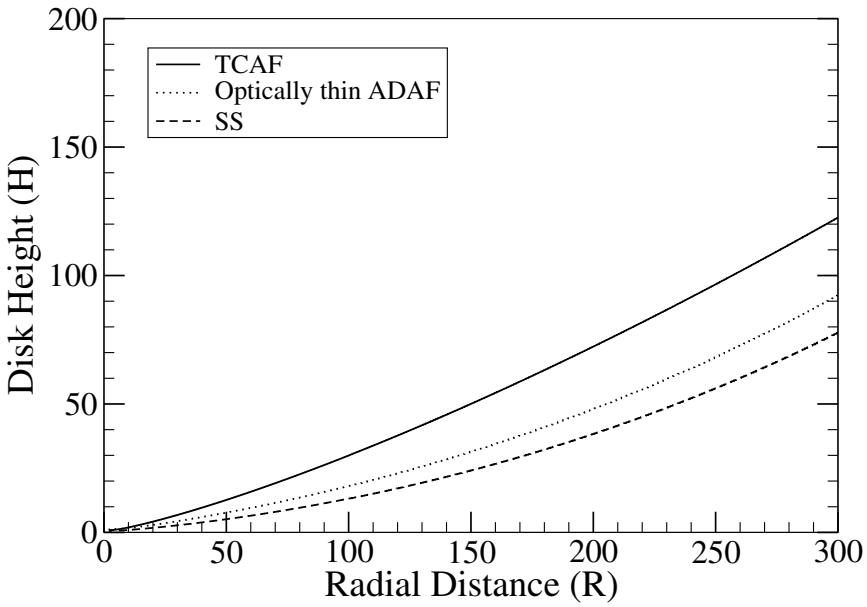


**Figure 6.10:** The variation of accretion disk height with the radial distance is presented using the rest-mass density of three well known disk model namely SS (Shakura & Sunyaev, 1973) TCAF (Chakrabarti, 1995, 1997; Chakrabarti & Titarchuk, 1995) and ADAF (Narayan & Yi, 1995b) for the Kerr parameter $a = 0.50$. The *dotted curve solid curve* and *dashed curve* is drawn for our height $H$ with the rest mass density given by SS, ADAF and TCAF disk model. We consider the other internal flow parameter same for all the cases.

# Chapter 7

## Final Conclusion & Future Work

The goal of this dissertation is to forecast the distinctive signature on the emitted gravitational wave signal, made by accretion disks surrounding the central supermassive black hole of an extreme/intermediate mass ratio inspiral system. We anticipate detecting signals from merging SMBH systems in the near future as the area of low-frequency (milli-hertz) GW astronomy advances. The objective of this research is to understand how an accretion disk influences an inspiralling SMBH binary, with the underlying goal of using this knowledge to interpret and supplement future GW detections. We investigate the perturbations caused to the orbit of the companion BH by the accretion embedded extreme/intermediate mass ratio inspiral using a hydrodynamic model of a thin disk governed by the transonic flow. The task of predicting accretion disk signatures surrounding coalescing black hole binaries requires modeling gas dynamics around accreting binary systems, which involves a variety of intricate physical processes. An in-depth investigation of accretion models reveals that no relativistically accurate accretion rate in curved space time is currently accessible. Therefore, as our main study progresses, we also calculate an accurate relativistic formalism to determine the accretion disk's vertical height in terms of the spin parameter. We summarize and discuss our significant findings and address remaining and future work in the rest of the section.

1. For the purpose of estimating the vertical height of the accretion disk, we provide a precise relativistic approach in Chapter 6. We determined a complete general relativistic connection between vertical height and accretion rate. When calculating the radial hydrodynamical equation, the formalism for relativistic mass accretion rate should be used instead of the well-known formula $\dot{M} = 2\pi r H \rho u^r$, which is used in the normal analysis of the accretion process around compact objects (Sądowski et al., 2011; Peitz & Appl, 1997; Chakrabarti, 1996a). The above expression has been amended using our formula, proving that height $H$ does not depend linearly on $\dot{M}$. The non-linearity is caused by the compact object's spin parameter $a$. The classic height-mass flux relation formula is true in Schwarzschild space-time for $a = 0$. Because the impact increases with disk thickness, it is significant for thin or thick disks and rapidly revolving compact stars. In order to obtain a comprehensive general relativistic version of the radial solutions, our height mass flux formula should be used in conjunction with a general relativistic version of an alternate expression of height in terms of flow parameters derived using static or dynamic equilibrium conditions in the vertical direction. As far as we are aware, there is no mention of such an expression in any recognized works of literature. However, in the near future, the general relativistic expression

of the accretion rate could be used to develop the exact relativistic vertical model of the thin accretion disk.

2. In our research work, we obtain the optimal orbital parameters (see Chapter 3) that LISA can detect with the desired precision/range. Our rigorous mathematical formulations ensure the validity of our findings. We used a semi-relativistic method in which radiation fluxes were estimated using Ryan's formula (Ryan, 1995, 1996) and particle motion was studied by taking into account the geodesic motion of the background space-time. Because Ryan's fluxes may also be calculated from Teukolosky formalism in the weak field limit, they are very significant. Our method works well over longer distances, but in strong field areas, especially when the separation is close to the ISCO, Teukolsky formalism or higher order PN corrections are more accurate than eqn. (3.24), (3.25). Those corrections, however, are at least an order of magnitude lower than the leading-order terms. As a result, in this regime, the priorities of such corrections are less relevant than the environmental effect induced by an accretion disk. Our results show that the effect of the accretion disk is obvious in the leading-order analysis of the radiation flow formula and that the values of the optimal parameters can be estimated from it unless high-order accuracy is required for these parameters. The readers may find some interesting insight into these problems in (Zwick et al., 2023). We used a method to determine the greatest hydrodynamic disk drag accessible for specific orbital configurations of the EMRIs at a distance of 1 GPc in order to arrive at the best orbital parameters. The impact of disk drag changes depending on system variables such as eccentricity ($e$), semi-major axis ($X$), mass ratio of EMRI, spin ($a$), and SMBH. Therefore, we investigate these variables to identify the elliptical form that has the greatest disk drag. A relativistic calculation of the effect of hydrodynamic drag yields a more accurate estimate of the disk-companion interaction than earlier Newtonian predictions (Barausse & Rezzolla, 2008). The companion motion is investigated using the geodesic equation in pure Kerr background space time, which may reliably estimate optimal parameters by providing sufficient information on the companion dynamics.

3. In chapter 4, we obtained observable effects of the transonic accretion disk, though small compared to the leading-order amplitude of the gravitational wave emitted from an E/IMRI, still detectable by the proposed detector LISA (see chapters 1, 4). In an EMRI system, we explored the total change in energy and angular momentum of a companion BH in an eccentric orbit around a spinning central SMBH generated by GW emission in the presence of an accretion disk.We investigate the influence of hydrodynamic drag in a relativistic context (e.g., Barausse & Rezzolla (2008)), which provides a more precise assessment of disk-companion interaction than earlier Newtonian predictions. We found that drag effects are most evident in the late stages of inspiral and vary greatly depending on the hydrodynamic model of the accretion flow as the drag effects become more substantial, mainly in the inner area of the disk. Moreover, we also see that the impact of disk drag is more pronounced in transonic accretion flow than in other disk models. This might be specifically why, in the early investigations, the influence of the disk was not thought to be relevant for calculating templates for matched filtering techniques. As a result, the phase acquired by the companion in a real or ideal E/IMRI system differs and is observable (Derdzinski et al.,

2019a; Kocsis et al., 2011), which we have obtained here. We also found that the impact due to hydrodynamic drag force in the disk's presence became significant in a long-term evolution. However, there are some issues that need to be discussed in order to address such consequences. The question arises regarding how many I/EMRI coalescence events there are in the universe that are detectable by GW detectors. The highest severe ratio that might be seen by GW detectors that are based on Earth is $1M_{\odot}/300M_{\odot}$. As opposed to this, the LISA range could detect the companion mass $> 1M_{\odot}$ spiraling into the central body of mass $3 \times 10^5 M_{\odot}$ to $3 \times 10^9 M_{\odot}$ at a distance of 3Gpc (Thorne, 1998). Local galaxies with such I/EMRI systems have already been discovered by recent observations, and LISA anticipates detecting a growing number of these occurrences. The next inquiry is: "Do these detected I/EMRIs have an accretion disk?" In our universe, most galaxies have accretion disks that may accrete at sub-Eddington, Eddington, or super-Eddington rates (Narayan, 2000). The majority of active galaxies, like AGNs, sometimes reach the Eddington or super-Eddington luminosity limit. Though minimal, the existence of AGN in the observed field of the space-based detector LISA is not insignificant. Examples of these include quasars, Seyfert galaxies, etc. At least 0.16% of active galaxies might be accessed by LISA's redshift range. Also, EMRIs formed through the wet channel increase the EMRI production rate by orders of magnitude (Tagawa et al., 2020; Pan & Yang, 2021; Pan et al., 2021; Vázquez-Aceves et al., 2022) Our main focus is on sources where the SMBHs accrete at the Eddington or super Eddington rate, where the hydrodynamic drag is more pronounced and hence more likely to be detected. The disk flow's velocity profile is crucial for estimating disk drag impacts. Choosing an accretion disk model will determine the result. So which model of accretion flow more accurately represents the attributes of the gas-rich environment? is the third problem that has now come to light. In the neighborhood of AGN, a low angular momentum flow is favored by a high Eddington luminosity and may sustain a high accretion rate. Furthermore, matter is predicted to be subsonic at a distance and transition to supersonic closer to the BH horizon. Transonic accretion flows are the most accurate and consistent mathematical model of this flow, as shown by (Muchotrzeb, 1983; Matsumoto et al., 1984; Lu, 1985; Fukue, 1987; Chakrabarti, 1990a,b). Such flows are non-Keplerian, and therefore, the difference between the Keplerian angular momentum of the companion and the disk causes significant changes in companion momentum. Furthermore, the transonic flows' large radial velocities further intensify the hydrodynamic drag's effects. Therefore, it is anticipated that the dynamics and trajectories of I/EMRI will have a noticeable impact on the long-term development of the orbit. We consider E/IMRIs embedded in transonic flows and obtain maximum disk drag than other models (Abramowicz & Zurek (1981); Chakrabarti (1990a, 1996a); Lu et al. (1997); Chakrabarti (1993); Yunes et al. (2011); Kocsis et al. (2011); Derdzinski et al. (2019a); Garg et al. (2022)).

4. We use SNR to determine the optimal parameters. When taking into account a 4-year duration for each observation in the LISA band, the estimated SNR is calculated from the dephasing of the transmitted GW signal (disk present or not). In each scenario, we consider the observation period from ISCO. In the majority of cases, we select a fixed Kerr parameter in our analysis, which fixes the ISCO radii. With the exception of the circumstances when

we modify the spin and some arbitrariness may result in some inaccuracy due to the non-fixing ISCO, the parameter estimate was therefore done well and accurately in the majority of cases. Particularly in the context of EMRIs, the problem of parameter measurement during GW monitoring is more complex than obtaining an SNR threshold of 8. When high precessional measurements are necessary, alternative processes may be more useful in predicting the parameters and become more significant. In order to maximize the values of the parameters in terms of detectability, we use the SNR estimation approach (see Chapter 4). Based on the initial orbital parameters, the disk drag's imprint changes. According on the system's initial configuration, different torques are provided. We come to the conclusion that a high eccentric orbit offers the most disk drag and would be more likely for detection after considering a variety of possible eccentric orbits, calculating the dephasing caused by them in the presence of an accretion disk, and finding the associated SNR for each dephasing. The ideal LISA observational parameters for sources that are 1 GPc distant are determined to be $e \geq 0.2$. We also determine the variance in dephasing and the likelihood that it would be detected by taking into account several orbits with semi-major axes $(200r_g, 500r_g, 900r_g)$. We discover that orbits with lower semi-major axes have the greatest effect on drag. The semi-major axis' ideal value for this study is $X = 1000r_g$. The corresponding value of semi-latus rectum $(p)$ can be obtained from here in order to specify an elliptical orbit with $(e, p)$. Then, by altering the SMBH and companion's mass as well, we compare the torque and SNR of dephasing (see Chapter 4). With two mass ratios, $10^{-3}\&10^{-4}$, and a central SMBH mass of $10^5 M_\odot$, we can observe that the amplitude of the torque grows by an order of magnitude for the $10^{-3}$ system. In contrast, the system with a mass ratio of $10^{-3}$ is more detectable. Finally, by altering the spin of the central SMBH, we compare the torque and SNR of dephasing. As the spin increases, the SNR degrades. We also discover that the prograde spins are less likely to be detected since the retrograde spins offer disk torque that is an order of magnitude larger. We present the SNR for each observation and calculate its corresponding detection probability as a final assessment. As previously stated, the event rate that LISA may detect is $1 - 10^2$ EMRIs per year from the dry channel and $10 - 10^4$ EMRIs per year from the wet channel (accretion embedded). One may filter the events and give precedence to the chosen orbits for future space-borne detectors by knowing the optimum orbital parameters, mass ratio, and spin of the SMBH.

5. The sensitivity of the emitted gravitational waveform to the drag effects opens up the possibility of inferring about the type of the accretion disk. The strength of the hydrodynamic drag and, consequently, the emitted GW profile noticeably vary with the chosen hydrodynamic models of the accretion flow (Basu, 2018)(see chapter 4). The gravitational wave can therefore act as a probe to learn more about the characteristics of accretion disks. Additionally, the accretion rate and the hydrodynamic model selection have an impact on the projected SNR. The differing choices made for these two factors may greatly change the estimated optimal parameters. Correct knowledge of the accretion disk's nature and the rate of accretion is necessary for an accurate parameter estimate. These problems mentioned above might be resolved through electromagnetic observations. One can also change the disk characteristics to increase the estimated orbital parameters' accuracy, but that is

outside the scope of the current investigation and will be covered later.

6. We concentrate on how the self-accretion of the companion BH affects the strain of the observed GW and how it affects the calculation of the companion BH's mass (see Chapter 5). In doing so, we also find out the parameter dependence of the loss rates, namely energy, angular momentum, mass accretion rate, companion trajectories, i.e., eccentricity, and radial distances. We particularly consider the drag effects on the estimation of mass of the companion BH due to its self-accretion and how this changes with various parameters in the presence of a thin and transonic accretion disk. We also discuss the detectability of the disk impacts.However, the main issue is whether the sensitivity of today's detectors can actually detect these drag effects. Here, we'd like to point out that a lot of research has already been done to explain dark energy and dark matter using concepts like $f(R)$ gravity, $f(T)$ gravity, scalar-tensor gravity, Gauss-Bonnet gravity, and teleparallel equivalent general relativity, a proposal for replacing Einstein's gravity theory (GR). The sensitivity of the detectors must be improved to be more precise and sophisticated in order to test these theorems (e.g., $h \sim 10^{24-26}$) (Bogdanos et al., 2010). The next step towards accurate astronomy must be the detector's ability to detect such dephasing. The precisional accuracy of the detectors is anticipated to grow by many orders in the near future, and with such accuracy, the influence of the accretion disk previously examined might be detectable. As a consequence, we draw the conclusion that mainstream research must take into account the effect of drag due to the presence of transonic flow while creating GW templates; otherwise, if the potential impact of accretion is disregarded, that may affect the accuracy of the outcome.

7. Our set of waveform models, established in vacuum, has to be upgraded to account for environmental factors in order to identify and reliably estimate parameters from these near-extremal sources. In this work (see chapter 5), we discuss the variations in several parameters of the EMRI companions immersed in a transonic accretion flow in Kerr space time, such that substantial precision may be obtained from limits on parameter estimations. The energy and angular momentum losses for various drag effects are compared. We talk about how these loss rates rely on several characteristics, such as the mass accretion rate, eccentricity, and Kerr parameter. We discovered that the largest loss rates for a compact massive companion are caused by GW emission, followed by accretion and deflection. Spinning black holes have higher loss rates from accretion and deflection. We found that lower eccentric orbits lost energy and angular momentum more slowly than more eccentric orbits when we compared orbits with different eccentricities. We also looked at the variations in the mass parameters with respect to factors like eccentricity, accretion rate, and spin in this work. We find that variations in mass rates rise with increasing accretion rates, and we also find that the companion black hole mass tends to fluctuate more in a low eccentric orbit. We observe from SNR calculations that these changes are observable, and hence these results must be included in the new GW waveform in order to precisely constrain the black hole parameters.

8. Since the accretion rate directly affects GW observations, it may be possible to estimate the accretion rate using GW observations, which will be helpful to confirm the connection indicated above. The Super Eddington accretion rate is supported by our chosen accretion disk model. However, this can be done in the future because it is outside the purview of

our current study. A number of alternate models of the accretion disks exist, and accretion processes are currently only understood in terms of EM signals. One may separately test the various accretion physics paradigms by utilizing the sensitivity of GW profiles to the disk's hydrodynamic variables (Chakrabarti, 1996c). As a result, by simultaneously observing GW and EM waves, it will be possible to evaluate different accretion physics paradigms and constrain the accretion parameters.

# Appendices

# Appendix A

## Relative velocity calculation

The expression of the relative velocity is obtained by considering the following:

$$W^a = \lambda U^a + U^a_\perp \tag{A.1}$$

where $W^a$ and $U^a$ are the four velocities of particle B and A respectively.

$$W^a U_a = \lambda U^a U_a + U^a_\perp U_a \tag{A.2}$$

Let us choose $\lambda = \frac{W^a U_a}{U^a U_a}$ , then $U^a_\perp U_a = 0$.

Therefore $U^a$ is time like and $U^a_\perp$ is space like in the rest frame of the particle A,

$$U^a = \begin{bmatrix} 1 \\ 0 \\ 0 \\ 0 \end{bmatrix} \qquad U^a_\perp = \begin{bmatrix} 0 \\ U'^1_\perp \\ U'^2_\perp \\ U'^3_\perp \end{bmatrix} \quad \text{and} \quad W^a = \begin{bmatrix} \lambda \\ U'^1_\perp \\ U'^2_\perp \\ U'^3_\perp \end{bmatrix} \tag{A.3}$$

Therefore

$$\frac{dt'_B}{d\tau_B} = \lambda = \frac{1}{\sqrt{1 - \frac{V'^2_B}{c^2}}} \tag{A.4}$$

Where $V'_B$ is the magnitude of the velocity of B in the rest frame of A.

$$\frac{1}{\sqrt{1 - \frac{V'^2_B}{c^2}}} = \lambda = W^a U_a \qquad [U^a U_a = +1] \tag{A.5}$$

$$\sqrt{1 - V'^2_B} = \frac{1}{W^a U_a} \qquad [c = 1] \tag{A.6}$$

$$1 - V'^2_B = \frac{1}{(W^a U_a)^2} \tag{A.7}$$

$$V'^2_B = 1 - \frac{1}{(W^a U_a)^2} \tag{A.8}$$

$$V'_B = \frac{\sqrt{(W^a U_a)^2 - 1}}{W^a U_a} \tag{A.9}$$

$$W^a U_a = W^0 U_0 + W^i U_i \tag{A.10}$$

In the rest frame of A , $U_i = 0$. Therefore $W^a U_a = W^0 U_0$. Both $W^0$ and $U^0 \geq 1$ for any particle following a time like world line. Therefore $(W^0 U_0)^2 \geq 1$ in the rest frame of A, but in that frame $W^0 U_0 = W^a U_a$ which is a scalar.
Therefore $W^a U_a \geq 1$ in any frame.

# Appendix B

## Lorentz Factor

Let us consider two particles A and B having four velocities $U^\mu$ and $V^\mu$ respectively. Let us write $V^\mu$ as ,

$$V^\mu = \lambda U^\mu + \tilde{V}^\mu \tag{B.1}$$

Let us choose

$$\lambda = \frac{U^\mu V_\mu}{U^\mu U_\mu} \qquad \text{then}$$

$$\begin{aligned} U^\mu V_\mu &= \lambda U^\mu U_\mu + U^\mu \tilde{V}_\mu \\ U^\mu V_\mu &= \frac{U^\mu V_\mu}{U^\mu U_\mu} U^\mu U_\mu + U^\mu \tilde{V}_\mu \\ U^\mu \tilde{V}_\mu &= 0 \end{aligned} \tag{B.2}$$

Let $\Lambda^\mu_\nu$ are the elements of Lorentz transformation which takes an observer to the rest frame of the particle A (having four velocity $U^\mu$) from the frame where A has the four velocity $U^\mu$ then

$$U'^\mu = \Lambda^\mu_\nu U^\nu \qquad \text{four velocity of A in its rest frame}$$

$\therefore$

$$U'^\mu = (U'^0, 0, 0, 0)$$

then

$$\tilde{V}'_\mu U^\mu = \tilde{V}_\mu U^\mu = 0$$

which imply

$$\tilde{V}'^0 = 0, \tilde{V}'^i \neq 0$$

Here

$$\tilde{V}'^\mu = \Lambda^\mu_\nu V^\nu$$

Further the condition
$U^\mu U_\mu = 1$ imply $U'^\mu U'_\mu = 1$ or $(U'^0)^2 = 1, U'^0 = 1$
The four velocity of the particle B in the rest frame of A is then given by,

$$\begin{aligned} V'^{\mu} &= \Lambda^{\mu}_{\nu} V^{\mu} \\ &= \lambda \Lambda^{\mu}_{\nu} U^{\nu} + \Lambda^{\mu}_{\nu} \tilde{V^{\nu}} \end{aligned} \tag{B.3}$$

$\therefore$

$$V'^{0} = \lambda U'^{0} = \lambda \qquad V'^{i} = \tilde{V}'^{i}$$

The Lorentz factor of B w.r.t the rest frame of A is

$$V'^{0} = \lambda = \frac{U^{\mu} V_{\mu}}{(U_{\nu} U^{\nu})} = \gamma \tag{B.4}$$

Therefore,

$$\gamma = \boldsymbol{U^{fluid}.U_{sat}} \tag{B.5}$$

# Appendix C

## Derivatives used in the Mass-strain Relation

We begin with a test body traveling in a Kerr gravitational field, whose radial coordinate is given by **?**,

$$r = \frac{p}{(1 + e\cos\chi)} \tag{C.1}$$

From here we obtain,

$$\frac{dr}{d\tau} = \frac{e\sin\chi}{p} V_r \tag{C.2}$$

The $\phi$ and $t$ are also given by**?**,

$$\phi(\chi) = \int_0^\chi d\chi \frac{V_\phi}{J.V_r}, \qquad \frac{d\phi}{d\chi} = \frac{V_\phi}{JV_r} \tag{C.3}$$

$$t(\chi) = \int_0^\chi d\chi \frac{V_t}{J.V_r}, \qquad \frac{dt}{d\chi} = \frac{V_t}{JV_r} \tag{C.4}$$

where

$$V_r = \sqrt{[(x^2 + a^2 + 2axE) - \frac{2x^2M}{p}(3 + e\cos\chi)]} \tag{C.5}$$

$$V_r' = \frac{dV_r}{d\chi} = \frac{Mx^2 e\sin\chi}{pV_r} \tag{C.6}$$

The derivative w.r.t $M$,

$$V_{rM} = -\frac{x^2}{V_r p}(3 + e\cos\chi) \tag{C.7}$$

$$V_{rM}' = \frac{x^2 e\sin\chi}{pV_r} - \frac{Mx^2 e\sin\chi}{pV_r^2} V_{rM} \tag{C.8}$$

$$V_\phi = (x + aE) - \frac{2Mx}{p}(1 + e\cos\chi) \tag{C.9}$$

$$V_{\phi M} = -\frac{2x}{p}(1 + e\cos\chi) \tag{C.10}$$

$$V_\phi' = \frac{dV_\phi}{d\chi} = \frac{2Mxe\sin\chi}{p} \tag{C.11}$$

$$V_{\phi M}' = \frac{2xe\sin\chi}{p} \tag{C.12}$$

$$V_t = a^2 E - \frac{2aMx}{p}(1 + e\cos\chi) + \frac{p^2 E}{(1 + e\cos\chi)^2} \tag{C.13}$$

$$V_{tM} = -\frac{2ax}{p}(1 + e\cos\chi) \tag{C.14}$$

$$V_t' = \frac{dV_t}{d\chi} = \frac{2aMxe\sin\chi}{p} + \frac{2p^2 Ee\sin\chi}{(1 + e\cos\chi)^3} \tag{C.15}$$

$$V_{tM}' = \frac{2axe\sin\chi}{p} \tag{C.16}$$

$$J = 1 - \frac{2M}{p}(1 + e\cos\chi) + \frac{a^2}{p^2}1 + e\cos\chi^2 \tag{C.17}$$

$$J_M = -\frac{2}{p}(1 + e\cos\chi) \tag{C.18}$$

$$J' = \frac{dJ}{d\chi} = \frac{2Me\sin\chi}{p} - \frac{2a^2 e\sin\chi}{p^2}(1 + e\cos\chi) \tag{C.19}$$

$$J_M' = \frac{2e\sin\chi}{p} \tag{C.20}$$

here $x = L - aE$. Note that $\chi = 0$ at $r = r_p$ to $\chi = \pi$ at $r = r_a$ and finally upto $\chi = 2\pi$ at $r = r_p$.

We have,

$$E(\chi) = \frac{pe\sin\chi}{(1 + e\cos\chi)^2} \tag{C.21}$$

$$E(\chi)' = \frac{dE(\chi)}{d\chi} = \frac{pe\sin\chi}{(1 + e\cos\chi)^2} + \frac{2pe^2\sin^2\chi}{(1 + e\cos\chi)^3} \tag{C.22}$$

$$E(\chi)_M = 0 \tag{C.23}$$

$$E(\chi)_M' = 0 \tag{C.24}$$

## C.1 Derivatives of $r$

We can write using the above quantities,

$$\dot{r} = \frac{dr}{d\chi}\frac{d\chi}{dt} = \frac{E(\chi)JV_r}{V_t} \tag{C.25}$$

where

$$\frac{dr}{d\chi} = \frac{pe\sin\chi}{(1 + e\cos\chi)^2} = E(\chi) \tag{C.26}$$

$$\frac{dt}{d\chi} = \frac{V_t}{JV_r} \qquad \text{From equation (C.4)} \tag{C.27}$$

The derivative w.r.t $M$ of $\dot{r}$ is,

$$\dot{r}_M = \dot{r}[\frac{E(\chi)_M}{E(\chi)} + \frac{J_M}{J} + \frac{V_{rM}}{V_r} - \frac{V_{tM}}{V_t}] \tag{C.28}$$

$$\begin{aligned}
\ddot{r} &= \frac{d}{d\chi}[\frac{E(\chi)JV_r}{V_t}].\frac{d\chi}{dt} \\
&= \frac{d}{d\chi}[\frac{E(\chi)JV_r}{V_t}].\frac{JV_r}{V_t} \\
&= \frac{\dot{r}^2}{E(\chi)}[\frac{E(\chi)'}{E(\chi)} + \frac{J'}{J} + \frac{V_r'}{V_r} - \frac{V_t'}{V_t}]
\end{aligned} \tag{C.29}$$

$$\begin{aligned}
\ddot{r}_M = {} & \frac{2\dot{r}\frac{\partial \dot{r}}{\partial M}}{E(\chi)}[\frac{E(\chi)'}{E(\chi)} + \frac{J'}{J} + \frac{V_r'}{V_r} - \frac{V_t'}{V_t}] - \frac{\dot{r}^2 E(\chi)_M}{E(\chi)^2}[\frac{E(\chi)'}{E(\chi)} + \frac{J'}{J} + \frac{V_r'}{V_r} - \frac{V_t'}{V_t}] \\
& + \frac{\dot{r}^2}{E(\chi)}[(\frac{E(\chi)'_M}{E(\chi)} - \frac{E(\chi)'E(\chi)_M}{E(\chi)^2}) + (\frac{J'_M}{J} - \frac{J'J_M}{J^2}) + (\frac{V'_{rM}}{V_r} - \frac{V_r'V_{rM}}{V_r^2}) - (\frac{V'_{tM}}{V_t} - \frac{V_t'V_{tM}}{V_t^2})] \\
= {} & \frac{2\dot{r}_M\ddot{r}}{\dot{r}} - \frac{\ddot{r}E(\chi)_M}{E(\chi)} + \frac{\dot{r}^2}{E(\chi)}[(\frac{E(\chi)'_M}{E(\chi)} - \frac{E(\chi)'E(\chi)_M}{E(\chi)^2}) + (\frac{J'_M}{J} - \frac{J'J_M}{J^2}) \\
& + (\frac{V'_{rM}}{V_r} - \frac{V_r'V_{rM}}{V_r^2}) - (\frac{V'_{tM}}{V_t} - \frac{V_t'V_{tM}}{V_t^2})] \\
= {} & \ddot{r}(\frac{2\dot{r}_M}{\dot{r}} - \frac{E(\chi)_M}{E(\chi)}) + \frac{\dot{r}^2}{E(\chi)}[(\frac{E(\chi)'_M}{E(\chi)} - \frac{E(\chi)'E(\chi)_M}{E(\chi)^2}) + (\frac{J'_M}{J} - \frac{J'J_M}{J^2}) \\
& + (\frac{V'_{rM}}{V_r} - \frac{V_r'V_{rM}}{V_r^2}) - (\frac{V'_{tM}}{V_t} - \frac{V_t'V_{tM}}{V_t^2})]
\end{aligned} \tag{C.30}$$

## C.2 Derivative of $\phi$

$$\begin{aligned}
\dot{\phi} &= \frac{d\phi}{d\chi}\frac{d\chi}{dt} = \frac{V_\phi}{V_t} \\
\dot{\phi}_M &= \frac{\partial \dot{\phi}}{\partial M} = \dot{\phi}[\frac{V_{\phi M}}{V_\phi} - \frac{V_{tM}}{V_t}]
\end{aligned} \tag{C.31}$$

$$\begin{aligned}
\ddot{\phi} &= \frac{d}{d\chi}(\frac{V_\phi}{V_t})\frac{JV_r}{V_t} \\
&= (\frac{V_\phi'}{V_t} - \frac{V_\phi V_t'}{V_t^2})\frac{\dot{r}}{E(\chi)} \\
&= \frac{\dot{\phi}\dot{r}}{E(\chi)}(\frac{V_\phi'}{V_\phi} - \frac{V_t'}{V_t})
\end{aligned} \tag{C.32}$$

$$\begin{aligned}\ddot{\phi}_M &= \frac{\dot{\phi}_M \dot{r}}{E(\chi)}(\frac{V'_\phi}{V_\phi} - \frac{V'_t}{V_t}) + \frac{\dot{\phi}\dot{r}_M}{E(\chi)}(\frac{V'_\phi}{V_\phi} - \frac{V'_t}{V_t}) - \frac{\phi\dot{r}E(\chi)_M}{E(\chi)^2}(\frac{V'_\phi}{V_\phi} - \frac{V'_t}{V_t}) \\ &+ \frac{\dot{\phi}\dot{r}}{E(\chi)}[(\frac{V'_{\phi M}}{V_\phi} - \frac{V'_\phi V_{\phi M}}{V_\phi^2}) - (\frac{V'_{tM}}{V_t} - \frac{V'_t V_{tM}}{V_t^2})] \\ &= \ddot{\phi}(\frac{\dot{\phi}_M}{\dot{\phi}} + \frac{\dot{r}_M}{r} - \frac{E(\chi)_M}{E(\chi)}) + \frac{\dot{\phi}\dot{r}}{E(\chi)}[(\frac{V'_{\phi M}}{V_\phi} - \frac{V'_\phi V_{\phi M}}{V_\phi^2}) - (\frac{V'_{tM}}{V_t} - \frac{V'_t V_{tM}}{V_t^2})]\end{aligned} \tag{C.33}$$

## C.3 Derivatives of the $R$

$$R = r^2 \tag{C.34}$$

$$R_M = 0 \tag{C.35}$$

$$\dot{R} = 2r\dot{r} \tag{C.36}$$

$$\dot{R}_M = 2r\dot{r}_M \tag{C.37}$$

$$\ddot{R} = 2r\ddot{r} + 2\dot{r}^2 \tag{C.38}$$

$$\ddot{R}_M = 2r\ddot{r}_M + 4\dot{r}\dot{r}_M \tag{C.39}$$

# BIBLIOGRAPHY


Abbott, B. P., & et. al. 2016, Phys. Rev. Lett., 116, 061102, doi: 10.1103/PhysRevLett.116.061102

—. 2017, ApJL, 851, L16, doi: 10.3847/2041-8213/aa9a35

Abbott, B. P. e. a., LIGO Scientific Collaboration, & Virgo Collaboration. 2019, Physical Review X, 9, 031040, doi: 10.1103/PhysRevX.9.031040

Abe, Y., Fukazawa, Y., & Kubota, A. 2004, Progress of Theoretical Physics Supplement, 155, 303, doi: 10.1143/PTPS.155.303

Abramowicz, M., Jaroszynski, M., & Sikora, M. 1978, A & A, 63, 221

Abramowicz, M. A., Chen, X., Kato, S., Lasota, J.-P., & Regev, O. 1995, ApJL, 438, L37, doi: 10.1086/187709

Abramowicz, M. A., Chen, X. M., Granath, M., & Lasota, J. P. 1996, ApJ, 471, 762, doi: 10.1086/178004

Abramowicz, M. A., Czerny, B., Lasota, J. P., & Szuszkiewicz, E. 1988, ApJ, 332, 646, doi: 10.1086/166683

Abramowicz, M. A., & Fragile, P. C. 2013, Living Reviews in Relativity, 16, 1, doi: 10.12942/lrr-2013-1

Abramowicz, M. A., Lanza, A., & Percival, M. J. 1997, ApJ, 479, 179, doi: 10.1086/303869

Abramowicz, M. A., & Zurek, W. H. 1981, ApJ, 246, 314, doi: 10.1086/158924

Aguiar, O. D., & et. al. 2006, Classical and Quantum Gravity, 23, S239, doi: 10.1088/0264-9381/23/8/S30

Akiyama, K., & et. al. 2022, ApJL, 930, L12, doi: 10.3847/2041-8213/ac6674

Alfonso, W. D., Sánchez, L. A., & Mosquera, H. J. 2015, Astronomische Nachrichten, 336, 815, doi: 10.1002/asna.201512222

Amaro-Seoane, P. 2018, Living Reviews in Relativity, 21, 4, doi: 10.1007/s41114-018-0013-8

Amaro-Seoane, P., Gair, J. R., Freitag, M., et al. 2007, Classical and Quantum Gravity, 24, R113, doi: 10.1088/0264-9381/24/17/R01

Amaro-Seoane, P., Gair, J. R., Pound, A., Hughes, S. A., & Sopuerta, C. F. 2015, in Journal of Physics Conference Series, Vol. 610, Journal of Physics Conference Series, 012002, doi: 10.1088/1742-6596/610/1/012002

Amaro-Seoane, P., Aoudia, S., Babak, S., et al. 2012, Classical and Quantum Gravity, 29, 124016, doi: 10.1088/0264-9381/29/12/124016

Amaro-Seoane, P., Audley, H., Babak, S., et al. 2017, arXiv e-prints, arXiv:1702.00786, doi: 10.48550/arXiv.1702.00786

Armano, M., Audley, H., Auger, G., et al. 2017, Phys. Rev. Lett., 118, 171101, doi: 10.1103/PhysRevLett.118.171101

Astone, P., Bassan, M., Bonifazi, P., et al. 1993, Phys. Rev. D, 47, 362, doi: 10.1103/PhysRevD.47.362

Astone, P., Bassan, M., Bonifazi, P., et al. 1996, Czechoslovak Journal of Physics, 46, 2907, doi: 10.1007/BF02570440

Babak, S., Gair, J., Sesana, A., et al. 2017, Physical Review D, 95, 103012, doi: 10.1103/PhysRevD.95.103012

Baibhav, V., Barack, L., Berti, E., et al. 2021, Experimental Astronomy, 51, 1385, doi: 10.1007/s10686-021-09741-9

Bailes, M., Berger, B. K., Brady, P. R., et al. 2021, Nature Reviews Physics, 3, 344, doi: 10.1038/s42254-021-00303-8

Balbus, S. A., & Mummery, A. 2018, Monthly Notices of the Royal Astronomical Society, 481, 3348, doi: 10.1093/mnras/sty2467

Barack, L., & Cutler, C. 2004a, Physical Review D, 70, 122002, doi: 10.1103/PhysRevD.70.122002

—. 2004b, Physical Review D, 69, 082005, doi: 10.1103/PhysRevD.69.082005

Barausse, E. 2007, Mon. Not. R. Astron. Soc., 382, 826, doi: 10.1111/j.1365-2966.2007.12408.x

Barausse, E., Cardoso, V., & Pani, P. 2014, Physical Review D, 89, 104059, doi: 10.1103/PhysRevD.89.104059

Barausse, E., Cardoso, V., & Pani, P. 2015, Journal of Physics: Conference Series, 610, 012044, doi: 10.1088/1742-6596/610/1/012044

Barausse, E., & Rezzolla, L. 2008, Physical Review D, 77, 104027, doi: 10.1103/PhysRevD.77.104027

Bardeen, J. M., Press, W. H., & Teukolsky, S. A. 1972, ApJ, 178, 347, doi: 10.1086/151796

Basu, P. 2018, in Exploring the Universe: From Near Space to Extra-Galactic, ed. B. Mukhopadhyay & S. Sasmal (Cham: Springer International Publishing), 39–49

Basu, P., Mondal, S., & Chakrabarti, S. K. 2008, Mon. Not. R. Astron. Soc., 388, 219, doi: 10.1111/j.1365-2966.2008.13368.x

Begelman, M. C. 1978, Mon. Not. R. Astron. Soc., 184, 53, doi: 10.1093/mnras/184.1.53

Begelman, M. C., & Meier, D. L. 1982, ApJ, 253, 873, doi: 10.1086/159688

Belloni, T. M. 2010, in Lecture Notes in Physics, Berlin Springer Verlag, ed. T. Belloni, Vol. 794, 53, doi: 10.1007/978-3-540-76937-8_310.48550/arXiv.0909.2474

Beloborodov, A. M. 1998, Mon. Not. R. Astron. Soc., 297, 739, doi: 10.1046/j.1365-8711.1998.01530.x

Berti, E., Yagi, K., & Yunes, N. 2018, General Relativity and Gravitation, 50, 46, doi: 10.1007/s10714-018-2362-8

Bezares, M., Bošković, M., Liebling, S., et al. 2022, Physical Review D, 105, 064067, doi: 10.1103/PhysRevD.105.064067

Blaes, O. 2014, Space Science Reviews , 183, 21, doi: 10.1007/s11214-013-9985-6

Blair, D. G., Ivanov, E. N., Tobar, M. E., et al. 1995, Phys. Rev. Lett., 74, 1908, doi: 10.1103/PhysRevLett.74.1908

Bogdanos, C., Capozziello, S., Laurentis, M. D., & Nesseris, S. 2010, Astroparticle Physics, 34, 236, doi: https://doi.org/10.1016/j.astropartphys.2010.08.001

Bondi, H. 1952, Mon. Not. R. Astron. Soc., 112, 195, doi: 10.1093/mnras/112.2.195

Bondi, H., & Hoyle, F. 1944, Mon. Not. R. Astron. Soc., 104, 273, doi: 10.1093/mnras/104.5.273

Bradley, C. K., & Frank, J. 2009, ApJ, 704, 25, doi: 10.1088/0004-637X/704/1/25

Brunner, H., Mueller, C., Friedrich, P., et al. 1997, A & A, 326, 885. https://arxiv.org/abs/astro-ph/9706118

Caditz, D. M., & Tsuruta, S. 1998, The Astrophysical Journal, 501, 242, doi: 10.1086/305794

Capozziello, S., & Bajardi, F. 2019, International Journal of Modern Physics D, 28, 1942002, doi: 10.1142/S0218271819420021

Carré, J., & Porter, E. K. 2010, arXiv e-prints, arXiv:1010.1641, doi: 10.48550/arXiv.1010.1641

Chakrabarti, S., & Titarchuk, L. G. 1995, ApJ, 455, 623, doi: 10.1086/176610

Chakrabarti, S. K. 1989, ApJ, 347, 365, doi: 10.1086/168125

—. 1990a, Theory of Transonic Astrophysical Flows, doi: 10.1142/1091

—. 1990b, Mon. Not. R. Astron. Soc., 243, 610

—. 1993, ApJ, 411, 610, doi: 10.1086/172863

Chakrabarti, S. K. 1995, in Seventeeth Texas Symposium on Relativistic Astrophysics and Cosmology, ed. H. Böhringer, G. E. Morfill, & J. E. Trümper, Vol. 759, 546, doi: 10.1111/j.1749-6632.1995.tb17605.x

—. 1996a, Mon. Not. R. Astron. Soc., 283, 325, doi: 10.1093/mnras/283.1.325

—. 1996b, ApJ, 471, 237, doi: 10.1086/177965

—. 1996c, Physical Review D, 53, 2901, doi: 10.1103/PhysRevD.53.2901

Chakrabarti, S. K. 1997, The Astrophysical Journal, 484, 313

Chakrabarti, S. K. 2017, in 14th Marcel Grossmann Meeting on Recent Developments in Theoretical and Experimental General Relativity, Astrophysics, and Relativistic Field Theories, Vol. 1, 369–384, doi: 10.1142/9789813226609_0020

Chakrabarti, S. K. 2018, in Fourteenth Marcel Grossmann Meeting - MG14, ed. M. Bianchi, R. T. Jansen, & R. Ruffini, 369–384, doi: 10.1142/9789813226609_0020

Chakrabarti, S. K., & Das, S. 2004, Mon. Not. R. Astron. Soc., 349, 649, doi: 10.1111/j.1365-2966.2004.07536.x

Chakrabarti, S. K., & Molteni, D. 1993, ApJ, 417, 671, doi: 10.1086/173345

Chakrabarti, S. K., Ryu, D., Molteni, D., et al. 1996, Journal of Korean Astronomical Society Supplement, 29, S229, doi: 10.48550/arXiv.astro-ph/9611071

Chakraborty, S., Navale, N., Ratheesh, A., & Bhattacharyya, S. 2020, Mon. Not. R. Astron. Soc., 498, 5873, doi: 10.1093/mnras/staa2711

Chandrasekhar, S. 1943, ApJ, 97, 255, doi: 10.1086/144517

Chatterjee, S., Mondal, S., & Basu, P. 2022, The Astrophysical Journal, 941, 131, doi: 10.3847/1538-4357/ac9f15

—. 2023, Monthly Notices of the Royal Astronomical Society, 526, 5612, doi: 10.1093/mnras/stad3132

Chatterjee, S., Mondal, S., & Basu, P. 2023, arXiv e-prints, arXiv:2307.12144, doi: 10.48550/arXiv.2307.12144

Chattopadhyay, I., & Chakrabarti, S. K. 2011, Int. J. Mod. Phys. D, 20, 1597, doi: 10.1142/S0218271811019487

Chen, X. 1995, Monthly Notices of the Royal Astronomical Society, 275, 641, doi: 10.1093/mnras/275.3.641

Chen, X., Abramowicz, M. A., & Lasota, J.-P. 1997, ApJ, 476, 61, doi: 10.1086/303592

Chen, X., Abramowicz, M. A., Lasota, J.-P., Narayan, R., & Yi, I. 1995, ApJL, 443, L61, doi: 10.1086/187836

Chen, X., & Han, W.-B. 2018, Communications Physics, 1, 53, doi: 10.1038/s42005-018-0053-0

Chen, X., & Taam, R. E. 1996, ApJ, 466, 404, doi: 10.1086/17751910.48550/arXiv.astro-ph/9606010

Chua, A. J. K., Moore, C. J., & Gair, J. R. 2017, Physical Review D, 96, 044005, doi: 10.1103/PhysRevD.96.044005

Coogan, A., Bertone, G., Gaggero, D., Kavanagh, B. J., & Nichols, D. A. 2022, Physical Review D, 105, 043009, doi: 10.1103/PhysRevD.105.043009

Cutler, C., & Thorne, K. S. 2002, arXiv e-prints, gr. https://arxiv.org/abs/gr-qc/0204090

Cutler, C., & Vallisneri, M. 2007, Physical Review D, 76, 104018, doi: 10.1103/PhysRevD.76.104018

Cutler, C., Apostolatos, T. A., Bildsten, L., et al. 1993, Physical Review Letters, 70, 2984, doi: 10.1103/PhysRevLett.70.2984

Daigne, F., & Font, J. A. 2004, Mon. Not. R. Astron. Soc., 349, 841, doi: 10.1111/j.1365-2966.2004.07547.x

Debnath, D., Chakrabarti, S. K., Mondal, S., et al. 2018, in Fourteenth Marcel Grossmann Meeting - MG14, ed. M. Bianchi, R. T. Jansen, & R. Ruffini, 1017–1022, doi: 10.1142/9789813226609_0054

Derdzinski, A., D'Orazio, D., Duffell, P., Haiman, Z., & MacFadyen, A. 2021, Mon. Not. R. Astron. Soc., 501, 3540, doi: 10.1093/mnras/staa3976

Derdzinski, A., & Mayer, L. 2023, Mon. Not. R. Astron. Soc., 521, 4522, doi: 10.1093/mnras/stad749

Derdzinski, A. M., D'Orazio, D., Duffell, P., Haiman, Z., & MacFadyen, A. 2019a, Mon. Not. R. Astron. Soc., 486, 2754, doi: 10.1093/mnras/stz1026

—. 2019b, Mon. Not. R. Astron. Soc., 489, 4860, doi: 10.1093/mnras/stz2435

Dokuchaev, V. P. 1964, Soviet Astronomy, 8, 23

Dominik, C. 2015, in European Physical Journal Web of Conferences, Vol. 102, European Physical Journal Web of Conferences, 00002, doi: 10.1051/epjconf/201510200002

Done, C., Gierliński, M., & Kubota, A. 2007, Publications of the Astronomical Society of Japan, 15, 1, doi: 10.1007/s00159-007-0006-110.48550/arXiv.0708.0148

Dunn, R. J. H., Fender, R. P., Körding, E. G., Belloni, T., & Cabanac, C. 2010, Mon. Not. R. Astron. Soc., 403, 61, doi: 10.1111/j.1365-2966.2010.16114.x

Eggum, G. E., Coroniti, F. V., & Katz, J. I. 1988, ApJ, 330, 142, doi: 10.1086/166462

Einstein, A. 1915a, Sitzungsber. Preuss. Akad. Wiss. Berlin (Math. Phys. ), 1915, 778

—. 1915b, Sitzungsber. Preuss. Akad. Wiss. Berlin (Math. Phys. ), 1915, 844

Esin, A. A., McClintock, J. E., & Narayan, R. 1997, ApJ, 489, 865, doi: 10.1086/30482910.48550/arXiv.astro-ph/9705237

Esin, A. A., Narayan, R., Cui, W., Grove, J. E., & Zhang, S.-N. 1998, ApJ, 505, 854, doi: 10.1086/306186

Event Horizon Telescope Collaboration, & Akiyama et. al. 2019, ApJL, 875, L1, doi: 10.3847/2041-8213/ab0ec7

Fafone, V. 2006, in Journal of Physics Conference Series, Vol. 39, Journal of Physics Conference Series, 42–45, doi: 10.1088/1742-6596/39/1/010

Fan, H.-M., Hu, Y.-M., Barausse, E., et al. 2020, Physical Review D, 102, 063016, doi: 10.1103/PhysRevD.102.063016

Fender, R. P., Belloni, T. M., & Gallo, E. 2004, Mon. Not. R. Astron. Soc., 355, 1105, doi: 10.1111/j.1365-2966.2004.08384.x10.48550/arXiv.astro-ph/0409360

Ferrari, V., Pizzella, G., Lee, M., & Weber, J. 1982, Phys. Rev. D, 25, 2471, doi: 10.1103/PhysRevD.25.2471

Finn, L. S., & Thorne, K. S. 2000, Physical Review D, 62, 124021, doi: 10.1103/PhysRevD.62.124021

Fishbone, L. G. 1973, ApJ, 185, 43, doi: 10.1086/152395

Font, J. A., & Daigne, F. 2002, Mon. Not. R. Astron. Soc., 334, 383, doi: 10.1046/j.1365-8711.2002.05515.x

Font, J. A., & Ibáñez, J. M. 1998, Mon. Not. R. Astron. Soc., 298, 835, doi: 10.1046/j.1365-8711.1998.01664.x

Font, J. A., Ibáñez, J. M., & Papadopoulos, P. 1999, Mon. Not. R. Astron. Soc., 305, 920, doi: 10.1046/j.1365-8711.1999.02459.x

Font, J. A., Ibáñez, J. M., & Papadopoulos, P. 1998, The Astrophysical Journal, 507, L67, doi: 10.1086/311666

Frank, J., King, A., & Raine, D. J. 2002, Accretion Power in Astrophysics: Third Edition

Fukue, J. 1987, Publications of the Astronomical Society of Japan, 39, 309

—. 2020, Mon. Not. R. Astron. Soc., 499, 3571, doi: 10.1093/mnras/staa3052

Gair, J. R., Babak, S., Sesana, A., et al. 2017, in Journal of Physics Conference Series, Vol. 840, Journal of Physics Conference Series, 012021, doi: 10.1088/1742-6596/840/1/012021

Gair, J. R., & Glampedakis, K. 2006, Phys. Rev. D, 73, 064037, doi: 10.1103/PhysRevD.73.064037

Gair, J. R., Vallisneri, M., Larson, S. L., & Baker, J. G. 2013, Living Reviews in Relativity, 16, 7, doi: 10.12942/lrr-2013-7

Gal'tsov, D. V. 1982, Journal of Physics A Mathematical General, 15, 3737, doi: 10.1088/0305-4470/15/12/025

Gammie, C. F., & Popham, R. 1998, ApJ, 498, 313, doi: 10.1086/305521

Garg, M., Derdzinski, A., Zwick, L., Capelo, P. R., & Mayer, L. 2022, Mon. Not. R. Astron. Soc., 517, 1339, doi: 10.1093/mnras/stac2711

Genzel, R., Eisenhauer, F., & Gillessen, S. 2010, Rev. Mod. Phys., 82, 3121, doi: 10.1103/RevModPhys.82.3121

Gertsenshteĭn, M. E., & Pustovoĭt, V. I. 1963, Soviet Journal of Experimental and Theoretical Physics, 16, 433

Ghez, A. M., & et. al. 2008, ApJ, 689, 1044, doi: 10.1086/592738

Giampieri, G. 1993, arXiv e-prints, astro. https://arxiv.org/abs/astro-ph/9305034

Gilfanov, M., Churazov, E., Sunyaev, R., et al. 1993, Astronomy and Astrophysics, Supplement Series, 97, 303

Giri, K., & Chakrabarti, S. K. 2013, Mon. Not. R. Astron. Soc., 430, 2836, doi: 10.1093/mnras/stt087

Giri, K., Garain, S. K., & Chakrabarti, S. K. 2015, Monthly Notices of the Royal Astronomical Society, 448, 3221, doi: 10.1093/mnras/stv223

Glampedakis, K., Hughes, S. A., & Kennefick, D. 2002, Physical Review D, 66, 064005, doi: 10.1103/PhysRevD.66.064005

Glampedakis, K., & Kennefick, D. 2002, Physical Review D, 66, 044002, doi: 10.1103/PhysRevD.66.044002

Gottardi, L., de Waard, A., Usenko, O., et al. 2007, Physical Review D, 76, 102005, doi: 10.1103/PhysRevD.76.102005

Guo, H.-K., Sinha, K., & Sun, C. 2019, Journal of Cosmology and Astroparticle Physics, 2019, 032, doi: 10.1088/1475-7516/2019/09/032

Ho, L. C. 2008, Annual Review of Astronomy and Astrophysics, 46, 475, doi: 10.1146/annurev.astro.45.051806.110546

Homan, J., & Belloni, T. 2005, Astrophys. Space Sci., 300, 107, doi: 10.1007/s10509-005-1197-410.48550/arXiv.astro-ph/0412597

Hoyle, F., & Lyttleton, R. A. 1939, Proceedings of the Cambridge Philosophical Society, 35, 405, doi: 10.1017/S0305004100021150

Hu, W.-R., & Wu, Y.-L. 2017, National Science Review, 4, 685, doi: 10.1093/nsr/nwx116

Hubeny, I. 1990, ApJ, 351, 632, doi: 10.1086/168501

Hubeny, I., & Hubeny, V. 1997, ApJL, 484, L37, doi: 10.1086/310774

—. 1998, ApJ, 505, 558, doi: 10.1086/306207

Hulse, R. A., & Taylor, J. H. 1974, ApJL, 191, L59, doi: 10.1086/181548

Ichimaru, S. 1977, ApJ, 214, 840, doi: 10.1086/155314

Jennison, R. C., & Das Gupta, M. K. 1953, Nature, 172, 996, doi: 10.1038/172996a0

Jiang, Y.-F., Stone, J. M., & Davis, S. W. 2014, ApJ, 796, 106, doi: 10.1088/0004-637X/796/2/106

—. 2019, ApJ, 880, 67, doi: 10.3847/1538-4357/ab29ff

Karas, V., & Šubr, L. 2001, A & A, 376, 686, doi: 10.1051/0004-6361:20011009

Kato, S., Fukue, J., & Mineshige, S. 2008, Black-Hole Accretion Disks — Towards a New Paradigm —

Kato, S., Honma, F., & Matsumoto, R. 1988, Publications of the Astronomical Society of Japan, 40, 709

Katz, J. I. 1977, ApJ, 215, 265, doi: 10.1086/155355

Kavanagh, B. J., Nichols, D. A., Bertone, G., & Gaggero, D. 2020, Physical Review D, 102, 083006, doi: 10.1103/PhysRevD.102.083006

Kim, H., Jang, U., & Yi, Y. 2019, arXiv e-prints, arXiv:1904.08110. https://arxiv.org/abs/1904.08110

Kim, H., & Kim, W.-T. 2007, ApJ, 665, 432, doi: 10.1086/519302

Kocsis, B., Yunes, N., & Loeb, A. 2011, Physical Review D, 84, 024032, doi: 10.1103/PhysRevD.84.024032

Kollmeier, J. A., Onken, C. A., Kochanek, C. S., et al. 2006, The Astrophysical Journal, 648, 128, doi: 10.1086/505646

Koratkar, A., & Blaes, O. 1999, Publications of the Astronomical Society of the Pacific, 111, 1, doi: 10.1086/316294

Kozlowski, M., Jaroszynski, M., & Abramowicz, M. A. 1978, A & A, 63, 209

Kubota, A., & Done, C. 2004, Mon. Not. R. Astron. Soc., 353, 980, doi: 10.1111/j.1365-2966.2004.08134.x

Kubota, A., & Makishima, K. 2004, The Astrophysical Journal, 601, 428, doi: 10.1086/380433

Kuroda, K., Ni, W.-T., & Pan, W.-P. 2015, International Journal of Modern Physics D, 24, 1530031, doi: 10.1142/S0218271815300311

Lasota, J. P. 1994, in NATO Advanced Study Institute (ASI) Series C, Vol. 417, Theory of Accretion Disks - 2, ed. W. J. Duschl, J. Frank, F. Meyer, E. Meyer-Hofmeister, & W. M. Tscharnuter, 341

Le, T., & Becker, P. A. 2005, The Astrophysical Journal, 632, 476, doi: 10.1086/432927

Le, T., Wood, K. S., Wolff, M. T., Becker, P. A., & Putney, J. 2016, ApJ, 819, 112, doi: 10.3847/0004-637X/819/2/112

Levin, J. 2000, Phys. Rev. Lett., 84, 3515, doi: 10.1103/PhysRevLett.84.3515

Levin, Y. 2007, Monthly Notices of the Royal Astronomical Society, 374, 515, doi: 10.1111/j.1365-2966.2006.11155.x

Li, L.-X., Zimmerman, E. R., Narayan, R., & McClintock, J. E. 2005, ApJS, 157, 335, doi: 10.1086/428089

Liu, B. F., Meyer, F., & Meyer-Hofmeister, E. 2005, A & A, 442, 555, doi: 10.1051/0004-6361:20053207

Lu, J. F. 1985, A & A, 148, 176

Lu, J. F., Yu, K. N., Yuan, F., & Young, E. C. M. 1997, A & A, 321, 665

Luo, B., Brandt, W. N., Hall, P. B., et al. 2015, ApJ, 805, 122, doi: 10.1088/0004-637X/805/2/122

Luo, J., Chen, L.-S., Duan, H.-Z., et al. 2016, Classical and Quantum Gravity, 33, 035010, doi: 10.1088/0264-9381/33/3/035010

Lynden-Bell, D. 1978, Physica Scripta, 17, 185, doi: 10.1088/0031-8949/17/3/009

Lynden-Bell, D., & Pringle, J. E. 1974, Mon. Not. R. Astron. Soc., 168, 603, doi: 10.1093/mnras/168.3.603

Lynden-Bell, D., & Rees, M. J. 1971, Mon. Not. R. Astron. Soc., 152, 461, doi: 10.1093/mnras/152.4.461

Maccarone, T. J., & Coppi, P. S. 2003, Mon. Not. R. Astron. Soc., 338, 189, doi: 10.1046/j.1365-8711.2003.06040.x

Maggiore, M. 2007, Gravitational Waves: Volume 1: Theory and Experiments (Oxford University Press), doi: 10.1093/acprof:oso/9780198570745.001.0001

Malkan, M. A., & Sargent, W. L. W. 1982, ApJ, 254, 22, doi: 10.1086/159701

Mandal, S., & Chakrabarti, S. K. 2008, ApJL, 689, L17, doi: 10.1086/595782

Matsumoto, R., Kato, S., Fukue, J., & Okazaki, A. T. 1984, Publications of the Astronomical Society of Japan, 36, 71

Mauceli, E., Geng, Z. K., Hamilton, W. O., et al. 1996, Phys. Rev. D, 54, 1264, doi: 10.1103/PhysRevD.54.1264

Mayer, L. 2013, Classical and Quantum Gravity, 30, 244008, doi: 10.1088/0264-9381/30/24/244008

McClintock, J. E., Narayan, R., & Steiner, J. F. 2014, Space Science Reviews , 183, 295, doi: 10.1007/s11214-013-0003-9

McClintock, J. E., & Remillard, R. A. 2006, Black hole binaries, ed. W. Lewin & M. Van der Klis, Vol. 39, 157–213

Memmesheimer, R.-M., Gopakumar, A., & Schäfer, G. 2004, Physical Review D, 70, 104011, doi: 10.1103/PhysRevD.70.104011

Merkowitz, S. M., & Johnson, W. W. 1997, Physical Review D, 56, 7513, doi: 10.1103/PhysRevD.56.7513

Meyer, F., Liu, B. F., & Meyer-Hofmeister, E. 2007, A & A, 463, 1, doi: 10.1051/0004-6361:20066203

Meyer-Hofmeister, E., Liu, B. F., & Meyer, F. 2005, A & A, 432, 181, doi: 10.1051/0004-6361:20041631

Miller, M. C., Freitag, M., Hamilton, D. P., & Lauburg, V. M. 2005, ApJL, 631, L117, doi: 10.1086/497335

Mineshige, S., Kawaguchi, T., Takeuchi, M., & Hayashida, K. 2000, Publications of the Astronomical Society of Japan, 52, 499, doi: 10.1093/pasj/52.3.499

Mino, Y. 2003, Physical Review D, 67, 084027, doi: 10.1103/PhysRevD.67.084027

—. 2005a, Progress of Theoretical Physics, 113, 733, doi: 10.1143/PTP.113.733

—. 2005b, Classical and Quantum Gravity, 22, S717, doi: 10.1088/0264-9381/22/15/007

Mishra, B., Kluźniak, W., & Fragile, P. C. 2019, Mon. Not. R. Astron. Soc., 483, 4811, doi: 10.1093/mnras/sty3124

Misner, C. W., Thorne, K. S., & Wheeler, J. A. 1973, Gravitation (San Francisco: W. H. Freeman)

Miyamoto, S., Kitamoto, S., Hayashida, K., & Egoshi, W. 1995, ApJL, 442, L13, doi: 10.1086/187804

Molteni, D., Gerardi, G., & Chakrabarti, S. K. 1994, ApJ, 436, 249, doi: 10.1086/174897

Molteni, D., Gerardi, G., Valenza, M. A., & Lanzafame, G. 1999, in Astrophysics and Space Science Library, Vol. 234, Observational Evidence for the Black Holes in the Universe, ed. S. K. Chakrabarti, 83, doi: 10.1007/978-94-011-4750-7_6

Molteni, D., Ryu, D., & Chakrabarti, S. K. 1996a, ApJ, 470, 460, doi: 10.1086/177877

Molteni, D., Sponholz, H., & Chakrabarti, S. K. 1996b, ApJ, 457, 805, doi: 10.1086/176775

Mondal, S. 2010, ApJ, 708, 1442, doi: 10.1088/0004-637X/708/2/1442

Mondal, S., Adhikari, T. P., Hryniewicz, K., Stalin, C. S., & Pandey, A. 2022a, A & A, 662, A77, doi: 10.1051/0004-6361/202243084

Mondal, S., Basu, P., & Chakrabarti, S. K. 2009, Monthly Notices of the Royal Astronomical Society, 396, 1038, doi: 10.1111/j.1365-2966.2009.14770.x

Mondal, S., Chakrabarti, S. K., & Nandi, P. 2022b, in Fifteenth Marcel Grossmann Meeting on General Relativity, ed. E. S. Battistelli, R. T. Jantzen, & R. Ruffini, 231–236, doi: 10.1142/9789811258251_0018

Mondal, S., & Choi, C. S. 2013, New Astron., 19, 109, doi: 10.1016/j.newast.2012.08.001

Mondal, S., Palit, B., & Chakrabarti, S. K. 2022c, Journal of Astrophysics and Astronomy, 43, 90, doi: 10.1007/s12036-022-09881-0

Mondal, S., Rani, P., Stalin, C. S., Chakrabarti, S. K., & Rakshit, S. 2022d, A & A, 663, A178, doi: 10.1051/0004-6361/202141990

Mondal, S., & Stalin, C. S. 2021, Galaxies, 9, 21, doi: 10.3390/galaxies9020021

Moore, C. J., Cole, R. H., & Berry, C. P. L. 2015, Classical and Quantum Gravity, 32, 015014, doi: 10.1088/0264-9381/32/1/015014

Mortlock, D. J., Warren, S. J., Venemans, B. P., et al. 2011, Nature, 474, 616, doi: 10.1038/nature10159

Muchotrzeb, B. 1983, Acta Astron., 33, 79

Muchotrzeb, B., & Paczynski, B. 1982, Acta Astron., 32, 1

Muehlner, D. J., & Weiss, R. 1972, Massachusetts Institute of Technology. Research Laboratory of Electronics. http://hdl.handle.net/1721.1/56271

Mummery, A., & Balbus, S. A. 2019a, Monthly Notices of the Royal Astronomical Society, 489, 143, doi: 10.1093/mnras/stz2142

—. 2019b, Monthly Notices of the Royal Astronomical Society, 489, 132, doi: 10.1093/mnras/stz2141

Nagakura, H., & Yamada, S. 2008, ApJ, 689, 391, doi: 10.1086/590325

Nagarkoti, S., & Chakrabarti, S. K. 2016, Monthly Notices of the Royal Astronomical Society, 462, 850, doi: 10.1093/mnras/stw1700

Nakayama, K. 1994, Mon. Not. R. Astron. Soc., 270, 871, doi: 10.1093/mnras/270.4.871

Nakayama, K., & Fukue, J. 1989, Publications of the Astronomical Society of Japan, 41, 271

Nandi, P., Chakrabarti, S. K., & Mondal, S. 2019, ApJ, 877, 65, doi: 10.3847/1538-4357/ab1d62

Nandi, P., Chatterjee, A., Chakrabarti, S. K., & Dutta, B. G. 2021, Monthly Notices of the Royal Astronomical Society, 506, 3111, doi: 10.1093/mnras/stab1699

Narayan, R. 2000, ApJ, 536, 663, doi: 10.1086/308956

Narayan, R., & Popham, R. 1993, Nature, 362, 820, doi: 10.1038/362820a0

Narayan, R., & Yi, I. 1994, ApJL, 428, L13, doi: 10.1086/187381

—. 1995a, ApJ, 444, 231, doi: 10.1086/175599

—. 1995b, ApJ, 452, 710, doi: 10.1086/176343

Nitz, A. H., Capano, C., Nielsen, A. B., et al. 2019, ApJ, 872, 195, doi: 10.3847/1538-4357/ab0108

Nobuta, K., & Hanawa, T. 1994, Publications of the Astronomical Society of Japan, 46, 257

Novikov, I. D., & Thorne, K. S. 1973, in Black Holes (Les Astres Occlus), ed. C. DeWitt & B. DeWitt, 343–450

Nowak, M. A. 1995, Publications of the Astronomical Society of the Pacific, 107, 1207, doi: 10.1086/133679

Onken, C. A., Bian, F., Fan, X., et al. 2020, Mon. Not. R. Astron. Soc., 496, 2309, doi: 10.1093/mnras/staa1635

Ostriker, E. C. 1999, ApJ, 513, 252, doi: 10.1086/306858

Owen, C. B., Haster, C.-J., Perkins, S., Cornish, N. J., & Yunes, N. 2023, Physical Review D, 108, 044018, doi: 10.1103/PhysRevD.108.044018

Pan, Z., Lyu, Z., & Yang, H. 2021, Physical Review D, 104, 063007, doi: 10.1103/PhysRevD.104.063007

Pan, Z., & Yang, H. 2021, Physical Review D, 103, 103018, doi: 10.1103/PhysRevD.103.103018

Peitz, J., & Appl, S. 1997, Mon. Not. R. Astron. Soc., 286, 681, doi: 10.1093/mnras/286.3.681

Peters, P. C. 1964, Phys. Rev., 136, B1224, doi: 10.1103/PhysRev.136.B1224

Peters, P. C., & Mathews, J. 1963, Physical Review, 131, 435, doi: 10.1103/PhysRev.131.435

Peters, P. C., & Mathews, J. 1963, Phys. Rev., 131, 435, doi: 10.1103/PhysRev.131.435

Petrich, L. I., Shapiro, S. L., Stark, R. F., & Teukolsky, S. A. 1989, ApJ, 336, 313, doi: 10.1086/167013

Petrucci, P.-O., Ferreira, J., Henri, G., & Pelletier, G. 2008, Monthly Notices of the Royal Astronomical Society: Letters, 385, L88, doi: 10.1111/j.1745-3933.2008.00439.x

Piran, T. 1978, ApJ, 221, 652, doi: 10.1086/156069

Poisson, E. 2004, A relativist's toolkit : the mathematics of black-hole mechanics. ISBN 978-0-521-83091-1

Popham, R., & Gammie, C. F. 1998, ApJ, 504, 419, doi: 10.1086/306054

Pound, A., Poisson, E., & Nickel, B. G. 2005, Physical Review D, 72, 124001, doi: 10.1103/PhysRevD.72.124001

Pounds, K. A., Done, C., & Osborne, J. P. 1995, Mon. Not. R. Astron. Soc., 277, L5, doi: 10.1093/mnras/277.1.L5

Pringle, J. E. 1981, Annu. Rev. Astron. Astrophys., 19, 137, doi: 10.1146/annurev.aa.19.090181.001033

Prodi, G. A., & et al. 1998, in Second Edoardo Amaldi Conference on Gravitational Wave Experiments, ed. E. Coccia, G. Veneziano, & G. Pizzella, 148

Pugliese, D., Montani, G., & Bernardini, M. G. 2013, Mon. Not. R. Astron. Soc., 428, 952, doi: 10.1093/mnras/sts051

Qian, L., Abramowicz, M. A., Fragile, P. C., et al. 2009, A & A, 498, 471, doi: 10.1051/0004-6361/200811518

Quinn, T. C., & Wald, R. M. 1999, Physical Review D, 60, 064009, doi: 10.1103/PhysRevD.60.064009

Raveh, Y., & Perets, H. B. 2021, Mon. Not. R. Astron. Soc., 501, 5012, doi: 10.1093/mnras/staa4001

Rees, M. J., Begelman, M. C., Blandford, R. D., & Phinney, E. S. 1982, Nature, 295, 17, doi: 10.1038/295017a0

Remillard, R. A., & McClintock, J. E. 2006, Annu. Rev. Astron. Astrophys., 44, 49, doi: 10.1146/annurev.astro.44.051905.092532

Ren, Z., Zhao, T., Cao, Z., et al. 2023, arXiv e-prints, arXiv:2301.02967, doi: 10.48550/arXiv.2301.02967

Rephaeli, Y., & Salpeter, E. E. 1980, ApJ, 240, 20, doi: 10.1086/158202

Rezzolla, L. 2003, arXiv e-prints, gr, doi: 10.48550/arXiv.gr-qc/0302025

Riffert, H., & Herold, H. 1995, ApJ, 450, 508, doi: 10.1086/176161

Robson, T., Cornish, N. J., & Liu, C. 2019, Classical and Quantum Gravity, 36, 105011, doi: 10.1088/1361-6382/ab1101

Rodriguez, J., Corbel, S., & Tomsick, J. A. 2003, ApJ, 595, 1032, doi: 10.1086/377478

Rossi, S., Homan, J., Miller, J. M., & Belloni, T. 2004, Nuclear Physics B Proceedings Supplements, 132, 416, doi: 10.1016/j.nuclphysbps.2004.04.075

Ruderman, M. A., & Spiegel, E. A. 1971, ApJ, 165, 1, doi: 10.1086/150870

Ryan, F. D. 1995, Phys. Rev. D, 52, R3159, doi: 10.1103/PhysRevD.52.R3159

Ryan, F. D. 1996, Physical Review D, 53, 3064, doi: 10.1103/PhysRevD.53.3064

Sadowski, A. 2009, ApJS, 183, 171, doi: 10.1088/0067-0049/183/2/171

Sathyaprakash, B. S., & Schutz, B. F. 2009, Living Reviews in Relativity, 12, 2, doi: 10.12942/lrr-2009-2

Schmidt, M. 1963, Nature, 197, 1040, doi: 10.1038/1971040a0

Schutz, B. F. 1989, in NASA Conference Publication, Vol. 3046, NASA Conference Publication, 7–13

Sesana, A., Haardt, F., Madau, P., & Volonteri, M. 2005, ApJ, 623, 23, doi: 10.1086/428492

Shakura, N. I., & Sunyaev, R. A. 1973, A & A, 500, 33

Shapiro, S. L., & Teukolsky, S. A. 1983, Black holes, white dwarfs, and neutron stars : the physics of compact objects (Wiley, New York,)

Sigurdsson, S., & Rees, M. J. 1997, Mon. Not. R. Astron. Soc., 284, 318, doi: 10.1093/mnras/284.2.318

Sądowski, A., Abramowicz, M., Bursa, M., et al. 2011, A & A, 527, A17, doi: 10.1051/0004-6361/201015256

Smak, J. 1992, Acta Astron., 42, 323

Smith, D. M., Dawson, D. M., & Swank, J. H. 2007, ApJ, 669, 1138, doi: 10.1086/521822

Smith, D. M., Heindl, W. A., & Swank, J. H. 2002, The Astrophysical Journal, 569, 362, doi: 10.1086/339167

Speri, L., Antonelli, A., Sberna, L., et al. 2022, arXiv e-prints, arXiv:2207.10086. https://arxiv.org/abs/2207.10086

—. 2023, Physical Review X, 13, 021035, doi: 10.1103/PhysRevX.13.021035

Straub, O., Bursa, M., Sądowski, A., et al. 2011, A & A, 533, A67, doi: 10.1051/0004-6361/201117385

Suleimanov, V. F., Lipunova, G. V., & Shakura, N. I. 2008, A & A, 491, 267, doi: 10.1051/0004-6361:200810155

Sun, W.-H., & Malkan, M. A. 1989, ApJ, 346, 68, doi: 10.1086/167986

Tagawa, H., Haiman, Z., & Kocsis, B. 2020, ApJ, 898, 25, doi: 10.3847/1538-4357/ab9b8c

Thorne, J., Robotham, A., Davies, L., & Bellstedt, S. 2022, AGN Unification Diagram, Zenodo, doi: 10.5281/zenodo.6381013

Thorne, K. S. 1995, in Particle and Nuclear Astrophysics and Cosmology in the Next Millenium, ed. E. W. Kolb & R. D. Peccei, 160, doi: 10.48550/arXiv.gr-qc/9506086

Thorne, K. S. 1998, in Black Holes and Relativistic Stars, ed. R. M. Wald, 41. https://arxiv.org/abs/gr-qc/9706079

Trakhtenbrot, B. 2014, ApJL, 789, L9, doi: 10.1088/2041-8205/789/1/L9

van der Klis, M. 1995, in X-ray Binaries, 252–307

Vázquez-Aceves, V., Zwick, L., Bortolas, E., et al. 2022, Mon. Not. R. Astron. Soc., 510, 2379, doi: 10.1093/mnras/stab3485

Vokrouhlicky, D., & Karas, V. 1993, Mon. Not. R. Astron. Soc., 265, 365, doi: 10.1093/mnras/265.2.365

—. 1998, Mon. Not. R. Astron. Soc., 298, 53, doi: 10.1046/j.1365-8711.1998.01564.x

Šubr, L., & Karas, V. 1999, A & A, 352, 452. https://arxiv.org/abs/astro-ph/9910401

Wald, R. M. 1984, General relativity (Chicago, University of Chicago Press, ISBN 0-226-87033-2 (paperback))

Wang, J.-M., Du, P., Valls-Gabaud, D., Hu, C., & Netzer, H. 2013, Physical Review Letters, 110, 081301, doi: 10.1103/PhysRevLett.110.081301

Wang, J.-M., & Zhou, Y.-Y. 1999, The Astrophysical Journal, 516, 420, doi: 10.1086/307080

Wang, Y. Y., Wang, F. Y., Zou, Y. C., & Dai, Z. G. 2019, ApJL, 886, L22, doi: 10.3847/2041-8213/ab55e2

Watarai, K.-y., Mizuno, T., & Mineshige, S. 2001, ApJL, 549, L77, doi: 10.1086/319125

Weber, J. 1969, Phys. Rev. Lett., 22, 1320, doi: 10.1103/PhysRevLett.22.1320

—. 1970, Phys. Rev. Lett., 25, 180, doi: 10.1103/PhysRevLett.25.180

Weber, J., & Karade, T. M., eds. 1986, Gravitational radiation and relativity. . proceedings, Sir Arthur Eddington Centenary Symposium, Nagpur, India, January 21-27, 1984. VOL. 3

Wiener, N. 1949, Extrapolation, interpolation, and smoothing of stationary time series, MIT press Cambridge, MA

Will, C. M. 2011, Proceedings of the National Academy of Science, 108, 5938, doi: 10.1073/pnas.1103127108

Wu, X.-B., Wang, F., Fan, X., et al. 2015, Nature, 518, 512, doi: 10.1038/nature14241

Yagi, K., & Seto, N. 2011, Physical Review D, 83, 044011, doi: 10.1103/PhysRevD.83.044011

Yang, R., & Kafatos, M. 1995, A & A, 295, 238

Ye, B.-B., Zhang, X., Zhou, M.-Y., et al. 2019, International Journal of Modern Physics D, 28, 1950121, doi: 10.1142/S0218271819501219

Yunes, N., Arun, K. G., Berti, E., & Will, C. M. 2009, Physical Review D, 80, 084001, doi: 10.1103/PhysRevD.80.084001

Yunes, N., Buonanno, A., Hughes, S. A., Miller, M. C., & Pan, Y. 2010, Phys. Rev. Lett., 104, 091102, doi: 10.1103/PhysRevLett.104.091102

Yunes, N., Kocsis, B., Loeb, A., & Haiman, Z. 2011, Phys. Rev. Lett., 107, 171103, doi: 10.1103/PhysRevLett.107.171103

Yunes, N., Kocsis, B., Loeb, A., & Haiman, Z. 2011, Physical Review Letters, 107, 171103, doi: 10.1103/PhysRevLett.107.171103

Yunes, N., Pani, P., & Cardoso, V. 2012, Physical Review D, 85, 102003, doi: 10.1103/PhysRevD.85.102003

Zanotti, O., Font, J. A., Rezzolla, L., & Montero, P. J. 2005, Mon. Not. R. Astron. Soc., 356, 1371, doi: 10.1111/j.1365-2966.2004.08567.x

Zanotti, O., Rezzolla, L., & Font, J. A. 2003, Mon. Not. R. Astron. Soc., 341, 832, doi: 10.1046/j.1365-8711.2003.06474.x

Zdziarski, A. A., & Gierliński, M. 2004, Progress of Theoretical Physics Supplement, 155, 99, doi: 10.1143/PTPS.155.99

Zhang, S. N., Cui, W., & Chen, W. 1997, ApJL, 482, L155, doi: 10.1086/310705

Zwick, L., Capelo, P. R., Bortolas, E., et al. 2021, Mon. Not. R. Astron. Soc., 506, 1007, doi: 10.1093/mnras/stab1818

Zwick, L., Capelo, P. R., & Mayer, L. 2023, Mon. Not. R. Astron. Soc., 521, 4645, doi: 10.1093/mnras/stad707

**"There is a certain sense in which I would say the universe has a purpose. It's not there by chance."**

**Roger Penrose**